



**HAL**  
open science

# Highly enantioselective synthesis of chiral molecules at modified mesoporous metal electrodes

Sopon Butcha

► **To cite this version:**

Sopon Butcha. Highly enantioselective synthesis of chiral molecules at modified mesoporous metal electrodes. Other. Université de Bordeaux; Vidyasirimedhi Institute of science and technology (Vis-tec), 2022. English. NNT : 2022BORD0234 . tel-03852518

**HAL Id: tel-03852518**

**<https://theses.hal.science/tel-03852518v1>**

Submitted on 15 Nov 2022

**HAL** is a multi-disciplinary open access archive for the deposit and dissemination of scientific research documents, whether they are published or not. The documents may come from teaching and research institutions in France or abroad, or from public or private research centers.

L'archive ouverte pluridisciplinaire **HAL**, est destinée au dépôt et à la diffusion de documents scientifiques de niveau recherche, publiés ou non, émanant des établissements d'enseignement et de recherche français ou étrangers, des laboratoires publics ou privés.

THÈSE EN COTUTELLE PRÉSENTÉE  
POUR OBTENIR LE GRADE DE  
**DOCTEUR DE**  
**L'UNIVERSITÉ DE BORDEAUX**  
**ET DE VIDYASIRIMEDHI INSTITUTE OF SCIENCE**  
**AND TECHNOLOGY**

ÉCOLE DOCTORALE SCIENCES CHIMIQUES

SPÉCIALITÉ : Chimie-Physique

Par Sopon BUTCHA

**Synthèse hautement énantiosélective de molécules  
chirales sur des électrodes métalliques mésoporeuses  
modifiées**

Sous la direction de Prof. Dr. Alexander KUHN  
et de Asst. Prof. Dr. Chularat WATTANAKIT

Soutenue le : 05.08.2022

Membres du jury :

M. HAPIOT, Philippe  
M. SOOKNOI, Tawan  
M. KUHN, Alexander  
Mme. WATTANAKIT, Chularat  
M. CRESPIY, Daniel  
Mme. TANTIRUNGROTECHAI, Jonggol

Research Director, Institute of Chemical Sciences Rennes  
Professor, King Mongkut's Institute of Technology Ladkrabang  
Professor, Institut des Sciences Moléculaire, Bordeaux INP  
Assistant Professor, Vidyasirimedhi Institute of Science and Technology  
Associate Professor, Vidyasirimedhi Institute of Science and Technology  
Associate Professor, Mahidol University

Rapporteur  
Rapporteur  
Directeur de thèse  
Directeur de thèse  
Examineur  
Examineur

# **Titre : Synthèse hautement énantiosélective de molécules chirales sur des électrodes métalliques mésoporeuses modifiées**

**Résumé :** L'un des besoins humains fondamentaux est celui de médicaments efficaces. Pour les applications pharmaceutiques, les composés utilisés comme médicament sont très souvent des molécules chirales. Ils ont deux configurations image-miroir possibles (énantiomères), mais une seule d'entre elles montre généralement une activité biologique, tandis que l'autre est soit inactive, soit même toxique. Ainsi, le développement de méthodes pour obtenir sélectivement un énantiomère est d'une importance cruciale. Cela peut être réalisé soit par la séparation de mélanges racémiques, soit par une synthèse chirale sélective. Notre groupe a établi des électrodes métalliques mésoporeuses imprimées avec une information chirale et a démontré qu'elles peuvent être utilisées pour l'électrosynthèse énantiosélective. Ces matériaux permettent d'atteindre pendant l'électroréduction de composés achiraux un excès énantiomérique de plus de 90%. Cependant, le temps de réaction assez long et la durée de vie limitée des électrodes restreint pour le moment leur utilité pratique.

Par conséquent, dans cette thèse, nous avons exploré différentes stratégies pour augmenter la performance de ces électrodes. Le premier chapitre présente une stratégie alternative pour fonctionnaliser la surface externe d'électrodes de platine mésoporeuses chirales avec des ligands organosoufrés. Cette modification vise à diminuer le degré de réactions indésirables. Les résultats ont révélé que l'enrobage d'une électrode de Pt avec un ligand thiol pouvait considérablement augmenter l'excès énantiomérique de la molécule désirée au-delà de 90%, tout en diminuant le temps de réaction.

Ensuite, une nouvelle stratégie d'impression chirales dans des alliages métalliques mésoporeux a été étudiée. Un métal promoteur, l'iridium, a été associé au Pt pour générer un alliage platine-iridium. La formation de l'alliage a été confirmée par spectroscopie photoélectronique à rayons X (XPS), révélant une composition élémentaire 90:10 at% de Pt et Ir.

Le matériau conçu a été par la suite appliqué à la fois comme catalyseur hétérogène et comme électrocatalyseur pour la synthèse asymétrique via l'hydrogénation et l'électroréduction respectivement. Dans le cas de l'électrosynthèse, une énantiosélectivité de presque 100% a pu être atteinte, combiné avec une stabilité électrochimique exceptionnelle. L'alliage nanostructuré a aussi été utilisé comme catalyseur hétérogène pour l'hydrogénation asymétrique de cétones aromatiques simples. Dans ce cas, les films de Pt-Ir chiraux ont été déposés sur une mousse de nickel à haute surface, afin d'améliorer l'accessibilité des sites imprimés par les précurseurs moléculaires. Dans des conditions expérimentales optimisés, un degré très élevé d'énantiosélectivité allant jusqu'à 85% a été obtenu, même après plusieurs cycles catalytiques successifs.

Enfin, l'alliage a été testée comme matériau d'électrode pour la discrimination énantiomérique par électrochimiluminescence (ECL). La phénylalanine (PA), qui se présente sous forme de L-PA et de D-PA, a été étudiée comme un acide aminé modèle qui peut servir simultanément d'analyte cible et de coréactif, avec le luminophore  $[\text{Ru}(\text{bpy})_3]^{2+}$ , pour générer des signaux ECL vingt fois plus élevés pour le bon énantiomère par rapport à son antipode.

En résumé, cette thèse souligne que la conception de ces surfaces d'électrodes chirales ouvre des perspectives fascinantes dans le cadre global des technologies chirales, allant de la catalyse asymétrique utilisant des voies électrochimiques et chimiques à une discrimination énantiomérique efficace basée à la fois des méthodes électrochimiques traditionnelles et des stratégies d'analyse opto-électrochimiques.

**Mots clés :** Empreinte chirale, Métaux mésoporeux, Synthèse asymétrique, Discrimination énantiomérique

---

**Title : Highly enantioselective synthesis of chiral molecules at modified mesoporous metal electrodes**

**Abstract :** One of the basic human needs is access to efficient drugs. For pharmaceutical applications, compounds used as drugs are very often chiral

molecules. They have two possible mirror-image configurations (enantiomers), but only one of them usually shows biological activity, while the other is either inactive or even toxic. Thus, the development of methods to selectively obtain one enantiomer is of crucial importance. The production of a pure enantiomer can be achieved either by the separation of racemic mixtures or by chiral selective synthesis. Our group has established mesoporous metal electrodes imprinted with chiral information and has demonstrated that they can be used for enantioselective electrosynthesis. During the electroreduction of achiral compounds, these materials allow reaching an enantiomeric excess of more than 90%. However, the long reaction time and the limited lifetime of the electrodes restrict their practical use for the moment.

Therefore, in this thesis, we explored different strategies to increase the performance of these electrodes. The first chapter presents an alternative strategy to functionalize the unselective surface of chiral mesoporous platinum electrodes with organosulfur ligands, mainly located at the external surface. This modification is intended to decrease the degree of undesirable reactions. The results revealed that coating a Pt electrode with a thiol ligand could significantly increase the enantiomeric excess of the desired molecule beyond 90% while decreasing the reaction time.

Next, a new strategy for chiral printing in mesoporous metal alloys was investigated. A promoter metal, iridium, was combined with Pt to generate a platinum-iridium alloy. The formation of the alloy was confirmed by X-ray photoelectron spectroscopy (XPS), revealing a 90:10 at% elemental composition of Pt and Ir.

The designed material was subsequently applied both as a heterogeneous catalyst and as an electrocatalyst for asymmetric synthesis *via* hydrogenation and electroreduction, respectively. In the case of electrosynthesis, the enantioselectivity of almost 100% could be achieved, combined with exceptional electrochemical stability. The nanostructured alloy was also used as a heterogeneous catalyst for the asymmetric hydrogenation of simple aromatic ketones. In this case, the chiral Pt-Ir films were deposited on a high surface area of nickel foam to improve the accessibility of the imprinted sites by the molecular precursors. Under optimized experimental conditions, a very high degree of enantioselectivity, up to 85%, was obtained, even after several successive catalytic cycles.

Finally, the alloy was tested as an electrode material for enantiomeric discrimination by electrochemiluminescence (ECL). Phenylalanine (PA), which exists

as L-PA and D-PA, was studied as a model amino acid that can simultaneously serve as a target analyte and co-reactant, along with the luminophore  $[\text{Ru}(\text{bpy})_3]^{2+}$ , to generate twenty-fold higher ECL signals for the correct enantiomer compared to its antipode.

In summary, this thesis highlights that the design of these chiral electrode surfaces opens up fascinating perspectives in the overall framework of chiral technologies, ranging from asymmetric catalysis using electrochemical and chemical pathways to efficient enantiomeric discrimination based on both traditional electrochemical methods and opto-electrochemical analysis strategies.

**Keywords :** Chiral imprinting, Mesoporous metals, Asymmetric synthesis, Enantiomeric discrimination

---

**Université de Bordeaux**

Bordeaux INP, Site ENSCBP, 16 avenue Pey Berland 33607 France

## **Acknowledgement**

First and foremost, I would like to express my deepest gratitude to my thesis supervisor, Asst. Prof. Dr. Chularat Wattanakit and Prof. Dr. Alexander Kuhn, for their valuable suggestions, immense knowledge, and attentive supervision throughout my study over the past five years. I am also most grateful to the jury members of my thesis defense, including Prof. Dr. Philippe Hapiot, Prof. Dr. Tawan Sooknoi, Assoc. Prof. Dr. Daniel Crespy and Assoc. Prof. Dr. Jonggol Tantirungrotechai for their valuable comments.

Furthermore, my sincere thanks for the oversea internship opportunity to conduct research at the NanoSystèmes Analytiques (NsysA), ISM, University of Bordeaux (U. of BOR), France, from November 2018 to October 2020. The obtained experiences led me to work on exciting projects, which gave me new perspectives on research different from what I used to do at the Vidyasirimedhi Institute of Science and Technology (VISTEC). I would like to thank many people who were contributing to the research projects, in particular Prof. Dr. Neso Sojic, Prof. Dr. Vincent Rodriguez, Dr. Sunpet Assavapanumat, Dr. Duangkamon Suttipat, Dr. Marisa Ketkaew, Dr. Somlak Ittisanronnachai, Dr. Jing Yu, Ms. Veronique Lapeyre, Ms. Sudatip Phromaruk, Mr. Bertrand Goudeau, Mr. Zikkawas Pasom and Mr. Thassanant Atithev. Likewise, I would also like to thank all the laboratory members in NsysA at U. of BOR. and the Porous Heterogeneous Catalysis Center (PHCC) at VISTEC for all kinds of support and encouragement and for always providing a friendly and motivating environment. I also would like to mention all supports for the characterization equipment from the Frontier Research Center (FRC), VISTEC.

I would acknowledge all the financial support during the study period, including a full scholarship at VISTEC funded by the PTT group and the Franco-Thai Scholarship Program from the French Embassy for a Ph.D. cotutelle program. This research and innovation activity is also funded by the National Research Council of Thailand (NRCT) (N41B650204). I could also benefit from

support by the Development and Promotion of Science and Technology Talents Project (DPST), the Thai government scholarship for the support during the whole period of my study since I was an undergraduate student. The research projects related to my thesis have also been funded and supported by the European Research Council (ERC) under the European Union's Horizon 2020 research and innovation program (grant agreement no. 741251, ERC Advanced Grant ELECTRA), the bilateral PICS program of CNRS, the bilateral CNRS IRP project ChiraChem, the Mid-Career Research Grant 2020 from National Research Council of Thailand (NRCT5-RSA63025-03), the Program Management Unit for Human Resources & Institutional Development, Research and Innovation NXPO (B05F630118 and B05F640207) and the National Nanotechnology Center (NANOTEC), NSTDA, Ministry of Science and Technology, Thailand, through the Research Network NANOTEC (RNN).

Getting through my thesis required more than pure academic support; I sincerely acknowledge support over the past five years by many people, including all my best friends and the Nangnarong channel for their powerful encouragement. Especially Mr.Jakkapan Kumsampao and his family, they never left me feeling alone and constantly showed their care for me. Last but not least, I most gratefully thank my beloved family, Butcha, for all their support throughout the study period. Without all the people mentioned above, I would not have been able to overcome a hard time and achieve this precious goal of my life.

SOPON BUTCHA

5 August 2022

# Contents

	<b>Page</b>
<b>Abstract</b>	II
<b>Acknowledgement</b>	VI
<b>Contents</b>	VIII
<b>List of Tables</b>	XIII
<b>List of Figures</b>	XV
<b>List of Schemes</b>	XXXI
<b>List of Abbreviations</b>	XXXIV
<b>Chapter 1 General Introduction</b>	1
1.1 The design of mesoporous metals by using soft templates	2
1.2 Metal alloys	7
1.3 Chirality	9
1.4 Preparation of chiral metal surfaces	11
1.5 Electrochemical deposition	16
1.6 Concept of chiral catalysts	18
1.7 Electrosynthesis	19
1.8 Recent progress in asymmetric heterogeneous electrocatalysis	20
<b>Chapter 2 Chiral-imprinted mesoporous platinum surfaces protected by organosulfur ligands for highly enantioselective synthesis</b>	25
2.1 Introduction	25
2.2 Experimental section	30
2.2.1 Chemicals	30
2.2.2 Substrate cleaning	30

## Contents (Cont.)

	<b>Page</b>
2.2.3 Synthesis of chiral-imprinted mesoporous platinum (Pt) by electrodeposition	31
2.2.4 Surface functionalization of chiral-imprinted mesoporous Pt electrodes with organosulfur ligands	32
2.2.5 Characterization	33
2.2.6 Enantioselective electrosynthesis of 1-phenylethanol (1-PE)	33
2.2.7 Asymmetric electrosynthesis of 1-(4-bromophenyl) ethanol (1-BrPE)	34
2.2.8 Reusability test of the electrocatalysts	34
2.2.9 Calculation of operational parameters	35
2.3 Results and Discussion	37
2.3.1 Synthesis and characterization of chiral imprinted mesoporous Pt electrodes	37
2.3.2 Modification of the mesoporous Pt electrodes with thiol ligand	39
2.3.3 Enantioselective synthesis	41
2.4 Conclusion	53
<b>Chapter 3 Synthesis and characterization of chiral-encoded mesoporous Platinum-Iridium (Pt-Ir) alloy films</b>	<b>54</b>
3.1 Introduction	54
3.2 Experimental section	57
3.2.1 Chemicals	57
3.2.2 Synthesis of non-imprinted and chiral-	57

## Contents (Cont.)

	<b>Page</b>
imprinted mesoporous platinum-iridium (Pt-Ir) alloy by electrodeposition supported on Au-coated glass slides	
3.2.3 Synthesis of mesoporous Pt-Ir alloys supported on Ni foams	58
3.2.4 Characterization of the mesoporous platinum-iridium (Pt-Ir) alloy electrodes	59
3.3 Results and Discussion	62
3.3.1 Preparation of plating gel for the synthesis of the mesoporous Pt-Ir electrodes	62
3.3.2 Morphological and topological characterization of mesoporous Pt-Ir alloys supported on Au-coated glass slide	64
3.3.3 Synthesis and characterization of chiral encoded mesoporous Pt-Ir alloy supported on Ni foam	71
3.3.4 Investigation of chiral features of mesoporous Pt-Ir surfaces by Secondary Harmonic Generation (SHG)	78
3.4 Conclusion	86
<b>Chapter 4 Chiral-imprinted mesoporous Platinum-Iridium (Pt-Ir) alloys for highly enantioselective electrocatalysis and asymmetric hydrogenation</b>	<b>88</b>
4.1 Introduction	88
4.2 Experimental section	91

## Contents (Cont.)

	<b>Page</b>
4.2.1 Chemicals	91
4.2.2 Preparation of chiral-imprinted mesoporous Pt-Ir alloy electrodes	91
4.2.3 Highly enantioselective electrosynthesis with PE-encoded mesoporous Pt-Ir alloys supported on Au-coated glass slides	92
4.2.4 Asymmetric hydrogenation with PE-imprinted Pt-Ir surfaces supported on Ni foam	92
4.2.5 Calculation and investigation of catalytic parameters	93
4.3 Results and Discussion	95
4.3.1 Highly selective chiral electrosynthesis with PE-imprinted mesoporous Pt-Ir alloys	95
4.3.2 Asymmetric synthesis via hydrogenation using chiral-encoded mesoporous Pt-Ir alloys supported on Ni foam	102
4.4 Conclusion	111
<b>Chapter 5 Enantiomeric discrimination by traditional electrochemistry and electrochemiluminescence (ECL) on chiral-imprinted mesoporous platinum-iridium (Pt-Ir) surfaces</b>	<b>112</b>
5.1 Introduction	112
5.2 Experimental section	113
5.2.1 Chemicals	113
5.2.2 Synthesis of chiral-encoded mesoporous Pt-Ir alloy electrodes	114

## Contents (Cont.)

	<b>Page</b>
5.2.3 Chiral recognition by traditional electrochemistry using DOPA-imprinted mesoporous Pt-Ir alloy electrodes	114
5.2.4 Chiral discrimination by electrochemiluminescence (ECL) using PA-imprinted mesoporous Pt-Ir alloy electrodes	115
5.3 Results and Discussion	116
5.3.1 Chiral recognition by traditional electrochemistry using DOPA-imprinted mesoporous Pt-Ir alloy electrodes	116
5.3.2 Chiral discrimination by electrochemiluminescence (ECL) using PA-imprinted mesoporous Pt-Ir alloy electrodes	122
5.4 Conclusion	131
<b>Chapter 6 Conclusions and perspectives</b>	<b>132</b>
<b>Résumé</b>	<b>136</b>
<b>Summary</b>	<b>141</b>
<b>References</b>	<b>145</b>
<b>Author's Biography</b>	<b>170</b>

## List of Tables

<b>Table</b>		<b>Page</b>
2.1	Summary of efficiency for the bare mesoporous Pt and the different thiol-coated mesoporous Pt electrodes for both continuous and pulsed electrosynthesis	50
3.1	Effect of electrodeposition potential and deposition charge density on the morphology and elemental composition of mesoporous Pt-Ir electrodes	65
3.2	Summary of elemental analysis results obtained by quantitative analysis with EDS, XPS, and ICP-OES	71
3.3	Quantitative analysis of elements in the mesoporous Pt-Ir films supported on Ni foam obtained by EDS, XPS, and ICP-OES	76
3.4	The second-order susceptibility tensors (in the Cartesian coordinates) for a macroscopically isotropic surface (x-y plane) of either achiral or chiral matter	81
4.1	Summarized results of the effect of pH on product selectivity for the electroreduction of acetophenone when using (S)-PE encoded mesoporous Pt- Ir electrodes	98
4.2	Effect of solution pH on the enantioselectivity of the hydrogenation of acetophenone using (R)-PE encoded Pt-Ir films supported on Ni foam	106
4.3	The impact of synthesis time on the enantioselectivity for cyclic hydrogenation of acetophenone using (R)-PE imprinted Pt-Ir on Ni foam	107

## List of Tables (Cont.)

<b>Table</b>		<b>Page</b>
4.4	Summary of catalytic performance of chiral imprinted mesoporous Pt- Ir alloys comparing heterogeneous catalysis and electrocatalysis	110
5.1	Calculated relative electrooxidation peak areas of the different chiral imprinted electrodes from DPV signals	119

## List of Figures

Figure		Page
1.1	IUPAC recommendation classifying porous materials according to their pore sizes	1
1.2	Chemical formula and schematic structure of octaethyleneglycol monohexadecyl ether ( $C_{16}EO_8$ ) bearing a hydrophilic head group and a hydrophobic alkyl chain	3
1.3	Illustration of LLC phases: A) Formation of the LLC phase in an aqueous system together with graphics of the non-ionic surfactant structures ( $C_{16}EO_8$ ); B) Formation of the LLC phase in the presence of hexachloroplatinic acid	4
1.4	The concept of mesostructure formation using the soft template strategy: A) Graphical explanation of the typical fabrication steps of mesoporous metals via the lyotropic liquid crystal (LLC) templating strategy; B) Fragmented periodic table indicating several promising candidates by circle with ditch lines that can be employed for the synthesis of mesoporous metals	5
1.5	Simple schematic illustration of substitutional and interstitial impurity atoms in the solid alloy solution	7
1.6	Solid-solution strengthening accomplished by A) imposing a tensile strain on a lattice of host atoms by substitution with a smaller impurity atom and B) imposing compressive strains on a lattice of host atoms by substitution with a larger impurity atom	8

## List of Figures (Cont.)

Figure		Page
1.7	Relationship between tensile strength and hardness of a Pt-Ir alloy as a function of percentages of Ir (wt%)	9
1.8	Illustration of chirality represented by the left and right hands and tetrahedral carbon molecules with four different substituents, demonstrating the two enantiomers are non-superimposable mirror images of each other	10
1.9	Graphical demonstration of chirally crystalline metal surfaces when breaking the symmetry of crystal planes	12
1.10	Graphical illustration demonstrating the elaboration of chiral-encoded mesoporous metals: A) The precursor plating gel composed of a lyotropic liquid crystal, chiral templates, and metal salts in an aqueous solution; B) Generation of the mesoporous metal <i>via</i> electroreduction of metal salts around the templates; C) The model structures of the obtained chiral-encoded mesoporous metals after the extraction of templates	15
1.11	A simplified electrodeposition mechanism involving the coordination chemistry of the solvated metal ions in a plating bath	17
1.12	Illustration of chiral catalysis demonstrated by A) energy diagrams for a catalyzed or uncatalyzed reaction, B) symbolic explanation of the concept of chiral catalysis by a handshake and C) energy diagram of kinetically controlled asymmetric catalysis	18

## List of Figures (Cont.)

Figure		Page
1.13	Important parameters governing asymmetric electrochemical synthesis in batch-type	20
1.14	Chiral-imprinted mesoporous Pt electrode for asymmetric electrosynthesis: A) Reduction of phenyl glyoxylic acid to mandelic acid; B) Electrohydrogenation of the prochiral starting compound at the chiral cavity, (R)-mandelic acid imprinted site; C) Formation of the particular chiral product after the reaction	22
2.1	Schematic explanation of the SAM formation of a linear alkyl thiol on Au(111); (i) Physisorption; (ii) Initial stage of chemisorption in a similar position; (iii) Phase transformation of alkanethiols from a horizontal to a vertical configuration; (iv) Dense packing of the thiol SAM	29
2.2	Apparatus for the asymmetric electrosynthesis composed of a potentiostat equipped with a three-electrode system, applying chronoamperometry, in a home-made electrochemical cell containing the stirred prochiral solution	34

## List of Figures (Cont.)

Figure		Page
2.3	Morphological and electrochemical characterization of Pt electrodes: A) Top-view and B) Cross-sectional SEM images; C) TEM images of an ultra-thin mesoporous Pt film; D) Cyclic voltammograms of mesoporous Pt (red) in comparison with a flat Pt electrode (black) measured in 0.5 M H <sub>2</sub> SO <sub>4</sub> at a scan rate of 100 mV s <sup>-1</sup>	38
2.4	Graphical illustration of the two thiol-coating strategies and the resulting surface blocking properties on mesoporous Pt electrodes: A) and B) Thiol coating <i>via</i> self-assembly from solution and microcontact printing ( $\mu$ CP), respectively; C) and D) Cyclic voltammograms of the solution-coated and $\mu$ CP-coated mesoporous Pt electrodes in 10 mM K <sub>4</sub> Fe(CN) <sub>6</sub> /1 M HNO <sub>3</sub> at a scan rate of 100 mV s <sup>-1</sup>	40
2.5	HPLC chromatogram indicating the peak positions of acetophenone, (R)- and (S)-PE present in the product solution after potentiostatic electrosynthesis with (S)-PE imprinted mesoporous Pt	42
2.6	Asymmetric synthesis with (S)-PE encoded mesoporous Pt electrodes after functionalization with heptanethiol by self-assembly from solution	43
2.7	Asymmetric synthesis with (S)-PE encoded mesoporous Pt electrodes after functionalization with heptanethiol by microcontact printing ( $\mu$ CP)	44

## List of Figures (Cont.)

Figure		Page
2.8	Cyclic voltammograms of a non-coated mesoporous Pt electrode (black) in comparison with the thiol-coating on mesoporous Pt <i>via</i> $\mu$ CP for five cycles (blue) and the classical solution coating for 4 h (red), recorded in 0.5 M H <sub>2</sub> SO <sub>4</sub> solution at a scan rate of 100 mV s <sup>-1</sup>	45
2.9	Summary of enantioselective synthesis results: A) and B) HPLC chromatograms of the product mixtures performed with (S)-PE and (R)-PE imprinted mesoporous Pt electrodes, respectively, which are either bare or thiol-coated; C) HPLC chromatograms of the product solution when using different electrodes: non-imprinted mesoporous Pt (orange), and thiol-functionalized (S)-PE imprinted mesoporous Pt electrodes synthesized by using different weight ratios of (S)-PE/PtCl <sub>6</sub> <sup>2-</sup> (0.0375 (green), 0.0750 (dark blue)); D) Histogram illustrating the enantiomeric excess (%ee) of different electrodes: bare (S)-PE (black) and (R)-PE (red) encoded mesoporous Pt electrodes (0.150 weight ratio PE/PtCl <sub>6</sub> <sup>2-</sup> ), functionalized (S)-PE imprinted mesoporous Pt electrodes with different (S)-PE/PtCl <sub>6</sub> <sup>2-</sup> weight ratios (0.0375 (green), 0.0750 (dark blue) and 0.150 (light blue)), and a functionalized (R)-PE imprinted mesoporous Pt electrode (0.150 weight ratio (R)-PE/PtCl <sub>6</sub> <sup>2-</sup> ) (pink)	46

## List of Figures (Cont.)

Figure		Page
2.10	Asymmetric electrosynthesis using a thiol SAM on (S)-BrPE and (R)-BrPE encoded mesoporous Pt electrodes	48
2.11	HPLC chromatograms of the product solutions, illustrating product selectivity when using (S)-PE imprinted mesoporous Pt electrodes without further thiol functionalization (black) and with thiol coating using the solution (red) or the microcontact printing (blue) strategy	49
2.12	Reusability test of the thiol-coated Pt electrodes: A) HPLC chromatograms of the products, obtained with (S)-PE imprinted mesoporous Pt modified with a single $\mu$ CP step only at the beginning, for two sequential electrocatalytic runs; B) HPLC chromatograms of the products, obtained with (R)-PE imprinted mesoporous Pt for two electrocatalytic runs, but with a renewal of the $\mu$ CP step after the first run; C) Histogram representating the enantiomeric excess for the two $\mu$ CP strategies used in A) and B)	51
3.1	Schematic illustration of the experimental set-up for electrodeposition of the chiral encoded catalyst on nickel foam	59
3.2	Illustration of the experimental set-up for investigating chiral information by Secondary Harmonic Generation (SHG) on chiral imprinted mesoporous metal films	61
3.3	Optical photograph of metal solutions: A) $\text{H}_2\text{PtCl}_6$ ; B) $\text{H}_2\text{IrCl}_6$ ; C) the mixture of $\text{H}_2\text{PtCl}_6$ and $\text{H}_2\text{IrCl}_6$ ; D) the precursor gel for electrodeposition composed of metal	62

## List of Figures (Cont.)

Figure		Page
	precursors (29 wt%), MilliQ water (29 wt%) and Brij <sup>®</sup> C10 (42 wt%)	
3.4	SEM images of mesoporous Pt-Ir films deposited at different potentials: A), B), and C) electrodeposition at -0.20, -0.10, and -0.05 V vs Ag/AgCl, respectively	64
3.5	Cyclic voltammograms of Pt-Ir electrodes in 0.5 M H <sub>2</sub> SO <sub>4</sub>	65
3.6	Cyclic voltammograms of metal electrodes in 0.5 M H <sub>2</sub> SO <sub>4</sub> measured with a scan rate of 100 mV s <sup>-1</sup> : A) mesoporous Pt-Ir alloys deposited with different charge densities of 6 (red), 8 (green), and 10 (blue) C cm <sup>-2</sup> , respectively; B) mesoporous Pt deposited with 8 C cm <sup>-2</sup> (black)	66
3.7	Microscopic characterization of the mesoporous Pt-Ir electrodes: A) a cross-sectional SEM image of a mesoporous Pt-Ir film deposited with a charge density of 8 C·cm <sup>-2</sup> (scale bar of 100 nm); B) TEM image of an ultrathin mesoporous Pt-Ir layer with well-organized mesopores (scale bar of 20 nm)	67
3.8	Investigation of alloy structures of the mesoporous Pt-Ir: A) XRD pattern of deposited Pt-Ir alloys obtained with 8 C cm <sup>-2</sup> (blue) and 4 C cm <sup>-2</sup> (red) compared to the standard cards of Pt (PDF #03-065- 2868) (green) and Ir (PDF #01-088-2342) (purple); B) HR-TEM image of ultra-thin Pt-Ir labeled with the Pt-Ir crystalline planes	68

## List of Figures (Cont.)

Figure		Page
	together with the measured d-spacing values; C) calculated lattice parameters of Pt-Ir samples versus the reference lattice constants of Pt and Ir	
3.9	XPS spectra of plain Pt-Ir electrodes with different thicknesses of 8 C cm <sup>-2</sup> (blue) and 4 C cm <sup>-2</sup> (red) plotted together with the standards of either Pt or Ir (black) in the binding energy regions of A) Pt and B) Ir, respectively	69
3.10	XPS spectra from depth-profile analysis of the alloy Pt-Ir 8 C: A) and B) narrow-scan XPS spectra in the binding energy regions of Pt and Ir (black), respectively, with respect to a fresh electrode at an initial time of 0 s (blue) and after etching for 160 s (red); C) Depth-profile XPS spectra obtained by a wide scan as a function of etching time varying from 0 to 160 s	70
3.11	Graphical explanation of the electrodeposition process to synthesize a chiral imprinted mesoporous Pt-Ir alloy supported on Ni foam: A) Illustration of the ingredients, the non-ionic surfactant forming a hexagonal close packed columnar structure, the metal salts and chiral molecules on Ni foam prior to electrodeposition; B) The growth of metallic Pt-Ir alloy throughout the structural templates; C) The obtained chiral imprinted mesoporous Pt-Ir alloy supported on Ni foam after eliminating all templates	72

## List of Figures (Cont.)

Figure		Page
3.12	Surface morphology of a chiral imprinted mesoporous Pt-Ir alloy supported on a Ni foam characterized by the EDS-SEM technique: A) SEM image of a bare Ni foam at low magnification together with B) the EDS mapping of Ni (red); C) SEM image of a Ni foam at high magnification together with D) the EDS mapping of Ni (red); E) and F) SEM images of chiral encoded mesoporous Pt-Ir deposited on Ni foam at low and high magnification, respectively, G) and H) EDS mapping of Pt (green) and Ir (blue); I) SEM image at the junction between the bare Ni support and the deposited Pt- Ir layer together with the actual sample picture (inset), and J), K) and L) EDS mapping of Pt (green), Ir (blue) and Ni (red), respectively	73
3.13	Characterization of the mesoporous Pt-Ir alloy supported on Ni foam prepared with different deposition charge densities; A), B), and C) Cross-sectional SEM images of mesoporous Pt-Ir alloy supported on Ni foam electrodes generated with 4, 8, and 12 C cm <sup>-2</sup> , respectively; D) Cyclic voltammograms of the electrodes prepared with several deposition charge densities in comparison with flat Pt and the bare Ni foam (inset) measured in 0.5 M H <sub>2</sub> SO <sub>4</sub> at a scan rate of 100 mV s <sup>-1</sup> ; E) Relationship between electroactive surface area and the deposition charge density	75

## List of Figures (Cont.)

Figure		Page
3.14	<p>Topology, crystallinity, and elemental composition of the mesoporous Pt-Ir alloy supported on Ni foam; A) and B) TEM images of mesoporous Pt-Ir alloy prepared by deposition on Ni foam electrodes with <math>8 \text{ C cm}^{-2}</math>, shown together with the selected area electron diffraction pattern (SAED) (inset) recorded in normal mode and STEM mode, respectively; C) XRD patterns of Pt-Ir (blue), Pt (green) and Ir (violet) on Ni foam; D) Selected area of the XRD pattern in the region of Pt(111) and Ir(111), for pure Pt (light green), and Pt-Ir alloys with different deposition charge densities of 4 (dark green), 8 (light blue) and 12 (dark blue) <math>\text{C cm}^{-2}</math>, together with pure Ir (violet) supported on Ni foam in comparison to the standard card of Pt (black) and Ir (red); E) and F) XPS spectra of Pt-Ir with 4 (red), 8 (green) and 12 (blue) <math>\text{C cm}^{-2}</math> compared to pure Ir and Pt (black) in the region of Ir and Pt binding energies, respectively</p>	77
3.15	<p>Illustration of photon diagrams for tensors <math>\chi^{eee}</math>, <math>\chi^{eem}</math> and <math>\chi^{mee}</math> and sum-frequency generation over the electric and magnetic transition moment.</p>	79
3.16	<p>Graphical illustration of an isotropic chiral thin film with <math>C_\infty</math> symmetry. Rotation around the z-axis of the film is a symmetry operation.</p>	81
3.17	<p>SEM images of the external surface of mesoporous Pt electrodes generated by electrodeposition at <math>-0.05 \text{ V}</math> vs Ag/AgCl with <math>4 \text{ C cm}^{-2}</math> of charge density for A) (D)-DOPA,</p>	82

## List of Figures (Cont.)

Figure		Page
	B) (L)-DOPA and C) (DL)-DOPA encoded Pt films and D) a non-imprinted Pt electrode (Scale bar of 10 $\mu\text{m}$ )	
3.18	Second-Harmonic Generation (SHG) signals obtained by the reflection mode on chiral DOPA Pt samples at 1030 nm in the polarizer-analyzer configurations as A) $\Psi_{\text{IN-P}_{\text{OUT}}}$ and B) $\Psi_{\text{IN-S}_{\text{OUT}}}$ .	83
3.19	SEM images revealing a topology of chiral mesoporous Pt-Ir alloys generated by electrodeposition at -0.05 V vs Ag/AgCl with 4 C $\text{cm}^{-2}$ charge density and imprinting with A) D-DOPA, B) L-DOPA and C) DL-DOPA (Scale bar of 10 $\mu\text{m}$ )	85
3.20	SHG response as a function of the azimuthal rotation angle. This result is an illustration of the effective averaged response (blue dot) and the simulation (red line) of the SHG intensity obtained from (L)-DOPA encoded mesoporous Pt-Ir alloy	85
3.21	Relationship between the circular-difference response for Pt-Ir alloys imprinted with (D)-, (L)- and (DL)-DOPA	86
4.1	Illustration of two electrosynthesis methods: conventional (upper) and pulsed (lower) asymmetric electrosynthesis	89
4.2	A simple explanation of the procedure for the pulsed hydrogen chemisorption on chiral encoded Pt-Ir deposited on Ni foam	94
4.3	HPLC chromatogram of the product solution after pulsed electrosynthesis of acetophenone (a pulse and relaxation time of 20 and 60 s, respectively, 39% conversion of	96

## List of Figures (Cont.)

Figure		Page
	acetophenone to PE) by using a non-imprinted porous Pt-Ir alloy as the working electrode	
4.4	Cyclic voltammograms at a scan rate of 100 mV s <sup>-1</sup> with a mesoporous Pt-Ir electrode in 1 M NH <sub>4</sub> Cl (red) and a solution containing 40 mM acetophenone (blue) at pH 5.0.	97
4.5	Products analysis after enantioselective electrosynthesis of (S)- or (R)-PE from acetophenone on chiral-imprinted Pt-Ir alloy surfaces as shown by A) HPLC chromatograms of the products obtained by either conventional electrosynthesis for 13 h or pulsed electrosynthesis with a pulse and relaxation time of 30 s, and B) Histograms of the enantiomeric excess (%ee) after electrosynthesis with non-imprinted Pt-Ir (black), (S)-PE (red) and (R)-PE (green) imprinted Pt-Ir electrodes, carried out by potentiostatic electrosynthesis, or (S)-PE-imprinted Pt-Ir electrodes studied in pulsed electrosynthesis with a global synthesis duration of 13 h (dark blue) and 9 h (light blue)	99
4.6	Investigation of pulsed synthesis conditions (defined by pulse time-relaxation duration, respectively) for the electroreduction of acetophenone to (S)-PE illustrated by A) HPLC chromatograms of the products obtained with different pulse conditions and B) Histograms of the enantiomeric excess (%ee) after electrosynthesis by pulsed electroreduction with 30-120 s (black), 30-60 s (red), 30-30 s (green) and 30-15 s (dark blue)	100

## List of Figures (Cont.)

Figure		Page
4.7	Reusability test of a (S)-PE imprinted Pt-Ir electrode: A) HPLC chromatograms of the product solution obtained from pulsed electrosynthesis (30-30 s) when reusing the same electrode for three electrochemical runs; B) Comparative graph of the %ee obtained for three reaction cycles of a (S)-PE imprinted Pt-Ir electrode (orange) and a (S)-PE imprinted monometallic Pt electrode, obtained from literature results (grey)	101
4.8	Selective production of phenylethanol enantiomers <i>via</i> catalytic hydrogenation of acetophenone following two approaches: A) Conventional hydrogenation and B) Pulsed synthesis strategy at chiral encoded Pt-Ir alloy interfaces	103
4.9	HPLC chromatogram of the solution mixtures of the molecules involved in the asymmetric hydrogenation, including acetophenone (9.6 min), (R)-PE (11.2 min), and (S)-PE (11.9 min)	104
4.10	HPLC chromatogram of the product solutions obtained from various reaction mediums with a pH of 1 (red), 3 (orange), 5 (green), and 7 (blue)	105
4.11	HPLC chromatograms of the product solutions obtained with different catalysts, including non-imprinted (black), (R)-PE (red), and (S)-PE (blue) encoded Pt-Ir alloys	106
4.12	HPLC chromatograms of the product solutions obtained with different hydrogenation methods and reaction times; A) Continuous hydrogenation for 5 (red), 10 (black), and	107

## List of Figures (Cont.)

Figure		Page
	15 (green) min; B) Cyclic hydrogenation, with an intermediate cleaning step of 15 min, for 5 (blue), 10 (green) and 15 (red) min of total reaction time	
4.13	Reusability test of the (R)-PE imprinted Pt-Ir catalyst performed with different reaction schemes: A) and B) HPLC chromatograms of chiral products and histograms summarizing the enantiomeric excess (%ee) obtained with a chiral Pt-Ir alloy imprinted with R-(PE) for three independent consecutive catalytic cycles in fresh educt solution for every cycle and rinsing in water after every full cycle: First catalytic cycle after a total reaction time of (i) 5 min (red), (ii) 7 min (orange), (iii) 9 min (light green); Second catalytic cycle after a total reaction time of (iv) 5 min (dark green), (v) 7 min (blue), (vi) 9 min (purple); (vii) Third catalytic cycle after a total reaction time of 5 min (brown)	108
4.14	Pulsed asymmetric catalysis with a chiral encoded Pt-Ir alloy supported on Ni foam: A) HPLC chromatograms of products obtained with R-(PE) imprinted mesoporous Pt-Ir in 1 mM acetophenone for continuous synthesis (black), pulsed asymmetric synthesis with a pulse time of 5 min (orange) and 3 min (purple) with a total synthesis time of 15 min; B) Relationship between the enantiomeric excess and catalytic efficiency comparing conventional and pulsed synthesis	109

## List of Figures (Cont.)

Figure		Page
5.1	Differential pulsed voltammograms of (L)-DOPA (black) and (D)- DOPA (red) obtained with different electrodes A) non-imprinted, B) and C) (L)-DOPA and (D)-DOPA-imprinted mesoporous Pt-Ir alloys, respectively	117
5.2	Differential pulse voltammograms of (L)-DOPA (black) and (D)- DOPA (red) electrooxidation recorded with the different DOPA-imprinted metal electrodes: A) fresh (L)-DOPA imprinted monometallic Pt; B), C) and D) destroyed (L)-DOPA imprinted Pt, (L)-DOPA and (D)-DOPA imprinted Pt-Ir alloys, respectively, after erasing chiral information by CV in 0.5 M H <sub>2</sub> SO <sub>4</sub> for 10 cycles in the potential window from -0.2 to 1.2 V	118
5.3	Differential pulse voltammograms of (L)-DOPA (black) and (D)-DOPA (red) electrooxidation performed with the destroyed (L)-DOPA (left column) and (D)-DOPA (right column) imprinted Pt-Ir electrodes: A) and B) the DPV signals of DOPA-imprinted Pt-Ir alloys after erasing chiral information by CV in 0.5 M H <sub>2</sub> SO <sub>4</sub> for 20 cycles in the potential window from -0.2 to 1.2 V; C) and D) the DPV signals of DOPA-imprinted Pt-Ir alloys after erasing chiral information by CV in 0.5 M H <sub>2</sub> SO <sub>4</sub> for 30 cycles in the potential window from -0.2 to 1.4 V; E) and F) the DPV signals of DOPA-imprinted Pt-Ir alloys after erasing chiral information by CV in 0.5 M H <sub>2</sub> SO <sub>4</sub> for 40 cycles in the potential window from -0.2 to 1.8 V	120

## List of Figures (Cont.)

Figure		Page
5.4	SEM images (scale bars 20 $\mu\text{m}$ ) of A) porous Pt-Ir alloy and B) porous monometallic Pt electrode obtained by electrodeposition with a deposition charge density of 6 C $\text{cm}^{-2}$	121
5.5	Molecular structures of phenylalanine enantiomers	124
5.6	The UV-Vis spectra of the two PA enantiomers	125
5.7	Differential pulse voltammogram (black) and ECL intensity (red) of the analyte solution containing 10 mM (L)-PA and 1 mM $[\text{Ru}(\text{bpy})_3]^{2+}$ dissolved in 0.1 M PBS solution (pH 7.33), using a classical Pt disk as a working electrode	126
5.8	Control experiments showing the characteristics of activated mesoporous Pt-Ir alloys measured in different solutions and using different techniques: A) Cyclic voltammetry, demonstrating a high capacitive current, and the ECL signal using CV-ECL; B) ECL intensity, illustrating the influence of PA concentration using CV-ECL; C) ECL intensity obtained with various analyte solutions, emphasizing the role of PA as a co-reactant in order to generate an ECL signal using DPV-ECL	127
5.9	ECL signals for enantiomeric PA discrimination on fresh (upper row) and regenerated (lower row) Pt-Ir alloy electrodes of A), C) (L)-PA, and B), D) (D)-PA imprinted Pt-Ir electrodes	128

## List of Figures (Cont.)

Figure		Page
5.10	Reusability test of (D)-PA imprinted mesoporous Pt-Ir for the discrimination of PA enantiomers by ECL analysis, performed with the (L)-PA (red) or (D)-PA (black) / $[\text{Ru}(\text{bpy})_3]^{2+}$ system: A)-E) Normalized ECL intensities for five consecutive detection experiments. F) Histogram summarizing the relationship between the enantioselectivity of (D)-PA with respect to (L)-PA as a function of the detection cycle	130

## List of Schemes

Scheme		Page
2.1	Graphical illustration of the preparation process of chiral encoded mesoporous Pt; A) Chiral molecules as molecular templates used in the present work, (R)- and (S)-Phenylethanol ((R)- and (S)-PE); B) Supramolecular structure of adsorbed chiral templates around the external walls of a columnar-non-ionic surfactant structure surrounded by the Pt precursor; C) Growth of Pt metal by electrodeposition in the presence of the mesoporegen and chiral template; D) The final structure of the synthesized Pt electrode after template removal	37
2.2	Electrochemical reduction of acetophenone into the racemic mixture of (S)- and (R)-phenylethanol by two electrons and two protons mechanism	42
2.3	Electroreduction of 4-bromoacetophenone to 1-(4-bromophenyl) ethanol <i>via</i> two electrons and two protons transfer mechanism at the electrode surface	47
2.4	Proposed reaction mechanism for the electroreduction of acetophenone on Pt surfaces	53
3.1	Schematic illustration of the procedure to synthesize a chiral-imprinted mesoporous Pt-Ir alloy: A) chiral molecular templates (S)-PE, (R)-PE, (L)-DOPA, and (D)-DOPA; B) formation of non-ionic surfactant columns with adsorbed chiral molecules in the presence of Pt and Ir salts; C) the growth of alloyed Pt and Ir around the self-assembled templates by co-electrodeposition; D) the	63

## List of Schemes (Cont.)

Scheme		Page
	obtained chiral-encoded mesoporous Pt-Ir alloy after the template removal	
4.1	Electrochemical reduction of acetophenone to (S)- or (R)-phenylethanol	95
4.2	Possible reaction pathway for acetophenone reduction to (i) 2,3-diphenyl-2,3-butanediol and (ii) 1-phenylethanol	96
5.1	Enantiomeric discrimination of an amino acid such as phenylalanine (PA) with chiral-encoded mesoporous Pt-Ir surfaces based on an electrochemiluminescence (ECL) readout	124
5.2	Proposed mechanism of the ECL generation in this study based on the PA/[Ru(bpy) <sub>3</sub> ] <sup>2+</sup> system	129

## List of Abbreviations

APE	Acetophenone
Ag/AgCl	Silver/Silver chloride
at%	Atomic percent
Brij <sup>®</sup> C10	Polyethylene glycol hexadecyl ether
BrAPE	4-bromoacetophenone
BrPE	1-(4-bromophenyl) ethanol
C cm <sup>-2</sup>	Charge density (coulomb/square meter)
C <sub>7</sub> -SH	Heptanethiol
CD	Circular dichroism
Cl <sup>-</sup>	Chloride anion
CV	Cyclic voltammetry
DOPA	3,4-dihydroxy phenylalanine
DPV	Different pulse voltammetry
e <sup>-</sup>	Electron(s)
ECL	Electrochemiluminescence
EDS	Energy Dispersive X-ray spectrometry
EPC	Enantiomerically pure compounds
ECSA	Electrochemically active surface area
%ee	Enantiomeric excess
fcc	Face-centered cubic
g	Gram(s)
H <sup>+</sup>	Proton(s)
H <sub>1</sub>	Hexagonal phase
H <sub>2</sub> O	Water
H <sub>2</sub> PtCl <sub>6</sub>	Hexachloroplatinic (IV) acid
H <sub>2</sub> IrCl <sub>6</sub>	Hexachloroiridic (IV) acid
<i>hkl</i>	Miller indices
h	Hour(s)

HPLC	High-performance liquid chromatography
ICP- OES	Inductively Coupled Plasma Optical Emission Spectroscopy
IUPAC	International Union of Pure and Applied Chemistry
LLC	Lyotropic liquid crystal
LSV	Linear sweep voltammetry
MA	Mandelic acid
min	Minute(s)
Ni	Nickel
NP(s)	Nanoparticle(s)
PA	Phenylalanine (Phe)
PBS	Phosphate buffer solution
PDA	Photodiode array
PE	Phenyl ethanol
Pt-Ir	Platinum-Iridium alloy
PGA	Phenyl glyoxylic acid
[Ru(bpy)] <sub>3</sub> <sup>2+</sup>	Tris(2,2'- bipyridyl) dichlororuthenium (II) complex
SAM	Self-assembled monolayers
SHG	Secondary Harmonic Generation
SEM	Scanning electron microscope
s.e.m	The standard error of the mean of the enantiomeric excess
TEM	Transmission electron microscope
v/v	% volume/volume
vs	Versus
wt%	Weight percent
XPS	X-ray photoelectron spectroscopy
XRD	X-ray diffraction
μCP	Microcontact printing

# Chapter 1

## General Introduction

Over the past decades, the design and development of porous materials with well-ordered structures has gained a lot of attention due to their outstanding properties, such as high porosity and absorption capacity. These characteristics open many applications, particularly for adsorption, separation, and catalysis. [1] Generally, porous substrates cover a large variety of pore dimensions. In the IUPAC recommendations,[2, 3] as shown in **Figure 1.1**,[1] they are classified into three different classes: microporous materials with pore diameters less than 2 nm, such as zeolites and clay; mesoporous materials for those ranging between 2 and 50 nm, for instance, mesoporous silica; macroporous materials containing porous cavities with a diameter over 50 nm such as sponges and activated carbons.

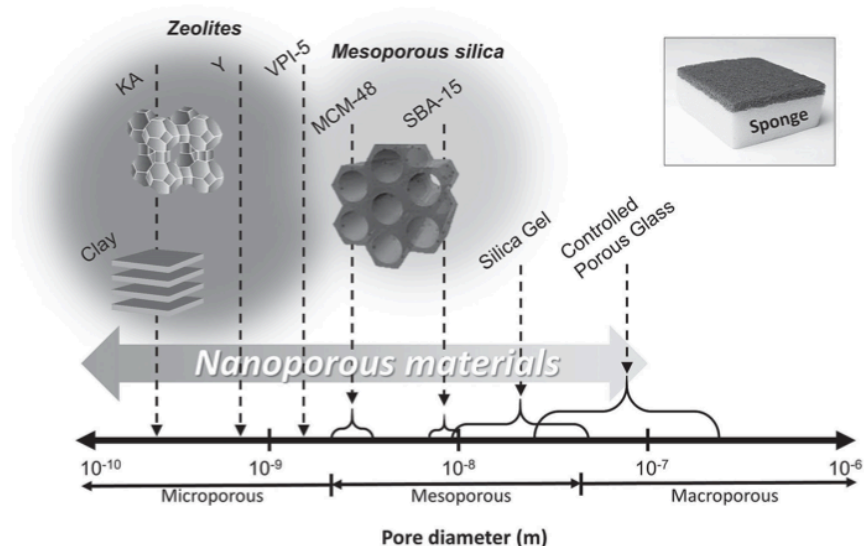


**Figure 1.1** IUPAC recommendation classifying porous materials according to their pore sizes. (Reproduced from [1])

For practical reasons, materials with a too small pore size often suffer from a lower performance in some applications,[4, 5] even though the materials reveal an excellent selectivity, significant absorption capacity, and efficient catalytic properties.[6] Since the discovery of ordered mesoporous silica in the 1990s,[7, 8] this advanced material exhibits many positive aspects, which do not exist in microporous materials, because their unique characteristics like superior surface area, tunable pore size, and identical pore diameter distribution facilitate the accessibility of guest molecules and thus enhance reaction rates.[9, 10] Apart from catalytic applications, mesoporous materials have also been employed in different other sectors, such as adsorption and separation of large species,[11, 12] drug delivery,[13, 14] sensors,[15, 16] functional electronic devices,[17, 18] and fuel cells.[19, 20] In addition, many research efforts have been devoted to generalize the concept of mesoporous materials to different types of substrates, for example, carbons,[21] metals,[22] metal oxides,[23] and hybrid materials.[24, 25] Among them, mesoporous metals reveal distinct physical and chemical properties, including high electrical and thermal conductivity or even significantly higher thermal and chemical stability against structural collapse during the synthesis or utilization.[1, 22] These advantages result in a wide range of implementations such as in electrochemical or photoelectrochemical catalysis,[26-29] surface-enhanced phonon scattering,[30] and highly sensitive biosensors.[31] Therefore, this thesis will propose and discuss the design of advanced mesoporous metals and some original perspectives for their practical use.

## **1.1 The design of mesoporous metals by using soft templates**

To date, various approaches have been introduced for the rational design of mesoporous metals. Typically, an ordered mesoporous structure of metals can be achieved through nanoengineering their morphology by using templating approaches (i.e., hard or soft templating methods).[1, 22] The different shapes and sizes of the required morphologies can be successfully tuned by changing

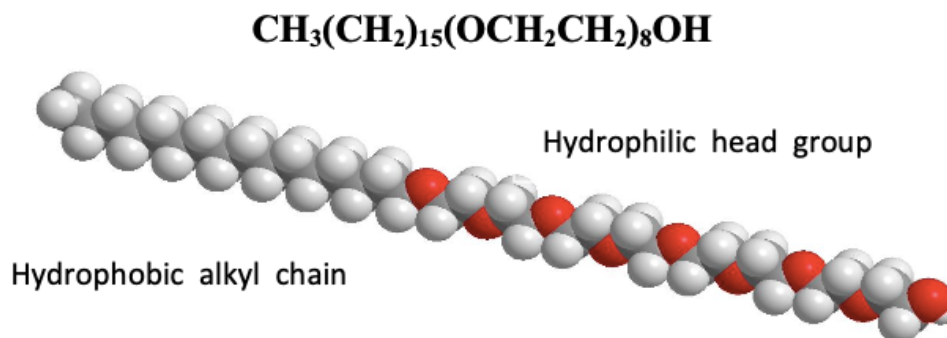


**Figure 1.2** Chemical formula and schematic structure of octaethyleneglycol monohexadecyl ether (C<sub>16</sub>EO<sub>8</sub>) bearing a hydrophilic head group and a hydrophobic alkyl chain. (Reproduced from [34])

the experimental conditions.[32] For instance, when platinum metal (Pt) precursors are mixed together with a high concentration of non-ionic surfactant (soft template) and water, lyotropic liquid crystalline (LLC) phases are obtained.[33] This thesis strongly focuses on octaethyleneglycol monohexadecyl ether (C<sub>16</sub>EO<sub>8</sub>), a non-ionic surfactant containing a long alkyl chain as a hydrophobic part and a head group of ethylene oxides as hydrophilic part (**Figure 1.2**).[34] The non-ionic surfactant is mixed with water to form the LLC phase, as shown in the phase diagram for the C<sub>16</sub>EO<sub>8</sub>/water system in **Figure 1.3A**. [35] The different defined structures of the LLC significantly depend on both the composition and preparation temperature of the plating mixture. At low weight proportions of C<sub>16</sub>EO<sub>8</sub> (wt%) in water, a spherical micellar structure is predominant, with the alkyl chains inside and the ethylene oxide groups on the outermost surface in contact with water, respectively. When the concentration of the non-ionic surfactant increases, the spherical micelles transform into well-packed long cylindrical micelles, resulting in a H<sub>1</sub> hexagonal phase. When the surfactant's concentration is continuously increased, the H<sub>1</sub> phase transforms into a V<sub>1</sub> cubic phase, and then, at a very high concentration, a L<sub>α</sub> lamellar phase is eventually formed.[33, 35] Moreover, it should be noted that in the simultaneous presence of hexachloroplatinic acid in the LLC phase, the stability of the hexagonal H<sub>1</sub> phase can be remarkably enhanced. The higher stability of the H<sub>1</sub> phase is translated by a more pronounced curvature of the

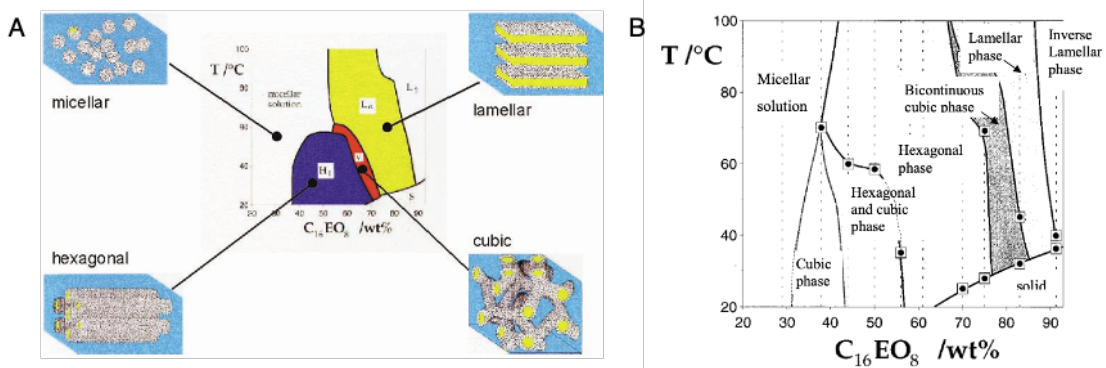


**Figure 1.3** Illustration of LLC phases: A) Formation of the LLC phase in an aqueous system together with graphics of the non-ionic surfactant structures ( $C_{16}EO_8$ ); B) Formation of the LLC phase in the presence of hexachloroplatinic acid (at a fixed concentration of 1.92 M). In the representative structures, blue, white, and yellow indicate the water domain, head groups of the hydrophobic ethylene oxide, and the hydrocarbon tails, respectively. (A and B reproduced from [35] and [33-34], respectively)

boundaries in **Figure 1.3B** between the phases as a function of temperature and composition, compared to the normal LLC phase reported in a recent study.[33]

Thanks to numerous unique features of a mesoporous hexagonal close packed structure, combined with an easy preparation process of such a soft template,[1, 22] it will be used in this contribution for the elaboration of mesoporous metals with high porosity and controllable pore arrangement, for either monometallic metal structures or more complex alloys.

The formed LLC phase of non-ionic surfactant can be used as a mesoporegen during the reduction of metal precursor, generating mesoporous metal structures (**Figure 1.4 A**).[1] It is noteworthy that the LLC geometrically confines the metal precursors in a limited three-dimensional space, thus altering the processes of nucleation and crystal growth of metals around templates. A systematic study using several *in-situ* characterization methods reported that the mesostructure formation occurs by following four steps; (i) reduction of

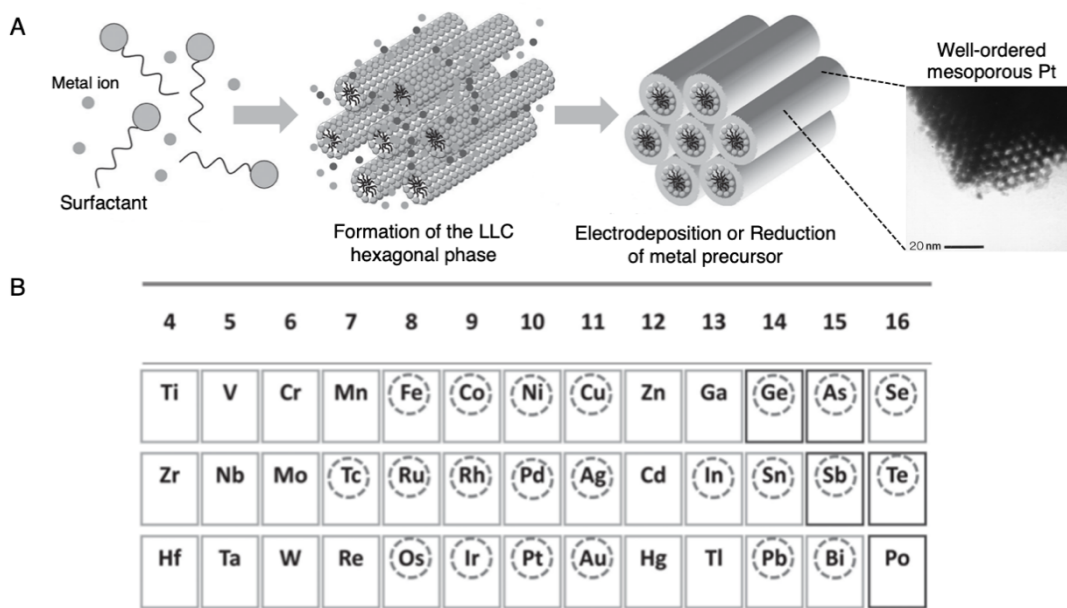


**Figure 1.4** The concept of mesostructure formation using the soft template strategy: A) Graphical explanation of the typical fabrication steps of mesoporous metals *via* the lyotropic liquid crystal (LLC) templating strategy; B) Fragmented periodic table indicating several promising candidates by circle with ditch lines that can be employed for the synthesis of mesoporous metals. (Reproduced and modified from [1] and [38] for the inserted-TEM image)

metallic precursors to initiate the formation of metal nuclei; (ii) generation of small metal nanoparticles; (iii) aggregation (connection) of nanoparticles; (iv) formation of the mesoporous metals *via* interconnecting metal framework structures.[36, 37]

Recently, various studies have reported the design of monometallic mesoporous metals. Indeed, various noble metals, e.g., platinum (Pt),[38] palladium (Pd),[39] ruthenium (Ru) [40] and rhodium (Rh),[41, 42] have been successfully employed for the generation of monometallic mesoporous metals and their oxide forms. The first report on the preparation of a mesoporous metal has been demonstrated by Attard *et al.*,[38] based on the reduction of chloroplatinic acid in the presence of soft templates *via* electrochemical deposition. Various conductive materials, for example, gold-coated substrates

and indium tin oxide (ITO), can be used as solid supports for depositing mesoporous Pt films. Several parameters strongly affect the morphology of the final Pt film, such as temperature, deposition potentials, electrode surface area and solvent.[43, 44] Furthermore, to extend the scope of electrodeposition of mesoporous metal films the synthesis of mesoporous Pd films [39] and ordered mesoporous Ru oxide layers [40] has been reported. This demonstrated that this approach allows generating well-ordered mesoporous structures with superior electrochemical active surface areas (as high as  $100 \text{ m}^2 \cdot \text{g}^{-1}$ ). Apart from precious metals, non-noble metals have also been elaborated for their mesoporous structures such as nickel (Ni) [45] and cobalt (Co);[46] in particular, their mesostructured oxide or hydroxide revealed a high efficiency in supercapacitor applications.[47, 48] Moreover, electrodeposition or chemical deposition has also been successfully employed to prepare various types of well-ordered mesoporous metals, including mesoporous copper (Cu), silver (Ag), gold (Au), zinc (Zn), cadmium (Cd) and tin (Sn).[49] However, it still suffers due to the concern of disordered mesoporous metal structures. In addition, the stability of materials is still a very important feature. For example, mesoporous Cu is easily further oxidized under ambient conditions, but Cd, Ni, and Sn were relatively stable. Furthermore, in some cases of the mesostructured design, it is difficult to form the uniform structure of several mesoporous materials i.e., Ag, Au, and Zn since metals intrinsically show a very fast crystallization rate with the rather slow rate of their mesostructured formation, resulting in achieving their nanoparticles instead of mesoporous structures. Nevertheless, this difficulty can be circumvented by improving the synthesis conditions, such as enlarging the area of the substrate for deposition, introducing the substituents in mesostructural templates, or diluting the plating mixture to reduce the crystal growth rate, eventually allowing the formation of mesostructures.[50-52]

Apart from the above-mentioned deposition of monometallic metals with mesoporous structures, this synthesis approach has also been applied to form mesostructured multi-metals layers using the LLC phase as a mesoporous template (**Figure 1.4 B**).[1] This strategy allows achieving unusual catalytic, mechanic, electronic, optical, and magnetic properties, interesting for various

applications.[1] Several mesoporous binary alloys have been synthesized by electrochemical co-deposition of two different metal sources with the LLC as mesoporegen, such as Pt-Au,[53] Pt-Ru [54] and Pt-Ni.[55] In most cases, this enabled a good control of the ordered mesoporous structure with high electrochemical stability, showcasing a high impact on a wide range of applications, for example, in methanol electrooxidation and fuel cells.

## 1.2 Metal alloys

Apart from a single metal, the design of alloys containing various metals is also attractive, particularly when in combination with mesoporous structures. Typically, there are two different strategies for making the alloys that have been proposed, namely the substitutional and interstitial solid case. For the substitutional situation, the impurities replace the host atoms in the lattice. In contrast, in the interstitial situation, the solute atoms firmly pack between the host atoms in the lattice (**Figure 1.5**).[56] It should be noted that the initial crystal structure should be maintained in both cases.

Generally, the purpose of the alloying technique is to strengthen and harden metals, denoted as a solid-solution strengthening. High-purity metals encounter many demerits, like softer and weaker characteristics in comparison with their alloy analogs. Increasing the concentration of the impurities can

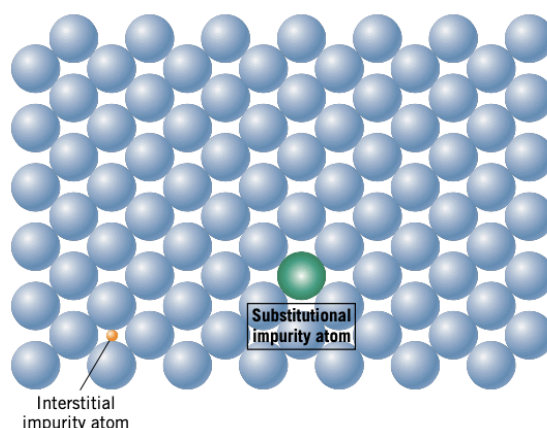


**Figure 1.5** Simple schematic illustration of substitutional and interstitial impurity atoms in the solid alloy solution. (Reproduced from [56])

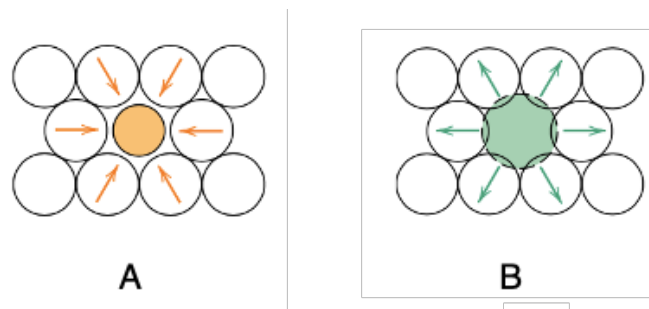


**Figure 1.6** Solid-solution strengthening accomplished by A) imposing a tensile strain on a lattice of host atoms by substitution with a smaller impurity atom and B) imposing compressive strains on a lattice of host atoms by substitution with a larger impurity atom. (Reproduced from [56])

enhance the tensile strengths of the solid solution, because the inserted impurity atoms significantly resist the lattice strain around the neighboring host atoms, preventing dislocation movements in the metal lattice. For instance, a small substituted impurity expands the tensile strain into the region of the surrounding solute atoms (**Figure 1.6 A**).[56] In contrast, a larger impurity atom has the tendency to cancel compressive strains in its surroundings (**Figure 1.6 B**).[56] Therefore, interactions between impurity atoms and host dislocations produce lattice strains that suppress lattice mobility.[56]

Among various types of metal alloys, platinum alloys seem to be promising candidates for many industrial implementations, such as in the automotive industry, as electrodes for energy storage, catalysis, and jewelry manufacturing.[57] Platinum alloys will be further discussed in this contribution, particularly as catalytic systems, because monometallic Pt often suffers from lower stability and limited selective catalytic activity. Typically, by mixing platinum with a promotor, metals such as ruthenium (Ru), rhodium (Rh), iridium (Ir), and gold (Au) are used to form platinum alloys for enhancing the mechanical properties of platinum.[57, 58] Among them, Ir is one of the most outstanding promoters. Theoretically, Ir is approximately four or five times harder than monometallic Pt.[59] Hence, when Pt and Ir are alloyed, the resulting matrix is noticeably more rigid and robust than pure Pt. In addition, introducing Ir into Pt

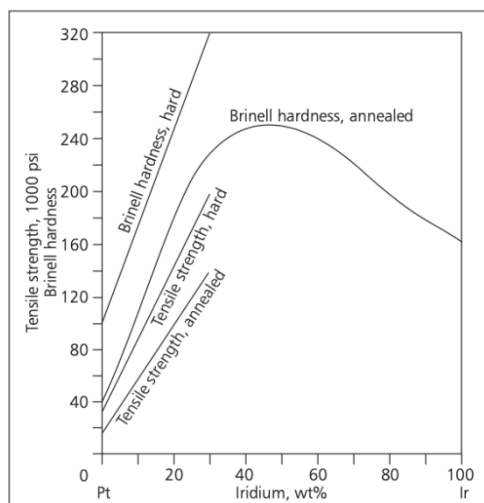


**Figure 1.7** Relationship between tensile strength and hardness of a Pt-Ir alloy as a function of percentages of Ir (wt%). (Reproduced from [57])

results in a significant increase in their hardness and strength;[60] for example, Pt-Ir with up to 30 wt% of Ir is extremely hardening the platinum alloy as shown by a sharp increase in the tensile strength, and the Brinell hardness (**Figure 1.7**).[57]

In addition, Ru also greatly impacts the hardness of a platinum alloy when using suitable amounts ranging from 10 to 20 wt%.[58, 61] Although, the addition of 5 to 40 wt% Rh to platinum has a less observable effect on the mechanical properties compared to other metals, the Rh alloy normally provides the lowest resistivity in comparison to others, eventually leading to a superior catalytic activity.[58, 62] Moreover, Pt containing a few percent of Au has a greater strength and a finer grain structure, and Pt-Au can enhance long-term stability in electrocatalysis.[58, 63]

### 1.3 Chirality

Chirality is the feature of an object or system for which the two mirror symmetric forms cannot be superimposed on each other, leading to distinct handedness (left or right) (**Figure 1.8**).[64] Chirality exists in various chemical compounds, especially in organic molecules containing at least one carbon atom bearing four different substituents. Accordingly, the two possible

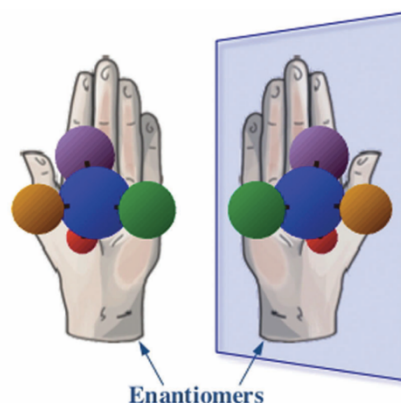


**Figure 1.8** Illustration of chirality represented by the left and right hands and tetrahedral carbon molecules with four different substituents, demonstrating the two enantiomers are non-superimposable mirror images of each other. (Reproduced from [64])

configurations with tetrahedral geometry, result in two distinct mirror-image forms, so-called enantiomers.[64] They play a crucial role due to their intrinsic specific features, in particular in chemical and biological systems. Indeed, chiral receptor sites interact with the two enantiomers in different ways.[65] However, only one corresponding enantiomer frequently tends to be active, whereas the other one is inactive or even toxic with respect to pharmaceutical applications, resulting sometimes in dramatic effects in the human body.[66] For instance, in the case of a commercial pharmaceutical molecule such as thalidomide, (R)-thalidomide seems to be safe and desirable for the calmative effect, while (S)-thalidomide causes fetal damage to pregnant women.[67, 68] Another good illustration is 3,4-dihydroxyphenylalanine or DOPA; (L)-DOPA is moderately effective in enhancing dopamine levels in the medical treatment of Parkinson's disease, whereas (D)-DOPA is biologically inactive.[69]

Typically, a homogeneous mixture of enantiomers, a so-called racemate, is obtained during chemical synthesis.[70] Even though enantiomers show the same chemical and physical properties, their optical activity is generally the opposite.[71] This optical activity of chiral molecules, namely the chiroptical effect, is due to the fact that the refractive index and the extinction coefficient oppose left- and right-hand circularly polarized light.[72] The difference in

refractive index gives rise to the in-plane optical rotation of linearly polarized light when the light interacts with chiral molecules. In contrast, the difference in extinction coefficient leads to circular dichroism, the measured different transmission between enantiomers upon interacting with left- and right-hand circularly polarized light.[72] The beneficial aspect of this chiroptical effect is that it can be used to quantify and classify substances, according to their chiral purity, and to calculate the enantiomeric excess.[72, 73]

#### **1.4 Preparation of chiral metal surfaces**

Due to the many positive aspects of metal surfaces mentioned above, i.e., high conductivity and activity, it is very interesting to modify their surfaces for specific functions. Over the past decades, the engineering of chiral metal surfaces has been an attractive topic in various fields of research. The designed chiral metal surfaces might be potentially used in many applications ranging from pharmaceutical and cosmetic manufacturing, catalysis, and sensing to separation.[74-79] Concerning the rational design of chiral metal surfaces, several approaches have been successfully proposed for the preparation following mainly one of the three principal strategies: (i) modification of metal surfaces with ligands;[80-82] (ii) symmetry breaking of the bulk metal structures;[83, 84] (iii) molecular imprinting with chiral templates.[85-92]

In the early stage of development, chiral information has been initiated by molecular adsorption on metal surfaces.[80, 81, 93] For example, Besenbacher and co-workers reported that chiral metal interfaces have been generated by the self-assembly of the achiral molecule 2,5,8,11,14,17-hexa-*tert*-butylhexabenzob[bc,ef,hi,kl,no,qr]coronene (HtB-HBC), adsorbed on a Cu(110) substrate. The resulting chiral surfaces depend on the rearrangement of the achiral molecules and their close-packed arrangement on the substrate.[93] In another example, chiral surfaces were elaborated by the immobilization of chiral molecules on metal fringes. Baddeley C. J. *et al.* demonstrated that adsorption of two-dimensional ordered (R,R)-tartaric acid on Cu(110) destroys all symmetry elements of the original metal on the interface, resulting in the creation of chiral surfaces. Interestingly, the obtained surfaces

could be applied as a catalyst for heterogeneous enantioselective reactions, i.e., the asymmetric hydrogenation of methyl acetoacetate to the (R)-methyl 3-hydroxybutyrate.[80] However, this concept encounters problems resulting from the ligand leaching during their utilization, leading to a loss of chirality.[94]

To overcome the problem mentioned above, intrinsically chiral metal surfaces can be generated by exposing high-Miller-index surfaces,  $M(hkl)$ . As a simple illustration in the case of the face-centered cubic (fcc) metal lattice shown in **Figure 1.9**, the bulk metal contains high symmetry crystal structures with low-Miller-index planes, e.g., (100), (110), (111), and (322), which relate to achiral surfaces. However, the surface of such metals can be chiral if the Miller indices follow the rule  $h \neq k \neq l \neq k$  and  $h \times k \times l \neq 0$ .[95] For instance, a high-Miller-index like  $(643)^S$  is considered to be a chiral surface. In other words, the chiral surface is present in the interior triangle created by the intersection of three low-Miller-

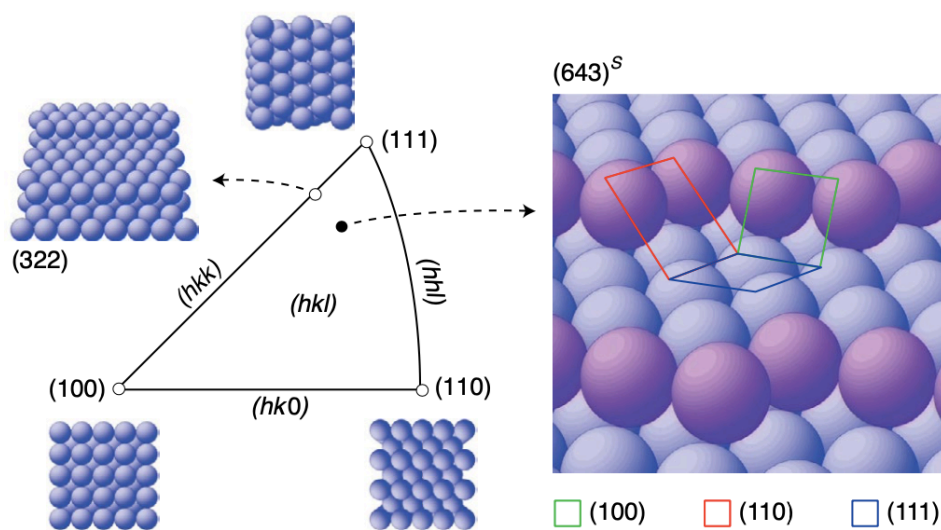


**Figure 1.9** Graphical demonstration of chirally crystalline metal surfaces when breaking the symmetry of crystal planes. The triangle projection showcases all possible mirror planes of the fcc lattice with low-Miller-index planes, having a high symmetry, and being achiral. However, any point in the interior region of the triangle indicates a metal interface with high-Miller-index planes, low-symmetry, and thus chiral character. The purple atoms emphasize the separating terraces at microfacet intersections. (Reproduced from [95])

index micro facets, i.e., terrace(111), step(100), and kink(110), around the kink site.

Indeed, the fabrication of chiral metal surfaces relies on the symmetry breaking of the bulk metal structures achieved by several techniques. For instance, precisely cutting a bulk crystal along specific high-Miller-index planes can create chiral metal surfaces.[76, 83] The first attempt demonstrated the presence of chiral sites on kinked metal surfaces, as reported by Gellman J. and co-workers.[76] Interestingly, by introducing this approach, the two mirror crystal planes,  $\text{Ag}(643)^{\text{R}}$  and  $\text{Ag}(643)^{\text{S}}$ , have been successfully generated. However, enantiospecific desorption kinetics of (R)- and (S)-2-butanol from each chiral surface was not well pronounced due to the almost identical heat of desorption of alcohols and energy barriers for decomposition into alkoxide. On the contrary, the asymmetric  $\text{Pt}(643)^{\text{R}}$  and  $\text{Pt}(643)^{\text{S}}$  surfaces reported by Attard *et al.* revealed significantly different rates for the enantioselective electrooxidation of (D)- and (L)-glucose on such chiral surfaces.[83]

Furthermore, the growth of chiral metal surfaces can be achieved by depositing metal layers onto chiral substrates. For example, pulsed laser deposition has been used for inducing an epitaxial growth of Pt thin films onto a low-symmetry-chiral surface of a  $\text{SrTiO}_3(621)$  substrate.[96, 97] The results illustrate the influence of the chiral  $\text{SrTiO}_3(621)$  surface on the generation of chiral Pt (621), confirmed by X-ray diffraction (XRD) and atomic force microscopy (AFM). This approach has been recently extended to other metals, including Ni, Cu, and Ag, deposited on chiral supports such as Si(643).[98] Epitaxial electrodeposition of Au onto Si(643) or  $\text{Si}(\bar{6}\bar{4}\bar{3})$ , which are enantiomorphs of each other, has allowed creating chiral Au films. Other metals such as Pt, Ni, Cu, and Ag subsequently electrodeposited onto the as-prepared Au films, showed also low symmetry-crystal structures. The chiral characteristics of such metal surfaces (e.g., Ag/Au/Si(643)) and Ag/Au/Si( $\bar{6}\bar{4}\bar{3}$ ) has been confirmed by the enantiospecific electrooxidation of (D)- and (L)-glucose. Notably, the developed approach allows generating chiral metal surfaces on various substrates, without the need of an expensive single-crystalline metal, as reported for cutting method.

One of the most successful processes for introducing chiral information on metal surfaces is imprinting chiral molecules in the reactive surfaces under symmetry-breaking conditions such as chiral solvents and reagents. Previously, a molecular imprinting approach using chiral molecules as templates was extensively applied for molecular imprinted polymers.[99] In the frame of chiral-encoded metals/metal oxides, Switzer *et al.* have described the electrodeposition of CuO onto Au(001) with a controlled chirality.[85] The successful synthesis of two minor crystal planes of CuO films with  $(1 \bar{1} \bar{1})$  and  $(\bar{1} 1 1)$  orientations was obtained by the electrodeposition of copper in the presence of (S,S)-tartrate, and (R,R)-tartrate, respectively. In addition, the chiral CuO films showed enantioselective recognition of (S,S)-tartrate and (R,R)-tartrate *via* their electrooxidation monitored by Linear Sweep Voltammetry (LSV). Apart from the chiral imprinting of metals by the electrodeposition technique, the elaboration of metals doped with organic compounds has been proposed *via* the chemical reduction of metal salts (e.g., Ag, Au, and Pd) in solutions containing chiral dopants.[86, 100] The resulting metal nanoparticles having an embedded chiral fingerprint, expose their different handedness when interacting with clockwise- and anticlockwise- circularly polarized light. In the case of Pd nanoparticles imprinted with cinchona alkaloids, the chiral information can be preserved even after the removal of the chiral dopant. However, only very modest enantioselectivity for the catalytic hydrogenation of ketone compounds was observed when using the doped Pd as a catalyst.[86] In order to increase the number of imprinted sites, which would result in a more pronounced enantiospecific reactivity, mesopores have been introduced into the bulk structure of metals such as Pt and Ni.[87, 91] As shown in **Figure 1.10**, supramolecular structures composed of self-assembled non-ionic surfactants and the dopant molecules, acting as a mesopore and chiral template, respectively, are present in an aqueous solution containing the metal precursor

(**Figure 1.10 A**). Electrodeposition of the metal from such a matrix allows the growth of the corresponding metals with chiral cavities around the oriented template (**Figure 1.10 B**). Finally, the generated internal mesopores and chiral active sites remain even after the extraction of the template molecules (**Figure 1.10 C**). Several chiral templates can be employed for this promising concept, ranging from essential amino acids to pharmaceutical and fine-chemical molecules, including tryptophan (Trp),[101] mandelic acid,[89] phenylethanol,[90, 91] and DOPA.[87, 102]

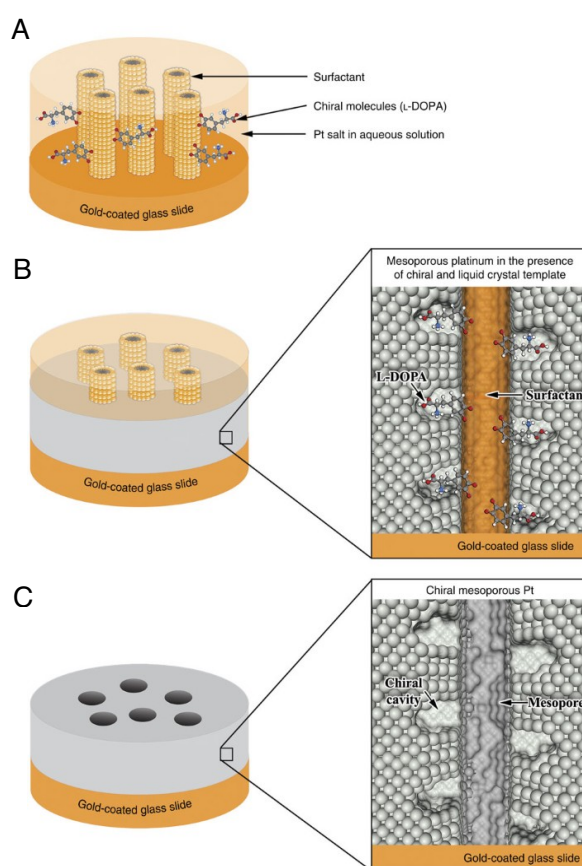


**Figure 1.10** Graphical illustration demonstrating the elaboration of chiral-enclosed mesoporous metals: A) The precursor plating gel composed of a lyotropic liquid crystal, chiral templates, and metal salts in an aqueous solution; B) Generation of the mesoporous metal *via* electroreduction of metal salts around the templates; C) The model structures of the obtained chiral-enclosed mesoporous metals after the extraction of templates. (Reproduced from [87])

## 1.5 Electrochemical deposition

Chemical and electrochemical deposition techniques have been widely used to elaborate micro- or nanoscale porous metals, which have been used for various applications ranging from catalysis, and energy storage to anti-corrosion.[59] Electrodeposition is considered the more controllable method to synthesize porous metals. Electrochemical deposition is a versatile technique that has many positive aspects, in particular the facile deposition on a support of thin-metallic layers with a thickness of a few microns or nanometers with a well-controlled smooth external surface. Therefore, in our case, the mesostructured metals have been synthesized by electrodeposition, allowing the generation of fine-tuned structures by optimizing several parameters, such as deposition temperature, pH of the deposition mixture, injected deposited charge density, and applied potential.[59, 103]

In principle, the electrodeposition of metals occurs in an aqueous solution on the cathode by applying a potential more negative than the thermodynamic redox potential of the metal. Generally, the electrochemical deposition of metals occurs in several steps, related among others to the coordination chemistry of the metal complexes present in the plating bath.[59, 104] The electrodeposition mechanism of a simple ligand-coordinated metal system is summarized in **Figure 1.11**. [59] In the first step (Step I), the formation of solvated metal ions in the electrolyte occurs. Subsequently, the formed complexes migrate from the bulk solution to the diffusion layer on the electrode surface, assisted by diffusion and convection (Step II). In the diffusion layer, the induced electric field from an external supply assists the complexes' alignment to liberate the free metal ion and facilitate its reaction in the Helmholtz layer (Step III). Owing to the high electric field strength in this layer, the hydrate ligands and metal ions are separated. Finally, at the interface occurs the electrodeposition of the released metal ions. Therefore, the ligand of the metal ions play an important role in the

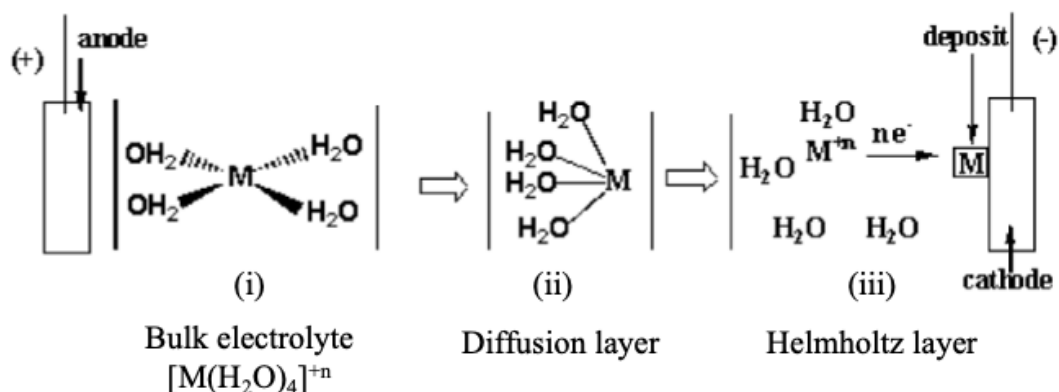
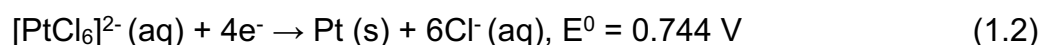
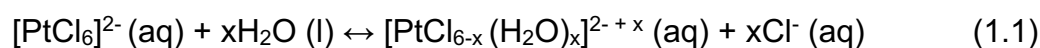


**Figure 1.11** A simplified electrodeposition mechanism involving the coordination chemistry of the solvated metal ions in a plating bath. (Reproduced from [59])

process because the system should not have a too strong metal-ligand interaction, in order to allow discharging of the metal ions at the electrode surface. Moreover, a plating bath should contain an excess of ligands to ensure the continuous formation of metal complexes, and additional supporting electrolyte which is required to improve the conductivity of the plating solutions.

In the present study, hexachloroplatinic (IV) acid or chloroplatinic acid ( $H_2PtCl_6$ ) is used as Pt precursor for the electrodeposition of mesoporous Pt. The platinum precursor is a strong acid, and consequently, the degree of hydrolysis is fast and quantitative. Spieker *et al.* have studied the coordination chemistry of Pt complexes in aqueous solution using the Extended X-ray absorption fine structure (EXAFS) technique.[105] In acidic conditions, as shown in equation 1.1 (1.1), coordination between platinum ( $Pt^{4+}$ ) and chloride ( $Cl^-$ ) ions is preferable, especially at very low pH and high  $Cl^-$  concentration, resulting in the dominant presence of  $[PtCl_6]^{2-}$  species. In the initial hydrolysis process, the exchange of  $Cl^-$  and water ( $H_2O$ ) ligands is rapid and reversible. Accompanied by the applied electric field, the electrochemical reduction of chloroplatinic acid is summarized in equation 1.2 (1.2).[59, 106]



## 1.6 Concept of chiral catalysts

Initially, homogenous chiral catalysts based on organometallic compounds were proposed and studied extensively by William S. Knowles.[107] This allows obtaining a particular chiral molecule by catalysis, a complementary approach with respect to the selective crystallization or deracemisation processes which were widely used in the past. This importance of the concept of asymmetric catalysis as a crucial technology has been recognized by the Nobel Prize in chemistry in 2001, awarded together with Ryoji Noyori [108] and K. Barry Sharpless,[109] and also by the latest Nobel prize in 2021,[110] given to Benjamin List [111] and David MacMillan.[112] This catalytic process, applied to produce an excess of one enantiomer, is named asymmetric synthesis or enantioselective synthesis. Generally, a catalyst is defined as a substance that enhances the reaction rate by reducing activation energy barrier, but the global Gibbs free energy ( $\Delta G$ ) of the reaction remains unchanged (**Figure 1.12A**).[113]

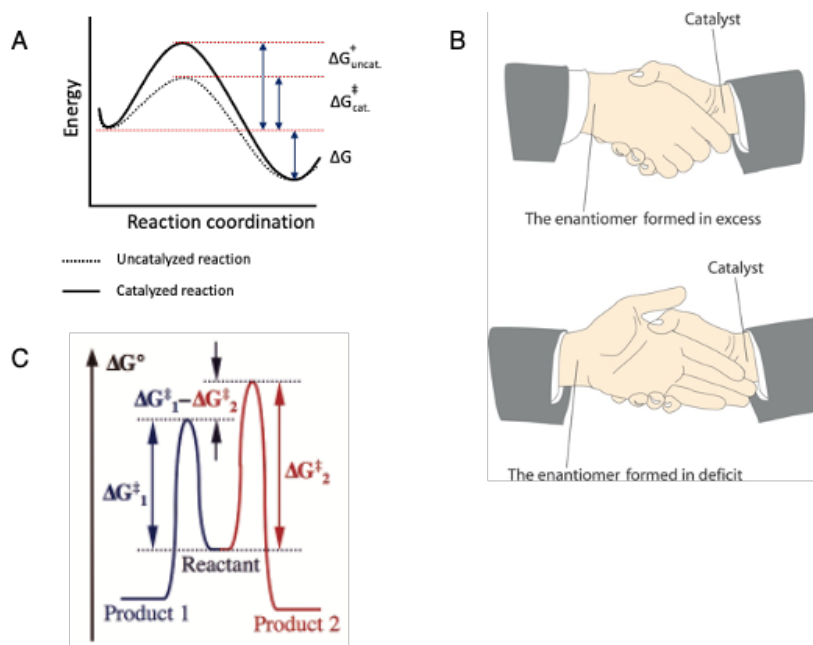


**Figure 1.12** Illustration of chiral catalysis demonstrated by A) energy diagrams for a catalyzed or uncatalyzed reaction, B) symbolic explanation of the concept of chiral catalysis by a handshake and C) energy diagram of kinetically controlled asymmetric catalysis. (Figure 1.12 B and C are reproduced from [114] and [115], respectively.)

Catalysts also play a vital role in the asymmetric synthesis, allowing a transfer of their chiral features to a prochiral starting compound to generate a specific enantiomer. **Figure 1.12 B** illustrates the concept of the right action of handshake for the comparison with the interaction of such a chiral catalyst.[114] The right and left hands represent the catalyst and product, respectively. The handshake *via* the two right hands is more comfortable than different hands, and therefore, such an interaction is preferable, favorably producing one product compared to the other. During asymmetric transformations, the process is kinetically controlled by the difference in activation enthalpies ( $\Delta G^{\#}_1 - \Delta G^{\#}_2$ ) of the two competitive reaction pathways. This difference results in a couple of controllable reaction products (**Figure 1.12 C**).[115, 116]

## 1.7 Electrosynthesis

Since the 18<sup>th</sup> century, the industrial revolution has caused excessive energy consumption, and this has become a global political issue.[117, 118] To date, novel production technologies have been extensively developed with the goal to take into account also ecological aspects. Particularly, alternative energies such as electricity, in opposition to petroleum and coal, are gaining much attention, as they allow the development of greener processes to reduce greenhouse gas emissions and waste generation.[117] Consequently, this strategy is also worth exploring for organically chemical synthesis. Electro-assisted organic synthesis (electrochemical synthesis or electrosynthesis) proceeds by directly using electricity to generate the desired organic compounds. The process can be achieved by an exchange of electrons at the electrode/electrolyte interface *via* redox reactions involving organic molecules. This leads to the transformation of an initial substance into a valuable product *via* an electrogenerated intermediate species (e.g., radical, cation, and anion).[119] Most importantly, it is possible to synthesize selectively organic molecules under very mild conditions without using hazardous chemicals as reducing or oxidizing agents. Such a green electrochemical synthesis platform could allow maintaining or eventually enhancing atomic efficiency and minimizing waste production.[120] Therefore, in modern chemistry,

electrosynthesis can stand out as an upcoming synthetic pathway, and it is even expected to transform into commercial synthesis scales in the near future.

## 1.8 Recent progress in asymmetric heterogeneous electrocatalysis

Asymmetric electrochemical synthesis is able to introduce the desired stereochemistry into target compounds, by using appropriate synthesis conditions controlled by several parameters summarized in **Figure 1.13**.<sup>[121]</sup> In this thesis, asymmetric synthesis will be mainly accomplished by using as heterogeneous electrocatalysts the encoded mesoporous metals mentioned earlier as chiral electrodes for obtaining products with a controlled stereoselectivity.

Over the past decades, numerous reports have described the progress of asymmetric electrocatalysis based on several strategies.<sup>[122, 123]</sup> However, asymmetric heterogeneous electrocatalysis based on chiral metal electrodes will be presented in the following. Chiral features on electrode surfaces have been generated *via* the grafting or the adsorption of chiral auxiliaries onto metal electrodes. For example, H.-P. Yang *et al.* reported electrochemically induced adsorption of alkaloids on copper (Cu) nanoparticles, which were compacted into a coin for asymmetric electro-hydrogenation.<sup>[124]</sup> Under mild conditions, moderate enantioselectivity, approximately 60%, with an excellent yield, was achieved. Furthermore, the introduction of chiral information into metal nanoparticles by encapsulation has been investigated. For example, alkaloids

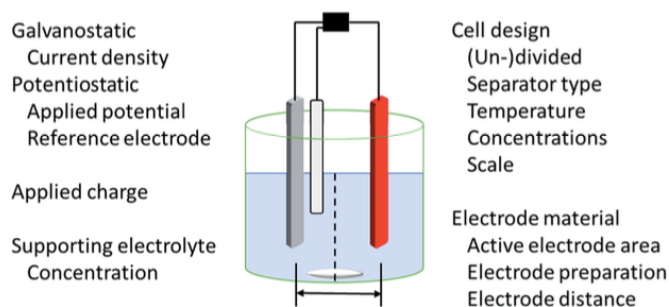


**Figure 1.13** Important parameters governing asymmetric electrochemical synthesis in batch-type. (This figure was taken from [121])

were entrapped in Cu nanoparticles, denoted as alkaloid@Cu, showing efficient electrocatalytic features in the frame of asymmetric hydrogenation with almost 80% enantioselectivity and yield.[125] This entrapment concept of metal-alkaloid hybrid materials has also been applied to bimetallic Pt@Cu nanoparticles for enantioselective electro-hydrogenation. Nevertheless, only very modest enantioselectivity together with relatively low yields was obtained.[126] Apart from these chiral metal nanoparticles, the concept of encoding chiral templates into mesoporous metal surfaces, as mentioned previously, has also been used for stereoselective electrochemical catalysis. Chiral-imprinted mesoporous metals can provide a high active surface area, accompanied by a considerable amount of specific chiral reaction sites. The porous metal electrode allows the diffusion of educt to the chiral imprinted sites, resulting in an enhanced enantioselectivity during the formation of the desired chiral molecules. It has already been demonstrated that by applying such designer electrodes for the asymmetric synthesis of chiral compounds, a significant enantiomeric excess (%ee) can be obtained. For example, when (R)-mandelic acid was imprinted in mesoporous Pt, the %ee values for the (R)-enantiomer were enhanced after enantioselective electroreduction of phenyl glyoxylic acid to mandelic acid (**Figure 1.14A**). Its performance in terms of enantioselectivity can be tuned by adjusting the amount of chiral template, leading to a variation of the density of chiral cavities in the metal structure.[89] The obtained enantioselectivity can be explained by the asymmetric environment in the imprinted cavities, allowing a side-selective electrohydrogenation of the prochiral starting compound (**Figure 1.14B and C**). Not only Pt, as an example for precious metals, but also low-cost metals like Ni can be successfully imprinted and applied to the stereoselective production of phenylethanol with a high %ee by electroreduction of acetophenone.[91] However, the catalyst encounters major difficulties, such as electrochemical stability after several catalytic cycles. A modest yield of chiral products, as well as a competition of non-stereoselective reactions at non-imprinted sites of the electrode, were observed. Therefore, there is need to solve these problems in order to adapt the technology to real industrial applications.

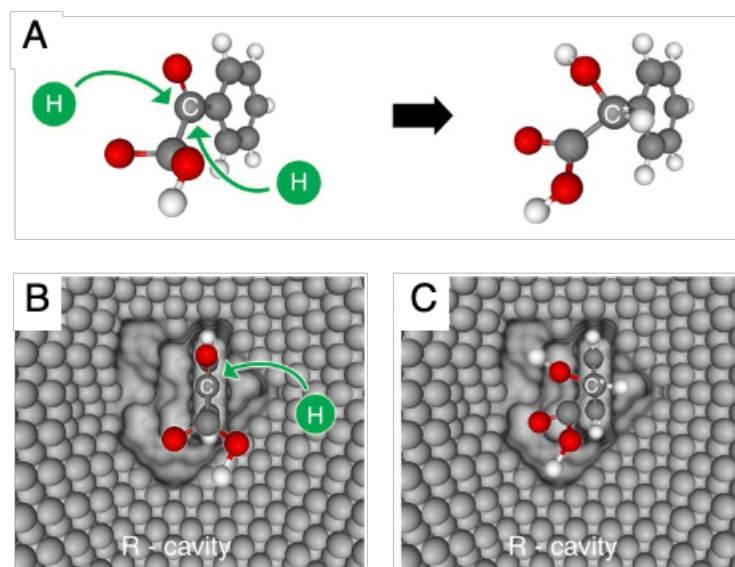


**Figure 1.14** Chiral-imprinted mesoporous Pt electrode for asymmetric electrosynthesis: A) Reduction of phenyl glyoxylic acid to mandelic acid; B) Electro-hydrogenation of the prochiral starting compound at the chiral cavity, (R)-mandelic acid imprinted site; C) Formation of the particular chiral product after the reaction. (This figure was taken from [89])

Consequently, and considering all these promising outcomes from the previous literature, we aim to design and develop new materials based on chiral imprinted mesoporous metals with improved features in order to make them more suitable chiral technologies, i.e., asymmetric electrocatalysis, heterogeneous hydrogenation, and chiral sensing. Moreover, our studies not only target applications, but are also meant to gain more fundamental knowledge about how chiral information can be encoded in metal surfaces. Therefore, these different aspects are addressed throughout this thesis in the following chapters:

Chapter 2 presents the asymmetric electrosynthesis of chiral compounds by using a conventional chiral-encoded mesoporous monometallic Pt, which is functionalized with an organosulfur ligand layer in order to improve its efficiency in terms of a shorter global synthesis time, as well as an enhanced enantiomeric

excess of the preferred enantiomer. In addition, this promising strategy was applied to the asymmetric synthesis of various types of chiral compounds.

Chapter 3 deals with the design of a new chiral-imprinted mesoporous metal electrode based on a metal alloy. In this case, Pt and Ir were alloyed to form such a matrix that can be used in the field of chiral technologies. Several parameters such as applied potential, current densities, and materials used as a substrate for electrodeposition have been investigated. Furthermore, characterization of these chiral imprinted mesoporous Pt-Ir alloys with several techniques have also been performed and the results are reported. In particular, the Secondary Harmonic Generation (SHG) method, one of the most powerful techniques for chiral analysis, provides pronounced information on chirality. The chiroptical effects in naturally presented materials tend to be rather small, but chiral metal nanostructures can generate a significant chiroptical effect and open a new perspective to novel concepts in terms of chiral characterization.

Chapter 4 describes the implementation of the chiral imprinted mesoporous Pt-Ir alloys as a catalyst for the asymmetric synthesis of chiral compounds. Due to the synergistic effects between Pt and Ir, the electrochemical stability of the developed metal alloy could be dramatically improved, translated by an only very small decrease of enantiomeric excess even after many catalytic cycles. In addition, the catalytic activity was significantly enhanced by applying pulsed electrosynthesis when compared to what could be achieved with the chiral monometallic Pt. Moreover, the chiral Pt-Ir alloy is used as a heterogeneous catalyst for asymmetric heterogeneous hydrogenation in order to broaden the range of applications for chiral-encoded mesoporous metals. The chiral Pt-Ir layers, supported on nickel foam, can enhance the accessibility of guest molecules to the active surface, allowing the design of materials showing a significantly higher production rate of chiral compounds and a shorter reaction time, compared to other recent enantioselective electrosynthesis approaches.

Chapter 5 illustrates the merits of combining the chiral Pt-Ir alloy with Electrochemiluminescence (ECL) to develop a novel analytical strategy for chiral discrimination. The synergy between the rigid chiral features of the Pt-Ir

alloy and the efficient and intrinsically sensitive detection via ECL, allows differentiating enantiomers by the emitted luminescence.

Chapter 6 contains a summary and the perspectives of this thesis with respect to the four presented main topics: (i) self-assembled monolayers of a thiol ligand on chiral imprinted monometallic structures for enantioselective electroynthesis; (ii) synthesis and characterization of chiral encoded mesoporous metal alloys; (iii) chiral-imprinted mesoporous metal alloys for chiral electroynthesis and heterogeneous catalysis *via* hydrogenation; (iv) chiral detection employing an ECL transduction strategy based on the use of chiral metal alloys.

## Chapter 2

# Chiral-imprinted mesoporous platinum surfaces protected by organosulfur ligands for highly enantioselective synthesis

### 2.1 Introduction

The biochemistry of life often uses a chiral molecule that acts as a key, together with a receptor playing the role of a lock, allowing the system to ensure biological processes, such as metabolism and neurotransmission.[108] Consequently, chiral compounds play significant roles in many areas, for instance, as active ingredients in pharmaceuticals and cosmetics or as additives in the food industry.[127] In order to effectively use chiral molecules in their proposed applications, a well-controlled production of each enantiomer with high purity is required. Indeed, there are numerous strategies for the highly selective synthesis of chiral compounds, e.g., asymmetric synthesis, separation, resolution, and crystallization.[128-130] Among them, asymmetric synthesis has been used as one of the most promising strategies due to many positive aspects, among others a highly selective production and decrease of waste in the form of by-products.[128] This chapter will illustrate the highly selective synthesis of chiral molecules *via* electrochemistry. This synthesis approach is considered a green process using electricity to drive a chemical reaction without adding further chemical reagents, reducing total operating costs.[131-133] However, this technique is usually associated with a modest control of the stereochemistry of the chiral products during the electro-conversion, leading to a low yield of the desired species.[134]

In order to overcome these drawbacks, the development of an electrocatalyst with a well-organized structure is the most challenging task to improve the efficiency of chiral electrocatalysis. Among various types of chiral

electrodes, carbon-based materials have been applied as chiral materials for discrimination between specific enantiomers, such as derivatives of poly(pyrrole) [135] and chiral poly(3,4-ethylene dioxythiophene) (PEDOT) based electrodes.[136] Considering their ability to act as an electrocatalyst, poor stability and complex fabrication processes hinder their promoting for practical uses in asymmetric electrosynthesis. Thus, in a modern electrosynthesis, metals or metal oxides with intrinsic chiral features have been proposed as suitable alternative materials for asymmetric synthesis due to many promising aspects, such as an easy fabrication and a rigid structure leading to high stability.[74, 137] To generate chiral features inside metals/metal oxides, organically doped metals/metal oxides, have been proposed. Recently, chemical or electrochemical reduction of metal precursors in the presence of chiral template molecules was proposed to prepare molecular doped metals/metal oxides. Up to date, there are various types of metals that have been successfully elaborated, including gold (Au),[100] silver (Ag),[100] copper oxide (CuO),[85, 138] and palladium (Pd).[86] Notably, even after removing the chiral molecular template, chiral features are retained, confirmed by electrochemical methods such as differential pulse voltammetry (DPV) [88] and optical characterization with circular dichroism spectroscopy (CD).[139] After confirming the chiral character inside the metals/metal oxides, the nanostructured materials have been used for various applications, for instance, as chiral sensors and actuators, as a stationary phase for chiral separation, and as a chiral catalyst for asymmetric synthesis.

These chiral imprinted metals/metal oxides can be used as an enantioselective matrix for asymmetric synthesis *via* either electrochemical or chemical catalytic approaches.[140, 141] For example, Wattanakit *et al.* have proposed a new concept for elaborating chiral electrodes by combining chiral-encoded metals with a mesoporous structure.[87, 89, 90] The nanostructured metals have been successfully obtained by electrodeposition from metal precursors in the simultaneous presence of non-ionic surfactants assembled in a supramolecular hexagonal columnar structure and chiral molecules. The non-ionic surfactants act as a mesoporous template, whereas chiral molecules serve

as a chiral template, which interacts with the head group of non-ionic surfactants (-OH) by a hydrogen bond located at the outermost surfaces of the columnar structure to generate chiral recognition sites in the bulk metal structure.[38, 142-144] To date, several kinds of chiral templates have been employed using this strategy, i.e. 3,4-dihydroxyphenylalanine (DOPA),[87, 102] which is an essential pharmaceutical compound and neurotransmitter, mandelic acid (MA),[88, 89] and phenylethanol (PE),[90, 91] which are active ingredients in cosmetics and food industry, respectively, and tryptophan (Trp),[101] which is one of the essential amino acids. These findings clearly demonstrated that it was possible to initiate various specific chiral structures in metal/metal oxides layers, opening a wide range of applications, for example, enantioselective recognition,[87, 88] chiral actuators and separation,[101, 102] and asymmetric synthesis.[89-91]

Initially, a monometallic metal structure based on platinum (Pt) was proposed for encoding chiral information.[87] Subsequently, a non-noble metal, e.g., nickel (Ni), was also used by Assavapanumat *et al* as a matrix to minimize the material costs.[91] Extremely high enantioselectivities of over 90 %ee could be obtained when this advanced material was applied as an electrode for asymmetric electrosynthesis.[90] The enhanced production of chiral molecules is due to the improved mass transport through the matrix having a very high active surface area.[38] In particular, using a pulsed electrosynthesis approach, based on many reaction cycles composed of a short reaction period and extended relaxation periods, allows improving the enantiomeric excess to a very high value due to the suppression of non-selective reduction at non-imprinted sites.[90]

Although a superior enantiomeric excess could be achieved with pulsed electrosynthesis, the approach suffers from a long global synthesis time. Moreover, as mentioned above, the main obstacle is the uncontrollable reaction at the non-imprinted sites, mainly located on the external surface.[89, 90] Therefore, strategies for specifically blocking the outermost surface of chiral imprinted mesoporous metal electrodes should indeed be investigated. The most common way to do so is to functionalize metal surfaces with organic groups.[145] Presently, there are many common functional groups that can be

applied for protecting metal surfaces such as amines,[146] ammonium ions,[147] carboxylic acids,[148] phosphoric acids,[149] alkyne,[150], trimethoxy silanes,[151] diazonium salts,[152, 153] thiols [154-157] and N-heterocyclic carbenes.[158] The modification of metal surfaces with either organosulfur compounds or N-heterocyclic carbenes has been reported to provide good catalytic activity and durability.[159] Cao *et al.* found that N-heterocyclic carbene-functionalized gold nanoparticles (Au NP) showed a superior faradaic efficiency of up to 83% for carbon dioxide (CO<sub>2</sub>) reduction to carbon monoxide (CO) compared to the one observed for bare Au NP, being only 53%.[160] Moreover, to promote electrochemical activity and stability for CO<sub>2</sub> reduction, the N-heterocyclic carbene, derived with long polymer chains, were used to functionalize Au NP as revealed by Zhang *et al.*[161] The activity and faradaic efficiency were increased to over 86%, due to a higher density of surface electrons on the Au NP from  $\sigma$ -donation, and the limitation of proton diffusion through the more hydrophobic polymer chains. Furthermore, the formation of Au NP clusters was prevented by the strong covalent bond (gold-carbene bond) with the Au NP surface. Nevertheless, even though the unusual activity and resistance has been demonstrated in terms of electrochemical functionality, a complex preparation process is still the major hindrance for practical applications, because N-heterocyclic carbenes are air-sensitive compounds.[159]

On the other hand, metal surface functionalization with organosulfur-based compounds has been widely used in the frame of catalysis of many reactions.[154-156] Primarily, linear alkanethiols are often used to generate a stable monolayer of organic moieties on metal surfaces. The success of this approach is due to several advantages, including an easy preparation process and the stability of the strong covalent bond between metal and sulfur atoms and the van der Waals interactions between the alkyl chains.[157] A simple preparation approach for self-assembled monolayers (SAM) of alkanethiols on metal surfaces requires only the immersion of a metal surface in a thiol solution at room temperature for a certain time. **Figure 2.1** illustrates the general process for forming a SAM of alkyl thiol on metal surfaces, such as Au(111).

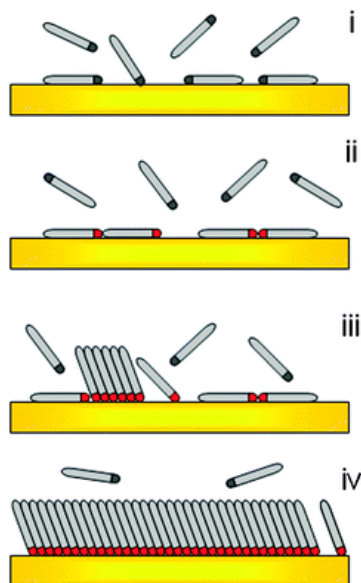


**Figure 2.1** Schematic explanation of the SAM formation of a linear alkyl thiol on Au(111); (i) Physisorption; (ii) Initial stage of chemisorption in a similar position; (iii) Phase transformation of alkanethiols from a horizontal to a vertical configuration; (iv) Dense packing of the thiol SAM. The figure is reproduced from [157].

Physisorption (black dot symbolizes the thiol group) of the molecules parallel to the Au surface occurs within the first period. Subsequently, chemisorption takes place (red dot for the chemisorbed thiol). After that, a reorganization of the alkanethiol molecules from a parallel to a vertical configuration is observed for higher surface coverages. Finally, an ideal SAM is obtained after several hours.[157, 159]

The electrochemical stability of SAMs on metal surfaces is one of the most critical parameters for modifying such materials. For example, a theoretical study of alkane thiolate-protected Pt nanoparticles (NPs) has been reported by Addato *et al.*, confirming that adsorbed sulfur atoms on Pt surfaces are indeed stable against desorption even at high reduction potentials. Thus, thiolate-modified Pt NPs are promising for hydrogen storage or electrocatalysis.[162] Nevertheless, the metal-sulfur bond can become completely passivating if the alkyl ligand is too long, resulting in a significant slowing down or a complete shutdown of the electrocatalysis.[155] Therefore, such this crucial parameter

must be optimized. Indeed, medium and long alkyl chains, such as hexanethiol ( $C_6H_{13}-SH$ ) and dodecanethiol ( $C_{12}H_{25}-SH$ ), respectively, immobilized on Pt NPs show a similar behavior for electrochemical durability in terms of desorption at very negative reduction potentials (up to  $-1.8$  V vs SCE). At the same time, the quality of SAM strongly depends on the length of the alkyl chain, e.g., a higher thiol coverage for a longer chain.[162, 163] These observations imply that a medium alkyl chain length (no less than  $C_6$ ) of the thiol ligand should be enough to protect Pt surfaces in electrochemical applications.

Accordingly, in the present study, heptanethiol is chosen as a protecting agent of the unselective surface of chiral-imprinted mesoporous Pt electrodes to minimize undesired reactions and nevertheless preserve the electrochemical activity of the Pt electrode for asymmetric electrosynthesis. We expect the chiral product selectivity to increase and the global synthesis time to shorten due to the blocking of non-imprinted sites by thiol layers.

## **2.2 Experimental section**

### **2.2.1 Chemicals**

Hexachloroplatinic acid hydrate ( $H_2PtCl_6 \cdot xH_2O$ ), polyethylene glycol hexadecyl ether (Brij<sup>®</sup> C10), (R)-phenylethanol ((R)-PE), (S)-phenylethanol ((S)-PE), acetophenone (APE), (R)-1-(4-bromophenyl) ethanol ((R)-BrPE), (S)-1-(4-bromophenyl) ethanol ((S)-BrPE), isopropanol, ethanol, heptane, ammonium chloride ( $NH_4Cl$ ), potassium ferrocyanide ( $K_4Fe(CN)_6 \cdot 3H_2O$ ), heptanethiol ( $C_7H_{15}-SH$ ) and nitric acid ( $HNO_3$ ) were obtained from the Merck, Sigma-Aldrich. Sulfuric acid ( $H_2SO_4$ ) was purchased from Alfa. 4-bromoacetophenone (4-BrAPE) was adopted from the TCI. For all sample preparations and electrochemical experiments, MilliQ water ( $18.2$  M $\Omega$  cm) was used, and all chemicals were directly utilized without further purification.

### **2.2.2 Substrate cleaning**

In this contribution, a gold-coated glass slide was employed as a substrate for electrodeposition. In the typical procedure, a gold-coated glass

slide was cut into pieces of 1 cm × 1 cm. Subsequently, the as-prepared substrate was cleaned by sonication in isopropanol for 15 min to remove organic impurities. Then, the cleaned substrate was rinsed with MilliQ water several times (a few minutes) to get rid of excess impurities, rinsed with alcohol and dried under nitrogen (N<sub>2</sub>) gas flow for removing adsorbed water. Before using the substrate for electrodeposition, the surface was connected with a standard wire by soldering. The active geometric area (0.25 cm<sup>2</sup>) was defined by painting the inactive parts with nail varnish.

### **2.2.3 Synthesis of chiral-imprinted mesoporous platinum (Pt) by electrodeposition**

Typically, a three-electrode system was set up, including Ag/AgCl (sat. KCl), Pt mesh, and a prepared gold-coated glass slide, used as the reference, counter, and working electrodes, respectively, for all electrochemical experiments. All experiments were performed using a potentiostat with the Metrohm  $\mu$ Autolab Type III model.

A precursor gel based on a lyotropic liquid crystal (LLC) phase was prepared following previous procedures for electrodeposition.[90] The plating mixture is composed of 39 wt% of Brij<sup>®</sup> C10, 28 wt% of chloroplatinic acid hydrates, 28 wt% of MilliQ water, and the chiral templates, (R)- or (S)-PE, with a weight ratio of PE/PtCl<sub>6</sub><sup>2-</sup> varying in the range of 0.0375 to 0.150. They were continuously mixed for 10 min and then heated at 40 °C in the oven for 20 min. This preparation procedure was repeated three times until getting a homogeneous mixture. Moreover, (R)- or (S)-BrPE imprinted mesoporous Pt was also synthesized following the above strategy but using the BrPE with a weight ratio of 0.150 BrPE/PtCl<sub>6</sub><sup>2-</sup>. The electrodeposition was carried out on the substrate by chronoamperometry. The LLC gel was positioned on the surface of the substrate. Then, Pt was allowed to grow through the template by applying a reduction potential of -0.05 V with a deposition charge density of 4 C cm<sup>-2</sup>. The Pt electrode was rinsed and soaked in MilliQ water overnight to remove templates to obtain the final chiral-imprinted mesoporous Pt. In addition, a non-imprinted mesoporous Pt electrode was prepared by following the same

procedure mentioned above, but without adding any chiral templates to the Pt precursor gel.

## **2.2.4 Surface functionalization of chiral-imprinted mesoporous Pt electrodes with organosulfur ligands**

The synthesized Pt electrodes were modified with an organosulfur ligand, heptanethiol, to form a self-assembled monolayer (SAM) on the outermost surface of the Pt electrodes following two strategies, comprising self-assembly from solution and microcontact printing ( $\mu$ CP)

### **2.2.4.1 Self-assembly from solution**

The freshly electrodeposited Pt electrodes were immediately rinsed with MilliQ water for approximately 15 min to remove the excess templates on the electrodes' external surfaces. Subsequently, the electrodes with the remaining templates inside the mesopores were immersed in 10 mM heptanethiol dissolved in ethanol for desired times varying from 30 min to 1, 2, and 4 h under ambient conditions. For the final stage, the functionalized Pt electrodes were cleaned with ethanol several times to remove the physisorbed heptanethiol species and stored in MilliQ water overnight to eliminate the remaining templates located inside the mesopores. The prepared electrodes were kept in the dark for the follow-up experiments.

### **2.2.4.2 Microcontact printing ( $\mu$ CP)**

Initially, a commercial rubber stamp made out of polychelating amphiphilic polymers (PAP) was cut into pieces of 1 cm<sup>2</sup> (1 cm × 1 cm) size and directly used as a stamp for the thiol coating process. An ethanol solution containing 50 mM heptanethiol was loaded on top of the stamp with a loading density of 1  $\mu$ l/cm<sup>2</sup>. The stamp was dried in ambient conditions for 60 s to evaporate the excess ethanol. Finally, the dried stamp was immediately gently pressed on the bare and cleaned Pt electrodes for 10 s. The process mentioned above of  $\mu$ CP was repeated for up to five cycles to investigate an

optimal coating time. The Pt electrodes functionalized with heptanethiol were kept in the dark before using them in the next experiments.

### 2.2.5 Characterization

The topology and morphology of the Pt electrodes generated with a deposition charge density of  $4 \text{ C cm}^{-2}$  were investigated by scanning electron microscopy (SEM) with a Hitachi TM-1000 tabletop microscope with either top or cross-sectional views. The mesoporous structure of the Pt electrodes was characterized by transmission electron microscopy (TEM) with a JEOL JEM-2100 microscope at 200 kV. For the sample preparation for TEM measurements, the mesoporous Pt films were prepared by electrodeposition with a deposition charge density of  $0.4 \text{ C cm}^{-2}$ . Subsequently, the ultra-thin films were gently scraped off from the Au-coated glass slide, transferred into ethanol solution, and dropped onto TEM grids.

The electrochemical surface areas of both standard flat and synthesized mesoporous Pt electrodes were measured and calculated by cyclic voltammetry in  $0.5 \text{ M H}_2\text{SO}_4$  at  $100 \text{ mV s}^{-1}$ . [87, 90, 164] The accessibility of the adsorbed heptanethiol-Pt electrodes was studied by cyclic voltammetry in  $10 \text{ mM K}_4\text{Fe}(\text{CN})_6$  dissolved in  $1 \text{ M HNO}_3$  at a scan rate of  $100 \text{ mV s}^{-1}$ .

### 2.2.6 Enantioselective electrosynthesis of 1-phenylethanol (1-PE)

Enantioselective electrosynthesis of the chiral compounds was conducted in a three-electrode system, with a potentiostat operating in the chronoamperometry mode (**Figure 2.2**). Asymmetric electrosynthesis by reducing acetophenone (APE) into 1-phenylethanol (1-PE) was carried out in the potentiostatic mode at  $-0.40 \text{ V}$  for 13 h in a constantly stirred solution (250 rpm) of  $5 \text{ mM}$  acetophenone dissolved in  $7 \text{ mL}$  of  $1 \text{ M NH}_4\text{Cl}$  as supporting electrolyte with an optimized solution pH of 4.0. Before analysis, the product solution was extracted with heptane, and then injected into a high-performance liquid chromatography (HPLC) instrument (JASCO LC-Net II/ADC) equipped with a chiral column (CHIRALPAK IB N-5,  $250 \times 4.6 \text{ mm}$  inner diameter), and photodiode array (PDA) as a detector operating at  $210 \text{ nm}$ . The analysis was

conducted using a mixture of 8/92 (v/v) isopropanol/heptane as a mobile phase at a flow rate of 0.5 ml min<sup>-1</sup>.

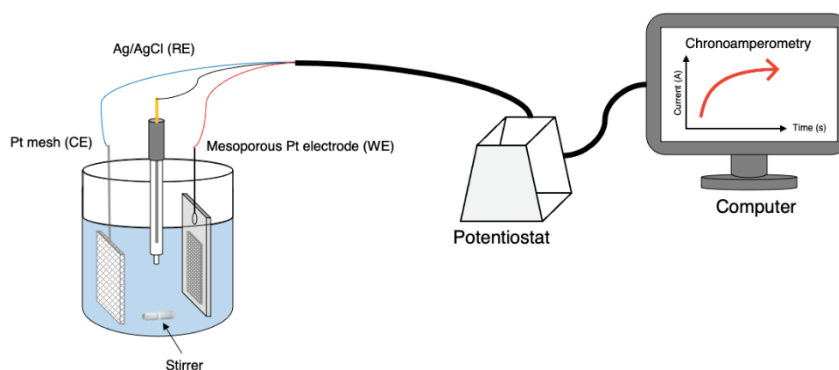


**Figure 2.2** Apparatus for the asymmetric electrocatalysis composed of a potentiostat equipped with a three-electrode system, applying chronoamperometry, in a home-made electrochemical cell containing the stirred prochiral solution

### 2.2.7 Asymmetric electrocatalysis of 1-(4-bromophenyl) ethanol (1-BrPE)

Potentiostatic electroreduction of 4-BrAPE to 1-BrPE was conducted using the same experimental set-up as the one shown in **Figure 2.2** under optimized catalytic conditions at -0.50 V for 13 h in a stirred solution of 5 mM 4-BrAPE dissolved in 7 mL of a mixture of 10/90 (v/v) isopropyl alcohol/1 M NH<sub>4</sub>Cl as supporting electrolyte for with a solution pH at 5.0. After the synthesis, the resulting products were extracted by heptane and analyzed by the HPLC (a Shimadzu LC-2030C3D) equipped with a CHIRALPAK IB (250 × 4.6 mm inner diameter) column and a photodiode array (PDA) detector at 220 nm, using a mobile phase containing 5% isopropyl alcohol and 95% heptane (v/v) at a flow rate of 0.5 ml min<sup>-1</sup>.

### 2.2.8 Reusability test of the electrocatalysts

In order to investigate the efficiency of the thiol-functionalized chiral Pt electrodes in terms of recyclability, the modified chiral electrodes were

regenerated after the initial catalytic cycle by rinsing several times and immersing them overnight in MilliQ water. Then, the cleaned electrode was directly used for the next catalytic cycle, following the same procedure as previously. The solution obtained after each catalytic cycle was analyzed by the HPLC (Shimadzu LC-2030C3D) performed with a CHIRALPAK IB column (250 × 4.6 mm inner diameter) and a PDA detector at 215 nm. A mixture of 7.5 isopropyl alcohol/92.5 heptane (v/v) was used as a mobile phase, with a flow rate of 0.5 ml min<sup>-1</sup>. Furthermore, repeating the  $\mu$ CP strategy was also repeated for the catalyst regeneration to enhance the catalyst's efficiency in the subsequent catalytic cycles, using the procedure mentioned above.

### 2.2.9 Calculation of operational parameters

Various parameters related to the electrocatalytic performance of the chiral catalyst have been investigated, including (2.2.9.1) Catalytic conversion, (2.2.9.2) Enantiomeric excess (%ee), (2.2.9.3) Standard error of the mean of the enantiomeric excess (s.e.m.) and (2.2.9.4) Production rate of a chiral compound.

#### 2.2.9.1 The degree of conversion

The overall conversion percentage of the reaction is calculated from the calibration curve in which mixtures of APE and 1-PE, representing 0, 5, 10, 15, and 20 % conversion of APE into 1-PE were prepared. The curve shows a linear relationship:  $y = 0.0019x$  ( $R^2 = 0.9969$ ), where  $y$  is the result obtained from the HPLC chromatograms (ratio of peak area of the desired product (1-PE) and reactant (APE)), and  $x$  is the degree of conversion (%).

#### 2.2.9.2 Enantiomeric excess

The enantiomeric excess (%ee) is defined in equation (2.1):

$$\text{Enantiomeric excess (\%ee)} = \left[ \frac{(R)PE - (S)PE}{(R)PE + (S)PE} \right] \times 100 \quad (2.1)$$

where (R)PE and (S)PE are the integrated peak areas of (R)-PE and (S)-PE in the HPLC chromatogram, respectively.

### 2.2.9.3 Standard error of the mean of the enantiomeric excess

The standard error of the mean of the enantiomeric excess (s.e.m) is expressed to represent an error range of the %ee, which is calculated by the following equation (2.2):

$$\text{s. e. m.} = \frac{S}{\sqrt{n}} \quad (2.2)$$

where  $S$  and  $n$  are the standard deviation and the number of repeated experiments, respectively.

### 2.2.9.4 Production rate of chiral compounds

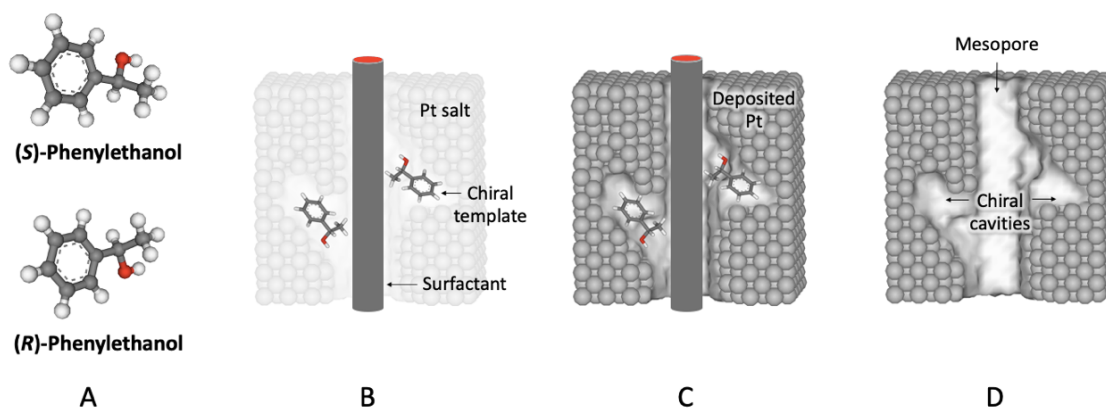
The production rate of a specific enantiomer is defined in terms of the amount of a selectively produced chiral molecule in mol ( $mol_{desired\ chiral\ product}$ ) regarding the electrochemically active surface area (ECSA) of the chiral metal electrode, evaluated from the cyclic voltammograms of the electrodes measured in  $H_2SO_4$  solution in the hydrogen adsorption/desorption region, and the global reaction time ( $t$ ), as indicated by equation (2.3):

$$\text{The production rate of chiral compound} \left[ \frac{mol}{m^2 \cdot h} \right] = \frac{mol_{desired\ chiral\ product}}{ESA \times t} \quad (2.3)$$

## 2.3 Results and Discussion

### 2.3.1 Synthesis and characterization of chiral imprinted mesoporous Pt electrodes

Initially, chiral encoded mesoporous Pt electrodes were generated by electrodeposition of a Pt precursor in the confined spaces of a supramolecular structure composed of non-ionic surfactants and chiral template molecules.[38, 87] To summarize, a selected chiral compound, either (R)- or (S)-PE (**Scheme 2.1A**), is adsorbed on the external surface of the non-ionic surfactant (Brij<sup>®</sup> C10) columns, which self-assemble due to the presence of a polar head group and a hydrophobic chain (**Scheme 2.1B**). When the Pt salt (hexachloroplatinic acid) is reduced, metallic Pt grows in the simultaneous presence of the above-mentioned hexagonal phase of surfactant and chiral templates (**Scheme 2.1C**). After the removal of templates in the final step, mesopores and chiral cavities, which promote an asymmetric environment in the Pt matrix, are generated (**Scheme 2.1D**)



**Scheme 2.1** Graphical illustration of the preparation process of chiral encoded mesoporous Pt; A) Chiral molecules as molecular templates used in the present work, (R)- and (S)-Phenylethanol ((R)- and (S)-PE); B) Supramolecular structure of adsorbed chiral templates around the external walls of a columnar-non-ionic surfactant structure surrounded by the Pt precursor; C) Growth of Pt metal by electrodeposition in the presence of the mesoporegen and chiral template; D) The final structure of the synthesized Pt electrode after template removal.

Smooth external surfaces and a very homogeneous thickness of about 1.0  $\mu\text{m}$  were observed in the top-view (**Figure 2.3A**) and cross-sectional (**Figure 2.3B**) SEM images. Additionally, as can be clearly seen from the TEM image (**Figure 2.3C**), the mesoporous structure has a hexagonal order with pore dimensions of approximately 5 nm, which is similar to what has been described previously using a similar non-ionic surfactant as a mesoporegen to synthesize mesoporous metals.[38, 87] In order to further verify the porous structure, the electrochemically active surface area of the mesoporous Pt electrodes is measured by cyclic voltammetry in 0.5 M  $\text{H}_2\text{SO}_4$  in a wide potential window from -0.20 to 1.20 V vs Ag/AgCl (**Figure 2.3D**). The signal below 0 V represents adsorption (cathodic peak) and desorption (anodic peak) of hydrogen. In addition, Pt oxidation and PtO reduction appear with characteristic signals at 0.70 and 0.55 V, respectively.[87] Interestingly, mesoporous Pt (red line) shows a much more intense electrochemical signal compared to standard flat Pt (black line), with a calculated roughness factor of around 177.

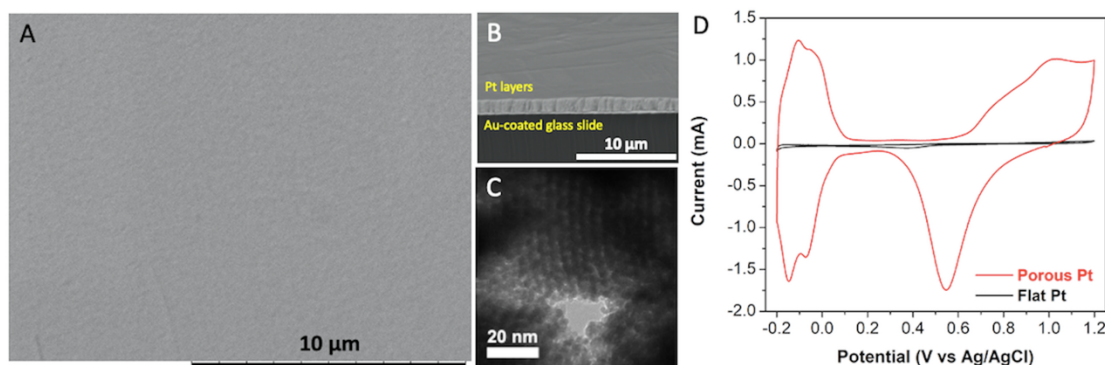


**Figure 2.3** Morphological and electrochemical characterization of Pt electrodes; A) Top-view and B) Cross-sectional SEM images; C) TEM images of an ultra-thin mesoporous Pt film; D) Cyclic voltammograms of mesoporous Pt (red) in comparison with a flat Pt electrode (black) measured in 0.5 M  $\text{H}_2\text{SO}_4$  at a scan rate of 100  $\text{mV s}^{-1}$ . SEM and CV characterization data were obtained using the Pt electrodes deposited by charge density of 4  $\text{C cm}^{-2}$ .

### 2.3.2 Modification of the mesoporous Pt electrodes with thiol ligands

In this contribution, two strategies have been applied to produce self-assembly monolayers (SAM) of thiol ligands covering the Pt surfaces, namely (i) the formation of SAM from a thiol solution; (ii) microcontact printing ( $\mu$ CP). In both systems, ethanol is used as a suitable solvent for the coating step because it is easy to remove by simple evaporation. In addition, ethanol has a low probability of getting incorporated into the thiol monolayer.[159]

Concerning the thiol coating from solution, SAMs of thiol ligands on Pt surfaces can be statically formed by the following steps: (i) ethanol adsorption covering the Pt surface, followed by (ii) the replacement of the adsorbed ethanol by thiol species.[163, 165-167] The formation rate and SAM quality can be controlled by the thiol concentration.[168] In the present study, a thiol molecule with medium chain length, heptanethiol ( $C_7$ -SH), dissolved in ethanol at an optimal concentration (10 mM), was used to trigger the formation of a well-established SAM on the Pt surface. The mesoporous Pt electrode, which still contains both surfactant and chiral template inside the pores, is transferred to a heptanethiol solution for the desired time. This procedure allows the formation of a SAM at the outermost Pt surface. However, the thiol layer should in principle not adsorb inside the mesopores due to the presence of mesopore. Subsequently, the template molecules and the remaining thiol residues are removed by rinsing with ethanol and MilliQ water (**Figure 2.4A**).[169]

On the other hand, a powerful technique, namely microcontact printing ( $\mu$ CP), allows a rapid and simple patterning of metal surfaces with thiol layers. A stamp, made of materials with elastic and flat surfaces, is inked with a thiol solution and then pressed onto the metal surface by direct physical contact for a given time and eventually for several printing cycles. The pattern of the

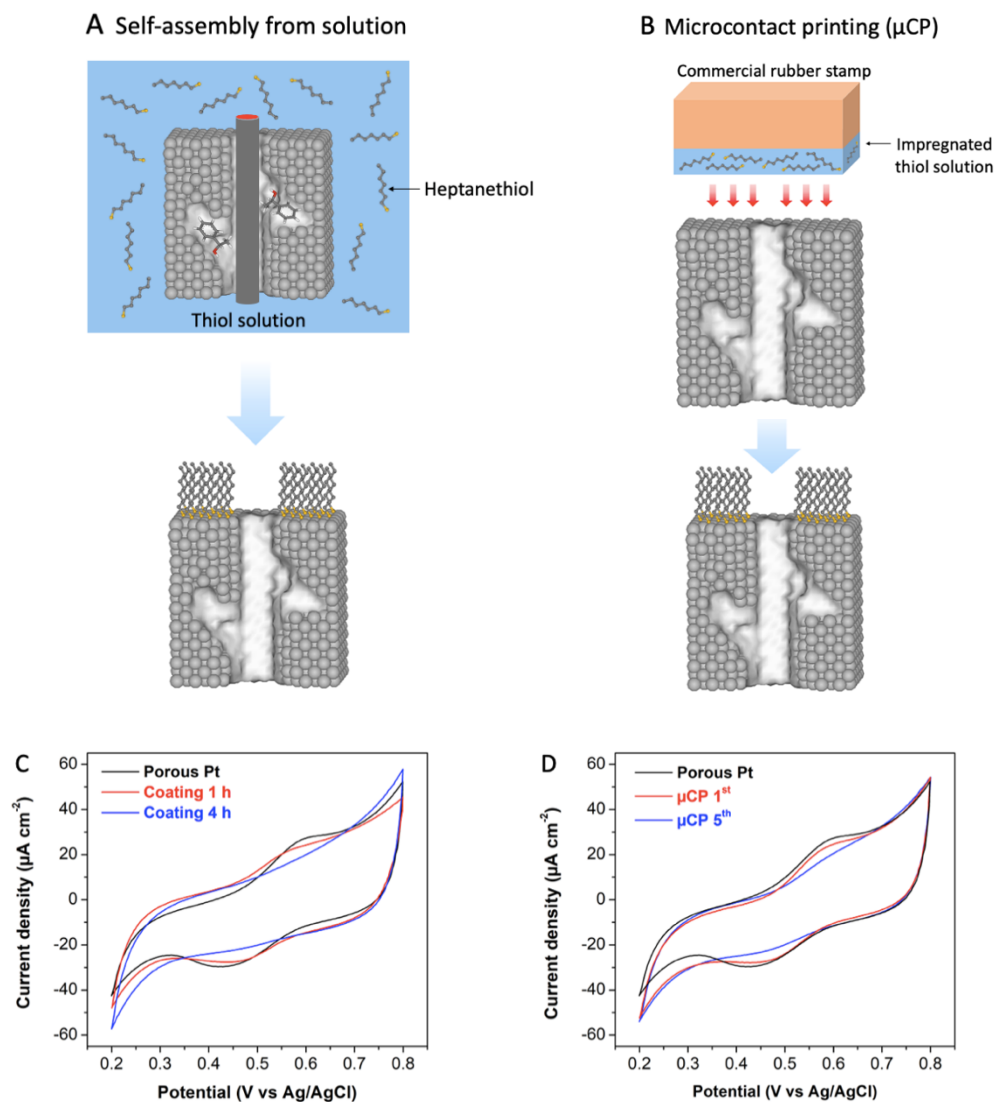


**Figure 2.4** Graphical illustration of the two thiol-coating strategies and the resulting surface blocking properties on mesoporous Pt electrodes; A) and B) Thiol coating *via* self-assembly from solution and microcontact printing ( $\mu$ CP), respectively; C) and D) Cyclic voltammograms of the solution-coated and  $\mu$ CP-coated mesoporous Pt electrodes in 10 mM  $\text{K}_4\text{Fe}(\text{CN})_6/1$  M  $\text{HNO}_3$  at a scan rate of  $100 \text{ mV s}^{-1}$  (black: uncoated electrode; blue: electrode with the final coating).

thiol layer is in this case governed by the contact points between the metal surface and the stamp.[170] The vital parameter that affects the quality of the

thiol layer is the initial ink concentration which should approximately be in the range of 20 to 50 mM.[169] In this work, a commercial rubber stamp is impregnated with 50 mM heptanethiol with an optimized stamp loading of 1  $\mu\text{l}/\text{cm}^2$ . The thiol species remaining on the stamp after evaporation of the solvent are then patterned on the outermost regions of a bare mesoporous Pt electrode by gently pressing. Contact times between the stamp and the Pt surface are predefined, and the formation of the thiol layer by  $\mu\text{CP}$  is illustrated in **Figure 2.4B**. [169-172]

In order to confirm that the thiol films completely protect the outer Pt surface, cyclic voltammetry of ferro/ferricyanide in  $\text{HNO}_3$  solution was employed. As expected, the apparent redox peaks of the ferro/ferricyanide redox couple ( $[\text{Fe}(\text{CN})_6]^{4-}/[\text{Fe}(\text{CN})_6]^{3-}$ ) appear at 0.60 V (oxidation) and 0.45 V (reduction) in the case of a bare porous Pt electrode (black) as shown in **Figure 2.4C**. In strong contrast to this, after modifying the Pt electrodes with a thiol by the solution strategy, the characteristic peaks of the ferro/ferricyanide redox couple are significantly lower and completely disappear after exposing the electrode surface to the thiol solution for four hours. These observations indicate an effective blocking of the mesoporous Pt by the adsorbed heptanethiol. Similarly, in the case of  $\mu\text{CP}$ , the external surface of the Pt electrode is modified significantly after printing with the thiol even already after a single printing step ( $\mu\text{CP}$  1<sup>st</sup>) and completely blocked when the number of printing cycles gets higher ( $\mu\text{CP}$  5<sup>th</sup>) as displayed in **Figure 2.4D**.

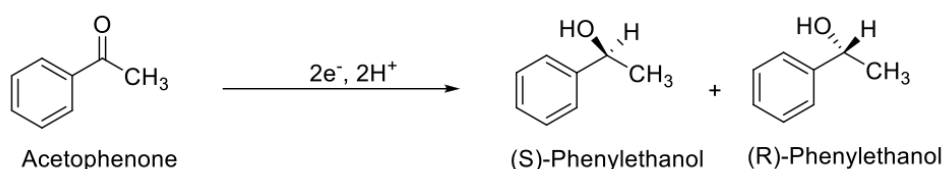
Due to the high active surface area of porous Pt electrodes, the capacitive current is dominating in all CV curves. Nevertheless, faradaic current can still be observed, but with only relatively small cathodic and anodic peaks (**Figure 2.4C** and **D**). The blocking properties of the SAM are directly related to the adsorbed thiol molecules because the electron transfer between the redox couple and the Pt atoms is hindered. [163, 167]

### 2.3.3 Enantioselective synthesis

The thiol-functionalized chiral-encoded mesoporous Pt has been employed as an electrocatalyst for asymmetric synthesis, by reducing

acetophenone (APE), which involves an overall two-electron two-proton transfer, to produce either (S)- or (R)-Phenylethanol ((S)- or (R)-PE) (**Scheme 2.2**).

The potentiostatic reduction at -0.40 V for 13 h is carried out under optimized conditions to obtain a high selectivity (pH of the solution at 4.0, 1 M NH<sub>4</sub>Cl as supporting electrolyte).[173] After the chiral electro-synthesis experiment, the product solution was extracted by heptane and subsequently analyzed by HPLC with a chiral column. The prochiral compound acetophenone and the desired enantiomers (S)-PE and (R)-PE have retention times of 10.50,



**Scheme 2.2** Electrochemical reduction of acetophenone into the racemic mixture of (S)- and (R)-phenylethanol by two electrons and two protons mechanism.

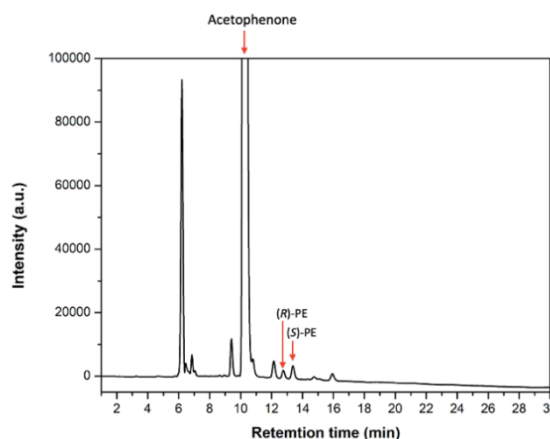


**Figure 2.5** HPLC chromatogram indicating the peak positions of acetophenone, (R)- and (S)-PE present in the product solution after potentiostatic electro-synthesis with (S)-PE imprinted mesoporous Pt. The supplementary peaks correspond to impurities that already exist in the starting substrate acetophenone.

13.00, and 13.75 min, respectively, as shown in the HPLC chromatogram of **Figure 2.5**.

After SAM protection of the (S)-PE encoded Pt surface using the self-assembly from solution, the enantiomeric excess (%ee) increases to 93% and gradually falls to 89, 84, and 79% when the coating time increases from 30 min to 1, 2 and 4h, respectively (**Figure 2.6**). The reason for a decrease in %ee as a function of coating time might be due to the fact that the non-ionic surfactant present inside the mesoporous structure of the Pt electrode in the initial step is dissolved by the ethanol solution during the coating process when prolonging the coating time. Consequently, thiol molecules do not adsorb only at the outermost part of the Pt electrode but also inside the mesoporous structure, where the chiral cavities are present. Hence, by fine-tuning the degree of blocking of the metal surfaces, the %ee can be optimized.

However, it is rather difficult to precisely control the degree of thiol surface functionalization when using the solution approach as the removal of mesopore is competing. Therefore, the alternative strategy of  $\mu$ CP of the thiol layer was studied because in this case the outermost surface of Pt can be protected without any passivation inside the mesopores. The results indicate

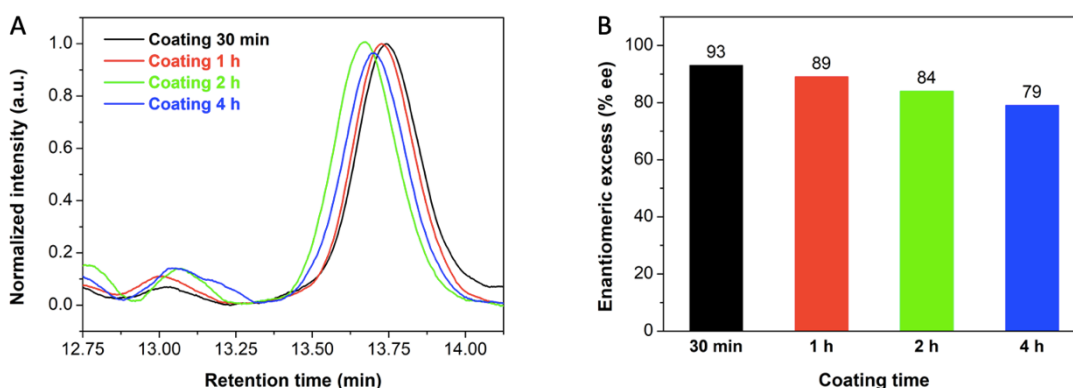


**Figure 2.6** Asymmetric synthesis with (S)-PE encoded mesoporous Pt electrodes after functionalization with heptanethiol by self-assembly from solution; A) HPLC chromatograms and B) Histogram of enantiomeric excess (%ee) as a function of different thiol coating times for 30 min (black), 1 h (red), 2 h (green) and 4 h (dark blue). The s.e.m value is around 3.0.

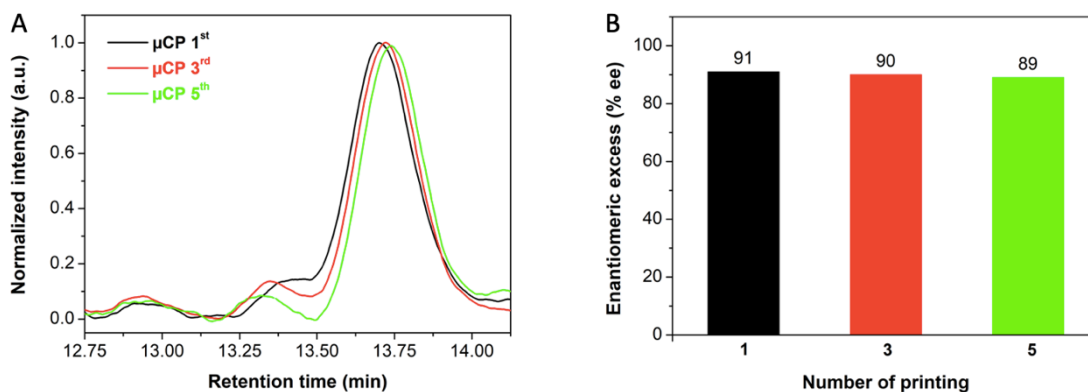


**Figure 2.7** Asymmetric synthesis with (S)-PE encoded mesoporous Pt electrodes after functionalization with heptanethiol by microcontact printing ( $\mu\text{CP}$ ); A) HPLC chromatograms and B) Histogram of enantiomeric excess (%ee) as a function of the number of  $\mu\text{CP}$  cycles, once (black), three times (red) and five times (green). The s.e.m value is around 1.0.

that a very high %ee value of  $90\% \pm 1.3$  can be achieved, irrespective of the contact times or the number of contact cycles (**Figure 2.7**). The stability of the %ee is due to the fact that the thiol loading is already quite high after the first  $\mu\text{CP}$  cycle. Thus, even though the thiol coating is repeated several times, the surface density of thiol molecules is not increasing significantly, resulting in a quite similar stereoselectivity for different numbers of printing cycles.[170-172]

This seems to confirm that thiol molecules are also adsorbed inside the mesopores when using the classical solution coating process. In contrast, when using the  $\mu\text{CP}$  approach, the thiol SAM is only present at the outermost surface of Pt. This is also illustrated by the CV curves in **Figure 2.8** comparing the three different cases of (i) non-coated porous Pt; (ii) thiol-coating *via* the solution approach for 4 h; (iii) thiol-coating *via* microcontact printing for five cycles. A decrease in the faradaic current associated with the H-adsorption/desorption region (-0.2 to 0.0 V) of thiol-coated electrodes is observed compared to the bare mesoporous Pt. However, the impact on the active surface area (ECSA) is much more pronounced for the electrode coated by following the solution coating approach, compared to the one modified *via*

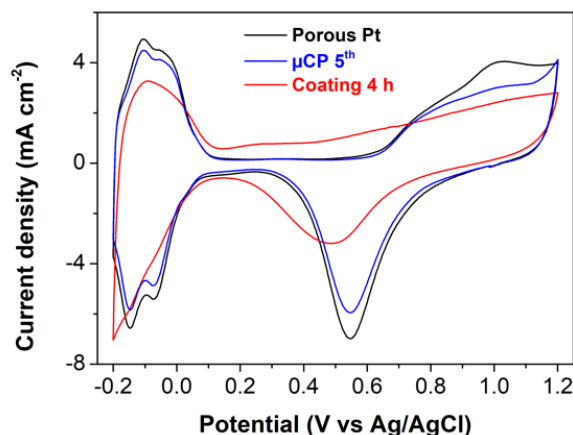


**Figure 2.8** Cyclic voltammograms of a non-coated mesoporous Pt electrode (black) in comparison with the thiol-coating on mesoporous Pt *via*  $\mu$ CP for five cycles (blue) and the classical solution coating for 4 h (red), recorded in 0.5 M  $\text{H}_2\text{SO}_4$  solution at a scan rate of  $100 \text{ mV s}^{-1}$ .

microcontact printing. The ECSA values of porous Pt modified by  $\mu$ CP for the fifth cycle and solution coating for 4 h are approximately  $39$  and  $25 \text{ cm}^{-2}$ , respectively, whereas bare porous Pt has the highest ECSA of  $44 \text{ cm}^{-2}$ . It therefore seems that using the  $\mu$ CP method allows better control in generating an efficient thiol layer protection while the high internal surface area is still preserved. Therefore, the  $\mu$ CP strategy was selected for all further experiments.

Turning back to the electrosynthesis, in the case of non-coated Pt electrodes (**Figure 2.9A and B**), the %ee values are mirror symmetric and rather modest when using (S)-PE or (R)-PE imprinted mesoporous Pt with the highest weight ratio (PE/ $\text{PtCl}_6^{2-}$  of 0.150), namely  $29\% \pm 3.2$  for (S)-PE and  $27\% \pm 5.5$  for (R)-PE (**Figure 2.9D** (black and red)). When modifying (R)-PE imprinted mesoporous Pt with thiol by  $\mu$ CP, a much higher %ee of  $88\% \pm 2.1$  was obtained (**Figure 2.9D** (pink)), with a symmetric mirror value for (S)-PE encoded mesoporous Pt with the same imprinting ratio (**Figure 2.9D** (light blue)). A porous Pt electrode without chiral encoding was used for a control experiment. As expected, a racemic mixture of (R)-PE and (S)-PE was generated with no significant selectivity for one or the other enantiomer (**Figure 2.9C** (orange)). The efficiency of the asymmetric synthesis was further studied for different

weight ratios of (S)-PE/PtCl<sub>6</sub><sup>2-</sup>. As displayed in **Figure 2.9C** and **D**, when enhancing the amount of chiral template in the plating mixture, the %ee value is remarkably increased from 57 ± 2.8 to 80 ± 2.5 and 90 ± 1.3 for ratios of 0.0375 (green), 0.0750 (dark blue), and 0.150 (light blue), respectively.

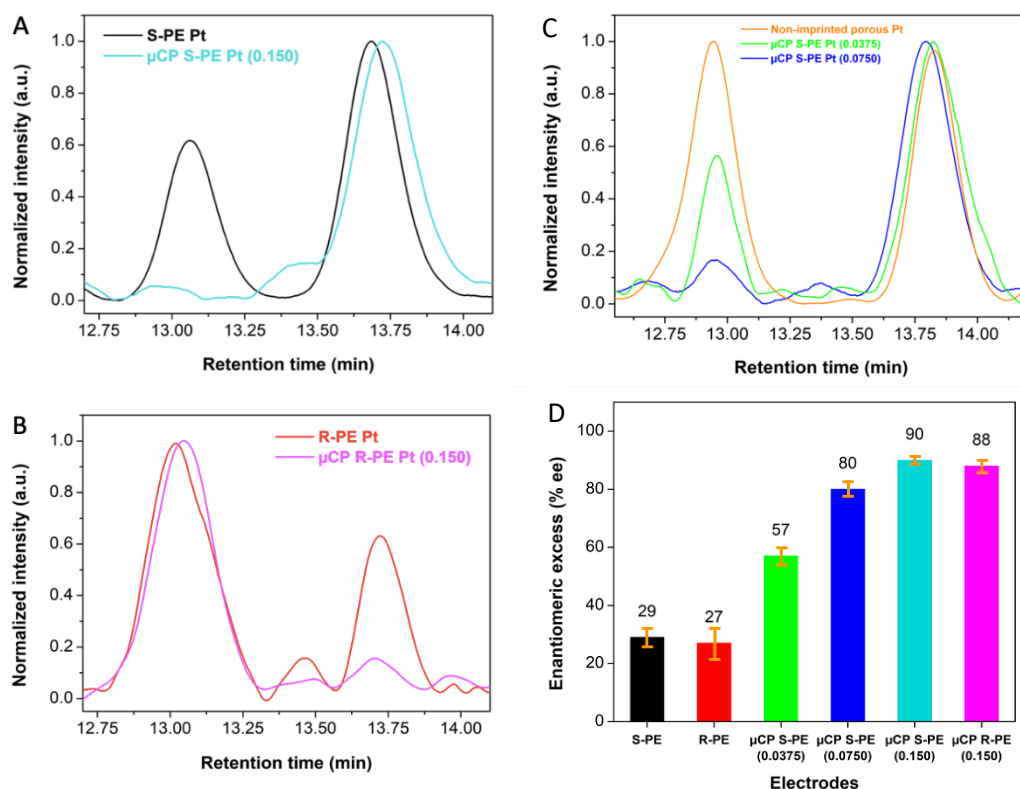
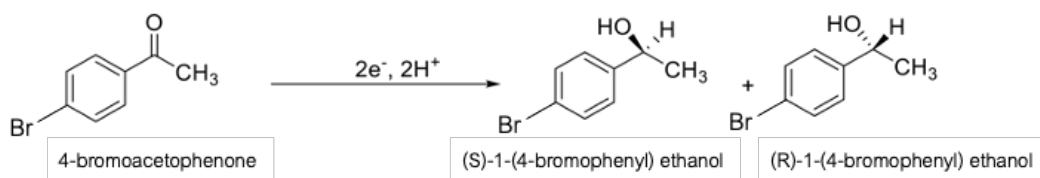


**Figure 2.9** Summary of enantioselective synthesis results: A) and B) HPLC chromatograms of the product mixtures performed with (S)-PE and (R)-PE imprinted mesoporous Pt electrodes, respectively, which are either bare or thiol-coated; C) HPLC chromatograms of the product solution when using different electrodes: non-imprinted mesoporous Pt (orange), and thiol-functionalized (S)-PE imprinted mesoporous Pt electrodes synthesized by using different weight ratios of (S)-PE/PtCl<sub>6</sub><sup>2-</sup> (0.0375 (green), 0.0750 (dark blue)); D) Histogram illustrating the enantiomeric excess (%ee) of different electrodes: bare (S)-PE (black) and (R)-PE (red) encoded mesoporous Pt electrodes (0.150 weight ratio PE/PtCl<sub>6</sub><sup>2-</sup>), functionalized (S)-PE imprinted mesoporous Pt electrodes with

different (S)-PE/PtCl<sub>6</sub><sup>2-</sup> weight ratios (0.0375 (green), 0.0750 (dark blue) and 0.150 (light blue)), and a functionalized (R)-PE imprinted mesoporous Pt electrode (0.150 weight ratio (R)-PE/PtCl<sub>6</sub><sup>2-</sup>) (pink). The %ee values were calculated from the integrated peak area of HPLC chromatograms, and all thiol-modified on Pt electrodes were obtained by using the  $\mu$ CP approach with the single coating cycle.

To further verify the beneficial effect of using the thiol-protected electrodes as electrocatalysts for electroreduction, not only acetophenone but also an acetophenone derivative, 4-bromoacetophenone (4-BrAPE), has been studied to illustrate that the asymmetric electrocatalysis strategy can be also applied for other reactants. By fine-tuning the reaction conditions of the asymmetric electroreduction of 4-BrAPE to 1-(4-bromophenyl) ethanol (4-BrPE) (**Scheme 2.3**) with a thiol-coated mesoporous Pt electrode modified *via* the  $\mu$ CP approach, a high enantiomeric excess of approximately 90% ( $\pm$  5.0) could be achieved. A mirror-symmetric result is obtained when using chiral Pt electrodes with both imprinted enantiomers, (S)- and (R)-BrPE (**Figure 2.10**). These findings open up interesting perspectives for extending this technology to other reactants.

Apart from the enantiomeric excess, the global yield of an enantioselective electrosynthesis has also to be considered as an important parameter. The overall yield in electrochemical synthesis depends on many parameters, such as the reaction time, the concentration of prochiral precursor, and the convection speed. In addition, the size of the electrode surface with



**Scheme 2.3** Electroreduction of 4-bromoacetophenone to 1-(4-bromophenyl) ethanol *via* two electrons and two protons transfer mechanism at the electrode surface.

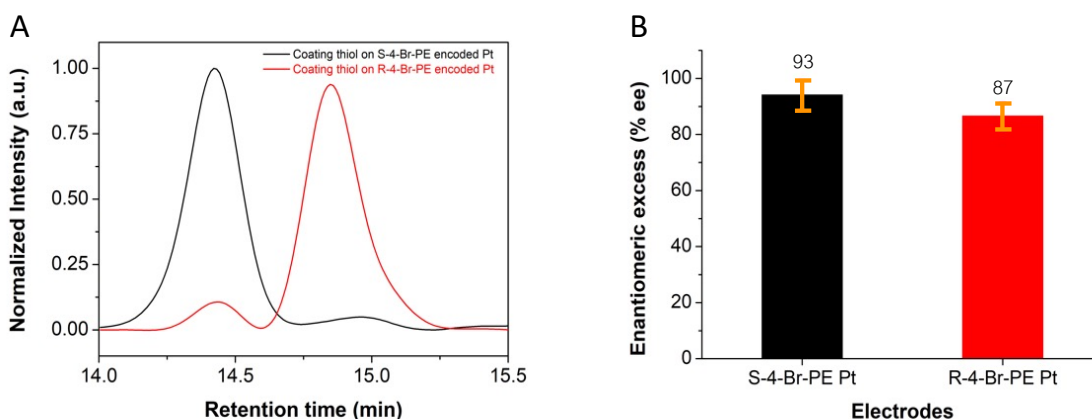


**Figure 2.10** Asymmetric electrocatalysis using a thiol SAM on (S)-BrPE and (R)-BrPE encoded mesoporous Pt electrodes: A) HPLC chromatograms of the product mixtures showing the enantiomers of (S)-BrPE (14.35 min) and (R)-BrPE (14.85 min) labeled in black and red colors respectively; B) Histogram illustrating enantiomeric excess values for the different working electrodes. The s.e.m value is around 2.4.

respect to the total volume of the electrolyte in the electrochemical cell is also an essential factor. Indeed, although all of these suggested parameters can be optimized in further studies, in the present proof-of-principle experiments, the primary focus has been to obtain the highest enantioselectivity. Therefore, although the total conversion using the present experimental set-up is relatively low, a high selectivity could be obtained in the case of the thiol functionalization, as demonstrated in **Figure 2.11** and summarized in **Table 2.1**. One of the reasons for a relatively low conversion could be that in the case of using the current set-up, a simple three-electrode system, there is no separation between the anodic and the cathodic compartments. This situation implies that side products, due to a partial reoxidation at the anodic side, leading to a kind of electrochemical short-circuit, are observed. This consumes current without a net formation of the desired products. Consequently, the global yield decreases and consequently improvements, e.g., in the cell design, include introducing a membrane separating the anodic and cathodic compartments, which should allow a considerable increase in the overall yield.

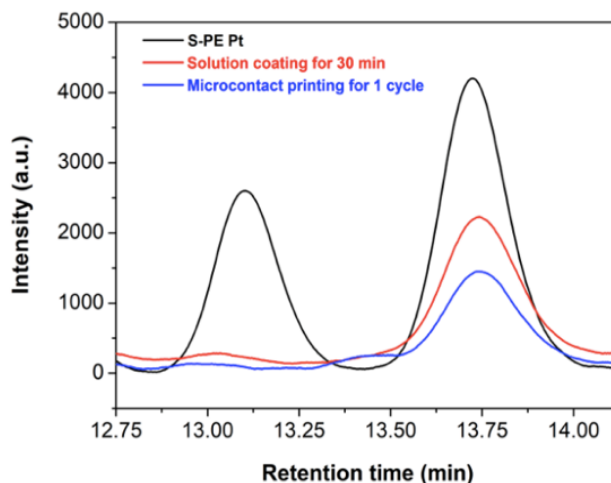


**Figure 2.11** HPLC chromatograms of the product solutions, illustrating product selectivity when using (S)-PE imprinted mesoporous Pt electrodes without further thiol functionalization (black) and with thiol coating using the solution (red) or the microcontact printing (blue) strategy.

Although the %ee of non-coated thiol SAM is rather low, even when using pulsed electro-synthesis with a quite long-pulse time (60 s),<sup>[90]</sup> the %ee can be significantly improved when using the thiol-coated mesoporous Pt (> 90%) even *via* continuous synthesis with a global synthesis time of 13 h. The thiol coated electrode leads to a decrease in the global active surface area of the electrode, resulting obviously in a lower total conversion of acetophenone in comparison with the non-coated one. However, the production rate of chiral compounds is not significantly reduced and can be even further improved by almost 30% compared to the bare mesoporous Pt when using the thiol coated one (**Table 2.1 entry 1 and 2.1**). Although the obtained %ee and overall conversion values when using the solution coating and the  $\mu$ CP approaches are comparable (approximately 90% and 0.7%, respectively), the  $\mu$ CP approach enables a higher production rate (**Table 2.1 entry 2.2, 3.1, and 3.2**). Furthermore, while the thiol layers entirely blocked the non-selective surface of the mesoporous Pt, confirmed by the disappearance of the faradaic current of the  $\text{Fe}^{2+}/\text{Fe}^{3+}$  redox couple as shown in **Figures 2.4 C and D**, the rate of the selective production of chiral molecules is up to 20% higher when using  $\mu$ CP

compared to the solution coating approach (**Table 2.1 entry 2.3 and 3.3**). These results again confirm that the controlled formation of thiol layers by the  $\mu$ CP approach, mainly on the outermost interface of the mesoporous Pt electrode, can enhance the production efficiency of chiral compounds (**Figure 2.8**). It should be noted that the production rate of chiral molecules using pulse electro-synthesis is much lower due to the long global synthesis time (**Table 2.1 entry 4**). Compared with our previous study regarding pulse synthesis, [90, 173, 174] this strategy of SAM protection shows an optimized performance in terms of a high %ee and a higher production rate of chiral molecules.

**Table 2.1** Summary of efficiency for the bare mesoporous Pt and the different thiol-coated mesoporous Pt electrodes for both continuous and pulsed electro-synthesis.

No.	Reaction conditions	ECSA (cm <sup>2</sup> )	Total reaction time (h)	%ee	%Conversion	Production rate of a chiral molecule [ $\mu$ mol/m <sup>2</sup> h]
1	Non-coated mesoporous Pt with continuous electro-synthesis	44	13	26.0	4.1	6.4
2.1	Thiol-coated mesoporous Pt <i>via</i> solution coating <u>for 30 min</u> with continuous electro-synthesis	42	13	93.3	1.5	8.8
2.2	Thiol-coated mesoporous Pt <i>via</i> solution coating <u>for 1 h</u> with continuous electro-synthesis	36	13	89.0	0.7	4.7
2.3	Thiol-coated mesoporous Pt <i>via</i> solution coating <u>for 4 h</u> with continuous electro-synthesis	25	13	78.6	0.4	3.6
3.1	Thiol-coated mesoporous Pt <i>via</i> microcontact printing <u>for once</u> with continuous electro-synthesis	42	13	91.2	0.9	5.1
3.2	Thiol-coated mesoporous Pt <i>via</i> microcontact printing <u>three times</u> with continuous electro-synthesis	40	13	90.4	0.8	5.1
3.3	Thiol-coated mesoporous Pt <i>via</i> microcontact printing <u>five times</u> with continuous electro-synthesis	39	13	88.7	0.7	4.3
4	Non-coated mesoporous Pt with pulse electro-synthesis (60-120 s)	44	39	38.3	0.4	0.3

To further investigate the stability and reusability of the thiol-SAM catalyst, the catalyst was rinsed after each catalytic cycle with MilliQ water overnight. Then it was immersed again in the new reaction solution for the next electrocatalytic cycle. Unfortunately, a certain decrease in enantioselectivity was observed due to the desorption of the SAM. However, the protective thiol layer can be regenerated by repeating the  $\mu$ CP with the already used chiral Pt electrode. Consequently, a high %ee of above 90% can be maintained in the next catalytic cycle (**Figure 2.12**).

Traditional metal catalysts are achiral, eventually producing racemic mixtures. However, in the present study we were able to introduce

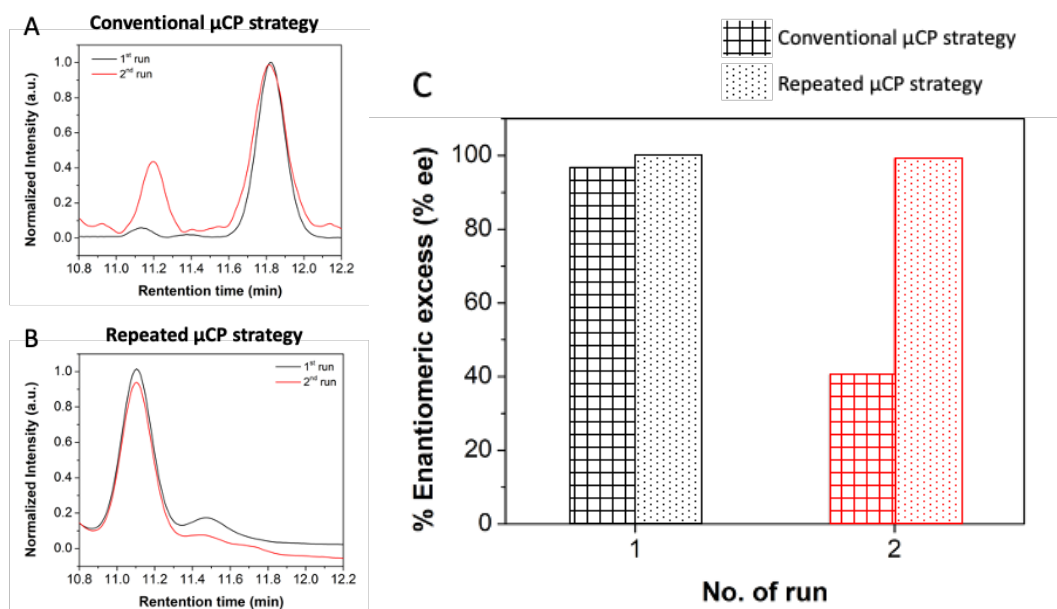
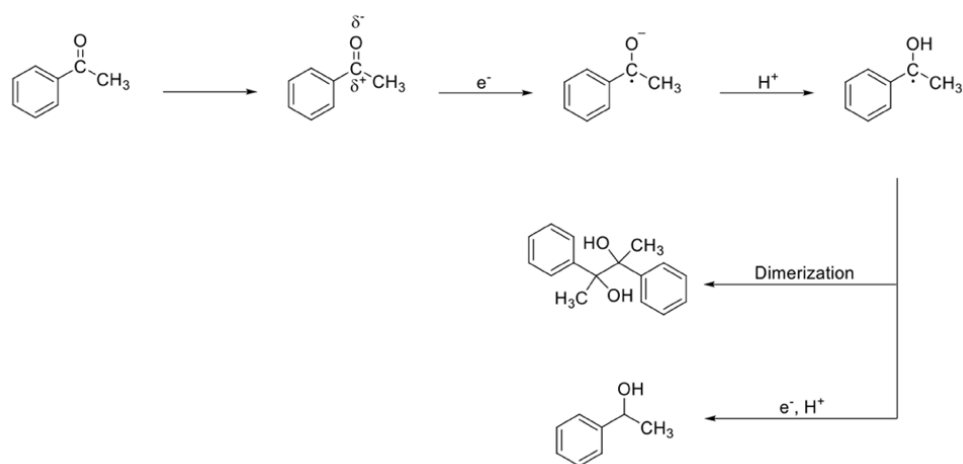


**Figure 2.12** Reusability test of the thiol-coated Pt electrodes: A) HPLC chromatograms of the products, obtained with (S)-PE imprinted mesoporous Pt modified with a single  $\mu$ CP step only at the beginning, for two sequential electrocatalytic runs; B) HPLC chromatograms of the products, obtained with (R)-PE imprinted mesoporous Pt for two electrocatalytic runs, but with a renewal of the  $\mu$ CP step after the first run; C) Histogram representing the enantiomeric excess for the two  $\mu$ CP strategies used in A) and B). Retention time of the enantiomers for (R)-PE and (S)-PE are 11.15 and 11.80 min, respectively. The s.e.m value is around 1.0.

chiral information in the metal matrix allowing the selective production of one chiral molecule.[90] It is therefore interesting to better understand the mechanism of how acetophenone can be converted into 1-phenylethanol on such chiral surfaces.[115, 175-178] As shown in **Scheme 2.1C** and according to our previous report,[87] chiral features can be present in the metal and decorate the mesopore walls, generated by using the lyotropic liquid crystal phase combined with chiral molecules to control the metal structures. Typically, the hydrophilic part of the chiral template molecules interacts directly with the non-ionic surfactant at its outermost surfaces. Therefore, the Pt matrix grows around the aromatic unit of the chiral template and the hexagonal column of surfactant, resulting in the formation of specific chiral sites corresponding to the shape and size of the chiral templates.[87] When this chiral electrode is then applied as an electrocatalyst, the prochiral reactants adsorb preferentially with the aromatic moiety located in the deeper part of the chiral site, eventually generating an asymmetric environment around the pore-mouth of the chiral cavity.[177] Concerning the electroreduction of acetophenone, the hydrogenation of a carbonyl group to alcohol requires the addition of two electrons and two protons, forming the more favorable enantiomer of the chiral product, either (R)- or (S)-PE (**Scheme 2.2**), according to the preferential configuration of the chiral active site. As illustrated by the mechanism proposed in **Scheme 2.4**, after the specific adsorption of the prochiral molecule at the asymmetric site, the polarized carbonyl can accept an electron and a proton, producing a phenolic radical intermediate.[176] Typically, dimerization between the phenolic radical species tends to be easy, eventually producing by-products. In this context, the pH of the electrolyte plays a crucial role in avoiding such a side reaction.[173, 175] If the process is carried out under acidic conditions, the reaction preferentially leads to the chiral products due to a high concentration of protons in the supporting solution, which prevents the dimerization by “quenching” the radical species.[173, 175] As this latter step occurs in a chiral environment, the proton and electron addition happens in a stereoselective way, eventually *via* hydrogen that is preabsorbed on the metal.



**Scheme 2.4** Proposed reaction mechanism for the electroreduction of acetophenone on Pt surfaces.

## 2.4 Conclusion

In this chapter, self-assembled monolayer protection of surfaces of chiral encoded Pt has been developed to promote high enantioselectivity during the electroreduction of chiral compounds. The observed beneficial effect originates from the passivation of the unselective outer surface of the electrodes, thus suppressing almost completely the non-stereospecific side-reaction. The results clearly demonstrate that using different thiol-functionalization techniques, either self-assembly from solution or microcontact printing ( $\mu$ CP), the enantiomeric excess of the product mixture is remarkably improved to up to 90%, which is three-times higher than what can be obtained with a non-modified Pt electrode. Moreover, this approach also significantly decreases the global reaction time from several days down to several hours. With these promising outcomes, the previously studied pulsed electroreduction concept is no longer needed; alternatively, conventional electroreduction can be used instead. Thus, the findings open up a novel era for highly controllable chiral electroreduction. After careful optimization of all experimental parameters, the approach might become a real alternative for asymmetric heterogeneous catalysis and photocatalysis, with elevated global yields.

## Chapter 3

# Synthesis and characterization of chiral-encoded mesoporous Platinum-Iridium (Pt-Ir) alloy films

### 3.1 Introduction

Over the past decades, although chiral technologies for the production of a specific chiral molecule have been proposed *via* various strategies,[132, 179, 180] enantioselective synthesis plays a vital role because it has been widely used to generate very high enantioselectivity, as well as to minimize the waste produced as by-products.[108, 181] Therefore, the rational design of chiral materials used as catalysts is essential to accomplish highly efficient asymmetric synthesis. Indeed, there are several strategies to design catalysts for asymmetric synthesis, such as coordination complexes,[108] enzymatic compounds,[122] chiral ligand-functionalizing supports,[80-82] breaking the symmetry of bulk metal crystals,[83, 84] and eventually molecular imprinting of the bulk of a solid structure.[85-92] Among these approaches, the molecular imprinting concept is promising as it allows a rational design of chiral structures, depending on the used chiral molecular templates.[85-92]

Indeed, the molecular imprinting strategy has been successfully applied to create chiral footprints in several materials, i.e., polymers, silicate compounds, and metals or metal oxides.[182-184] Nevertheless, due to the superior properties in terms of high conductivity and stability of metals, it is promising to apply such a chiral molecular imprinting approach to different metals. For instance, Switzer and his co-workers have synthesized (R,R)- or (S,S)-tartrate imprinted CuO films by electrodeposition. The materials were applied to differentiate the rate of electrooxidation between tartrate enantiomers on imprinted oxide surfaces with different chiral configurations.[85] Apart from metal oxides, Rothenberg G. *et al.* have illustrated the synthesis of the metallo-

organic hybrid materials using chiral cinchona alkaloids to imprint Pd nanoparticles. Interestingly, after removing the chiral templates, the retention of chiral information could be confirmed by photoelectron emission spectroscopy with clockwise circularly polarized light (cw-CPL) or counterclockwise circularly polarized light (ccw-CPL). However, utilizing these chiral Pd nanoparticles as a catalyst for enantioselective synthesis resulted only in modest enantioselectivity.[86]

Recently, we have demonstrated the first proof-of-concept to elaborate advanced chiral metals, namely the Chiral-Imprinted Mesoporous Metals, based on the beneficial combination of the imprinting approach of chiral molecules into metal structures and mesoporous features of the metal. This material has been elaborated by the electrodeposition in the simultaneous presence of self-assembled non-ionic surfactant molecules and chiral templates.[87, 89, 90] The quite versatile fabrication process of the mesoporous chiral metal has been applied not only for noble metals such as Pt,[87, 89, 90] but also for non-noble metals like Ni.[91] In addition, various types of chiral features have been successfully generated inside the mesoporous channels depending on the use of chiral template molecules, such as 3,4-dihydroxyphenylalanine (DOPA),[87] mandelic acid,[88, 89] and phenylethanol.[90, 91] Accordingly, the designed materials have been employed in a great variety of potential applications ranging from chiral recognition,[87, 88] and enantioselective separation [101] to chiral actuators [102] and asymmetric synthesis.[89-91] In the latter case, chiral encoded mesoporous metals were used as catalysts to produce selectively chiral compounds *via* electroreduction of prochiral precursors such as phenyl glyoxylic acid [89] and acetophenone.[90, 91] The designed chiral metal structures exhibit outstanding features, such as very high surface areas, favoring mass transport, and high enantioselectivity of up to 90 % when using pulsed electrosynthesis.[90] Even though a high enantiomeric excess (%ee) could be obtained using Pt, the limited stability of such chiral imprinted metals has been a disadvantage evidenced by a significant decrease of %ee after several electrocatalytic cycles.[90] Therefore, the further improvement of chiral

metals to achieve higher structural stability is crucial for practical applications in chiral synthesis.

In order to enhance the structural stability of chiral encoded metals, i.e., avoiding a gradual loss of the chiral information, herein, the design of a metal alloy is one promising strategy.[185] The more pronounced mechanical stability of metal alloys is attributed to the reduction of the lattice strain around the host atoms, due to the insertion of a promoter into the bulk metal structure, which leads to the canceling of the dislocation motion of metal atoms in their bulk structures.[56] For instance, by introducing a promoter to the bulk Pt structure, platinum alloys can exhibit a greater hardness and strength compared to their pure forms.[58] Typically, various noble metals, such as ruthenium (Ru), rhodium (Rh), iridium (Ir), and gold (Au), can be integrated into Pt. However, Ir seems to be the most promising promoter to increase the hardness by up to four times higher compared to pure Pt when using Ir concentrations from 5 to 30 wt% in the Pt-Ir alloys.[57, 59] Typically, Ir has a similar lattice structure to Pt and can be reduced *via* electrodeposition in a similar range of potentials as Pt, between 0.0 to -0.1 V (vs Ag/AgCl), implying that Ir is readily incorporated in the alloy structure.[59, 186]

To date, several bimetallic mesoporous Pt alloys, prepared by co-electrodeposition in the presence of a lyotropic liquid crystal (LLC), have been successfully fabricated, such as Pt-Au and Pt-Ru.[1] However, a mesoporous Pt-Ir alloy with chiral features obtained by electrodeposition has not yet been proposed. In this chapter, Ir has been selected as a promoter to form an alloy with Pt for generating chiral-encoded mesoporous Pt-Ir alloys. Encoding mesoporous Pt-Ir alloys with chiral information was successfully achieved *via* co-electrodeposition of Pt and Ir salts in the simultaneous presence of a LLC phase and chiral templates. Either two-dimensional (2D) Au-coated glass slides or three-dimensional (3D) porous Ni foams were employed as substrates for the electrodeposition of the Pt-Ir alloy. Various independent techniques, including transmission electron microscopy (TEM), cyclic voltammetry (CV), and X-ray photoelectron spectroscopy (XPS), have been employed to confirm the porous alloy structure. Most importantly, since the Pt-Ir alloy structure tends to improve

the mechanical properties such as hardness and strength compared to monometallic Pt, chiral features of the metal matrix should be better preserved, even under severe conditions (such as high positive potential and temperature). Hence, the characterization technique of Secondary Harmonic Generation (SHG) spectroscopy has been employed to identify chiral features on the electrode surfaces. Indeed, such a technique could allow us to observe a significant difference in the asymmetric factor values between the signals collected from left- and right-hand circular polarized light if it interacts with chiral surfaces.

## **3.2 Experimental section**

### **3.2.1 Chemicals**

Hydrogen hexachloroplatinate(IV) hexahydrate ( $\text{H}_2\text{PtCl}_6 \cdot 6\text{H}_2\text{O}$ ), dihydrogen hexachloroiridate(IV) hydrate ( $\text{H}_2\text{IrCl}_6 \cdot x\text{H}_2\text{O}$ ), polyethylene glycol hexadecyl ether (Brij<sup>®</sup> C10), 3,4-dihydroxy-L-phenylalanine ((L)-DOPA) and 3,4-dihydroxy-D-phenylalanine ((D)-DOPA), (R)-phenylethanol and (S)-phenylethanol ((R)-PE and (S)-PE), were purchased from Sigma-Aldrich. Sulfuric acid ( $\text{H}_2\text{SO}_4$ ) was obtained from Alfa. Au-coated glass slides (Au (300 nm)/Chromium (Cr)/glass slide) and a nickel (Ni) foam ( $200 \text{ m}^2\text{g}^{-1}$ , Gelon) were directly used as a substrate for the Pt-Ir alloy electrodeposition. For all experiments, ultrapure deionized water with an  $18.2 \text{ M}\Omega \text{ cm}$  (MilliQ water) resistivity was applied. All chemicals were utilized as received without further purification.

### **3.2.2 Synthesis of non-imprinted and chiral-imprinted mesoporous platinum-iridium (Pt-Ir) alloy by electrodeposition supported on Au-coated glass slides**

The electrochemical deposition was carried out with a potentiostat (Metrohm  $\mu$ Autolab Type III) with a three-electrode system comprising Ag/AgCl (sat. KCl), a Pt mesh, and a gold-coated glass slide ( $0.25 \text{ cm}^2$ ) as a reference, counter and working electrodes, respectively. Data analysis was performed using Nova (version 1.11) program provided with the potentiostat.

Gold-coated glass slides were cleaned by following three steps: (i) sonicating in isopropanol for 15 min; (ii) rinsing with MilliQ water several times; (iii) drying under nitrogen (N<sub>2</sub>) gas flow. The selected area of 0.25 cm<sup>2</sup> was defined by taping with transparent adhesive tape the protected sites.

The plating gel was prepared based on a mixture of H<sub>2</sub>PtCl<sub>6</sub>·6H<sub>2</sub>O and H<sub>2</sub>IrCl<sub>6</sub>·xH<sub>2</sub>O (29 wt%, 85Pt:15Ir at%) in 29 wt% of MilliQ water, homogenized by ultra-sonication for 5 min. After that, Brij<sup>®</sup> C10 was added to the solution with a weight ratio of 42 % and continuously mixed for 15 min, followed by heating at 40 °C for 45 min. This procedure was repeated for three consecutive cycles to allow the formation of a mesoporous hexagonal close-packed structure of the non-ionic surfactant. The as-prepared gel was placed on the cleaned gold-coated glass slide surface. Then, electrodeposition was carried out by chronoamperometry with the desired charge density (up to 10 A cm<sup>-2</sup>) at various applied potentials (-0.05, -0.1, and -0.2 V). Finally, the electrode was rinsed several times and soaked overnight in MilliQ water for the removal of templates.

For chiral-imprinted mesoporous Pt-Ir electrodes, the same process was used. However, the desired chiral molecule such as (L)- and (D)-DOPA or (R)- and (S)-phenylethanol (PE) was added to the precursor gel with a weight ratio of the chiral molecules and metal ions of 0.04 and 0.15 for DOPA or PE/(PtCl<sub>6</sub><sup>2-</sup> + IrCl<sub>6</sub><sup>2-</sup>), respectively.[87, 90]

### 3.2.3 Synthesis of mesoporous Pt-Ir alloys supported on Ni foams

The Pt-Ir alloys were synthesized by electrodeposition following the procedure mentioned above with some modifications, using an Autolab PGSTAT204 and a Ni foam (geometrical area of 1 cm<sup>2</sup>) as a working electrode. The electrochemical apparatus is illustrated in **Figure 3.1**. Ni foam is elaborated with a mixture of Pt-Ir plating gel on both the top and bottom sides. A couple of Pt meshes (counter electrodes) are placed on the outsides of the plating gel. The reference electrode (Ag/AgCl sat. KCl) is connected to the system on the upper part. The plating gel, composed of the metal precursors (29 wt%), MilliQ water (29 wt%), Brij<sup>®</sup> C10 (42 wt%), and the amount of optimized chiral

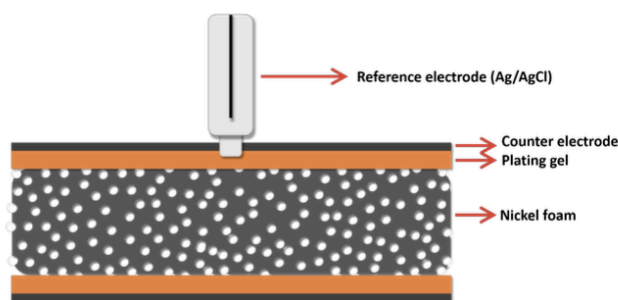


**Figure 3.1** Schematic illustration of the experimental set-up for electrodeposition of the chiral encoded catalyst on nickel foam.

templates, was prepared with the aforementioned procedure (section 3.2.2). Subsequently, the gel was positioned on the working electrode. A reduction potential at  $-0.05$  V vs Ag/AgCl was applied, and a given charge density ( $\text{C}\cdot\text{cm}^{-2}$ ) which controls the thickness of the deposited Pt-Ir films. Removal of the excess plating gel after the electrodeposition was conducted by rinsing with MilliQ water several times, followed by immersion in MilliQ water for several days. The rinsed water must be regularly changed to ensure that the templates are removed entirely from the prepared metal structure.

### **3.2.4 Characterization of the mesoporous platinum-iridium (Pt-Ir) alloy electrodes**

The surface morphology of the Pt-Ir electrodes was monitored by Scanning Electron Microscopy (SEM) operated on a Hitachi TM-1000 tabletop microscope. Additionally, SEM was also used for cross-sectional imaging. The composition and dispersion of elements were analyzed by the Energy Dispersive X-ray spectrometry (SEM/EDS) performed on a JEOL, JSM-7610F.

The topological properties and lattice fringes of Pt-Ir were characterized by Transmission Electron Microscopy (TEM) performed on a JEOL JEM-ARM200F microscope at 200 kV. Concerning the deposited Pt-Ir supported on an Au-coated glass slide, an ultra-thin Pt-Ir sample was prepared following the mesoporous Pt-Ir electrodeposition procedure with a current density of  $4 \text{ C cm}^{-2}$ . Subsequently, the deposited Pt-Ir layers were removed from the substrate by gentle mechanical scraping. The samples were dispersed in

ethanol, and the prepared solution was finally dropped onto the Cu-TEM grids for analysis. For the deposited Pt-Ir layers supported on Ni foam, the Pt-Ir alloy films were removed from the support by manual scratching. The as-prepared samples were sonicated in ethanol (1 mL) for 5 min to peel off the small Pt-Ir pieces from the Ni foam. Then, the Pt-Ir samples were directly transferred onto a carbon-coated Cu TEM grid on a TEM sample holder and dried overnight.

Inductively Coupled Plasma Optical Emission Spectroscopy (ICP-OES) performed on an Agilent Technologies, 700 series, using an argon (Ar) plasma as the ionization source, was conducted for the elemental composition analysis. All deposited Pt-Ir samples were digested in aqua regia solution (the mixture of 1 M nitric acid (HNO<sub>3</sub>) and 3 M hydrochloric acid (HCl)) at 80 °C for 4 h, and the solution was diluted ten times by volume before analysis. Calibration curves of Pt and Ir metals were measured by dissolving H<sub>2</sub>PtCl<sub>6</sub> in aqua regia at 5, 10, 20, 40, and 60 ppm ( $R^2 = 0.999897$ , detection wavelength at 214.424 nm), and dissolving H<sub>2</sub>IrCl<sub>6</sub> in aqua regia at 1, 5, 10, 20 and 40 ppm ( $R^2 = 0.999890$ , detection wavelength at 224.268 nm), respectively.

In order to confirm the alloy structure of Pt-Ir, an X-ray diffractometer (XRD) was used on a Bruker D8 ADVANCE instrument. The Pt-Ir electrode was placed in a sample holder. The experiment was carried out with Cu-K $\alpha$  radiation with a wavelength of 1.54 Å, 40 kV, 40 mA, 2 $\theta$  scan range from 30 to 60°, increment of 0.02°, and a scan speed of 0.2 s step<sup>-1</sup>.

To investigate the metallic states and the elemental surface composition of the Pt-Ir films, X-ray Photoelectron Spectroscopy (XPS) was performed on a JEOL JPS-9010, coupled with a monochromatic Al K $\alpha$  X-ray source ( $h\nu = 1486.6$  eV) for the Pt-Ir deposits supported on the Au-coated glass slide and equipped with a monochromatic Mg K $\alpha$  X-ray source ( $h\nu = 1253.6$  eV) in the case of Pt-Ir films supported on Ni foam. The Pt-Ir electrodes were treated with a low-energy electron flood gun for sample pre-treatment. Positions of the XPS spectra were corrected by the reference carbon (C) 1s peak, at 284.7 eV. XPS depth-profile analysis of the mesoporous Pt-Ir films was carried out by etching the Pt-Ir electrodes with argon (Ar) ion gun for desired times until 160 s with an etching rate of around 2.67 nm s<sup>-1</sup>, meaning that the thickness of the Pt-

Ir layer which is etched is around 400 nm after 160 s. Surface compositions are reported in atomic percentages (at %) and were quantitated using the relative integrated peak areas of the Pt (Pt  $4f_{7/2}$  and  $4f_{5/2}$ ) and Ir (Ir  $4f_{7/2}$  and Pt  $4f_{5/2}$ ).

For electrochemical characterization, cyclic voltammetry (CV) was applied in 0.5 M  $H_2SO_4$  at a scan rate of  $100 \text{ mV s}^{-1}$ . The electrochemically active surface area (ECSA) of the electrodes was calculated from the hydrogen adsorption/desorption regions of the obtained CV curves following a previous report.[87, 164]

Detailed investigation of chiral features at chiral-imprinted mesoporous metals has been carried out by Secondary Harmonic Generation (SHG) (**Figure 3.2**) using various types of mesoporous Pt-Ir electrodes including (D)-DOPA, (L)-DOPA, racemic (DL- or rac-) DOPA and non-imprinted mesoporous Pt and Pt-Ir alloy electrodes obtained with a molar ratio between  $[Pt^{2+}]$  or  $[Pt^{2+} + Ir^{2+}]$  salts and DOPA enantiomers of 12 and deposited with a charge density of  $4 \text{ C cm}^{-2}$ . The chiral metal samples were irradiated at a  $70^\circ$  angle of incidence (AOI), a pulsed laser beam at 1030 nm ( $2.9 \times 10^{14} \text{ Hz}$ ), a repetition rate at 80 MHz, and pulsed time at 250 fs. The SHG light was detected at 515 nm ( $5.8 \times 10^{14} \text{ Hz}$ ) using the reflected direction. In this case, polarization scans were adjusted manually. The second-harmonic light has been deconvoluted into P- and S-polarized components with an incident beam power of 1000 and 250 mW, respectively.

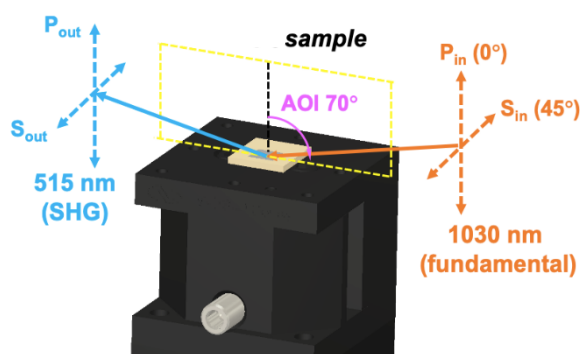


**Figure 3.2** Illustration of the experimental set-up for investigating chiral information by Secondary Harmonic Generation (SHG) on chiral imprinted mesoporous metal films.

### 3.3 Results and Discussion

#### 3.3.1 Preparation of plating gel for the synthesis of the mesoporous Pt-Ir electrodes.

$\text{H}_2\text{PtCl}_6$  and  $\text{H}_2\text{IrCl}_6$  can easily dissolve in water. **Figure 3.3A and B** represent the colors of Pt and Ir solutions as transparent orange and dark brown, respectively. Eventually, when the Pt and Ir precursor solutions were mixed, there was no significant difference in the color of the solution, yellow-brownish, implying that  $\text{H}_2\text{PtCl}_6$  and  $\text{H}_2\text{IrCl}_6$  did not form new metal complexes (**Figure 3.3C**). Mixing the metal ion solution and the non-ionic surfactant (polyethylene glycol hexadecyl ether, Brij<sup>®</sup> C10) led to a homogeneous yellow-brownish gel, as shown in **Figure 3.3D**.

The co-electrodeposition from the mixture of Pt and Ir precursors with a weight ratio of 4.5 [ $\text{IrCl}_6^{2-}$ ] / [ $\text{PtCl}_6^{2-}$ ] (15 Ir: 85 Pt atomic ratio (at%)) was carried out to synthesize mesoporous Pt-Ir alloy films in the presence of chiral templates in the lyotropic liquid crystal phase (LLC). The chiral templates tested

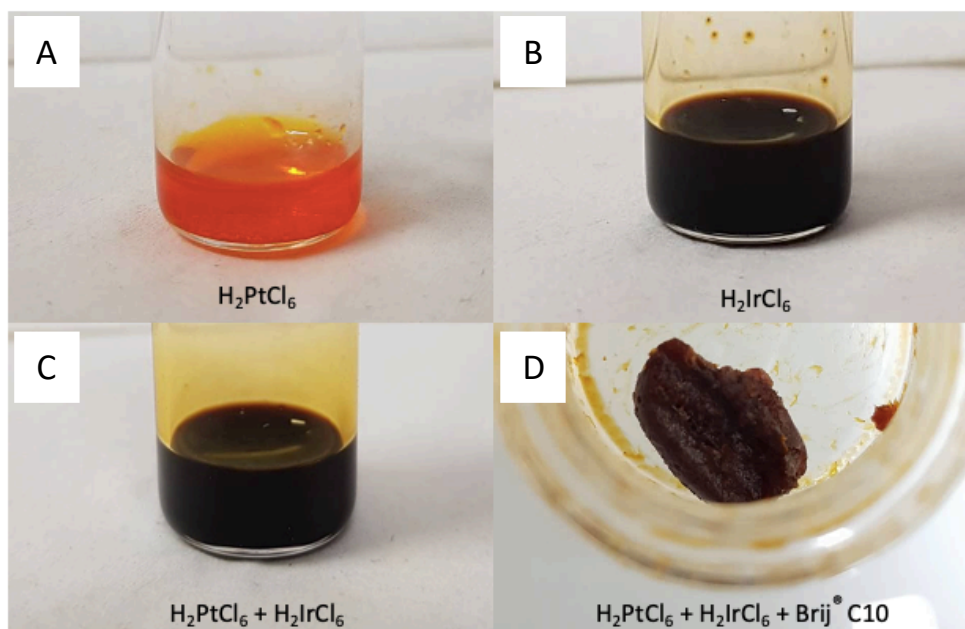
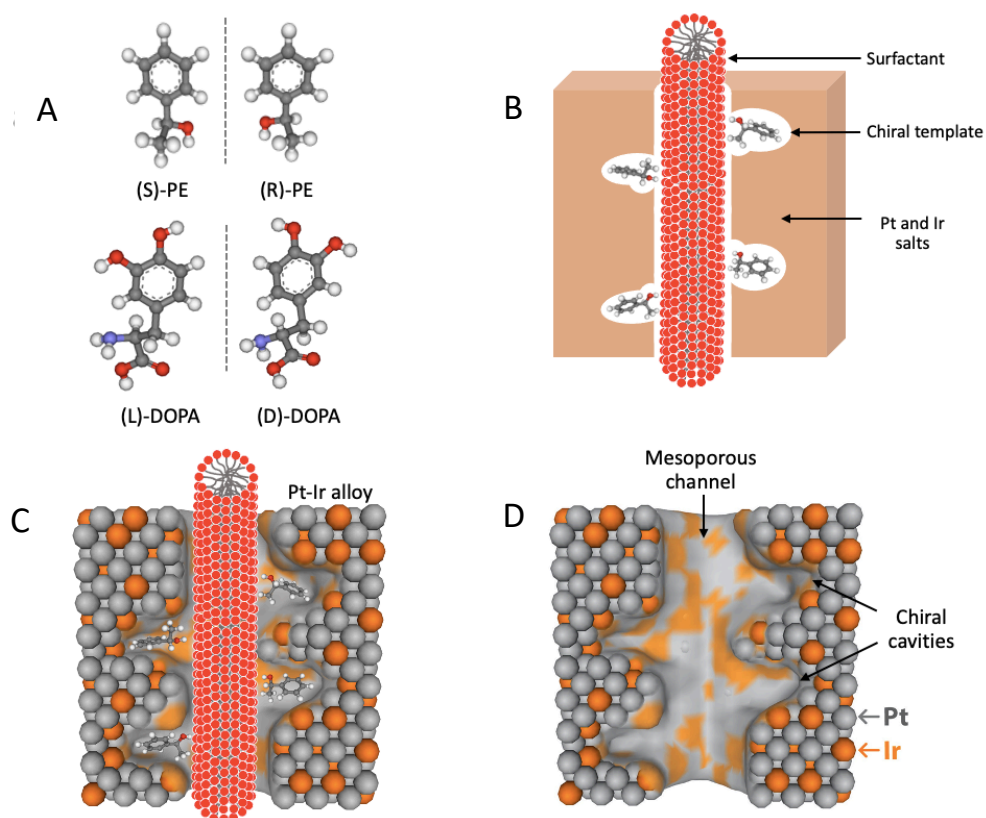


**Figure 3.3** Optical photograph of metal solutions: A)  $\text{H}_2\text{PtCl}_6$ ; B)  $\text{H}_2\text{IrCl}_6$ ; C) the mixture of  $\text{H}_2\text{PtCl}_6$  and  $\text{H}_2\text{IrCl}_6$ ; D) the precursor gel for electrodeposition composed of metal precursors (29 wt%), MilliQ water (29 wt%) and Brij<sup>®</sup> C10 (42 wt%).

in these experiments were (S)-PE, (R)-PE, (L)-DOPA, and (D)-DOPA (**Scheme 3.1A**). The chiral templates are adsorbed preferentially at the outermost surface of the non-ionic surfactant columns forming a self-assembled hexagonal structure ( $H_1$ ) (**Scheme 3.1B**). Subsequently, electrodeposition leads to the formation of alloy structures around the assembled supramolecular templates (**Scheme 3.1C**). Eventually, mesopores and chiral cavities located at the outermost regions of the channel are obtained after the removal of templates, as illustrated in **Scheme 3.1D**.



**Scheme 3.1** Schematic illustration of the procedure to synthesize a chiral-imprinted mesoporous Pt-Ir alloy: A) chiral molecular templates (S)-PE, (R)-PE, (L)-DOPA, and (D)-DOPA; B) formation of non-ionic surfactant columns with adsorbed chiral molecules in the presence of Pt and Ir salts; C) the growth of alloyed Pt and Ir around the self-assembled templates by co-electrodeposition; D) the obtained chiral-encoded mesoporous Pt-Ir alloy after the template removal.

### 3.3.2 Morphological and topological characterization of mesoporous Pt-Ir alloys supported on Au-coated glass slide

The electrodeposition rate of Pt is around four times higher than that of Ir.[186] Therefore, to achieve homogeneous incorporation of Ir into the Pt bulk structure, the effect of electrodeposition potential on the film morphology and elemental composition was investigated for a charge density of  $10 \text{ C cm}^{-2}$ . A rough surface is observed when applying a potential of  $-0.20 \text{ V}$  vs Ag/AgCl, as shown in the scanning electron microscopy (SEM) image of **Figure 3.4A**. In contrast, a slower electrodeposition rate at potentials of  $-0.10$  and  $-0.05 \text{ V}$  vs Ag/AgCl leads to a smoother surface (**Figure 3.4B and C**, respectively).

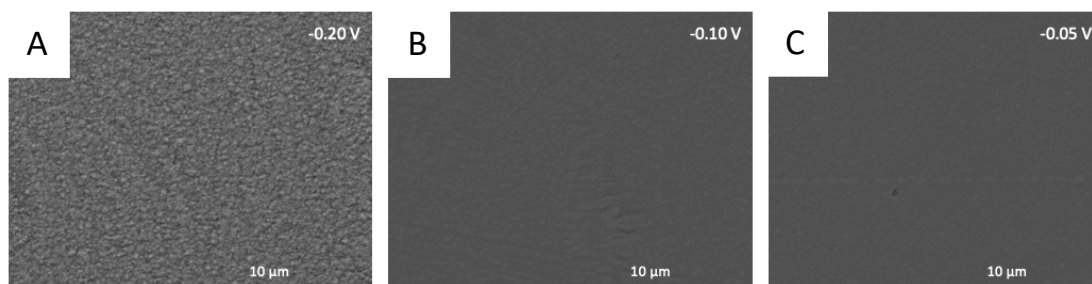


**Figure 3.4** SEM images of mesoporous Pt-Ir films deposited at different potentials: A), B), and C) electrodeposition at  $-0.20$ ,  $-0.10$ , and  $-0.05 \text{ V}$  vs Ag/AgCl, respectively.

Cyclic voltammetry in sulfuric acid ( $\text{H}_2\text{SO}_4$ ) solution was used in the potential window from  $-0.2$  to  $1.2 \text{ V}$  to verify the electrochemical active surface area (ECSA) of the electrodes. As shown in **Figure 3.5**, a higher current density is observed when a more negative potential is applied for Pt-Ir electrodeposition. This relates to a very high ECSA measured from the peak in the region of hydrogen adsorption/desorption (below  $0 \text{ V}$ ).[87, 164, 186] The calculation of the ECSA is described in **Table 3.1**. It was found that when using more negative potentials for deposition, larger ECSA values are observed. The enhanced ECSA suggests that deposition at more negative potentials, a rougher external surface is generated (**Figure 3.4A**).

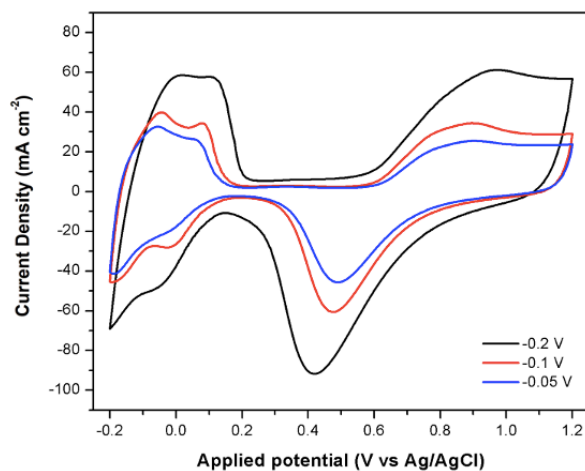


**Figure 3.5** Cyclic voltammograms of Pt-Ir electrodes in 0.5 M H<sub>2</sub>SO<sub>4</sub> generated at a potential of -0.20 (black), -0.10 (red), and -0.05 (blue) V vs Ag/AgCl, respectively, measured with a scan rate of 100 mV s<sup>-1</sup>.

**Table 3.1** Effect of electrodeposition potential and deposition charge density on the morphology and elemental composition of mesoporous Pt-Ir electrodes.

Applied potential (V)	Charge density (C cm <sup>-2</sup> )	ECSA (cm <sup>2</sup> )	Roughness factor <sup>a</sup>	Pt <sup>b</sup> (at%)	Ir <sup>b</sup> (at%)
-0.20	10	649	2,596	100.0	-
-0.10	10	384	1,536	100.0	-
-0.05	10	354	1,416	99.5	0.5
-0.05	8	100	400	97.5	2.5
-0.05	6	66	264	97.0	3.0

<sup>a</sup> The roughness factor is calculated by dividing the electrochemically active surface by the geometrical area (0.25 cm<sup>2</sup> in all cases) of the electrode.

<sup>b</sup> Pt and Ir atomic percent (at%) values are estimated from EDS-SEM measurements.

Furthermore, the applied potential for Pt-Ir deposition also directly influences the Ir content. Ir is detectable when using -0.05 V as deposition

potential (**Table 3.1**), measured by elemental analysis with a SEM equipped with an energy dispersive X-ray spectrometry (EDS-SEM). However, Ir cannot be determined in the remaining cases at higher negative potentials (-0.1 and -0.2 V). The different electrodeposition rates of Pt and Ir is the essential factor.[186] In the case of Ir, the electrodeposition has the best charge efficiency for potentials between -0.1 and 0.0 V. However, for Pt, the more negative the potential, the faster the deposition rate. Therefore, deposition at a potential of -0.05 V is a reasonable compromise to synthesize Pt-Ir alloys.

Apart from fine-tuning the optimized applied potential, the surface thickness is another essential parameter to control the film composition and surface properties. It can be easily controlled by varying the deposited charge density. Layers of different thicknesses were obtained by varying the charge density from 6 to 10 C cm<sup>-2</sup>, when applying -0.05 V for electrodeposition. In **Figure 3.6A**, the cyclic voltammograms of mesoporous Pt-Ir electrodes with varying thicknesses are comparable to typical mesoporous Pt (**Figure 3.6B**). The CV curves show the Pt oxidation between 0.60 and 1.00 V, the PtO reduction peak in the region from 0.70 to 0.25 V, and the hydrogen adsorption/reduction signals by the cathodic/anodic peaks below 0.10 V.[87, 187] The bigger current intensities translate the increasing ECSA (**Table 3.1**)

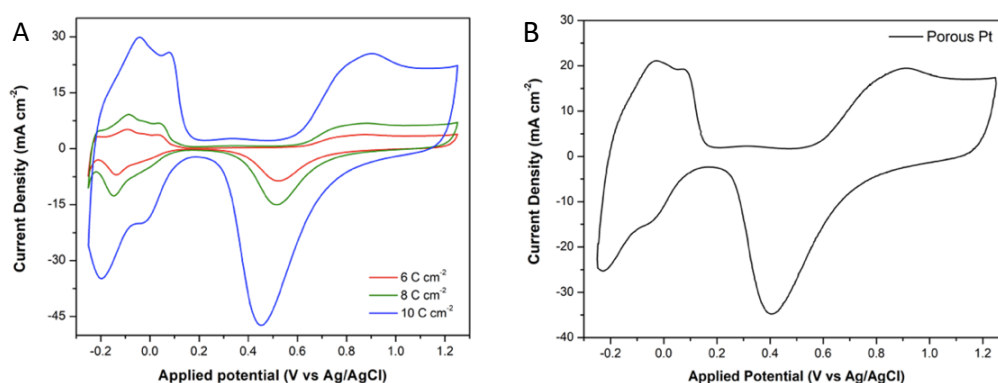


**Figure 3.6** Cyclic voltammograms of metal electrodes in 0.5 M H<sub>2</sub>SO<sub>4</sub> measured with a scan rate of 100 mV s<sup>-1</sup>: A) mesoporous Pt-Ir alloys deposited with different charge densities of 6 (red), 8 (green), and 10 (blue) C cm<sup>-2</sup>, respectively; B) mesoporous Pt deposited with 8 C cm<sup>-2</sup> (black).

which is a function of deposition charge, but the at% of Ir decreases significantly (**Table 3.1**). The reason for a decrease in Ir content when increasing the deposition charge density, leading to a higher film thickness, relates to the fact that the Pt-Ir alloy is preferably formed at a lower part of the mesoporous Pt-Ir film, which is the interface between the gel precursor and the Au-coated slides. In addition, EDS sensing is limited to the outermost regions of the electrodes, whereas the Pt-Ir alloy primarily originates in the interface with the gold electrodes. The small concentration of Ir in the initial precursor gel results in a gradual depletion of Ir salt in the plating gel when the electrodeposition is progressing, thus decreasing the Ir content in the upper parts of the Pt-Ir films. Hence, to maintain a measurable Ir content, the charge density used for electrodeposition should not exceed  $8 \text{ C cm}^{-2}$ .

**Figure 3.7A** shows a cross-sectional SEM image of a Pt-Ir film generated at  $-0.05 \text{ V}$  with a charge density of  $8 \text{ C cm}^{-2}$ . It illustrates the uniform character of the Pt-Ir film grown on top of the Au-coated glass slide with a film thickness of  $900 \text{ nm}$ . To further confirm the mesoporous feature of the synthesized Pt-Ir, an ordered-hexagonal mesoporous structure with pore dimensions of approximately  $5 \text{ nm}$  is observed by transmission electron microscopy (TEM) (**Figure 3.7B**), similar to what has been described in the case of monometallic Pt using the same type of surfactant.[38]

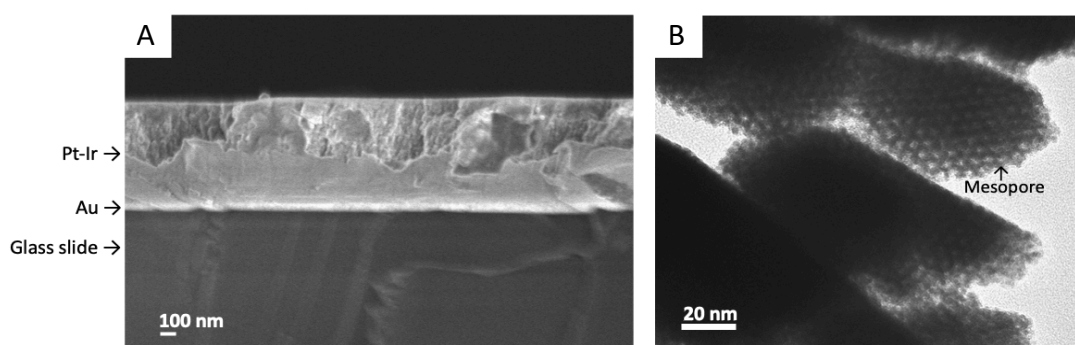


**Figure 3.7** Microscopic characterization of the mesoporous Pt-Ir electrodes: A) a cross-sectional SEM image of a mesoporous Pt-Ir film deposited with a charge density of  $8 \text{ C cm}^{-2}$  (scale bar of  $100 \text{ nm}$ ); B) TEM image of an ultrathin mesoporous Pt-Ir layer with well-organized mesopores (scale bar of  $20 \text{ nm}$ ).

In order to confirm the formation of alloy structures, the Pt-Ir alloys with different film thicknesses were synthesized with controlled deposition charge densities of  $4 \text{ C cm}^{-2}$  and  $8 \text{ C cm}^{-2}$  for the thinner and thicker ones, respectively. The two Pt-Ir electrodes have been characterized by comparing their X-ray diffraction patterns (XRD with those of either standard monometallic Pt or Ir (**Figure 3.8A**). A gold signal at  $38^\circ$ , originating from the Au-coated glass slide used as a substrate, is predominant. However, the (111) and (200) crystalline planes of both Pt and Ir at approximately  $40.0^\circ$  and  $46.4^\circ$  can also be observed, confirming that Pt and Ir are present in the alloy structure in the same face-center cubic (fcc) configuration.[188, 189] Notably, peaks are slightly shifted to higher degrees, when the thickness is increased, suggesting that a Pt-Ir alloy is formed even for thicker layers. These results are in agreement with high-resolution transmission electron microscopy (HR-TEM) images of the ultra-thin Pt-Ir sample (**Figure 3.8B**). Lattice fringes of the (111) and (200) Pt-Ir crystal planes with d-spacing values of 0.24 and 0.20 nm are measured. Lattice constants of Pt-Ir were calculated,[190] and are indistinguishable for Pt-Ir 4 C and Pt-Ir 8 C. However, these parameters are obviously smaller and higher than those of isolated Pt and Ir, respectively (**Figure 3.8C**). This result suggests that

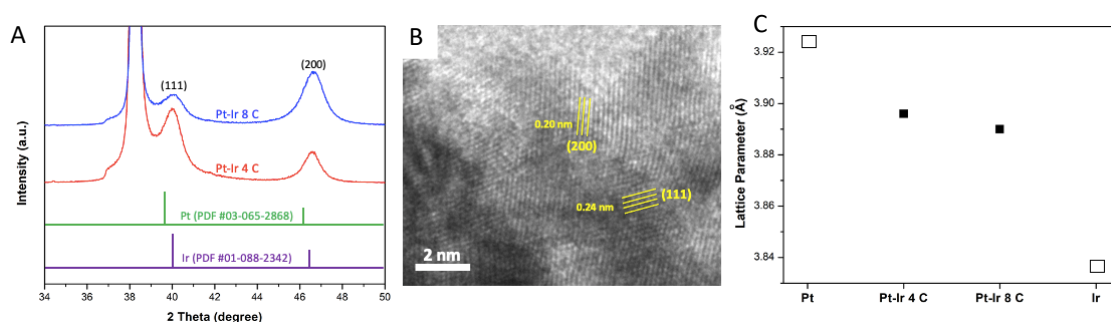


**Figure 3.8** Investigation of alloy structures of the mesoporous Pt-Ir: A) XRD pattern of deposited Pt-Ir alloys obtained with  $8 \text{ C cm}^{-2}$  (blue) and  $4 \text{ C cm}^{-2}$  (red) compared to the standard cards of Pt (PDF #03-065-2868) (green) and Ir (PDF #01-088-2342) (purple); B) HR-TEM image of ultra-thin Pt-Ir labeled with the Pt-Ir crystalline planes together with the measured d-spacing values; C) calculated lattice parameters of Pt-Ir samples versus the reference lattice constants of Pt and Ir adopted from [190].

Pt and Ir are alloyed and induce a compressive strain on the Pt-Ir alloy surface, which might further influence their electrocatalytic activity.[191]

The surface composition of the prepared Pt-Ir films was analyzed by X-ray photoelectron spectroscopy (XPS). Standard monometallic Pt exhibits major characteristic peaks at 71.0 and 74.4 eV representing Pt  $4f_{7/2}$  and Pt  $4f_{5/2}$ , respectively, whereas Ir shows doublet peaks at 59.7 and 62.7 eV belonging to Ir  $4f_{7/2}$  and  $4f_{5/2}$ , respectively (**Figure 3.9A and B**).[187, 192] XPS signals of the fresh Pt-Ir alloy films in both the Pt and Ir region were shifted to higher binding energies by approximately 0.3 and 1.1 eV for the corresponding monometallic Pt and Ir, respectively. A slight difference in the shift of XPS signals of Pt-Ir films prepared with 4 C and 8 C  $\text{cm}^{-2}$  was observed.

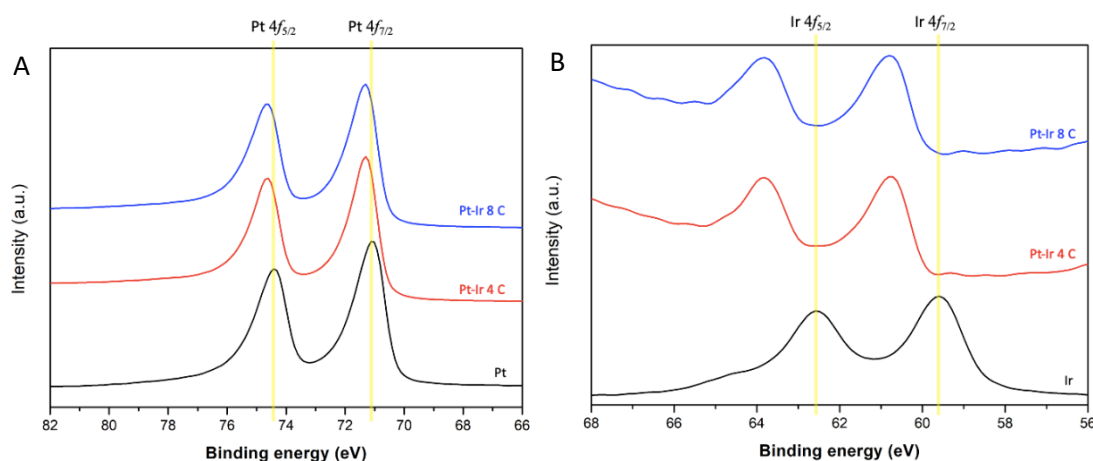


**Figure 3.9** XPS spectra of plain Pt-Ir electrodes with different thicknesses of 8 C  $\text{cm}^{-2}$  (blue) and 4 C  $\text{cm}^{-2}$  (red) plotted together with the standards of either Pt or Ir (black) in the binding energy regions of A) Pt and B) Ir, respectively.

To elucidate the alloy formation, a depth-profile analysis of XPS for the thicker sample, Pt-Ir 8 C  $\text{cm}^{-2}$ , was carried out by bombarding the sample with an argon ion gun. **Figure 3.10** displays the depth-profile XPS spectra in the regions of the Pt and Ir binding energies from 90 to 55 eV, as a function of etching time from 0 to 160 s. The summary information of the fresh Pt-Ir (without etching) and the etched sample (Pt-Ir etching 160 s) is presented in the narrow-scan XPS spectra (**Figure 3.10A and B**). **Figure 3.10C** clearly demonstrates

the remarkable gradual shift of the doublet peaks of Pt and Ir to higher binding energies when the sample is etched for a longer time. Furthermore, Pt and Ir are more apparent when the Pt-Ir was etched in the deeper layers, confirming the preferential formation of the Pt-Ir alloy at the initial stages of the co-electrodeposition as discussed in the previous characterization session. This

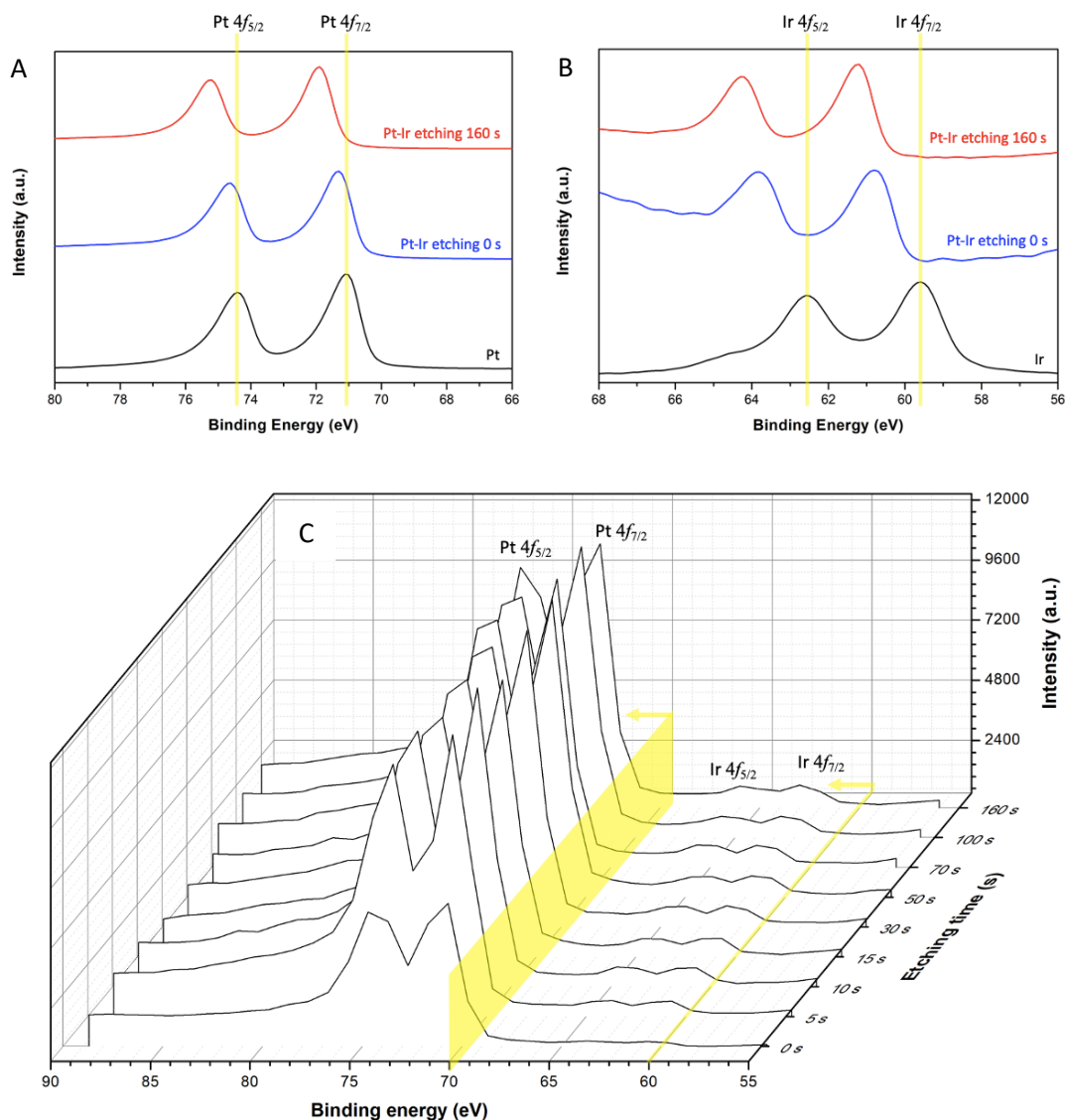


**Figure 3.10** XPS spectra from depth-profile analysis of the alloy Pt-Ir 8 C: A) and B) narrow-scan XPS spectra in the binding energy regions of Pt and Ir (black), respectively, with respect to a fresh electrode at an initial time of 0 s (blue) and after etching for 160 s (red); C) Depth-profile XPS spectra obtained by a wide-scan as a function of etching time varying from 0 to 160 s.

shift in binding energy relates to a charge transfer between Pt and Ir atoms in their alloy structure.[187] Moreover, elemental analysis recorded by various techniques is summarized in **Table 3.2**. However, the most reliable value is obtained by inductively coupled plasma optical emission spectroscopy (ICP-OES). The result reveals a composition with approximately 90 at% of Pt and 10 at% of Ir.

**Table 3.2** Summary of elemental analysis results obtained by quantitative analysis with EDS, XPS, and ICP-OES.

Samples	Elements	Theoretical at%	at% from EDS	at% from XPS	at% from ICP-OES
Pt-Ir 4 C	Pt	85.00	95.0	89.0	90.5
	Ir	15.00	5.0	11.0	9.5
Pt-Ir 8 C	Pt	85.00	97.5	91.5	90.7
	Ir	15.00	2.5	8.5	9.3

### 3.3.3 Synthesis and characterization of chiral encoded mesoporous Pt-Ir alloy supported on Ni foam

The fabrication of the chiral Pt-Ir layers on a 2D support such as the Au-coated glass slides may diminish the accessibility of guest molecules to the mesopores, especially for sensing and catalytic applications. Hence, an alternative material that has a more pronounced surface area was studied in this part of the work. In general, nickel (Ni) foams have been utilized as a solid template for a wide range of applications due to their porous structure, a high percentage of void space (up to 95%) versus its bulk structure, vast internal surface area, excellent stability as well as low production cost.[193, 194] Hence, in the present case, Ni foam was selected as solid support for the deposition of chiral metal to enable better diffusion of guest molecules towards the active metal sites.

The chiral encoded mesoporous Pt-Ir alloy supported on Ni foam was successfully synthesized as previously mentioned by electrodeposition of metal in the simultaneous presence of a self-assembled lyotropic liquid crystal and a chosen chiral template (**Figure 3.11**). **Figure 3.11A** symbolizes the

prepared plating gel, which is mainly composed of non-ionic surfactants formed in the hexagonal liquid crystal phase ( $H_1$ ) accompanied by the chiral compound and metal precursors (platinum (IV) and iridium (IV) salts). Phenylethanol (PE), as an example of a chiral template, was introduced to generate the specific chiral cavities at the internal walls of the mesopores. The hydrophilic part of the non-ionic surfactant polyoxyethylene (10) cetyl ether (Brij<sup>®</sup> C10) can interact with the hydroxy group of PE by hydrogen bonding. The Pt-Ir alloy is subsequently electrodeposited on a porous Ni foam as a substrate with the desired injection of charge density, as shown in **Figure 3.11B**. Finally, the chiral imprinted mesoporous Pt-Ir alloy supported on Ni foam is obtained after the

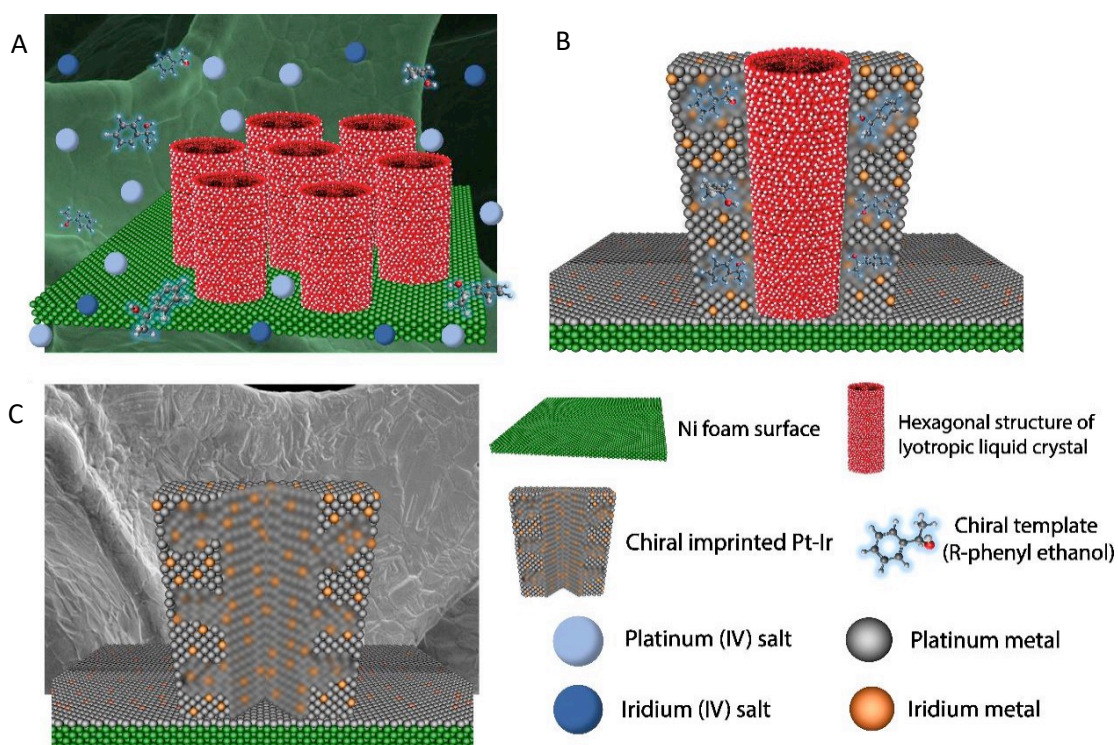


**Figure 3.11** Graphical explanation of the electrodeposition process to synthesize a chiral imprinted mesoporous Pt-Ir alloy supported on Ni foam: A) Illustration of the ingredients, the non-ionic surfactant forming a hexagonal close packed columnar structure, the metal salts and chiral molecules on Ni foam prior to electrodeposition; B) The growth of metallic Pt-Ir alloy throughout the structural templates; C) The obtained chiral imprinted mesoporous Pt-Ir alloy supported on Ni foam after eliminating all templates.

removal of the templates by washing and rinsing with MilliQ water several times (**Figure 3.11C**).

Scanning electron microscopy (SEM) accompanied by EDS elemental mapping was conducted to observe the morphology. Initially, the bare Ni foam reveals a homogeneous and smooth texture with Ni as the essential component for both low (**Figure 3.12A and B**) and high (**Figure 3.12C and D**) magnification. After Pt-Ir has been deposited on the Ni foam with  $8 \text{ C cm}^{-2}$ , a

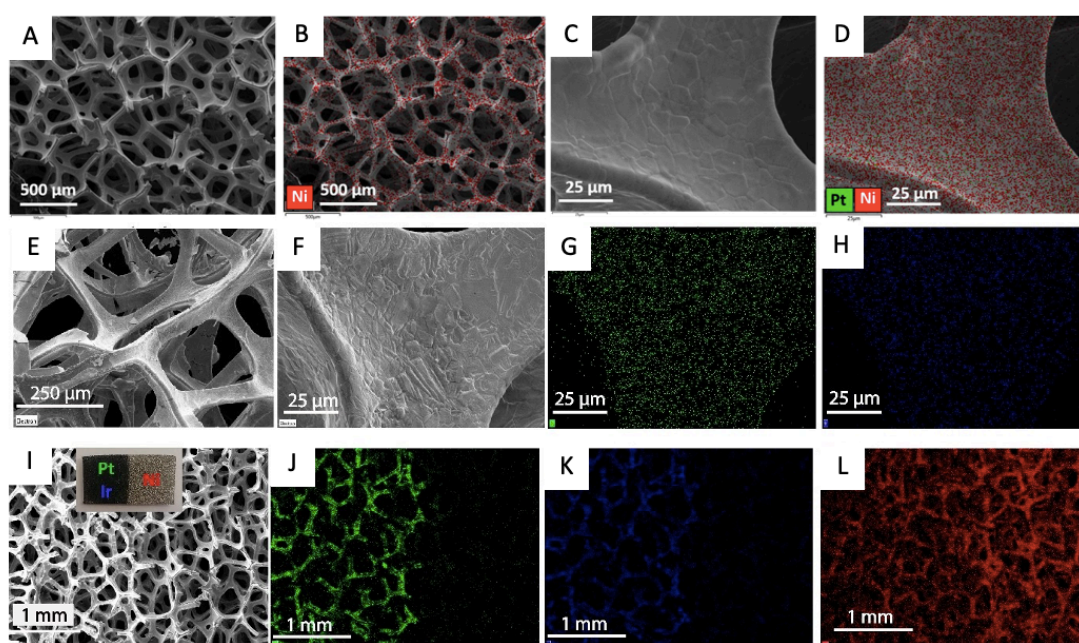


**Figure 3.12** Surface morphology of a chiral imprinted mesoporous Pt-Ir alloy supported on a Ni foam characterized by the EDS-SEM technique: A) SEM image of a bare Ni foam at low magnification together with B) the EDS mapping of Ni (red); C) SEM image of a Ni foam at high magnification together with D) the EDS mapping of Ni (red); E) and F) SEM images of chiral encoded mesoporous Pt-Ir deposited on Ni foam at low and high magnification, respectively, G) and H) EDS mapping of Pt (green) and Ir (blue); I) SEM image at the junction between the bare Ni support and the deposited Pt-Ir layer together with the actual sample picture (inset), and J), K) and L) EDS mapping of Pt (green), Ir (blue) and Ni (red), respectively.

darker and rougher film that covers the Ni foam was observed (**Figure 3.12E and F**), and the EDS mapping could confirm the existence of well-dispersed Pt and Ir metal on the Ni foam (**Figure 3.12G and H**). Furthermore, focusing on the interface between bare Ni support and the Pt-Ir layer, bright silver and dark black colors can be clearly distinguished, as shown in **Figure 3.12I** (inset), respectively. This was verified by EDS mapping, demonstrating a coherent elemental distribution for the Ni support and the Pt-Ir film (**Figure 3.12J-L**).

The thickness of the deposited Pt-Ir films on the Ni foam can be easily tuned by varying the charge density during the electrodeposition process. Deposition charge densities of 4, 8, and 12 C cm<sup>-2</sup> result in a thickness of 145, 297, and 458 nm, respectively (**Figure 3.13A-C**). To further investigate the ECSA, several Pt-Ir alloy films with various deposition charge densities were studied by CV in 0.5 M H<sub>2</sub>SO<sub>4</sub> in the potential window ranging from -0.25 to 1.25 V (**Figure 3.13D**). Characteristic peaks related to proton adsorption and desorption on Pt surfaces are present between -0.25 and 0.20 V, whereas the cathodic and anodic peaks implying oxidation of Pt and reduction of the PtO are visible at 0.80 and 0.45 V, respectively.[195] It should be noted that the small signal at 0.6 V originates from the oxidation of the Ni support (**Figure 3.13D (inset)**) but has no significant interference with the hydrogen adsorption/desorption region. Therefore, the active surface area of the prepared Pt-Ir films supported on Ni foam can be estimated from the hydrogen region,[173] increases from 341 to 826, 1680, and 2560 cm<sup>2</sup> according to the higher deposition charge densities of 4, 6, 8 and 12 C cm<sup>-2</sup>, respectively, as shown in **Figure 3.13E**.

HR-TEM images were recorded, which confirm a highly ordered porous hexagonal structure with a pore diameter in the mesopore range of 6.52 ±0.35 nm either obtained by standard or scanning (STEM) modes, as shown in **Figure 3.14A and B**, respectively. In addition, the crystalline structure of the Pt-Ir films was investigated using X-ray diffraction (XRD). As can be seen in **Figure 3.14C**, three prominent characteristic peaks of Pt and Ir are observed for the Pt-Ir on Ni foam (blue) compared to the pure Pt (green) and Ir (violet) on Ni foams, showcasing at 2θ of 40.0°, 41.0° and 46.5° for Pt(111), Ir(111) and Pt(200),

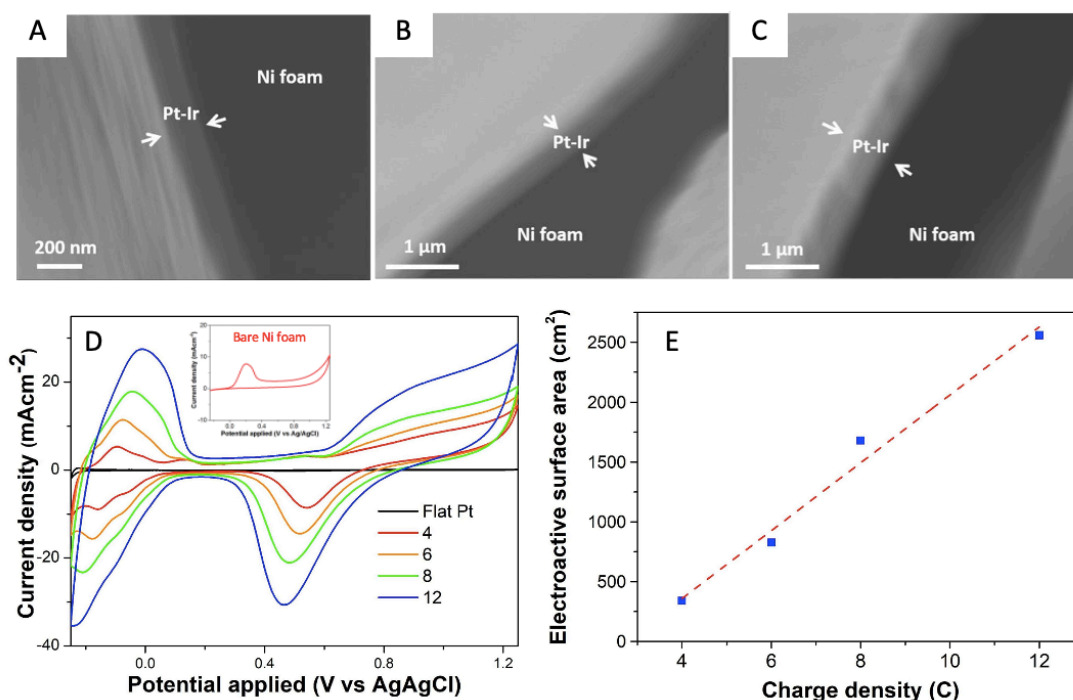


**Figure 3.13** Characterization of the mesoporous Pt-Ir alloy supported on Ni foam prepared with different deposition charge densities: A), B), and C) Cross-sectional SEM images of mesoporous Pt-Ir alloy supported on Ni foam electrodes generated with 4, 8, and 12 C cm<sup>-2</sup>, respectively; D) Cyclic voltammograms of the electrodes prepared with several deposition charge densities in comparison with flat Pt and the bare Ni foam (inset) measured in 0.5 M H<sub>2</sub>SO<sub>4</sub> at a scan rate of 100 mV s<sup>-1</sup>; E) Relationship between electroactive surface area and the deposition charge density.

respectively. In addition, both majority peaks regarding the supporting Ni foam appear at  $2\theta$  of  $44.5^\circ$  (Ni(111)) and  $52.0^\circ$  (Ni(200)), without any overlap with the Pt and Ir signals.[196] Interestingly,  $2\theta$  values of the Pt(111) are slightly shifted to higher  $2\theta$  angles when the alloyed Pt-Ir structure is formed in thicker layers, as shown in **Figure 3.14D**. The shifted peaks could imply the presence of Ir atoms in the Pt-Ir alloy, even though the characteristic peak of Ir cannot be directly observed in each of the Pt-Ir electrodes due to the very low amount of Ir (10 at%) (**Table 3.3**).[173, 197] Furthermore, the metallic character of the Pt-Ir film supported on Ni foam was also studied by X-ray photoelectron

spectroscopy (XPS). The binding energies of Ir (**Figure 3.14E**) and Pt (**Figure 3.14F**) appear at 58.8 (Ir 4f<sub>7/2</sub>), 61.8 (Ir 4f<sub>5/2</sub>), 69.7 (Pt 4f<sub>7/2</sub>), and 73.1 (Pt 4f<sub>5/2</sub>) eV, correlating with the elemental standard tables.[173, 192, 195, 197] The characteristic peaks of either Pt or Ir of the Pt-Ir samples, prepared with several deposition charge densities, are somewhat shifted to higher binding energies. This finding could indicate a charge transfer between Pt and Ir atoms, confirming the existence of the Pt-Ir alloy structure.[187] The principal component of the alloy structure is Pt, but Ir is the foreign atom embedded in the Pt matrix. Thus, the peak shifts of Ir are more pronounced (approximately 1.2 eV), compared to those of Pt (around 0.6 eV). Moreover, the proportion of elements in the Pt-Ir alloy was analyzed by inductively coupled plasma optical emission spectroscopy (ICP-OES), indicating around 90 and 10 at% of Pt and Ir, respectively, summarized in **Table 3.3**.

**Table 3.3** Quantitative analysis of elements in the mesoporous Pt-Ir films supported on Ni foam obtained by EDS, XPS, and ICP-OES.

Deposition charge densities of the Pt-Ir (C cm <sup>-2</sup> )	Elements	at% from EDS	at% from XPS	at% from ICP-OES
4	Pt	89.9	87.4	88.7
	Ir	10.0	12.6	11.3
8	Pt	92.0	89.3	89.9
	Ir	8.1	9.7	10.1
12	Pt	94.9	89.7	90.4
	Ir	5.1	9.3	9.6

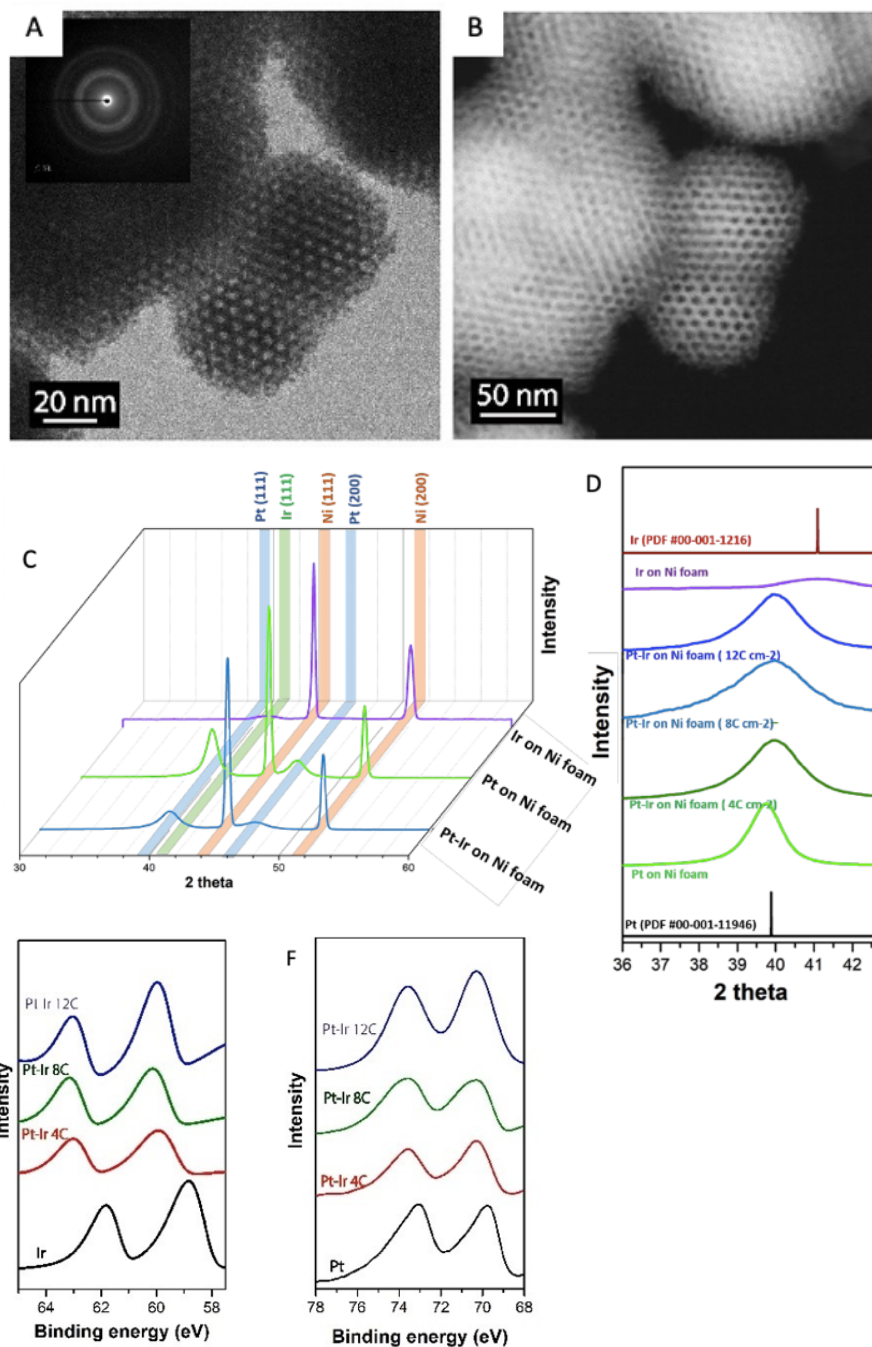


**Figure 3.14** Topology, crystallinity, and elemental composition of the mesoporous Pt-Ir alloy supported on Ni foam: A) and B) TEM images of mesoporous Pt-Ir alloy prepared by deposition on Ni foam electrodes with  $8 \text{ C cm}^{-2}$ , shown together with the selected area electron diffraction pattern (SAED) (inset) recorded in normal

and STEM mode, respectively; C) XRD patterns of Pt-Ir (blue), Pt (green) and Ir (violet) on Ni foam; D) Selected area of the XRD pattern in the region of Pt(111) and Ir(111), for pure Pt (light green), and Pt-Ir alloys with different deposition charge densities of 4 (dark green), 8 (light blue) and 12 (dark blue) C cm<sup>-2</sup>, together with pure Ir (violet) supported on Ni foam in comparison to the standard card of Pt (black) and Ir (red); E) and F) XPS spectra of Pt-Ir with 4 (red), 8 (green) and 12 (blue) C cm<sup>-2</sup> compared to pure Ir and Pt (black) in the region of Ir and Pt binding energies, respectively.

### **3.3.4 Investigation of chiral features of mesoporous Pt-Ir surfaces by Secondary Harmonic Generation (SHG)**

In a majority of our work, chiral features inside the mesoporous metals, a usually revealed with simple electrochemical techniques, such as differential pulse voltammetry (DPV), leading to signals with different intensities for the electrooxidation of each enantiomer.[87, 88] However, these observations are rather indirect because they only provide information with respect to the different electron transfer kinetics observed for different enantiomers at the chiral metal interfaces. To further characterize the chiral character of the metal, an independent method to confirm the chiral features of the metal would be helpful. Second-harmonic generation (SHG) is one of the most powerful methods for gaining insights into the chiral features of solid surfaces because of its unique advantages with respect to other optical characterization techniques, e.g., the traditional circular-dichroism (CD).[198] SHG provides high sensitivity with respect to the difference in surface interactions between the left- and right-handedness of polarized light.[72] The interaction between material and electromagnetic field is typically described by the Hamiltonian ( $H$ ) of equation 3.1 (3.1):

$$H = -\mu \cdot E - m \cdot B - Q \quad (3.1)$$

where  $E$ ,  $B$ , and  $Q$  are the electric field, magnetic induction field, and electric quadrupole operators, respectively, and  $\mu$  and  $m$  stand for the electric and

magnetic dipoles, respectively, of the matter.[199] The first, second, and third terms can describe electric, magnetic, and quadrupole interactions, respectively. However, only the first and second terms are considered for SHG. The latter case is neglected due to the fact that (i) the electric quadrupole interaction is too weak compared to the electric-dipole interaction, and (ii) the magnetic interaction is preferable at chiral interfaces, even though the magnetic and quadrupole interactions are almost identical in terms of the symmetry properties. Therefore, the quadrupole interaction is already included in the magnetic interaction.

In the experimental set-up, a laser beam, composed of several optical fields of different frequencies ( $\omega$ ), is illuminating a nonlinear medium, and second harmonic fields at new frequencies ( $2\omega$ ) are generated due to nonlinear interactions in both reflection and transmission directions.[200] Generation of a new frequency at  $2\omega$  is usually described by photon diagrams for tensors ( $\chi$ ) shown in **Figure 3.15**. Initially, the electric-dipole interaction allows for the annihilation of input photons and the generation of an output photon ( $\chi^{eee}$ ). As mentioned before, the magnetic-dipole interaction contributes to the nonlinearity of the material and results in its nonlinear responses. This interaction can lead

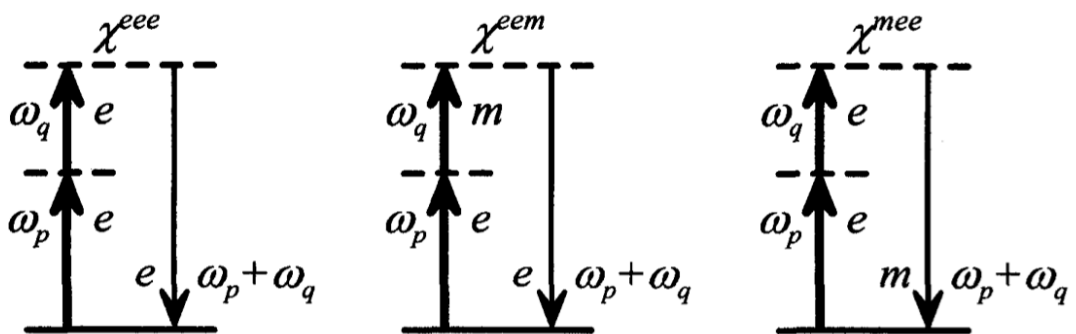


**Figure 3.15** Illustration of photon diagrams for tensors  $\chi^{eee}$ ,  $\chi^{eem}$  and  $\chi^{mee}$  and sum-frequency generation over the electric and magnetic transition moment.  $\omega_q$  and  $\omega_p$  are representative of the input photons ( $\omega$ ), whereas  $\omega_p + \omega_q$  is the output photon ( $2\omega$ ) generated via the nonlinear interactions. This figure is adopted from [199].

to the annihilation of a photon at the initial frequency of  $\omega$  ( $\chi^{eem}$ ) or the generation of a photon at the second-harmonic frequency of  $2\omega$  ( $\chi^{mee}$ ).

In general, the second-harmonic response obtained by a nonlinear polarization can be expressed by the simply electric dipole approximation shown in equation 3.2 (3.2).

$$P_i(2\omega) = \chi_{ijk}^t E_j(\omega) E_k(\omega) \quad (3.2)$$

where the subscripts ( $ijk$ ) refer to Cartesian indices. Nevertheless, magnetic dipole interactions should be included to explain the nonlinear polarization for specific chiral systems, depending on the structure of the materials. Up to the first order, the second-order nonlinear surface polarization and magnetization at the generated frequency of  $2\omega$  can be described by equation 3.3 (3.3) and equation 3.4 (3.4), respectively:

$$P_i(2\omega) = \chi_{ijk}^{eee} E_j(\omega) E_k(\omega) + \chi_{ijk}^{eem} E_j(\omega) B_k(\omega) \quad (3.3)$$

$$M_i(2\omega) = \chi_{ijk}^{mee} E_j(\omega) E_k(\omega) \quad (3.4)$$

However, because chirality is related to the absence of reflection symmetry, the system which generates the single enantiomeric scenario will have no mirror planes. At the same time, racemic surfaces would have reflecting planes, and thus such a system is achiral and centrosymmetric. Consequently, the determination of the transformation of susceptibility tensors on chiral interfaces has to be particularly taken into account.[199, 201] The symmetry of materials can also be affected by the number of independent components of all three tensors. Focusing on the most common illustration such as nonlinear optical responses of chiral isotropic surfaces (**Figure 3.16**), they demonstrate  $C_\infty$  symmetry, and the non-vanishing elements of  $\chi^{eee}$ ,  $\chi^{eem}$ , and  $\chi^{mee}$  have four, seven, and four independent components, respectively, summarized in **Table 3.4**. In contrast, isotropic achiral surfaces, are categorized in  $C_{\infty v}$  symmetry and have only three, three, and one non-vanishing independent components of  $\chi^{eee}$ ,  $\chi^{eem}$ , and  $\chi^{mee}$  tensors, respectively (**Table 3.4**).[201, 202]

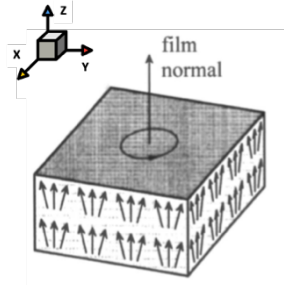


**Figure 3.16** Graphical illustration of an isotropic chiral thin film with  $C_\infty$  symmetry. Rotation around the z-axis of the film is a symmetry operation. This figure is adopted from [199].

**Table 3.4** The second-order susceptibility tensors (in the Cartesian coordinates) for a macroscopically isotropic surface (x-y plane) of either achiral or chiral matter. The information is adopted from [202].

Susceptibility	Independent non-vanishing tensor elements	
	Chiral material	Achiral material
$\chi^{eee}$	$zzz$ $zxx=zyy$ $xxz=xzx=yyz=yzy$ $xyz=xzy=-yxz=-yzx$	$zzz$ $zxx=zyy$ $xxz=xzx=yyz=yzy$
$\chi^{eem}$	$zzz$ $zxx=zyy$ $xxz=yyz$ $xzx=yzy$ $xyz=-yxz$ $xzy=-yzx$ $zxy=-zyx$	$xyz=-yxz$ $xzy=-yzx$ $zxy=-zyx$
$\chi^{mee}$	$zzz$ $zxx=zyy$ $xxz=xzx=yyz=yzy$ $xyz=xzy=-yxz=-yzx$	$xyz=xzy=-yxz=-yzx$

It is noteworthy that if the susceptibility components are non-vanishing for chiral surfaces, they are determined as chiral components; however, the components which are non-vanishing for both chiral and achiral surfaces are implied as achiral components.

In this case, the SHG signals reflected on thin films of the chiral imprinted mesoporous metals obtained for either monometallic Pt or Pt-Ir alloys have been investigated. To begin with, the fundamental beam at a frequency of  $2.9 \times 10^{14}$  Hz is pulsed at the angle of incidence (AOI) for  $70^\circ$  on the chiral encoded mesoporous Pt layers (**Figure 3.2**). As illustrated in **Figure 3.17**, SEM images of the chiral Pt electrodes exhibit smooth external surfaces prepared by electrodeposition at an applied potential of  $-0.05$  V (vs Ag/AgCl) with  $4 \text{ C cm}^{-2}$  (by the thickness of approximately 600 nm).[87, 101, 203] Indeed, a very homogeneous chiral Pt film is necessary to investigate clear SHG responses due to the suppression of anisotropic contributions of metal surfaces such as scattering or absorption phenomena. In addition, to obtain predominant SHG signals, chiral encoded Pt films with a high density of chiral imprinted sites are required. Therefore, the highest possible molar ratio between the imprinted chiral molecule as DOPA and  $[\text{Pt}^{2+}]$  ( $\text{DOPA}/[\text{Pt}^{2+}]$ ) of 1/12 is used, eventually achieving a high density of chiral sites with a uniform hexagonal close-packed

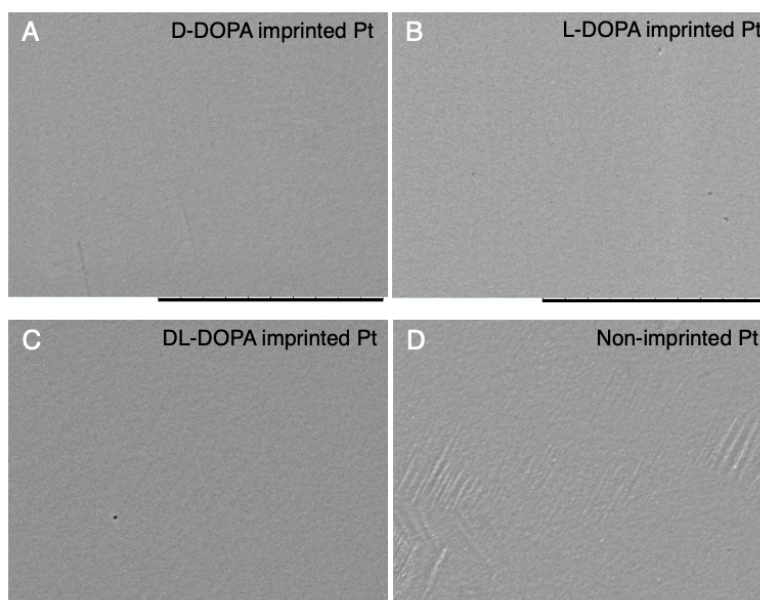


**Figure 3.17** SEM images of the external surface of mesoporous Pt electrodes generated by electrodeposition at  $-0.05$  V vs Ag/AgCl with  $4 \text{ C cm}^{-2}$  of charge density for A) (D)-DOPA, B) (L)-DOPA and C) (DL)-DOPA encoded Pt films and D) a non-imprinted Pt electrode (Scale bar of  $10 \mu\text{m}$ ).

mesoporous structure of the metal.[87] After removing the templates, the samples were scanned with an azimuthal rotation angle from  $-45.0$  to  $+45.0$  degrees. They lead to SHG signals in the polarizer-analyzer configuration in the form of  $\Psi_{IN-P_{OUT}}$  and the  $\Psi_{IN-S_{OUT}}$ , respectively (**Figure 3.18A** and **B**). The P- and S-components of the analyzer are generated along with the horizontal and vertical directions, respectively, analyzed in the reflected direction. In the case of  $\Psi_{IN-P_{OUT}}$ , a strong inversion of signals between the left-circular polarizer ( $LC_{in-P_{out}}$ ) and the right-circular polarizer ( $RC_{in-P_{out}}$ ) are evident at  $-22.5^\circ$  and  $22.5^\circ$ , respectively, for Pt electrodes imprinted with (D)- or (L)-DOPA. In contrast, the non-imprinted and (DL)-DOPA encoded Pt samples show almost identical SHG signals. This induced SHG signal is significant for a bulk chiral Pt substrate due to the enhanced surface plasmon resonance field induced by the nanostructures.[204] Hence, these results confirm that the SHG originates from the chiral nature of the sample, and different SHG signals are generated with significantly different efficiency related to the handedness of the sample.[204] Notably, the SHG signal analysis in the  $\Psi_{IN-P_{OUT}}$  direction (**Figure 3.18A**)

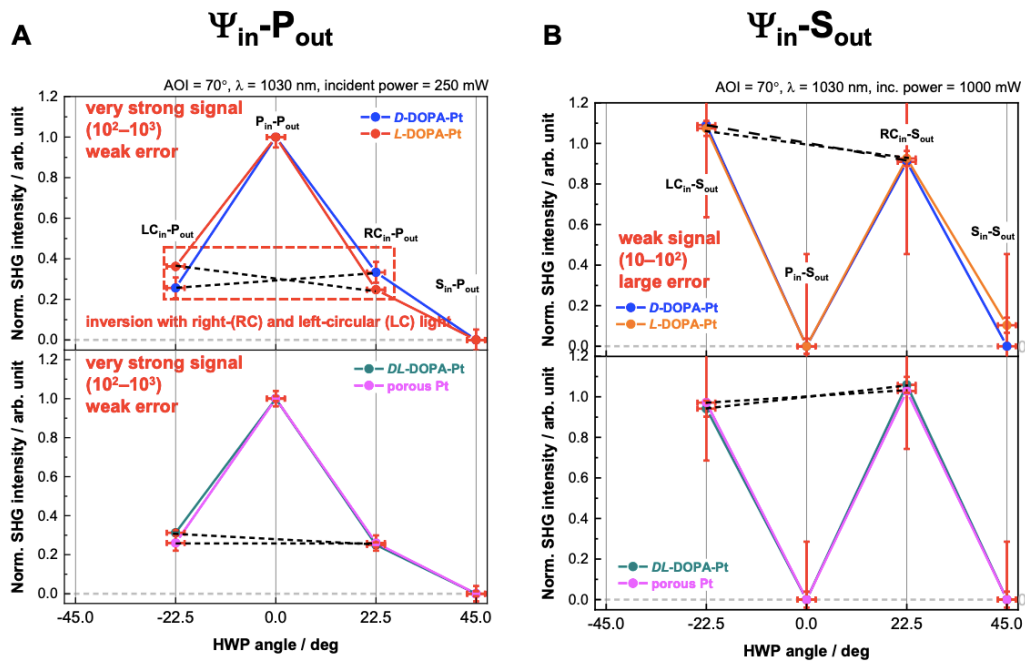


**Figure 3.18** Second-Harmonic Generation (SHG) signals obtained by the reflection mode on chiral DOPA Pt samples at 1030 nm in the polarizer-analyzer configurations as A)  $\Psi_{IN-P_{OUT}}$  and B)  $\Psi_{IN-S_{OUT}}$ .

displays a notably larger amplitude compared to the  $\Psi_{\text{IN-S}_{\text{OUT}}}$  (**Figure 3.18B**) thanks to forbidden electric-dipole contributions in the latter polarizer-analyzer configuration ( $\Psi_{\text{IN-S}_{\text{OUT}}}$ ).[204] Consequently, discrimination between DOPA enantiomers from the non-stereoisomeric Pt films would not be clearly observed. Therefore, an investigation of the SHG signal in the  $\Psi_{\text{IN-P}_{\text{OUT}}}$  position will be applied for the latter study.

It should be noted that during the investigation, the laser spot induces local heating, resulting in partial damage to the metal surfaces, especially *via* higher mobility of the surface atoms, and thus chirality can be erased. In this context, the developed mesoporous Pt-Ir alloy is considered as a more promising material for investigating the chirality by the SHG technique because Ir can enhance the hardness as well as the tolerance against higher temperatures.[59, 186, 205] More details regarding the improved chiral properties of the Pt-Ir alloy will be exposed in the following chapters.

Herein, (L)-DOPA, (D)-DOPA, and (DL)-DOPA imprinted mesoporous Pt-Ir alloys were generated using similar conditions to those of monometallic Pt electrodes. Electrodeposition was performed at -0.05 V (vs Ag/AgCl) with 600 nm thickness (charge density of 4 C cm<sup>-2</sup>) and using 1/12 molar ratio of DOPA/[Pt<sup>2+</sup>+Ir<sup>2+</sup>]. As shown in **Figure 3.19**, SEM images of the prepared chiral Pt-Ir alloys show very smooth and homogeneous external surfaces. Initially, an optimal incident laser power of 55 mW at 800 mV was chosen for a better noise-to-signal ratio of the SHG intensity generated from the chiral Pt-Ir alloy. **Figure 3.20** shows the SHG response from a (L)-DOPA imprinted mesoporous Pt-Ir alloy, recorded with the sample interacting with the laser beam with an azimuthal rotation angle from 0 to +180.0 degrees, leading to a twofold pattern.

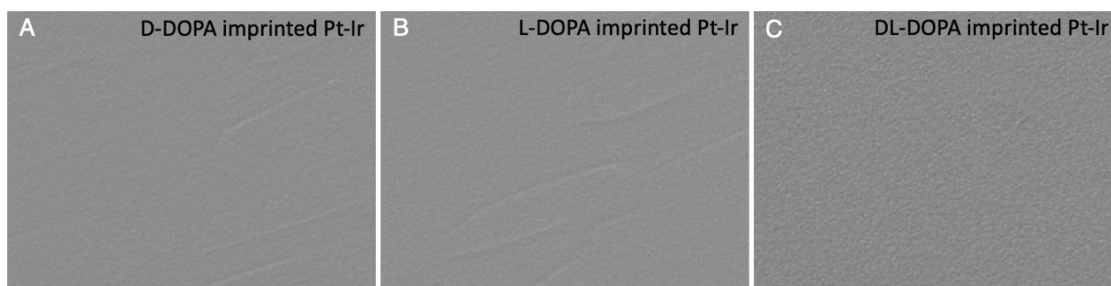


**Figure 3.19** SEM images revealing a topology of chiral mesoporous Pt-Ir alloys generated by electrodeposition at -0.05 V vs Ag/AgCl with 4 C cm<sup>-2</sup> charge density and imprinting with A) D-DOPA, B) L-DOPA and C) DL-DOPA (Scale bar of 10 μm).

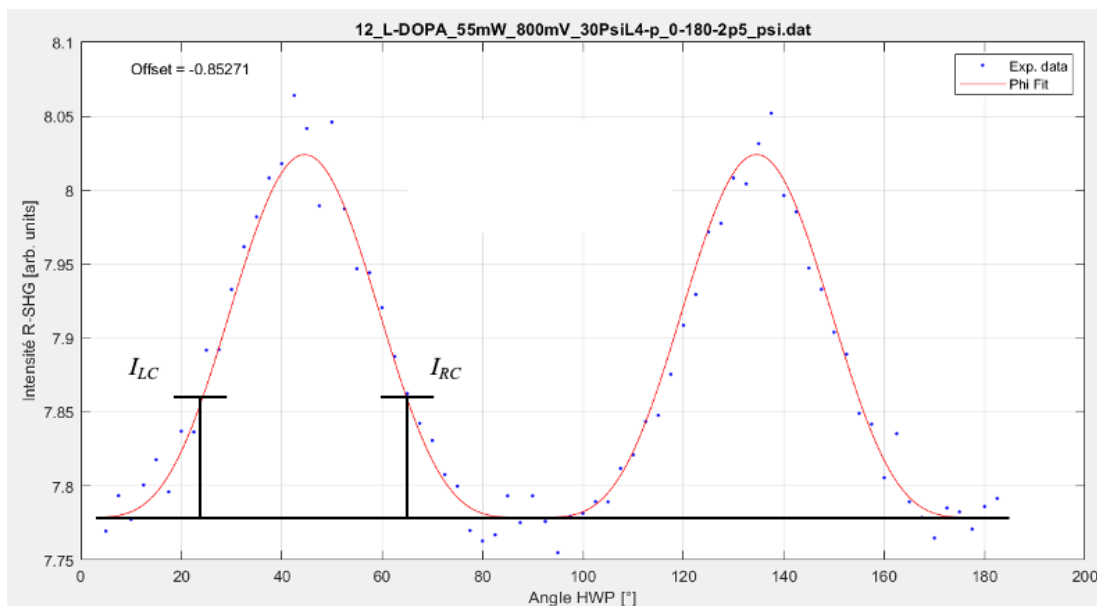


**Figure 3.20** SHG response as a function of the azimuthal rotation angle. This result is an illustration of the effective averaged response (blue dot) and the simulation (red line) of the SHG intensity obtained from (L)-DOPA encoded mesoporous Pt-Ir alloy.

In order to demonstrate a dependence of the SHG response on the handedness, the circular-difference response ( $\Delta\Psi$ ) has been studied and simply described in linear optics by equation 3.5 (3.5):

$$\Delta\Psi = \frac{I_{RC} - I_{LC}}{\frac{1}{2}(I_{RC} + I_{LC})} \quad (3.5)$$

where  $I_{LC}$  and  $I_{RC}$  represent the SHG intensities obtained from left- and right-hand circularly polarized beams, respectively.[198] The results are plotted in **Figure 3.21** for the three different samples, (D)-, (L)- and (DL)-DOPA encoded mesoporous Pt-Ir alloys. These observations indicate the presence of chirality on chiral encoded Pt-Ir films, as can be seen from the correlation between the (D)- and (L)-DOPA Pt-Ir films and the racemic (DL)-DOPA imprinted one. Since they evolve in opposite directions, compared to (DL)-DOPA, it is reasonable to conclude that chiral information is present on the Pt-Ir surfaces. However, further studies need to confirm the relationship between the SHG response and chirality in such alloys.

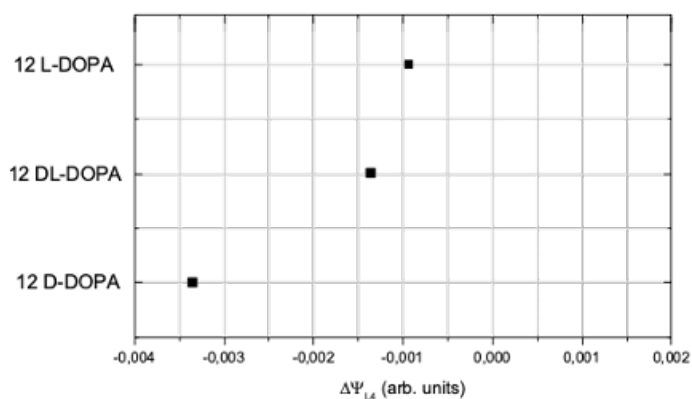


**Figure 3.21** Relationship between the circular-difference response for Pt-Ir alloys imprinted with (D)-, (L)- and (DL)-DOPA

### 3.4 Conclusion

As reported in the previous chapter, the modest stability of chiral-imprinted mesoporous monometallic metals, even when using noble metals such as Pt, is a drawback for developing this kind of material for practical applications. To overcome this obstacle, designing alloys combining Pt with a small amount of metallic promoter is a suitable strategy. It is well-known that metal alloys can have an enhanced hardness due to the different sizes of the metal atoms, canceling out their movement at local atomic sites. In this chapter, Ir was selected as a promoter for an alloy with Pt. Mesoporous Pt-Ir alloys were

successfully generated by electrodeposition from  $\text{H}_2\text{PtCl}_6$  and  $\text{H}_2\text{IrCl}_6$  in the simultaneous presence of lyotropic liquid crystals and chiral compounds, supported on either an Au-coated glass slide or on a Ni foam. An appropriated electrochemical condition was identified for the synthesis of the mesoporous Pt-Ir alloy, and it was found that the reduction potential of  $-0.05\text{ V}$  with no more than  $8\text{ C cm}^{-2}$  of electrodeposition charge density to control the film thickness is appropriate. Concerning the characterization, very homogeneous outermost surfaces with a full Pt-Ir layer were confirmed by the top and cross-sectional SEM images. Mesopores with a dimension of  $5\text{ nm}$  and a well-ordered hexagonal structure resulting in high porosity were characterized by TEM and CV in acid solution. To confirm the elemental composition of the prepared mesoporous Pt-Ir, ICP-OES was employed, and a value of 90:10 at% of Pt to Ir was obtained. The formation of the alloy structure was confirmed by XRD and XPS, showing a good dispersion of Ir in the bulk Pt structure. Importantly, the alloy structure preferentially forms during the initial period of deposition, while a higher Pt content is obtained at the outermost surfaces of electrodes due to a gradual decrease in Ir content in the upper parts of the deposit. In addition, the improved mechanical stability of such Pt-Ir structures also allows a more detailed investigation of chiral features on the metal interface by the Secondary Harmonic Generation (SHG) measurements. Monometallic Pt and the Pt-Ir alloy showed a significant difference between SHG responses obtained with left- and right-hand circular polarized beams, even though more evidence and experiments have to be performed to confirm and optimize the signals. In conclusion, these chiral Pt-Ir alloys have unique chiral features, combined with high stability, opening several perspectives for practical applications as catalysts, sensors, and for the selective production of chiral compounds in the future.

## Chapter 4

# Chiral-imprinted mesoporous Platinum-Iridium (Pt-Ir) alloys for highly enantioselective electrosynthesis and asymmetric hydrogenation

### 4.1 Introduction

The production of enantiomerically pure compounds (EPC) *via* asymmetric electrosynthesis has gained much attention from both an academic and an industrial point of view.[122, 132, 179, 180] Asymmetric electrosynthesis is an environment-friendly approach based on converting electricity into specific chemical reactions without the unessential addition of chemical reagents, allowing low-cost production of high added-value compounds for practical applications.[128, 132, 181] Consequently, the development of advanced well-designed materials acting as catalysts to induce a particular stereochemistry of chiral compounds is an interesting challenge that is worth investigating.[134, 140]

Recently, we have successfully demonstrated the proof-of-the-principle to elaborate novel chiral materials, namely chiral-imprinted mesoporous metals.[87] This concept has been adapted to several types of metals ranging from noble to non-noble metals.[90, 91] Synergistic properties of such chiral metals, their specific chiral features [95] together with improved mass transport capabilities due to the presence of mesopores,[38] allow us to propose them for many practical applications, e.g., as electrochemically chiral sensors,[87, 88, 102] as a stationary phase for chiral separation,[101] and as catalysts for asymmetric synthesis.[89-91]

Because of the outstanding chiral characteristics of the designed mesoporous metals, they were successfully applied as electrocatalysts for several reactions such as the electroreduction of phenyl glyoxylic acid (PGA) to

mandelic acid (MA),[89] and of acetophenone (APE) to (1)-phenyl ethanol (PE).[89-91, 206] However, in the initial stage of the development, only a moderate enantiomeric excess (%ee) of approximately 20 % of the desired chiral product could be achieved when using potentiostatic electrocatalysis.[89] As described in **Figure 4.1** (upper), due to the non-imprinted sites mainly located at the external surface of the electrode, a racemic mixture of enantiomers is obtained as a significant by-product. This uncontrollable reaction results in a decrease of the overall enantioselectivity in the case of steady-state electrocatalysis.

To overcome these drawbacks, pulsed electrocatalysis has been proposed instead of continuous electrocatalysis (**Figure 4.1** (lower)). This strategy is based on the fact that the potential is applied only for a short period, alternating with a long relaxation time, and repeating both steps for many cycles. This allows for achieving a very high enantiomeric excess in the global reaction mixture, as the unwanted reaction at the outermost parts of the electrode is suppressed.[90]

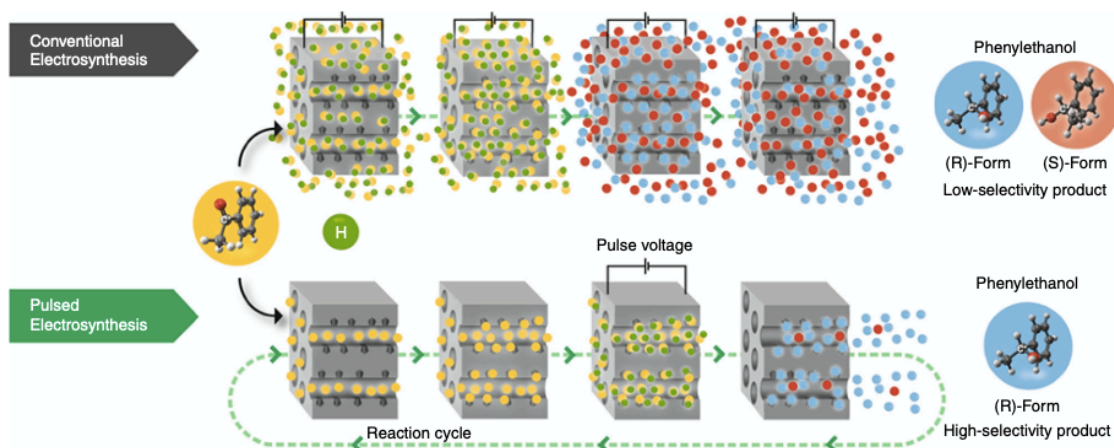


**Figure 4.1** Illustration of two electrocatalysis methods: conventional (upper) and pulsed (lower) asymmetric electrocatalysis. Herein, the achiral compound, acetophenone (yellow dots), is electro-converted into chiral products, (R)- and (S)-Phenylethanol, denoted as (R)-PE and (S)-PE (blue and red dots, respectively) in the presence of hydrogen (green dots) using chiral-imprinted metal electrodes as electrocatalysts. The figure is adopted from [90].

Under optimized conditions, pulsed electrosynthesis leads to a very high stereoselectivity of up to 90 %ee.[90] Nevertheless, in order to achieve such an outstanding value, either very short pulse times or excessive relaxation times must be employed. Consequently, the whole process requires a long time of synthesis. Moreover, in terms of stability and reusability, the enantiomeric excess values significantly decrease after several catalytic cycles, which is of primary concern for using this approach in practical applications.[90, 91] To further develop a more efficient chiral metal electrocatalyst, we intensively focused on improving the stability of the employed material, while keeping high enantioselectivity.

Indeed, the stability of metals can be improved when they are combined with a promoter. In particular, Ir has been selected as one of the most promising promoters to enhance the electrochemical stability of mesoporous Pt because Ir can tolerate rather harsh electrochemical conditions. As previously illustrated, alcohol oxidation and oxygen reduction efficiency can be improved when using a Pt-Ir alloy. [188, 191, 207] In fact, the improved electrocatalytic activity of Pt-Ir alloys can be explained by compressive surface strain induced by the lattice mismatch between Pt and Ir, which eventually alters the surface energy.[95, 191, 207] Therefore, using Pt-Ir alloys also for asymmetric synthesis seems to be quite promising.

In this chapter, the concept of chiral-imprinted mesoporous Pt-Ir alloys is adapted for asymmetric catalysis. The chiral-imprinted mesoporous Pt-Ir alloys can be synthesized *via* the co-electrodeposition of Pt and Ir salts in the simultaneous presence of lyotropic liquid crystals and desired chiral templates such as 1-PE. The chiral fingerprint can be preserved even after the removal of the templates, resulting in improved electrochemical durability during the asymmetric electrosynthesis of chiral molecules when compared to monometallic chiral Pt.[173] It therefore constitutes an alternative approach to produce EPC. Heterogeneous chiral catalysts are generally composed of enantiospecific areas at the interface, allowing achieving a high %ee value and a quick recovery after the reaction.[75] The generation of chiral features inside metal structures is a promising concept to elaborate heterogeneous chiral

catalysts not only for electrocatalysis,[173] but also for the selective production of chiral compounds *via* chemical reactions. The Pt-Ir alloys were generated on Ni foam, and then the catalyst was employed to produce selectively aromatic alcohols *via* the hydrogenation of an aromatic ketone. In particular, applying a pulsed synthesis strategy enables high enantioselectivity, and enhances the production rate of a chiral target compound.

## 4.2 Experimental section

### 4.2.1 Chemicals

(R)-phenylethanol ((R)-PE), (S)-phenylethanol ((S)-PE), acetophenone, isopropyl alcohol, heptane, and ammonium chloride (NH<sub>4</sub>Cl) were received from Sigma-Aldrich. Hydrochloric acid (HCl) and sulfuric acid (H<sub>2</sub>SO<sub>4</sub>) were obtained from Alfa. MilliQ water (18.2 MΩ cm) was used for all experiments. All chemicals were employed without further purification.

### 4.2.2 Preparation of chiral-imprinted mesoporous Pt-Ir alloy electrodes

Electrochemical experiments were carried out using a potentiostat (Metrohm  $\mu$ Autolab Type III) equipped with a three-electrode system including (i) Ag/AgCl (sat. KCl) as a reference electrode (ii) a Pt mesh (geometrical area for 1 cm<sup>2</sup>) as a counter electrode and (iii) imprinted Pt-Ir alloy supported on either gold-coated glass slides (geometric area for 0.25 cm<sup>2</sup>) or Ni foam (geometric area for 1 cm<sup>2</sup>) as working electrodes. All signals were collected using Nova (version 1.11) program initially provided with the potentiostat.

The procedures to synthesize chiral-imprinted mesoporous Pt-Ir electrodes using (S)-PE or (R)-PE as chiral templates were adopted from the previous chapter and previous reports.[173] In the typical procedure, co-electrodeposition from H<sub>2</sub>PtCl<sub>6</sub> and H<sub>2</sub>IrCl<sub>6</sub> at -0.05 V with the desired charge density was performed by using the previously described plating gel, containing a weight ratio of 0.15 PE/(PtCl<sub>6</sub><sup>2-</sup>+IrCl<sub>6</sub><sup>2-</sup>).

#### **4.2.3 Highly enantioselective electrosynthesis with PE-encoded mesoporous Pt-Ir alloys supported on Au-coated glass slides**

The asymmetric electrosynthesis of a chiral compound was carried out *via* the electroreduction of the functional carbonyl group (-C=O) of acetophenone into alcohol (-OH) to produce (S)- or (R)-PE. All reactions were performed with 5 mM acetophenone in 1 M NH<sub>4</sub>Cl as a supporting electrolyte under stirring at 250 rpm. Moreover, the effect of the pH of supporting electrolyte was studied in the range from 5.0 to 2.0 by adjusting the pH with 1 M HCl. Applied reduction potentials were also varied in the range from -0.4 to -0.3 V to optimize the enantiomeric excess.[173] After the synthesis, the product solution was extracted with heptane and then analyzed by High-Performance Liquid Chromatography (HPLC), JASCO LC-Net II/ADC with a chiral column (CHIRALPAK IB N-5, 250 × 4.6 mm inner diameter) under the following conditions: a photodiode array (PDA) detector at a wavelength of 210 nm, a flow rate of 0.5 ml min<sup>-1</sup> and a mixture of 8/92 (v/v) isopropyl alcohol/heptane as a mobile phase. All HPLC chromatograms were collected and analyzed using the chromNAV program.

#### **4.2.4 Asymmetric hydrogenation with PE-imprinted Pt-Ir surfaces supported on Ni foam**

Enantioselective synthesis of 1-PE was conducted with 1 mM acetophenone dissolved in MilliQ water, and the pH of the solution was carefully adjusted with 1 M HCl. The Pt-Ir alloy catalyst was pretreated by drying at room temperature for 1-day prior to the catalytic study. Then, the prepared catalyst was placed into 3 mL of prochiral solution. This precursor solution was homogeneously stirred for 15 min, allowing the penetration of the acetophenone into the porous structure of the Ni foam. After that, in the case of the continuous synthesis, H<sub>2</sub> gas was continuously flown into the solution at 0.1 ml min<sup>-1</sup> for 5 min. However, in the case of pulsed synthesis, the reaction medium was bubbled with H<sub>2</sub> gas for either 3 or 5 min, and then the solution was purged with N<sub>2</sub> gas for 15 min to remove the remaining H<sub>2</sub> from the reaction mixture. This sequence was repeated for several cycles. Finally, the chiral Pt-Ir catalyst was

removed from the solution mixture and cleaned several times by rinsing with MilliQ water. The product was extracted with 1 mL of heptane and subsequently analyzed using the High-performance Liquid Chromatography (HPLC), a Shimadzu LC-2030C3D, connected with a chiral HPLC column, CHIRALPAK IB, 250 ×4.6 mm inner diameter. For the HPLC analysis, 7.5:92.5 (v/v) of isopropyl alcohol and heptane, a flow rate of 0.5 ml/min, and the Photodiode Array Detector (PDA) with a tungsten (W) lamp at 215 nm were employed. All HPLC chromatograms were collected and analyzed using the Lab Solution software (Version 1.1).

#### 4.2.5 Calculation and investigation of catalytic parameters

Enantiomeric excess (%ee) is defined as the product selectivity during the catalytic process as indicated in equation (4.1);

$$\text{Enantiomeric excess (\%ee)} = \left[ \frac{(R)\text{PE} - (S)\text{PE}}{(R)\text{PE} + (S)\text{PE}} \right] \times 100 \quad (4.1)$$

where (R)PE and (S)PE indicate the integrated peak areas of (R)-PE and (S)-PE, respectively, obtained from the HPLC chromatogram.

The error of the mean of the enantiomeric excess (s.e.m) is calculated by equation (4.2);

$$\text{s.e.m.} = \frac{S}{\sqrt{n}} \quad (4.2)$$

where  $S$  represents the standard deviation and  $n$  is the number of experiments.

In the case of asymmetric hydrogenation, pulsed chemisorption of hydrogen was applied to study the dispersion of catalytically active sites. The analysis was performed on a BELCAT II chemisorption analyzer equipped with thermal conductivity detectors (TCDs). The chiral imprinted Pt-Ir deposited on Ni foam with a charge density of 8 C cm<sup>-2</sup> was used for this analysis. To begin with, the catalyst surfaces were cleaned under Ar gas flow at 100 °C. Next, H<sub>2</sub> gas diluted in Ar (2 %v/v) was pulse-injected at 35 °C until the H<sub>2</sub> peak area became saturated since the H<sub>2</sub> gas was chemisorbed on the entire metal surface. The procedure of this characterization is illustrated in **Figure 4.2**. In this case, the pulsed chemical adsorption analysis was performed for 8 cycles to allow the system to reach saturation. The metal dispersion referring to the total

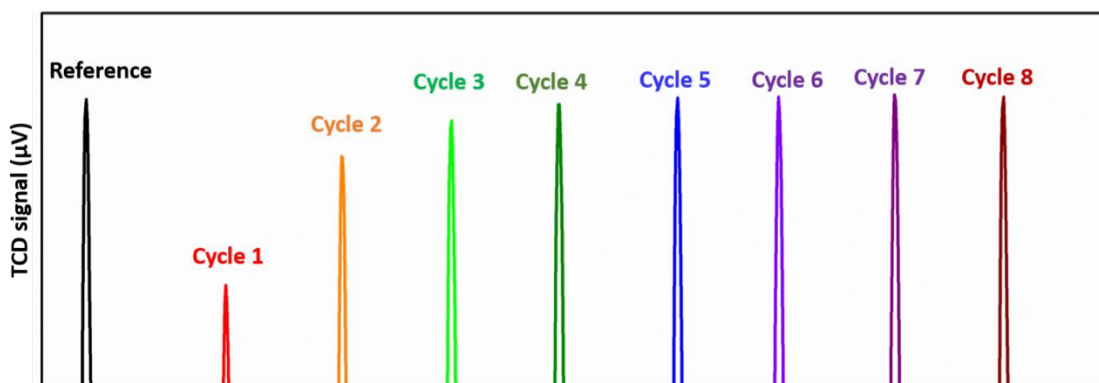


**Figure 4.2** A simple explanation of the procedure for the pulsed hydrogen chemisorption on chiral encoded Pt-Ir deposited on Ni foam.

amount of gas adsorbed on the catalyst surface ( $V_t$ ) was estimated by the total amount of  $H_2$  adsorbed in a given cycle ( $\sum_{i=1}^N V_{ai}$ ) until reaching full saturation, equation (4.3):

$$V_t = \sum_{i=1}^N V_{ai} \quad (4.3)$$

where  $N$  is the pulse cycle required to fully occupy the active metal sites, and  $V_{ai}$  is the volume of gas adsorbed during an individual cycle, calculated by the difference in the pulse signal of each cycle compared to the pulse area from the reference.[208]

The catalytic efficiency of the asymmetric hydrogenation is defined by equation (4.4);

$$\text{Catalytic efficiency} = \frac{\text{mol}_{\text{chiral product}}}{\text{mol } H_2 \times D_m \times \text{mol}_{\text{catalyst}}} \quad (4.4)$$

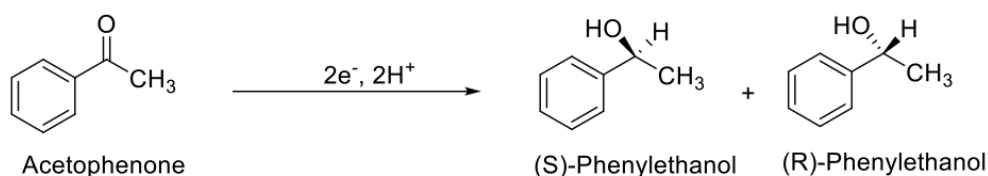
In the present case, the catalytic efficiency is determined by the amount of chiral product ( $\text{mol}_{\text{chiral product}}$ ) in comparison with (i) the number of introduced  $H_2$  ( $\text{mol } H_2$ ), (ii) the amount of catalytically active sites which can be estimated from the total amount of metal ( $\text{mol}_{\text{catalyst}}$ ), and (iii) the metal dispersion value ( $D_m$ ) obtained from the pulsed chemisorption of hydrogen. For example, if the reaction occurs for 15 min, the calculated catalytic efficiency is 158.9 [ $\text{mol}_{\text{chiral product}} / \text{mol } H_2 \cdot \text{mol}_{\text{catalyst}}$ ] when using values for the amount of product, hydrogen, catalysts and the metal dispersivity of 3.28 nmol, 67  $\mu\text{mol}$ , 15.4  $\mu\text{mol}$ , and 0.02, respectively.

## 4.3 Results and Discussion

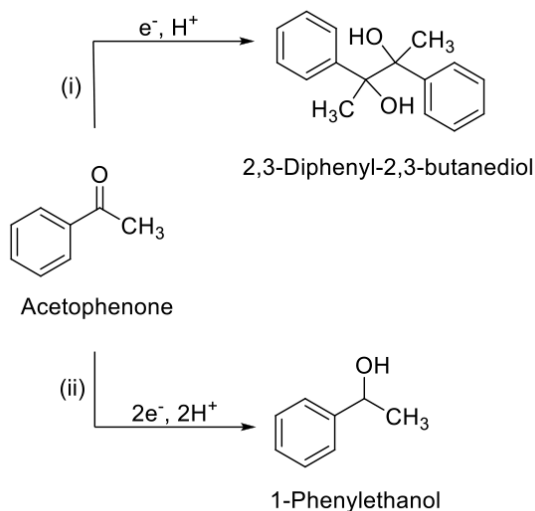
### 4.3.1 Highly selective chiral electrosynthesis with PE-imprinted mesoporous Pt-Ir alloys

As reported previously, although a high %ee could be obtained from asymmetric electrosynthesis at pure chiral-encoded Pt surfaces, the long global synthesis time and poor stability of monometallic Pt are still the main drawbacks.[90, 91] To circumvent these limitations, the designed chiral-imprinted mesoporous Pt-Ir alloy was also tested for the asymmetric electrosynthesis of chiral compounds, hoping that the efficiency of chiral electrosynthesis might be improved in terms of both catalytic activity and stability. To illustrate these potential beneficial aspects, the electroreduction of ketone (C=O) into alcohol (-OH), has been carried out, with the transformation of acetophenone to (R)-PE or (S)-PE (**Scheme 4.1**) as a model reaction using the chiral imprinted Pt-Ir alloy as an electrocatalyst. In fact, acetophenone can be reduced to either 1-PE by gaining two electrons and protons or to 2,3-diphenyl-2,3-butanediol by accepting an electron and a proton (**Scheme 4.2**).[175] By optimizing the experimental conditions, highly selective production of PE should be observed. For example, the product selectivity should be shifted towards 1-PE according to reaction equilibrium by increasing the proton concentration in the supporting electrolyte.

In order to investigate the beneficial effect of the chiral imprinted Pt-Ir alloy for the asymmetric synthesis of 1-PE, (S)-PE was used as a chiral template by keeping the weight ratio of 0.15 PE / [PtCl<sub>6</sub><sup>2-</sup> + IrCl<sub>6</sub><sup>2-</sup>] for the co-



**Scheme 4.1** Electrochemical reduction of acetophenone to (S)- or (R)-phenylethanol.



**Scheme 4.2** Possible reaction pathway for acetophenone reduction to (i) 2,3-diphenyl-2,3-butanediol and (ii) 1-phenylethanol.

electrodeposition of Pt-Ir.[173] The product was analyzed by high-performance liquid chromatography (HPLC) with a CHIRALPAK IB column. As demonstrated in **Figure 4.3**, the peaks in the chromatograms of acetophenone, (R)-PE, and (S)-PE are entirely separated, as illustrated by the corresponding retention times of 10.5, 13.0, and 13.9 min, respectively.

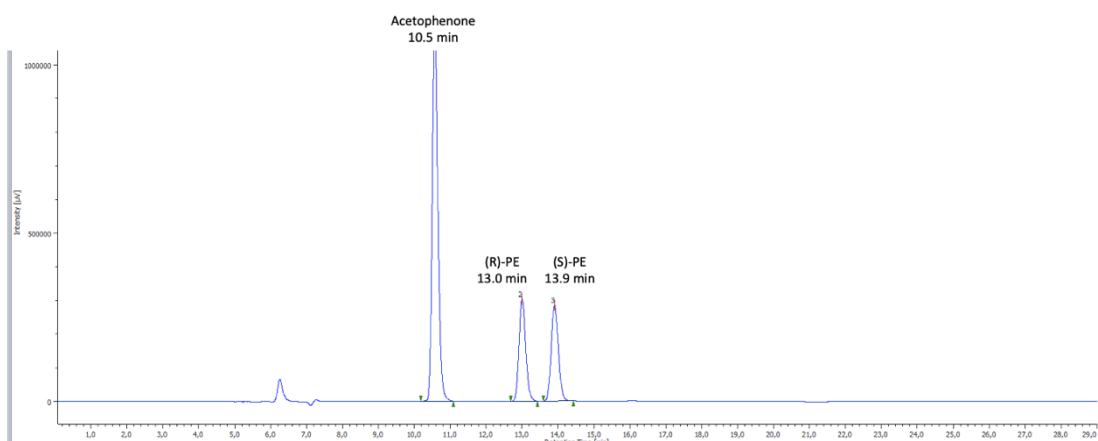


**Figure 4.3** HPLC chromatogram of the product solution after pulsed electrosynthesis of acetophenone (a pulse and relaxation time of 20 and 60 s, respectively, 39 % conversion of acetophenone to PE) by using a non-imprinted porous Pt-Ir alloy as the working electrode.

A suitable potential for the electroreduction of acetophenone was identified, by investigating the onset potential of the reduction of acetophenone, as being approximately -0.4 V (**Figure 4.4**). Although a more negative potential could induce faster reaction kinetics, the reaction should not proceed at too negative potentials to prevent the reduction of protons (1 M NH<sub>4</sub>Cl as a supporting electrolyte, pH of the solution at 5.0). As mentioned earlier, the reaction equilibrium is shifted to the preferential product of 1-PE at a lower pH. Therefore, the pH of the reaction mixture was adjusted by 1 M HCl solution in a range from 5.0 to 2.0, and applied potentials were approximately increased by +60 mV per the decrease of pH unit following the theoretical relationship between potential and pH derived from Nernst's equation.[209] As summarized in **Table 4.1**, the results reveal that by decreasing the pH of the solution from 5.0 to 4.0, the enantiomeric excess (%ee) of PE remarkably increases from 28 % to 52 %, respectively. However, the enantiomeric excess dramatically decreases when the pH of the solution is lower (24% and 2% at pH 3.0 and 2.0, respectively). This might be due to the fact that the faster the reaction rate, the less selective the reaction because there is only a limited number of chiral sites available. To conclude, appropriate conditions for electrosynthesis with chiral

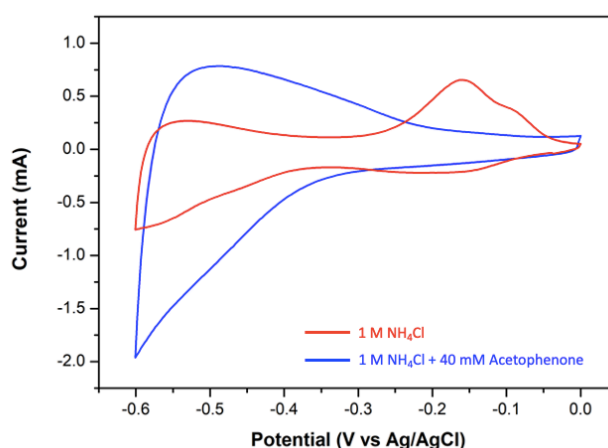


**Figure 4.4** Cyclic voltammograms at a scan rate of 100 mV s<sup>-1</sup> with a mesoporous Pt-Ir electrode in 1 M NH<sub>4</sub>Cl (red) and a solution containing 40 mM acetophenone (blue) at pH 5.0. The onset potential for the reduction of acetophenone is determined to be in the range from -0.3 to -0.4 V.

imprinted Pt-Ir alloys are an applied potential of -0.35 V and a solution pH of 4.0. These conditions were used for further studies.

**Table 4.1** Summarized results of the effect of pH on product selectivity for the electroreduction of acetophenone when using (S)-PE encoded mesoporous Pt-Ir electrodes.

A pH of reactant solution	Applied Potentials (V vs Ag/AgCl)	%Enantiomeric excess of (S)-PE
5.0	-0.40	28
4.0	-0.35	49
3.0	-0.30	24
2.0	-0.30	2

As illustrated in the HPLC chromatograms (**Figure 4.5A**) and histograms (**Figure 4.5B**), the steady-state synthesis for 13 h shows, as expected, no enantioselectivity when using a non-imprinted mesoporous Pt-Ir as a working electrode. However, when performing the experiment with a (S)-PE imprinted mesoporous Pt-Ir electrode, an enantiomeric excess of 49% can be achieved. A mirror value of enantiomeric excess can be observed when using an electrode imprinted with (R)-PE (-52%). The opposite sign of enantiomeric excess demonstrates that the chiral imprinted Pt-Ir alloys can preferentially synthesize the corresponding enantiomers. Most importantly, the enantiomeric excess is much more pronounced compared to what was achieved with the monometallic structures (%ee for around 15% and 20% in the case of pure Pt and Ni, respectively).[90, 91] The significantly improved activity in the case of alloyed Pt-Ir relates to a more asymmetric environment of bimetallic structures [185, 210] and lower adsorption energy of protons ( $H^+$ ) in comparison with monometallic Pt and Ir.[189] Moreover, an enhancement in stereoselectivity when Ir is inserted in bulk Pt could also be explained by surface roughening. Terraces, steps, or even kink sites present at the intersection of polycrystalline planes in alloy could play a major role in the activity enhancement.[95, 207]

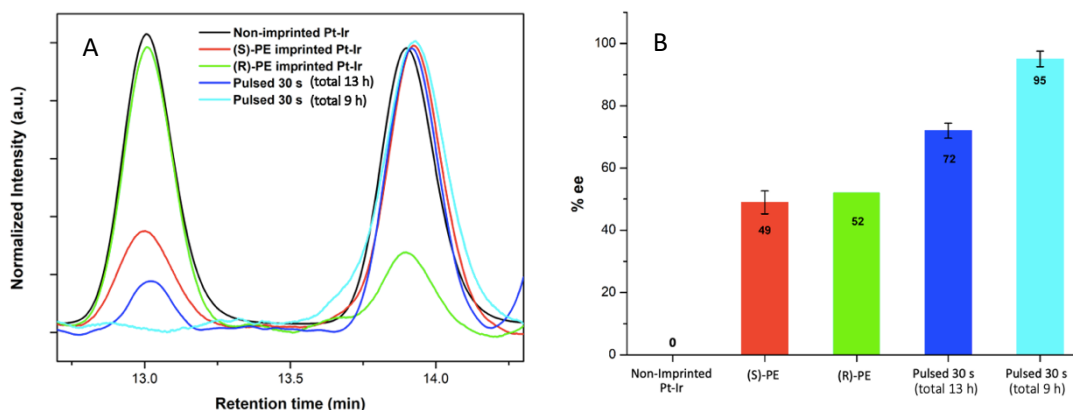


**Figure 4.5** Products analysis after enantioselective electrosynthesis of (S)- or (R)-PE from acetophenone on chiral-imprinted Pt-Ir alloy surfaces as shown by A) HPLC chromatograms of the products obtained by either conventional electrosynthesis for 13 h or pulsed electrosynthesis with a pulse and relaxation time of 30 s, and B) Histograms of the enantiomeric excess (%ee) after electrosynthesis with non-imprinted Pt-Ir (black), (S)-PE (red) and (R)-PE (green) imprinted Pt-Ir electrodes, carried out by potentiostatic electrosynthesis, or (S)-PE-imprinted Pt-Ir electrodes studied in pulsed electrosynthesis with a global synthesis duration of 13 h (dark blue) and 9 h (light blue). The s.e.m. is 2.16 %ee.

To further enhance the enantiomeric excess, the recently developed pulsed electrosynthesis strategy was applied to suppress the competitive reactions at the non-imprinted sites.[90] Firstly, a suitable condition for pulsed electrosynthesis was investigated, denoted by A-B s, where A and B represent pulse and relaxation times for each condition, respectively. As shown in **Figure 4.6A** and **B**, the pulse time is fixed at 30 s, but relaxation times are varied, ranging from 120 s to 60, 30, and eventually 15 s. By lowering the relaxation time, the %ee of the desired enantiomer is dramatically enhanced from 6% (30-120 s) to 31% (30-60 s) and is the highest for the 30-30 s condition (69%). These might be explained by the fact that the longer the relaxation time, the higher probability of accumulating reactants at non-imprinted sites, resulting in the formation of a higher portion of the racemic product. On the other hand,

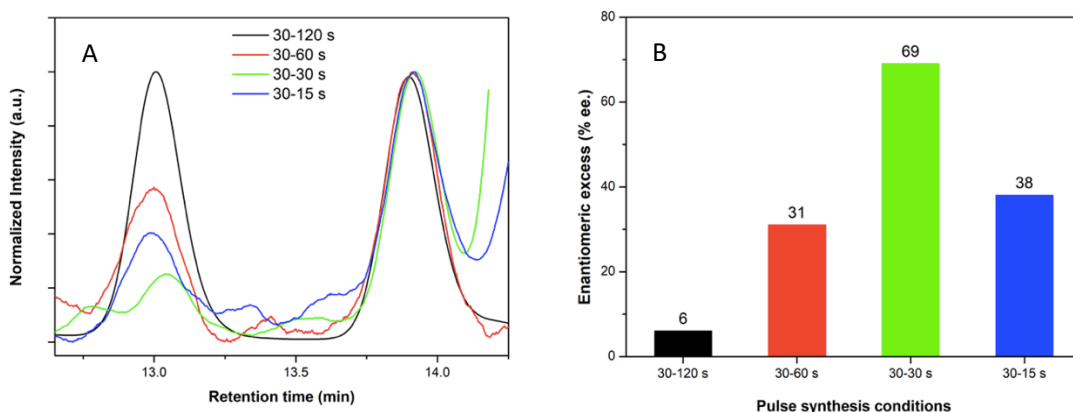


**Figure 4.6** Investigation of pulsed synthesis conditions (defined by pulse time-relaxation duration, respectively) for the electroreduction of acetophenone to (S)-PE illustrated by A) HPLC chromatograms of the products obtained with different pulse conditions and B) Histograms of the enantiomeric excess (%ee) after electroreduction with 30-120 s (black), 30-60 s (red), 30-30 s (green) and 30-15 s (dark blue).

by shortening the relaxation time to 15s, the product selectivity is significantly decreased to 38%, due to a too short period for acetophenone to migrate into the mesopores and react at the chiral cavities. Therefore, the reaction is forced to occur mostly at the external surface of the electrode, and enantiomeric excess is consequently lower. Hence, the equal pulse duration and relaxation time of 30 s is the most suitable condition for this study.

The enantiomeric excess is significantly enhanced, up to an average of  $72 \pm 2\%$ , when using the pulse synthesis (30 s) for the same global synthesis time as for the steady-state electroreduction (13h). Interestingly, an even better enantiomeric excess can be achieved (up to  $95 \pm 3\%$ ), when decreasing the total duration of the pulses to 9 h (**Figure 4.5A** and **B**). As reported previously, although a high enantiomeric excess of above 90% can be achieved with the monometallic chiral encoded Pt surfaces, a much longer synthesis time is needed; in contrast, when applying a similar situation with the pulse duration of 30 s, only 58 %ee could be observed.[90] This might be explained by a longer global synthesis time, allowing the gradual accumulation

of by-products resulting from the dimerization (**Scheme 4.2**). Also, as alcohol compounds like the butanediol derivatives, prefer to adsorb on Pt surfaces,[211-213] a gradual deactivation of the chiral surfaces is initiated when prolonging the synthesis time, leading to a less pronounced enantioselectivity.

As the electrochemical stability of pure chiral imprinted metals is one of the most critical problems,[90, 91] additional experiments were carried out to investigate the stability and reusability of the chiral-imprinted mesoporous alloy metals as electrocatalysts for several catalytic cycles. HPLC chromatograms of products obtained by pulsed electrosynthesis were recorded when using the (S)-PE imprinted mesoporous Pt-Ir for three cycles, as shown in **Figure 4.7A**. The chiral encoded Pt-Ir alloy demonstrates outstanding electrochemical stability, preserving an enantiomeric excess of up to 90% (from 98 %ee in the 1<sup>st</sup> run to 90 %ee in the 3<sup>rd</sup> run) (**Figure 4.7B** (orange)). In strong contrast, pure chiral imprinted Pt,[90] shows a decrease of enantiomeric excess by almost 30% after three electrocatalytic cycles (67 %ee in the 1<sup>st</sup> run and 39 %ee in the 3<sup>rd</sup> run) (**Figure 4.7B** (gray)). The preserved enantioselectivity

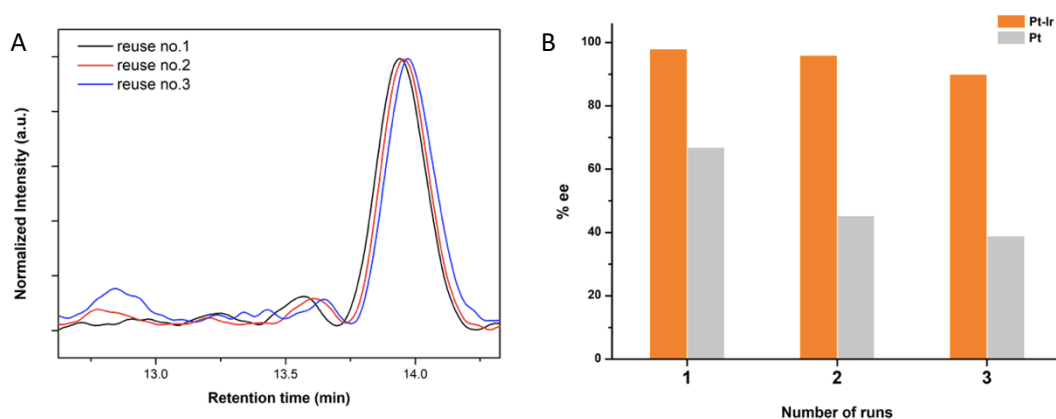


**Figure 4.7** Reusability test of a (S)-PE imprinted Pt-Ir electrode A) HPLC chromatograms of the product solution obtained from pulsed electrosynthesis (30-30 s) when reusing the same electrode for three electrochemical runs; B) Comparative graph of the %ee obtained for three reaction cycles of a (S)-PE imprinted Pt-Ir electrode (orange) and a (S)-PE imprinted monometallic Pt electrode, obtained from literature results (gray) [90].

confirms that the chiral features can be stabilized by introducing a promoter such as Ir into the Pt lattice. These findings illustrate that the electrodes can be used practically even for several electrocatalytic cycles. The decrease of enantioselectivity after many cycles might be explained by surface energy relaxation through the segregation of the metal atoms into metal nano-islands at the outermost surface of the electrode.[207, 214] However, the overall improved stability of Pt-Ir might be explained by the local cohesive energy ( $CE_{local}$ ), the sum of bond energies of metal-metal neighbors, of the metal atoms at the binding site. It has been reported that the  $CE_{local}$  of Ir atom sites is lower than that of Pt by approximately 1.5 eV. This lower energy implies that when Pt-Ir is formed in an alloy structure, its stability is enhanced, compared to bulk monometallic Pt, by the influence of the inserted Ir atoms.[215]

#### **4.3.2 Asymmetric synthesis *via* hydrogenation using chiral-encoded mesoporous Pt-Ir alloys supported on Ni foam**

Many phenolic compounds containing ketone groups are present in biomass derivatives,[216] and they can be converted into high-added value products, i.e., phenolic alcohols which play a crucial role as an initial building block for several applications ranging from food additives and cosmetics to pharmaceuticals.[217] Therefore it is interesting to study the conversion of aromatic ketones into the corresponding alcohols not only through catalytic electrosynthesis but also *via* processes that are largely already used in industry such as hydrogenation on heterogeneous catalysts, e.g., platinum black in the presence of excess hydrogen.[218] However, in this case, it is mandatory and rather difficult to control stereochemistry during the catalytic process in order to prevent the formation of a racemic mixture of the resulting products. In this context, a number of well-designed metal surfaces have been used as catalysts for enantioselective hydrogenation.[219] In addition, fine-tuning the synthesis conditions is an important issue. Although asymmetric electrosynthesis using chiral electrocatalysts, i.e., pure noble and non-noble metals such as Pt and Ni has been reported,[87, 89-91] the Pt-Ir alloy described in the previous session demonstrated a better performance in terms of enantioselectivity and stability

compared to monometallic catalysts. Nevertheless, using the catalyst as a planar film supported on a gold-coated glass slide restricts the accessibility of reactants, resulting in modest catalytic performances, e.g., low conversion and a slow production rate. In order to overcome this drawback, using support with high porosity, resulting in a large surface area, for the deposition of the chiral metal layers, should be a promising strategy. Hence, in this present case, high surface area Ni foam was selected as solid support for the synthesis of chiral Pt-Ir to allow a better mass transport of molecules to and from the active catalytic sites.

The designed chiral-encoded Pt-Ir alloy was explored as a heterogeneous catalyst for the production of chiral compounds *via* hydrogenation. As illustrated in **Figure 4.8A**, when the reaction is continuously taking place, denoted as conventional hydrogenation, the chiral-imprinted sites on the Pt-Ir surface allow the initial adsorption of a prochiral molecule, which

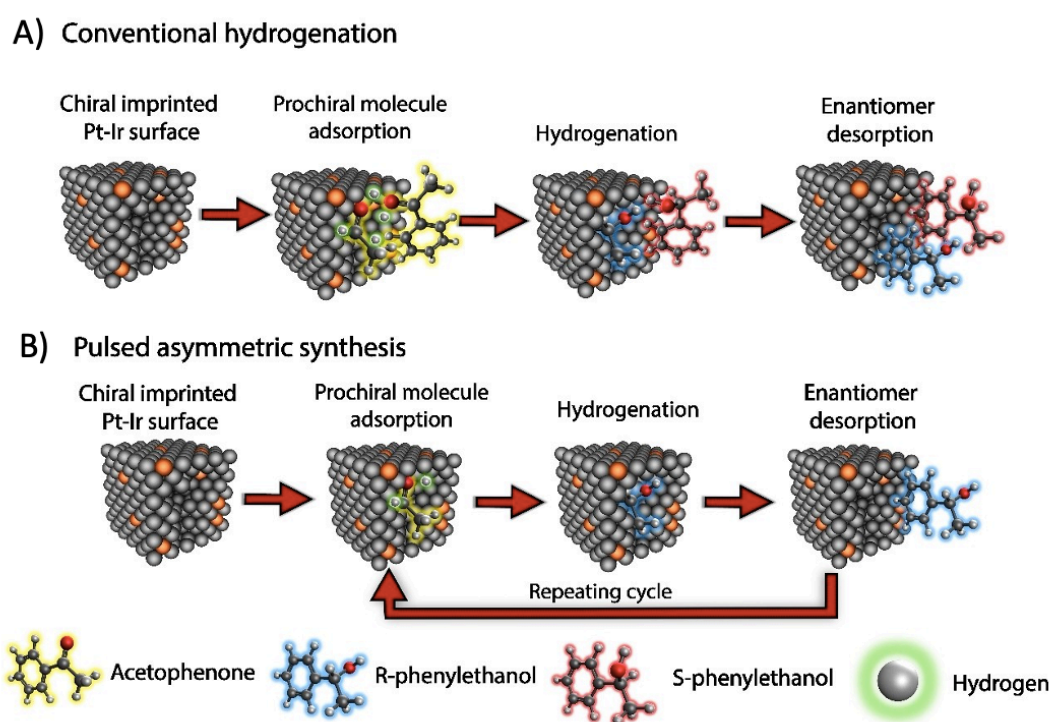


**Figure 4.8** Selective production of phenylethanol enantiomers *via* catalytic hydrogenation of acetophenone following two approaches: A) Conventional hydrogenation and B) Pulsed synthesis strategy at chiral encoded Pt-Ir alloy interfaces.

then further reacts with the hydrogen also present at the chiral Pt-It interface. The enantioselective hydrogenation is followed by the desorption of the chiral product. However, competitive reactions such as the production of racemic mixtures, mainly initiated at non-imprinted sites, seem to be unavoidable. During continuous synthesis, mass transport limitations inside the mesopores slow down product evacuation and the provision of fresh precursor molecules. This may result in only relatively modest enantioselectivity. In order to achieve a more significant enantiomeric excess, a promising alternative concept is pulsed asymmetric synthesis, illustrated in **Figure 4.8B**. This strategy allows the prochiral molecules to interact with the chiral surface for a specific time to undergo hydrogenation, followed by desorption of the chiral products during a certain relaxation time, during which hydrogen supply is stopped. This type of cycle is then repeated several times.

Conventional asymmetric synthesis of PE was conducted under a static hydrogen flow in an aqueous solution of 1 mM acetophenone. After the hydrogenation, the product mixtures were analyzed using the HPLC, with corresponding retention times of 9.6, 11.2, and 11.9 min for acetophenone, (R)-PE and (S)-PE, respectively (**Figure 4.9**). Several parameters related to the catalyst performance were systematically investigated. The first important

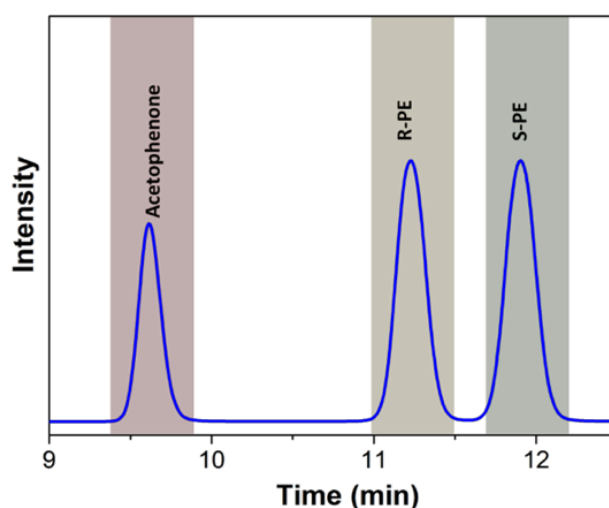


**Figure 4.9** HPLC chromatogram of the solution mixtures of the molecules involved in the asymmetric hydrogenation, including acetophenone (9.6 min), (R)-PE (11.2 min), and (S)-PE (11.9 min).

parameter is the solution pH. As illustrated in **Figure 4.10** and summarized in **Table 4.2**, the results show that by lowering the pH from 7 to 3, the enantiomeric excess remarkably increases from 49 to 80 %ee. However, when the pH is too low, such as 1, enantioselectivity decreases to 66 %ee due to a too fast hydrogenation rate, resulting in a more unselective reaction. Therefore, in the present study, the optimal pH of the reaction medium is about 3, which allows producing the highest possible enantiomeric excess. Under the most suitable conditions, a series of experiments was performed with non-imprinted and (R)-PE or (S)-PE imprinted Pt-Ir catalysts for the hydrogenation of acetophenone. As expected, there is no enantioselectivity ( $0.4 \pm 0.6$  %ee) when the surface has no chiral features. In comparison, the chiral Pt-Ir materials demonstrate very high enantiomeric excess values of  $80.2 \pm 2.7$  %ee and  $78.4 \pm 3.1$  %ee for (R)-PE and (S)-PE imprinted Pt-Ir alloys, respectively. These results confirm the benefit of chiral features on Pt-Ir surfaces to promote enantioselectivity during the hydrogenation reaction (**Figure 4.11**).

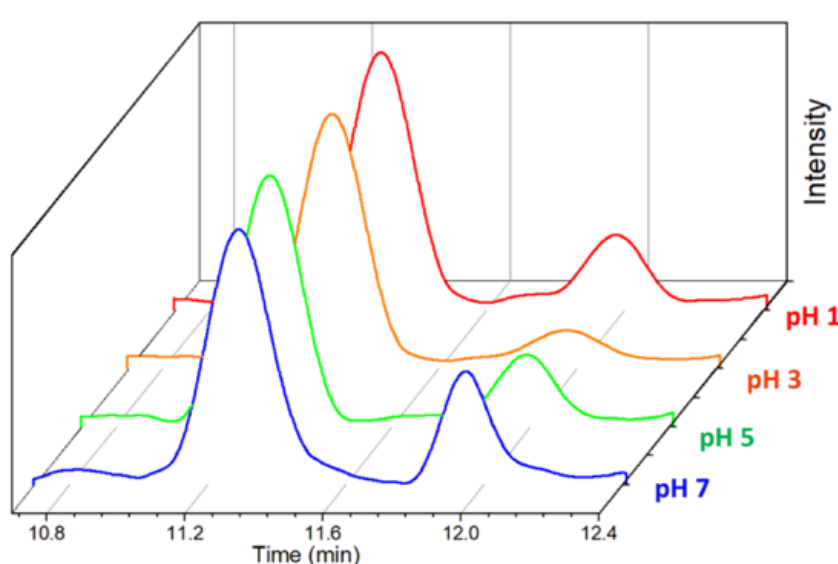


**Figure 4.10** HPLC chromatogram of the product solutions obtained from various reaction mediums with a pH of 1 (red), 3 (orange), 5 (green), and 7 (blue).

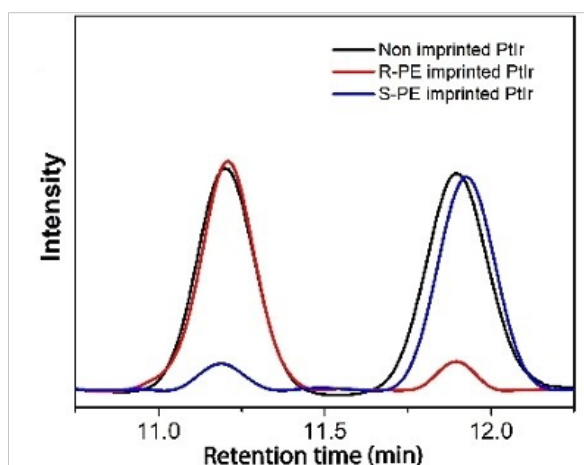


**Figure 4.11** HPLC chromatograms of the product solutions obtained with different catalysts, including non-imprinted (black), (R)-PE (red), and (S)-PE (blue) encoded Pt-Ir alloys.

**Table 4.2** Effect of solution pH on the enantioselectivity of the hydrogenation of acetophenone using (R)-PE encoded Pt-Ir films supported on Ni foam.

pH of solution	Enantiomeric excess (%ee)
1	66
3	80
5	62
7	49

Furthermore, the reaction time was varied to study its impact on product selectivity. As shown in **Figure 4.12A**, a lower degree of enantioselectivity is obtained for longer reaction times, decreasing from 79.6 and 29.8 to 4.0 %ee for 5, 10, and 15 min, respectively. This might be explained that the chiral active sites are blocked by organic compounds after a prolonged time, leading to temporary passivation of the chiral surface.[220] This surface passivation can be overcome when after 5 min of hydrogenation the catalyst is rinsed in water for 15 min, then immersed again in the same solution for the next catalytic run, and repeating this process for three cycles. There is no significant difference between the %ee values for each catalytic cycle, with an average of

79.5 %ee (**Figure 4.12B** and **Table 4.3**). These observations indicate the presence of surface passivation after prolonged hydrogenation. However, a simple rinsing in water can effectively avoid the surface passivation problem.

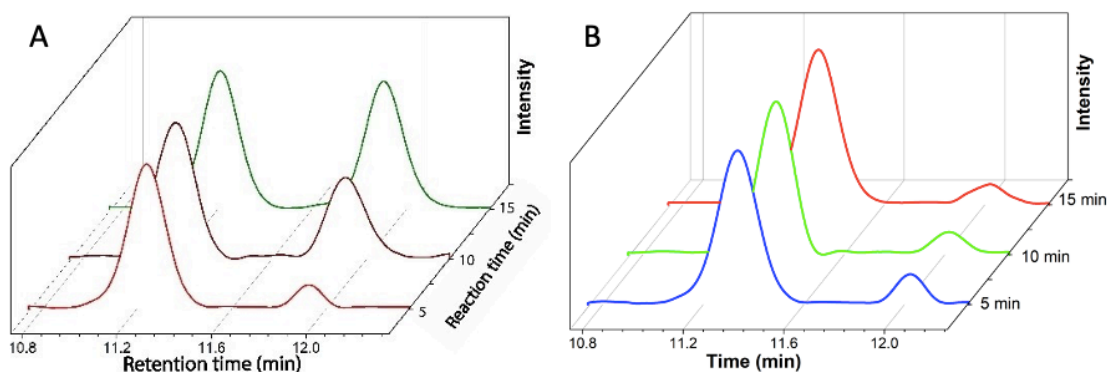


**Figure 4.12** HPLC chromatograms of the product solutions obtained with different hydrogenation methods and reaction times; A) Continuous hydrogenation for 5 (red), 10 (black), and 15 (green) min; B) Cyclic hydrogenation, with an intermediate cleaning step of 15 min, for 5 (blue), 10 (green) and 15 (red) min of total reaction time.

**Table 4.3** The impact of synthesis time on the enantioselectivity for cyclic hydrogenation of acetophenone using (R)-PE imprinted Pt-Ir on Ni foam.

Global reaction time	Enantiomeric excess (%ee)
5	79.6
10	80.4
15	78.6

The stability of the catalyst was further evaluated by using the chiral Pt-Ir alloy for several independent catalytic cycles and rinsing in water after each catalytical run. When hydrogenation is performed with different reaction times (5, 7, and 9 min), a decrease of enantioselectivity from 82.0 to 58.6 and 42.5 %ee, respectively, is observed for the initial catalytic cycle (**Figure 4.13A** and **B** (cases i, ii and iii)). However, in the following catalytic cycles enantioselectivity

is maintained, i.e., almost 80 %ee for a reaction time of 5 min even during the third cycle (cases iv and vii) and 60 %ee and 40 %ee for reaction times of 7 min (cases v) and 9 min (case vi), respectively, during a second run. This satisfying stability of the chiral Pt-Ir alloy, when using it as a heterogeneous catalyst for hydrogenation, is comparable with what has been observed for the asymmetric electro-synthesis in the previous session. Again, the improved stability can be ascribed to the Ir atoms inserted in the Pt matrix, influencing the atomic surface mobility.[173]

Not only continuous or cyclic hydrogenation but also a pulsed hydrogenation strategy has been applied to enhance the enantiomeric excess and improve the global yield (**Figure 4.8B**). In the case of the pulsed synthesis, the hydrogen gas flow is switched on and off for many cycles to allow novel

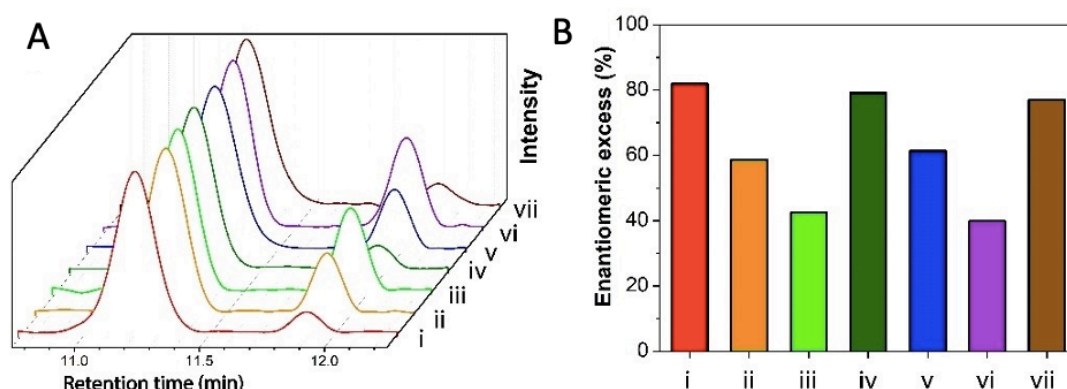


**Figure 4.13** Reusability test of the (R)-PE imprinted Pt-Ir catalyst performed with different reaction schemes A) and B) HPLC chromatograms of chiral products and histograms summarizing the enantiomeric excess (%ee) obtained with a chiral Pt-Ir alloy imprinted with R-(PE) for three independent consecutive catalytic cycles in fresh educt solution for every cycle and rinsing in water after every full cycle: First catalytic cycle after a total reaction time of (i) 5 min (red), (ii) 7 min (orange), (iii) 9 min (light green); Second catalytic cycle after a total reaction time of (iv) 5 min (dark green), (v) 7 min (blue), (vi) 9 min (purple); (vii) Third catalytic cycle after a total reaction time of 5 min (brown).

reactant molecules to reach the active sites and the produced chiral molecules to diffuse out from the mesopores. The total reaction time is still 15 min, as in the previous experiment of continuous synthesis, but the pulse durations were varied from 5 to 3 min (3 and 5 catalytic cycles, respectively). This leads to a very significant increase in enantioselectivity from 4 %ee (continuous synthesis) to 79.8 %ee (5 min of the pulse time) and 85 %ee for the shortest pulse time of 3 min (**Figure 4.14A and B**).

To further characterize the performance of the catalytic system, %yield, enantiomeric excess, and catalytic efficiency are calculated and summarized in **Figure 4.14B** and **Table 4.4**. The catalytic efficiency is defined as the amount of desired product generated per unit of spent H<sub>2</sub> and per active area of catalyst ( $\text{mol}_{\text{product}}/(\text{mol}_{\text{H}_2} \text{mol}_{\text{active sites}})$ ). Values in the range between 116 and 159 mol<sup>-1</sup>, are obtained, depending on the individual experimental conditions. It is interesting to note that using the pulsed synthesis strategy gives

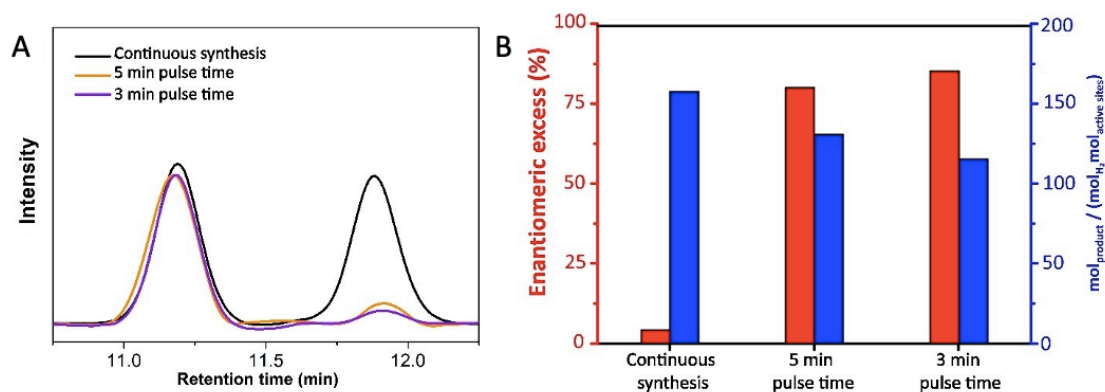


**Figure 4.14** Pulsed asymmetric catalysis with a chiral encoded Pt-Ir alloy supported on Ni foam A) HPLC chromatograms of products obtained with R-(PE) imprinted mesoporous Pt-Ir in 1 mM acetophenone for continuous synthesis (black), pulsed asymmetric synthesis with a pulse time of 5 min (orange) and 3 min (purple) with a total synthesis time of 15 min. B) Relationship between the enantiomeric excess and catalytic efficiency comparing conventional and pulsed synthesis. The retention times of 11.2 and 11.9 min correspond to R-(PE) and S-(PE), respectively.

a lower catalytic efficiency than continuous synthesis. However, this reduction is compensated by the significantly improved enantiomeric excess (from 4 %ee to as high as 85 %ee).

**Table 4.4** Summary of catalytic performance of chiral imprinted mesoporous Pt-Ir alloys comparing heterogeneous catalysis and electrocatalysis.

Synthesis methods	Approaches	Yield (%)	Enantiomeric excess (%ee)	Reaction time (min)
Heterogeneous catalysis	Conventional	0.11	4	15
	Pulse (3 min)	0.08	80	15
	Pulse (5 min)	0.09	85	15
Electrocatalysis	Conventional	0.13	49	780
	Pulse	0.10	98	540

As illustrated in **Table 4.4**, conventional hydrogenation provides a modest yield of 0.11% together with a very low of 4 %ee; however, when applying the pulsed strategy with short pulse durations (3 or 5 min), enantioselectivity is dramatically enhanced to 85 %ee with a slightly diminished yield (0.09 %). Although these yield values are relatively low, there is a remarkable improvement with respect to recent work, reporting acetophenone reduction using a cinchonine-doped Pd (CN@Pd) catalyst with very low enantiomeric excess values (approximately 5 %ee).[86] Another beneficial aspect of the chiral imprinted Pt-Ir alloy supported on porous Ni is that this approach allows obtaining a similar catalytic efficiency in terms of both %yield and %ee values, compared to electrocatalysis.[173] However, the global reaction time is much shorter than with the electrosynthesis approach, decreasing from several hours to only several minutes. These proof-of-principle experiments of asymmetric hydrogenation on chiral Pt-Ir alloy surfaces still need to be further improved in terms of catalytic efficiency, to meet the requirements of practical relevance. For example, it would be possible to design a flow-through set-up, allowing a continuous switching of H<sub>2</sub> gas flow.

## 4.4 Conclusion

This chapter demonstrated the benefits of the chiral-imprinted mesoporous Pt-Ir films, compared to the pure chiral Pt, showcasing excellent electrochemical durability for the asymmetric electrosynthesis of chiral compounds. For example, (S)-PE imprinted Pt-Ir films show a high activity and electrochemical stability with enantioselective electroreduction yielding up to 90 %ee even after the third electrocatalytic cycle, which is much higher than the previous results obtained using a monometallic Pt electrode. Furthermore, chiral-imprinted mesoporous Pt-Ir alloys, supported on a 3-D matrix of Ni, revealed a synergy between the high porosity of Ni-foam and the mesoporous alloy, accompanied by the chiral features, resulting in a hybrid material with promising features for asymmetrical catalysis. Interestingly, the designed material can also be effectively used as a heterogeneous catalyst for the asymmetric hydrogenation of acetophenone to produce selectively phenylethanol enantiomers, depending on chiral recognition sites in the metal alloy. For instance, when pulsed synthesis and fine-tuned reaction conditions are used, a very high degree of enantioselectivity of up to 85 %ee can be achieved even after the use for several successive catalytic cycles. The significant improvements in terms of activity and stability of chiral-encoded alloy surfaces allow overcoming some of the mechanical, chemical, and even electrochemical difficulties of the pure metal counterparts. This allows envisioning their use as chiral sensors, heterogeneous chiral catalysts, or even in the frame of other applications like chiral photocatalysis to produce valuable chemicals from the natural feedstock.

## Chapter 5

# Enantiomeric discrimination by traditional electrochemistry and electrochemiluminescence (ECL) on chiral-imprinted mesoporous platinum-iridium (Pt-Ir) surfaces

### 5.1 Introduction

The enantiomeric discrimination of chiral molecules is vital for various applications.[77, 221-223] Chiral recognition can be studied by various analytical techniques, but they often require advanced instrumentation, resulting in high costs for sample purification or derivation and time-consuming analytical processes.[224-226] Consequently, developing novel and eventually more straightforward strategies to discriminate between chiral enantiomers is still an important challenge.[227, 228]

Apart from chiral synthesis reported in the previous chapters, enantioselective analysis and chiral separation are still a very active field of research, targeting higher efficiencies and better performance in differentiating between chiral enantiomers.[87, 91, 102] In addition, electrochemical concepts have several beneficial features, such as low detection limits and fast/real-time analysis. Therefore, in this context, the benefit of developed chiral metal structures will be demonstrated for enantiomeric discrimination based on electrochemical approaches. As exemplified with chiral monometallic Pt and Ni using differential pulse voltammetry (DPV),[87, 91] the electrodes could retain a chiral character even after removal of the chiral templates, transduced by different amplitudes of the DPV signals for the right and wrong enantiomers, with respect to the stereochemistry of the imprinted cavities. Accordingly, the

improved electrochemical and structural stability of the chiral Pt-Ir alloy should make this alloy also a promising candidate for enantioselective analysis.[173]

The alloy's stability also potentially opens a promising perspective for using it not only for traditional electrochemical techniques, but also in the frame of other more recent electrochemical approaches. An electrochemical concept that has gained much attention as a straightforward electrochemical readout is electrochemiluminescence (ECL). ECL signals allow an ultrasensitive response due to the nearly zero background signal, enabling the detection of analytes at very low concentrations (down to femtomolar, fM).[229-231] This results in the possibility of imaging at the single-molecule level, and electroactive species can be investigated both at the qualitative and quantitative level, depending on the luminescence produced by a controllable electrochemical reaction at the electrode interfaces.[232-234] This versatile approach has been widely used and associated with other techniques for various clinical and biological applications, ranging from bioassays for immune-sensing to exploring (bio)chemical reactions by ECL imaging.[233-237]

Therefore, an interesting question to explore, is whether it is possible to use ECL in combination with the chiral-encoded mesoporous Pt-Ir alloy and benefit from its high structural and electrochemical stability to design an opto-electrochemical readout scheme of chiral information. In this case, the chiral-imprinted mesoporous Pt-Ir alloy electrode is used as a working electrode, for the enantioselective electrooxidation of either the luminophore or the co-reactant, in the case that at least one of them has chiral features.

## 5.2 Experimental section

### 5.2.1 Chemicals

(L)-phenylalanine ((L)-PA) was purchased from Tokyo Chemical Industry (TCI). (D)-phenylalanine ((D)-PA), 3,4-dihydroxy-L-phenylalanine ((L)-DOPA), 3,4-dihydroxy-D-phenylalanine ((D)-DOPA), hydrogen hexachloroplatinate (IV) hexahydrate ( $\text{H}_2\text{PtCl}_6 \cdot 6\text{H}_2\text{O}$ ), dihydrogen hexachloroiridate (IV) hydrate ( $\text{H}_2\text{IrCl}_6 \cdot x\text{H}_2\text{O}$ ), polyethylene glycol hexadecyl ether (Brij<sup>®</sup> C10), sodium phosphate dibasic heptahydrate ( $\text{Na}_2\text{HPO}_4 \cdot 7\text{H}_2\text{O}$ ),

sodium phosphate monobasic monohydrate ( $\text{NaH}_2\text{PO}_4 \cdot \text{H}_2\text{O}$ ), and Tris(2,2'-bipyridyl) dichlororuthenium (II) hexahydrate ( $\text{Ru}(\text{bpy})_3\text{Cl}_2 \cdot 6\text{H}_2\text{O}$ ) were received from Sigma-Aldrich. A 1 M phosphate buffer solution (PBS) with a pH of 7.33 was prepared from  $\text{Na}_2\text{HPO}_4 \cdot 7\text{H}_2\text{O}$ , and  $\text{NaH}_2\text{PO}_4 \cdot \text{H}_2\text{O}$  dissolved in MilliQ water. Sulfuric acid ( $\text{H}_2\text{SO}_4$ ) and hydrochloric acid (HCl) were obtained from Alfa. MilliQ water (18.2 M $\Omega$  cm) was used for all experiments. All chemicals were immediately used without further purification.

### 5.2.2 Synthesis of chiral-encoded mesoporous Pt-Ir alloy electrodes

All electrochemical experiments were carried out with a three-electrode system, performed on a potentiostat (Metrohm  $\mu$ Autolab Type III) using Ag/AgCl (sat. KCl), Pt mesh (geometrical area as 1 cm<sup>2</sup>), and the prepared Pt-Ir alloy electrodes (geometrical area as 0.25 cm<sup>2</sup>) as the reference, counter and working electrodes, respectively. All results were analyzed with the Nova (version 1.11) program.

Chiral-imprinted mesoporous Pt-Ir electrodes were prepared by a procedure reported by Butcha *et al.* with some modifications.[173] Typically, co-electrodeposition of  $\text{H}_2\text{PtCl}_6$  and  $\text{H}_2\text{IrCl}_6$  (28 wt%, containing 85 at% Pt and 15 at% Ir, respectively) was performed in the presence of the columnar structure of non-ionic surfactant (Brij<sup>®</sup> C10, 28 wt%) dissolved in water (36 wt%), by using either DOPA or PA as chiral templates to adsorb at the external surface of the self-assembled surfactants columns. Chiral templates were added with molar ratios of 1 DOPA or PA per 12 ( $\text{PtCl}_6^{2-} + \text{IrCl}_6^{2-}$ ). All layers were generated on a cleaned gold-coated glass slide at -0.05 V with a charge density of 6, and 4 C cm<sup>-2</sup> for DOPA and PA encoded Pt-Ir, respectively. Finally, all templates, including desired chiral molecule and surfactant, were entirely removed by rinsing several times and immersion overnight in MilliQ water.

### 5.2.3 Chiral recognition by traditional electrochemistry using DOPA-imprinted mesoporous Pt-Ir alloy electrodes

To examine the chiral recognition ability of all the prepared chiral encoded Pt-Ir electrodes, two individual electrodes imprinted with (L)-DOPA and

(D)-DOPA were used in parallel for this study. Chiral recognition was examined by the electrooxidation of DOPA on the DOPA-imprinted mesoporous Pt-Ir electrodes with a film thickness of 6 C cm<sup>-2</sup>. Differential pulse voltammetry (DPV) was employed to increase the sensitivity of the faradaic DOPA oxidation signal with respect to the capacitive background signal.[87, 173] DPV was performed in a 4 mM solution of either (L)-DOPA or (D)-DOPA dissolved in a 50 mM HCl solution as a supporting electrolyte (pH 1.4). For DPV, a step potential of 10 mV, modulation amplitude of 50 mV, a modulation time of 50 ms and interval time of 500 ms were used. After the first scan, the chiral structure of the imprinted Pt-Ir electrodes was completely erased by cyclic voltammetry (CV), scanning the potential in the range between -0.20 to 1.80 V in 0.5 M H<sub>2</sub>SO<sub>4</sub> solution. Then, the erased Pt-Ir electrodes were used further for control experiments. The alternating analysis of DOPA electrooxidation by DPV and erasing of chiral information by the CV was performed several times until there was no more significant recognition of the two enantiomers.

#### **5.2.4 Chiral discrimination by electrochemiluminescence (ECL) using PA-imprinted mesoporous Pt-Ir alloy electrodes**

The enantiomeric discrimination was performed by either DPV or CV combined with an electrochemiluminescence (ECL) set-up, denoted as DPV-ECL and CV-ECL, respectively. The DPV-ECL was carried out in a potential window from -0.1 to 1.3 V, with a step potential of 10 mV, modulation amplitude of 50 mV, a modulation time of 50 ms, and an interval time of 500 ms. In contrast, CV-ECL was studied in a potential window from -0.1 to 1.5 V, with a scan rate of 100 mV s<sup>-1</sup>. Most of the analysis was done using 10 mM PA and 1mM [Ru(bpy)<sub>3</sub>]<sup>2+</sup> dissolved in 1 M PBS solution as supporting electrolyte (pH 7.33). Either a classic Pt electrode (1.6 mm of dimension) or the prepared chiral-imprinted Pt-Ir electrodes were used as working electrodes. In addition, platinum mesh (geometrical area for one cm<sup>-2</sup>) and Ag/AgCl/KCl (sat. KCl) were employed as counter and reference electrodes, respectively, equipped with a  $\mu$ Autolab type III potentiostat. The classic Pt electrode was polished prior to analysis with a 0.25  $\mu$ m diamond paste (Struers), followed by rinsing with

acetone and MilliQ water several times. Surface regeneration of the electrodes was carried out by chronoamperometry at -0.1 V for 30 s in 1 M PBS solution.

ECL responses were recorded in a homemade cell with a Hamamatsu R5070 photomultiplier tube (PMT detector) placed at a distance of around 3 mm in front of the working electrode. The PMT detector was held at -750 V with a Hamamatsu C9525 high-voltage power supply. The obtained signal was amplified by a Keithley 6485 Picoammeter, and the resulting signal was acquired *via* a second input channel of the  $\mu$ Autolab type III potentiostat. In practice, all electrodes were soaked in the solution containing only PA dissolved in PBS solution for an hour to allow the analyte to diffuse inside the mesopores. Then, these electrodes were put in the solution containing both PA and the  $[\text{Ru}(\text{bpy})_3]^{2+}$  dissolved in PBS solution. ECL spectra were collected in a dark room immediately after the electrode was placed into the solution.

Enantioselectivity between (L)-PA and (D)-PA for the ECL experiments was calculated following equation 5.1:

$$\text{Enantioselectivity} = \frac{I_L}{I_D} \text{ or } \frac{I_D}{I_L} \quad (5.1)$$

where  $I_L$  and  $I_D$  are the maximum ECL intensities, which were analyzed in (L)-PA and (D)-PA solutions, respectively.

## 5.3 Results and Discussion

### 5.3.1 Chiral recognition by traditional electrochemistry using DOPA-imprinted mesoporous Pt-Ir alloy electrodes

The electrooxidation of (D)-DOPA and (L)-DOPA was investigated at chiral encoded Pt-Ir surfaces imprinted by either (D)-DOPA or (L)-DOPA in the region of DOPA oxidation potentials ranging from 0.35 to 0.65 V using the DPV technique. This potential region was chosen because it allows only the characteristic of DOPA oxidation without interference from Pt oxidation.[87] As expected, in the case of the non-imprinted mesoporous Pt-Ir, there is no difference between (D)- and (L)-DOPA electrooxidation signals (**Figure 5.1A**). In strong contrast to this, the (L)-DOPA imprinted Pt-Ir film shows an excellent recognition of DOPA having the right-handedness, translated by a much higher

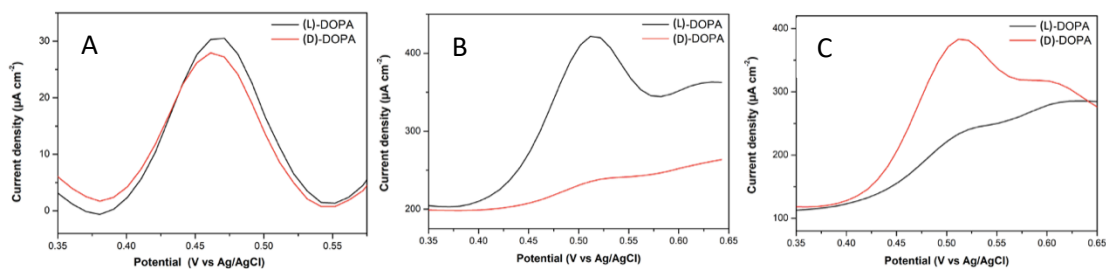


**Figure 5.1** Differential pulsed voltammograms of (L)-DOPA (black) and (D)-DOPA (red) obtained with different electrodes A) non-imprinted, B) and C) (L)-DOPA and (D)-DOPA-imprinted mesoporous Pt-Ir alloys, respectively.

amplitude of current density (**Figure 5.1B**). On the other hand, the (D)-DOPA imprinted Pt-Ir alloy preferably converts the (D)-DOPA enantiomer on its surface, as illustrated by a higher oxidation peak in (D)-DOPA solution compared to (L)-DOPA (**Figure 5.1C**). These observations confirm that chiral features of the Pt-Ir alloy surfaces are retained even after the elimination of the chiral template.

Chiral imprinted monometallic Pt exhibits a less pronounced enantioselective recognition of DOPA enantiomers compared to the chiral imprinted Pt-Ir (**Figure 5.2A**). The stability of the chiral-imprinted mesoporous metal was tested by oxidizing it at higher positive potential regions ( $> 0.65$  V vs Ag/AgCl). At this potential, monometallic Pt starts to get oxidized, eventually destroying the chiral information. To verify this hypothesis, the fresh DOPA-encoded pure Pt or alloyed Pt-Ir electrodes were oxidized in 0.5 M  $\text{H}_2\text{SO}_4$  from -0.20 to 1.20 V for ten cycles. As expected, the electrooxidation of (L)- and (D)-DOPA at the pure Pt encoded with (L)- DOPA is identical after destroying the chiral information by the afore-mentioned potential treatment (**Figure 5.2B**). In strong contrast to this, significant discrimination of (L)- and (D)- DOPA is preserved when retesting both oxidized (L)- and (D)- DOPA imprinted mesoporous Pt-Ir electrodes after ten cycles (**Figure 5.2C and D**). This illustrates again the significant improvement in the stability of chiral imprinted mesoporous Pt-Ir alloy with respect to pure Pt.

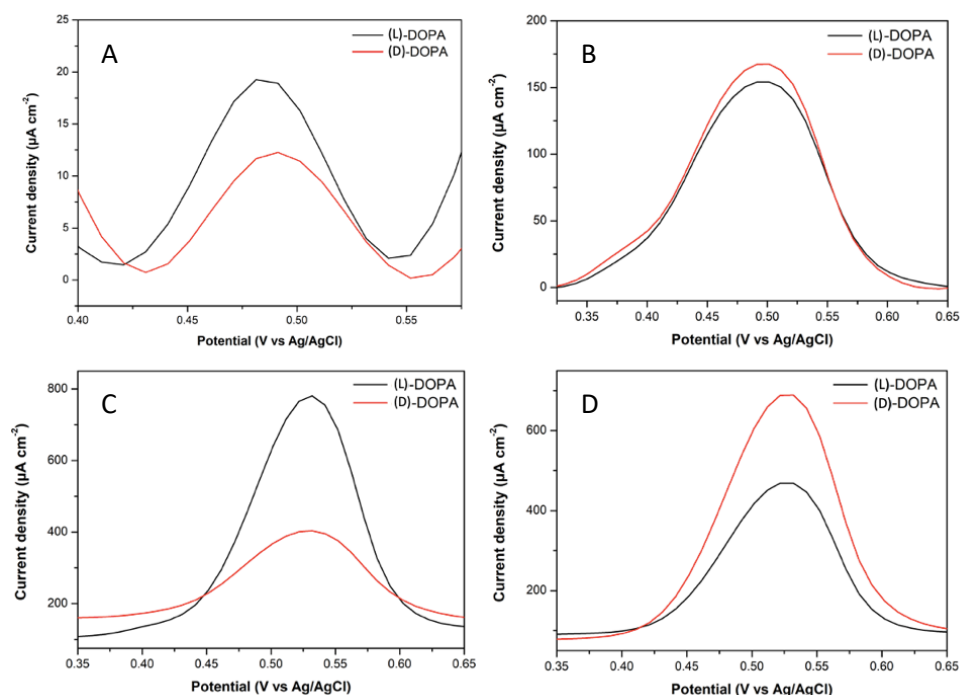


**Figure 5.2** Differential pulse voltammograms of (L)-DOPA (black) and (D)-DOPA (red) electrooxidation recorded with the different DOPA-imprinted metal electrodes: A) fresh (L)-DOPA imprinted monometallic Pt; B), C) and D) destroyed (L)-DOPA imprinted Pt, (L)-DOPA and (D)-DOPA imprinted Pt-Ir alloys, respectively, after erasing chiral information by CV in 0.5 M H<sub>2</sub>SO<sub>4</sub> for 10 cycles in the potential window from -0.2 to 1.2 V.

Most importantly, the highly efficient chiral-recognition properties of Pt-Ir are still observed, even after continuously erasing chiral information for 20 cycles (**Figure 5.3A** and **B**) and 30 cycles (**Figure 5.3C** and **D**) in the full range of potentials from -0.20 to 1.40 V. However, to confirm that there are no other artifacts interfering with the chiral recognition, the oxidation of the electrodes has finally been carried out under extreme conditions to destroy the chiral imprints. The electrodes were scanned in sulfuric solution for 40 cycles in an even further extended potential range from -0.2 to 1.8 V. Chiral features of the alloys are finally completely lost, indicated by the similar peak amplitudes for both enantiomers (**Figure 5.3E** and **F**).

The peak areas of current density in the DOPA oxidation region were integrated, as demonstrated in **Table 5.1**, to verify once more the chiral recognition properties by calculating the ratios of peak areas,  $A_L/A_D$  or  $A_D/A_L$ , respectively. Acceptable chiral discrimination is achieved when these ratios are significantly higher than 1.0.

**Table 5.1** Calculated relative electrooxidation peak areas of the different chiral imprinted electrodes from DPV signals.

Electrodes	Peak Area of (L)-DOPA ( $A_L$ ) <sup>b</sup>	Peak Area of (D)-DOPA ( $A_D$ ) <sup>c</sup>	Relative peak area <sup>a</sup>	
			$A_L/A_D$	$A_D/A_L$
(L)-DOPA Pt	0.0003	0.0002	1.5	-
Erased (L)-DOPA Pt after 10 cycles	0.0486	0.0518	0.9	-
(L)-DOPA Pt-Ir	0.0246	0.0017	14.5	-
Erased (L)-DOPA Pt -Ir after 10 cycles	0.2409	0.1817	1.3	-
Erased (L)-DOPA Pt -Ir after 20 cycles	0.2853	0.2173	1.3	-
Erased (L)-DOPA Pt -Ir after 30 cycles	0.1355	0.1088	1.2	-
Erased (L)-DOPA Pt -Ir after 40 cycles	0.0993	0.0982	1.0	-
(D)-DOPA Pt-Ir	0.0021	0.0284	-	13.5
Erased (D)-DOPA Pt -Ir after 10 cycles	0.1578	0.2129	-	1.4
Erased (D)-DOPA Pt -Ir after 20 cycles	0.2479	0.3404	-	1.4
Erased (D)-DOPA Pt -Ir after 30 cycles	0.0865	0.1190	-	1.3
Erased (D)-DOPA Pt -Ir after 40 cycles	0.0466	0.0432	-	0.9

<sup>a</sup> Peak area of either (L)-DOPA or (D)-DOPA signals was calculated with OriginPro version 8.5.

<sup>b</sup>  $A_L/A_D$  is determined for (L)-DOPA imprinted electrodes.

<sup>c</sup>  $A_D/A_L$  is calculated for (D)-DOPA imprinted electrodes.

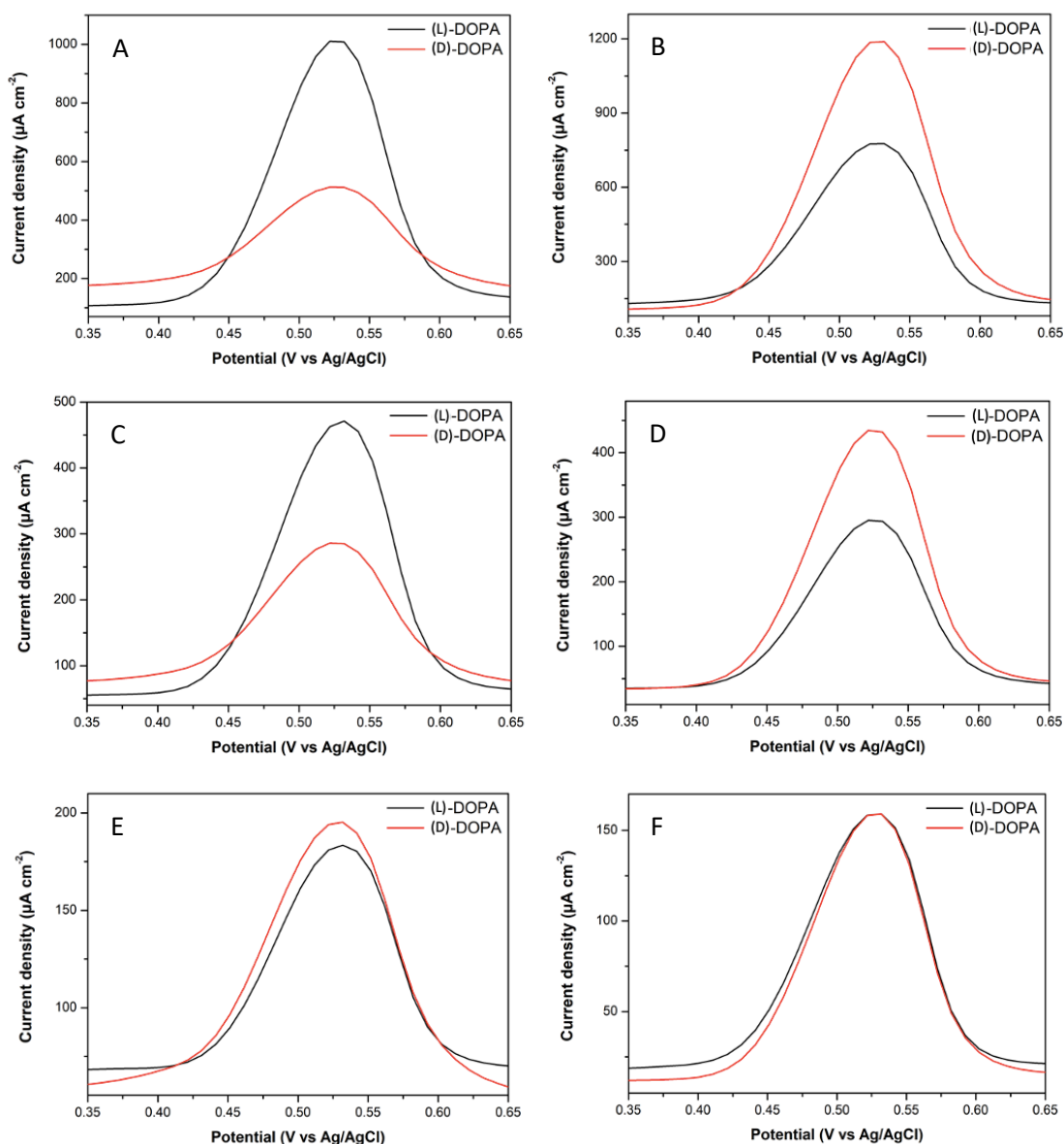


**Figure 5.3** Differential pulse voltammograms of (L)-DOPA (black) and (D)-DOPA (red) electrooxidation performed with the destroyed (L)-DOPA (left column) and (D)-DOPA (right column) imprinted Pt-Ir electrodes: A) and B) the DPV signals of DOPA-imprinted Pt-Ir alloys after erasing chiral information by CV in 0.5 M H<sub>2</sub>SO<sub>4</sub> for 20 cycles in the potential window from -0.2 to 1.2 V; C) and D) the DPV signals of DOPA-imprinted Pt-Ir alloys after erasing chiral information by CV in 0.5 M H<sub>2</sub>SO<sub>4</sub> for 30 cycles in the potential window from -0.2 to 1.4 V; E) and F) the DPV signals of DOPA-imprinted Pt-Ir alloys after erasing chiral information by CV in 0.5 M H<sub>2</sub>SO<sub>4</sub> for 40 cycles in the potential window from -0.2 to 1.8 V

The obtained  $A_L/A_D$  and  $A_D/A_L$  values are mirror symmetric, i.e., similar values for  $A_L/A_D$  and  $A_D/A_L$  of 14.47 and 13.52, respectively, are obtained with fresh bimetallic Pt-Ir electrodes encoded with (L)-DOPA and (D)-DOPA. On the other hand, the  $A_L/A_D$  ratio for (L)-DOPA imprinted monometallic Pt is only 1.50. The reason for the enhanced recognition activity of chiral imprinted Pt-Ir might be threefold: (i) limited adsorption on unselective sites on the smoother external surface of porous Pt-Ir compared to porous Pt, as illustrated by the SEM images in **Figure 5.4 A** and **B**;<sup>[238]</sup> (ii) the modification of adsorption properties originating from the different arrangement of the surface atoms (decrease of the Pt–Pt bond distance or increase of the Pt d-electron vacancy) of platinum;<sup>[239, 240]</sup> (iii) generation of a more asymmetric environment due to the lower symmetry of the metal structures obtained by introducing a different metal atom in the bulk metal.<sup>[185, 210]</sup>

Enantioselectivity values drop down to 1.0 in the case of monometallic Pt, even after only a few potential cycles. However, for the Pt-Ir alloy, these values decrease only moderately even after many cyclic excursions to rather drastic oxidation potentials. Only after 40 cycles up to very harsh positive potentials allows entirely destroying the chirality of the bimetallic surface. These observations confirm that the chiral imprinted mesoporous Pt-Ir electrodes display exceptional electrochemical stability, in contrast to chiral

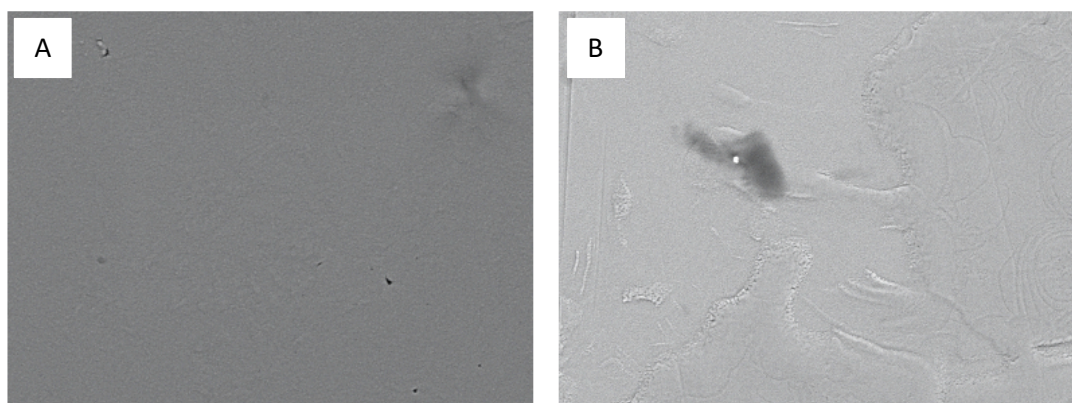


**Figure 5.4** SEM images (scale bars 20  $\mu\text{m}$ ) of A) porous Pt-Ir alloy and B) porous monometallic Pt electrode obtained by electrodeposition with a deposition charge density of 6 C  $\text{cm}^{-2}$ .

imprinted monometallic Pt. Hence, the chiral Pt-Ir alloy surfaces can be potentially applied not only as a catalyst for the asymmetric synthesis, clearly demonstrated in the previous chapter but also as a substrate for enantioselective analysis under more severe potential conditions, like the ones required for most of the ECL experiments.

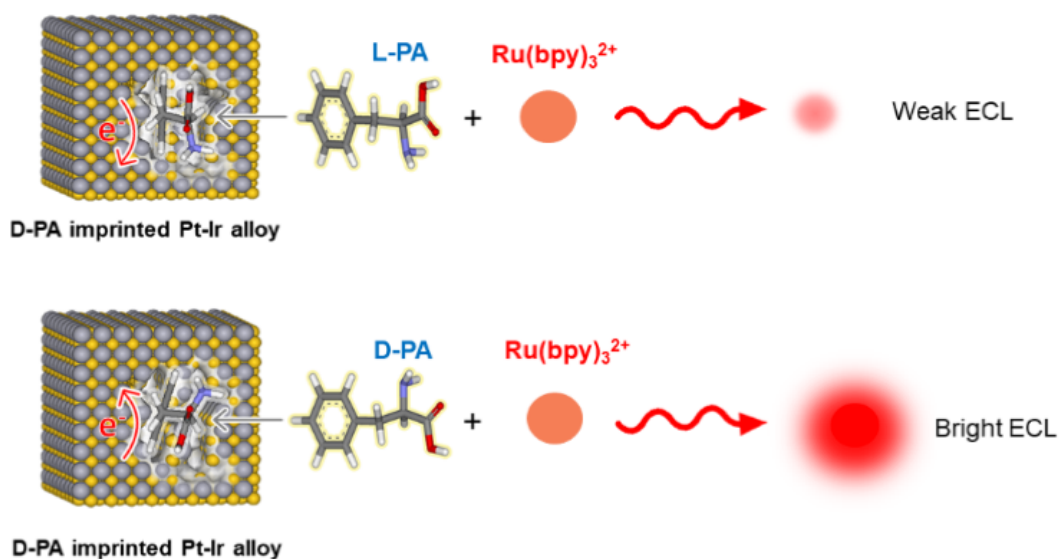
### **5.3.2 Chiral discrimination by electrochemiluminescence (ECL) using PA-imprinted mesoporous Pt-Ir alloy electrodes**

Although a simple electrochemical approach, such as DPV, can be used for chiral discrimination, alternative and straightforward strategies are still strongly needed. In this context, one of the possible strategies is to explore electrochemiluminescence (ECL). ECL is a phenomenon that is based on the conversion of a chemical process into radiative energy (emission of light), by the electrooxidation of certain species. The generation of ECL involves essentially three sequential steps: i) the generation of reactive intermediates by the electrochemical activation of a luminophore and a co-reactant at high positive potentials; ii) a homogeneous reaction between both reactive intermediates, resulting in the formation of an excited state of the luminophore; iii) photon emission by its relaxation to the ground state.[232]

Generally, it is impossible to discriminate two enantiomers by a simple ECL measurement because intrinsically obtained signals, e.g., the current intensity, or the wavelength ( $\lambda_{\max}$ ) of the emitted photon, are indistinguishable for enantiomers. Consequently, differentiating ECL signals would require that one of the ingredients, the luminophore, the co-reactant, or the electrode interface, has chiral features. To address this challenge, we have recently reported the possibility of generating ECL emitting circularly polarized light as a novel method to discriminate between enantiomers, so-called circularly polarized-electrochemiluminescence (CP-ECL).[241, 242] CP-ECL allows discrimination between the individual enantiomers of luminophores such as bispyrene organic macrocycles and the model  $[\text{Ru}(\text{bpy})_3]^{2+}$ . Lui and co-workers have reported an ECL sensor based on the design of a chiral molecular selector,  $[\text{Ru}(\text{bpy})_3]^{2+}$  coordinated with chiral cyclic pillar[5]arene (P[5])

rings.[243] When the developed selector, acting as the luminophore, undergoes the redox reaction required for the ECL process, and at the same time, a chiral molecule is binding inside the chiral P[5] moieties; different ECL intensities are obtained for the two enantiomers of the target molecule. An alternative to this is to use an appropriately designed material as the working electrode. For instance, a selector based on hemoglobin (Hb) anchored on gold (Au), which was then immobilized on graphite-like carbon nitride nanosheets (g-C<sub>3</sub>N<sub>4</sub>) and finally deposited on glassy carbon electrodes (Hb/Au-g-C<sub>3</sub>N<sub>4</sub> /GCE), could be used for the recognition of penicillamine (Pen) enantiomers.[244] In another case, cysteine (Cys) modified nitrogen-doped copper oxide/cobalt oxide CuO/CoO nanofibers (Cys@N-CuO/CoO NFs), employed as a chiral electrode for ECL, have been shown to be able to distinguish between DOPA enantiomers.[245] Although all studies are able to meet the requirements of practical applications in terms of high productivity, low-cost manufacturing, and biocompatible issues, only very modest stereoselectivity and a more or less complex design are still significant drawbacks.

Since high positive potentials must be applied to the electrode in order to trigger the conversion of electroactive species for ECL experiments, the very stable Pt-Ir alloy seems to be a promising electrode material in this context.[173] We therefore explore this possibility to propose a new approach to chiral ECL detection, which is rather different compared to recent other work.[241, 242] The metal interfaces encoded with chiral information are used for chiral discrimination based on the fact that certain analytes can also play simultaneously the role of ECL co-reactants. The imprinted Pt-Ir alloy is suitable for coupling with ECL analysis due to its structural and electrochemical stability against harsh oxidative conditions, as clearly demonstrated in the previous section dealing with chiral recognition by traditional electrochemistry. The imprinted Pt-Ir surfaces were tested as working electrodes for the electrooxidation of amino acid, i.e., phenylalanine (Phe), denoted in this manuscript as PA, acted as a chiral target molecule and simultaneously as an ECL co-reactant, accompanied by [Ru(bpy)<sub>3</sub>]<sup>2+</sup> as a luminophore (**Scheme 5.1**).



**Scheme 5.1** Enantiomeric discrimination of an amino acid such as phenylalanine (PA) with chiral-encoded mesoporous Pt-Ir surfaces based on an electrochemiluminescence (ECL) readout.

During the initial stage of electrochemical triggering, molecules are excited in a stereoselective way for achieving enantioselective ECL detection. The structures of the PA enantiomers are shown in **Figure 5.5**, revealing a chiral center at the carbon atom located next to an amino group. This chemical structure allows an amino acid to act simultaneously as the chiral target as well

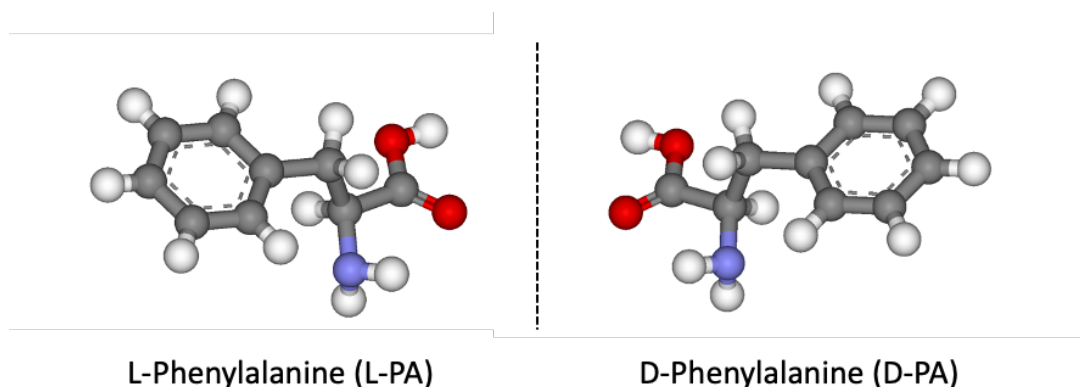


**Figure 5.5** Molecular structures of phenylalanine enantiomers. The chemical structures were calculated *via* Density Functional Theory (DFT), (6-31G(d,p) B3LYP), using the Gaussian program (09W)

as the co-reactant in the ECL mechanism. [173, 246] As illustrated in **Scheme 5.1**, a (D)-PA imprinted Pt-Ir alloy is used as an electrochemical interface for enantiomeric discrimination using the ECL approach. At the specific chiral recognition sites, (D)-PA leads to an ECL signal with higher amplitude compared to (L)-PA, whereas the normal optical properties of both enantiomers are perfectly identical, as illustrated by the UV-Vis spectra in **Figure 5.6**.

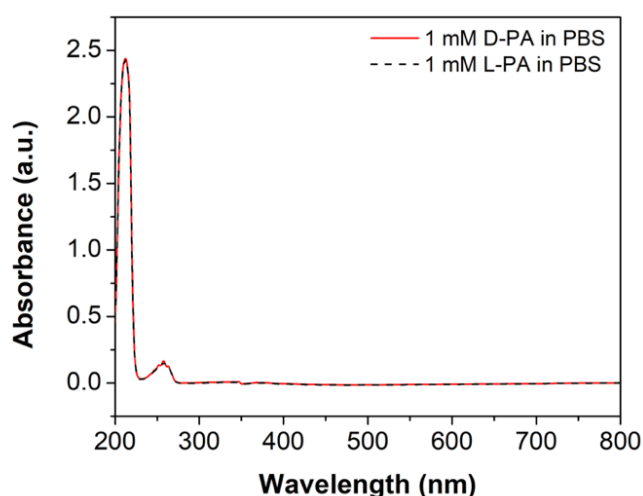


**Figure 5.6** The UV-Vis spectra of the two PA enantiomers. The results were obtained from the 1 mM of PA dissolved in phosphate buffer solution (PBS, pH 7.3).

The electrochemical behavior of PA and  $[\text{Ru}(\text{bpy})_3]^{2+}$  in PBS solution has been first verified with a classic Pt electrode, and DPV-ECL was recorded in a potential range from 0.10 to 1.3 V vs Ag/AgCl. As illustrated in **Figure 5.7**, the DPV signal clearly reveals the oxidation characteristics of PA and  $[\text{Ru}(\text{bpy})_3]^{2+}$  at approximately 0.75 and 1.10 V, respectively.[247-249] In addition, the ECL signal starts to rise around 1.00 V concomitant with the electrooxidation of the Ru complex and reaches maximum intensity at 1.15 V.[247] As expected, there is no enantioselectivity for the PA enantiomers on a classic Pt disk electrode, indicated by enantioselectivity of  $1.0 \pm 0.3$  ( $n=5$ ).

On the other hand, using non-imprinted mesoporous Pt-Ir alloys as working electrodes (**Figure 5.8A**), a huge capacitive current is observed, due to the high active surface area, making it difficult to identify the faradaic currents.

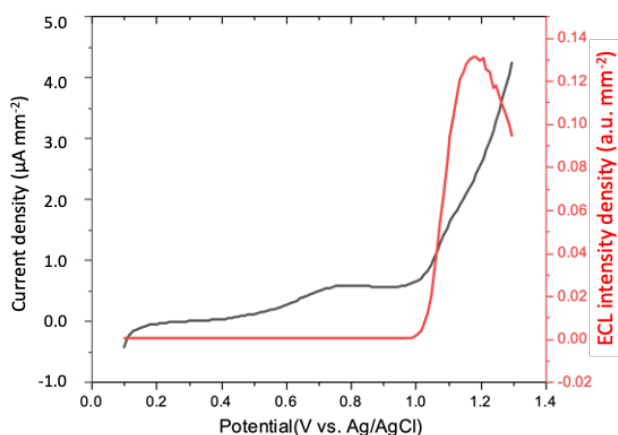


**Figure 5.7** Differential pulse voltammogram (black) and ECL intensity (red) of the analyte solution containing 10 mM (L)-PA and 1 mM  $[\text{Ru}(\text{bpy})_3]^{2+}$  dissolved in 0.1 M PBS solution (pH 7.33), using a classical Pt disk as a working electrode.

However, the ECL signal still appears in the same potential region as previously. It should be noted that the ECL signal strongly increases as a function of PA concentration (**Figure 5.8B**). In order to avoid the huge capacitive currents, DPV-ECL detection was preferentially used for the subsequent experiments. As illustrated in **Figure 5.8C**, the ECL signal has been recorded for solutions with different compositions. When using only pure PBS solution as a supporting electrolyte (black), there are no ECL signals, and only a very weak ECL signal was recorded in the  $[\text{Ru}(\text{bpy})_3]^{2+}$  solution (red). In strong contrast to this, a very pronounced ECL signal is observed (blue) when adding PA to the  $[\text{Ru}(\text{bpy})_3]^{2+}$  solution due to the fact that PA acts as a co-reactant in the  $[\text{Ru}(\text{bpy})_3]^{2+}$  based ECL system, similar to the well-known *tri-n*-propylamine (TPrA)/ $[\text{Ru}(\text{bpy})_3]^{2+}$  system.[247, 248]

Although DPV can be used for studying the enantioselective recognition of chiral compounds,[87, 90] as explained in the previous section, it often suffers from low sensitivity and a less direct readout. The integrated DPV-ECL approach is proposed here as a more direct readout *via* the generated light emission. Freshly (L)-PA imprinted mesoporous Pt-Ir reveals remarkable chiral recognition properties, translated by a significantly higher ECL intensity for the

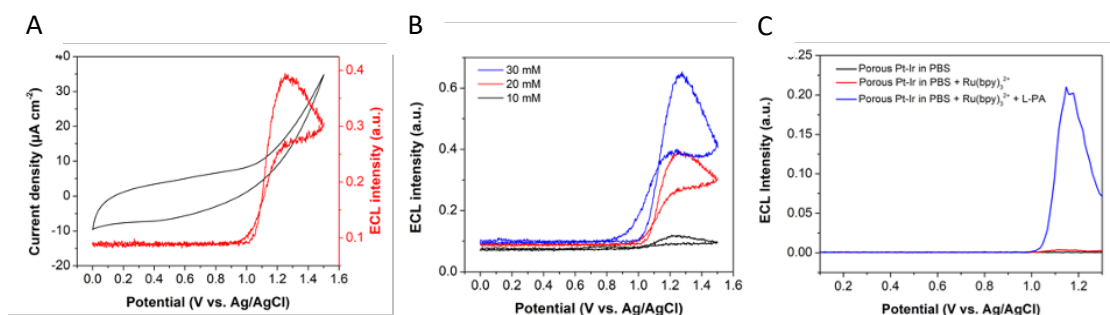


**Figure 5.8** Control experiments showing the characteristics of activated mesoporous Pt-Ir alloys measured in different solutions and using different techniques: A) Cyclic voltammetry, demonstrating a high capacitive current, and the ECL signal using (CV-ECL); B) ECL intensity, illustrating the influence of PA concentration using CV-ECL; the analyte solutions contain (L)-PA concentrations ranging from 10 to 30 mM and 10 mM  $[\text{Ru}(\text{bpy})_3]^{2+}$  dissolved in 0.1 M PBS solution (pH 7.33), with a scan rate of  $100 \text{ mV s}^{-1}$ . C) ECL intensity obtained with various analyte solutions, emphasizing the role of PA as a co-reactant in order to generate an ECL signal using DPV-ECL. The activated mesoporous Pt-Ir alloys were immersed in the solution for 1 h before analysis. DPV-ECL was studied in a solution containing 10 mM (L)-PA and 1 mM  $[\text{Ru}(\text{bpy})_3]^{2+}$  dissolved in 0.1 M PBS solution (pH 7.33). Electrochemical surface regeneration was applied before every experiment.

(L)-PA compared to the other enantiomer (**Figure 5.9A**). A mirror symmetric behavior was obtained for the opposite situation. For (D)-PA imprinted mesoporous Pt-Ir electrodes, a more significant ECL signal of (D)-PA compared to (L)-PA was obtained (**Figure 5.9B**). Even though the fresh Pt-Ir electrodes could discriminate between PA enantiomers, resulting in reasonable enantioselectivity, the sensitivity is limited due to gradual surface passivation by the adsorption of molecules. Therefore, the metal surface was activated and cleaned using chronoamperometry, applying a constant negative potential of  $-0.1 \text{ V}$  for 30 s, in order to remove physisorbed species from the metal surface

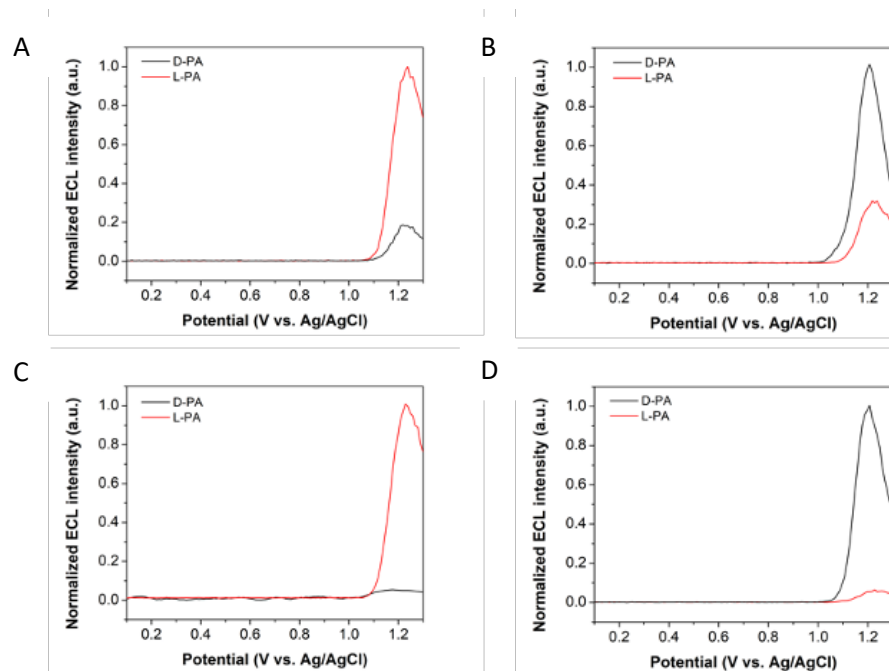
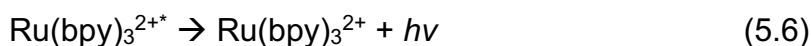
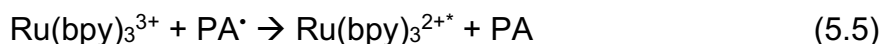


**Figure 5.9** ECL signals for enantiomeric PA discrimination on fresh (upper row) and regenerated (lower row) Pt-Ir alloy electrodes of A), C) (L)-PA, and B), D) (D)-PA imprinted Pt-Ir electrodes. The experiments were conducted in both 10 mM (L)-PA and (D)-PA/1 mM  $[\text{Ru}(\text{bpy})_3]^{2+}$  dissolved in 0.1 M PBS solutions using the DPV-ECL technique.

before ECL analysis.[250] Interestingly, as shown in **Figure 5.9C** and **D**, the discrimination ability is dramatically improved. The enantioselectivity values are reaching over 20.0, which is approximately five times ( $4.9 \pm 1.6$ ) higher than those obtained with the non-activated PA imprinted Pt-Ir electrodes. This enhanced enantioselectivity can be ascribed to the activated and cleaned chiral cavities located inside the mesopores, which tend to enhance the concentration of oxidized PA species, generated from the proper PA configuration. This induces a higher probability for the bimolecular reaction between oxidized PA species and the activated  $[\text{Ru}(\text{bpy})_3]^{2+}$  to occur, and thus generate a stronger ECL signal for the encoded enantiomer (**Scheme 5.2**).[87, 88, 229, 247] The present study relies on an ECL pathway that is similar to the well-known  $[\text{Ru}(\text{bpy})_3]^{2+}/\text{TPrA}$  system.[247] The reaction mechanism can be divided into

several steps, including (i) and (ii) the direct oxidation of PA (5.2 and 5.3) and  $[\text{Ru}(\text{bpy})_3]^{2+}$  at the Pt-Ir surface (5.4), respectively, (iii) the reduction of  $[\text{Ru}(\text{bpy})_3]^{3+}$  by the  $\text{PA}^\bullet$  radical species, generating the excited state (5.5) needed for light emission (5.6). The very high enantioselectivity value of up to 20.0 can overcome some limitations of chiral recognition when using classic electrochemical analysis, for which only maximum enantioselectivity of approximately 13.0 could be achieved, as reported in the previous section.



**Scheme 5.2** Proposed mechanism of the ECL generation in this study based on the  $\text{PA}/[\text{Ru}(\text{bpy})_3]^{2+}$  system.

As rather high positive potentials are required to activate both, co-reactant and luminophores in ECL experiments, this might lead to gradual passivation of chiral metal surfaces due to metal oxidation. Hence, the reusability of the chiral imprinted Pt-Ir alloy for several cycles of enantioselective discrimination *via* the ECL strategy was investigated. As illustrated in **Figure 5.10A-E**, the (D)-PA imprinted Pt-Ir electrode reveals enantiomeric discrimination ability and can be reused for up to four cycles, but with the expected gradual decrease of the enantioselectivity values summarized in **Figure 5.10F**, from 18.0 (1<sup>st</sup> cycle) to 10.0 (2<sup>nd</sup> cycle), 3.8 (3<sup>rd</sup> cycle), and 2.0 (4<sup>th</sup> cycle). After the fifth cycle, the chiral electrode completely lost its chiral feature ( $0.8 \pm 0.25$ ). Although the surface regeneration by chronoamperometry at a cathodic potential can regenerate the clean active metal surface, prolonged

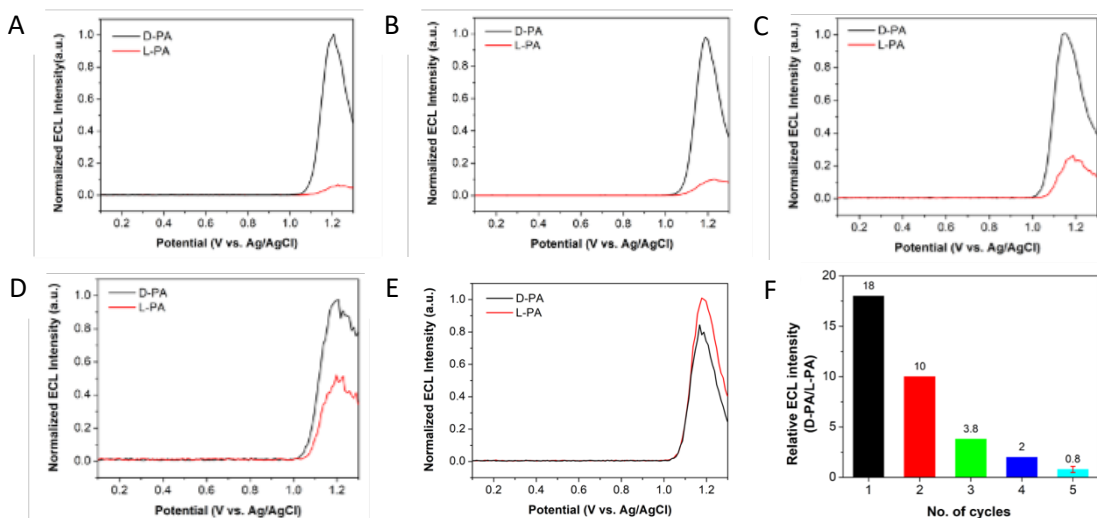


**Figure 5.10** Reusability test of (D)-PA imprinted mesoporous Pt-Ir for the discrimination of PA enantiomers by ECL analysis, performed with the (L)-PA (red) or (D)-PA (black) /  $[\text{Ru}(\text{bpy})_3]^{2+}$  system: A-E) Normalized ECL intensities for five consecutive detection experiments; F) Histogram summarizing the relationship between the enantioselectivity of (D)-PA with respect to (L)-PA as a function of the detection cycle. The experiment was conducted in 10 mM PA dissolved in a 1mM  $[\text{Ru}(\text{bpy})_3]^{2+}$  solution. After each analysis, the Pt-Ir electrode was rinsed and cleaned in MilliQ water for six hours. Surface regeneration by chronoamperometry at -0.1 V for 30 s was applied before each analysis. The same Pt-Ir electrode was used in all experiments.

use leads to the presence of an oxide layer and thus a deactivation of the selective electrooxidation of PA, translated by a decrease of the absolute value of ECL intensity by 0.4 a.u.[251, 252]

These findings are somewhat in contrast with the stability reported in the previous section, where the electrodes kept a chiral character even at high positive potentials for up to 30 detection cycles. However, these experiments were performed in hydrochloric acid solution (HCl, pH at 1.3). The halide species may prevent the growth of metal oxide, resulting in a conservation of high electrooxidation currents of the reactants.[253] In contrast,

the ECL analysis in the present case was carried out in a neutral phosphate buffer solution (PBS, pH at 7.3), and therefore the surface passivation can be more pronounced, leading to faster degradation of the enantiomeric discrimination efficiency.

## 5.4 Conclusion

Chiral-imprinted mesoporous Pt-Ir was successfully applied as a working electrode for chiral analysis using both classic electrochemistry and an approach based on electrochemiluminescence. DPV clearly demonstrates the existence of chiral information on the Pt-Ir alloy surfaces even after the removal of chiral templates. Most importantly, the chiral Pt-Ir retains its chiral features even after several enantiomeric detection cycles and after excursions to highly positive potentials. Such outstanding performance is a very significant improvement with respect to what was observed with chiral monometallic materials. In order to further enlarge the range of detection schemes, the material was also employed as a substrate for ECL analysis. In this case, the model amino acid phenylalanine ensures simultaneously the role of an analyte and of a co-reactant for the selective emission of ECL signals, depending on the configuration of the chiral recognition site imprinted in the metal structure. Most importantly, the results indicate that, whether fresh or activated, the Pt-Ir electrodes can be used for the first example of chiral ECL detection with a significantly improved enantioselectivity factor of up to 20. These results open up novel and promising perspectives for developing the molecularly encoded Pt-Ir alloy with chiral discrimination features, which can be extended in the future not only to other amino acids but also to a variety of chiral molecules with more or less complex structures.

## Chapter 6

### Conclusions and perspectives

In summary, this thesis is devoted to the design, development and improvement of the performance of chiral-imprinted mesoporous metals, using two main strategies, i.e., molecular grafting of thiol molecules on their surfaces and replacing monometallic structures with metal alloys. The elaborated materials have been studied in the frame of several scientific challenges such as (i) to use of the thiol-modified monometallic chiral Pt for stereoselective electrosynthesis, (ii) the nano-engineering of chiral Pt-Ir alloys, (iii) enantioselective electrosynthesis and asymmetric heterogeneous hydrogenation with the help of chiral Pt-Ir alloy surfaces; (iv) advanced chiral discrimination of enantiomers *via* electrochemical and electrochemiluminescence approaches.

In order to enhance the selectivity of the formation of chiral products, during the enantioselective electrosynthesis with chiral monometallic electrodes, chiral-imprinted mesoporous Pt electrodes were modified with a self-assembled monolayer of thiol ligands. In this case, the thiol layer grafted on the non-selective Pt surface, mainly located at the outermost parts, could diminish the production of the racemate, typically occurring at the outermost electrode surface. This strategy eventually allows for achieving a very high enantiomeric excess above 90%, combined with a short global reaction time. These findings could be potentially used in practical applications, as a complementary strategy to classic asymmetric chemical synthesis. However, there are still some challenging aspects that need to be further developed. For example, a novel design of the electrochemical cell should be investigated to avoid crosstalk between cathode and anode, without slowing the rate of reaction to prevent the backward reaction. This should lead to an enhanced production rate of chiral

molecules. Another crucial point is the reusability of the electrodes. Even though a renewal of the thiol layer has been proposed, tested, and shown to maintain the product selectivity in consecutive catalytic runs, this strategy could be repeated only a few times, and therefore there is still room for improvement. An alternative to protect the unselective surface with thiols could be, for example, a grafting of diazonium-based layers as they might show better stability at the negative potentials that have to be applied for the electro-organic reduction.

Another limitation concerning stability is the degradation of the metal structure itself. As mentioned earlier, chiral-encoded mesoporous monometallic Pt has only a limited lifetime, even though it is a noble metal. We therefore have explored the possibility of using chiral-imprinted mesoporous metal alloys instead of pure metal. It is well-known that alloying metals can improve the hardness of the bulk metal structure by decreasing atomic movement due to the presence of a promoter. In the present study, Ir was alloyed with Pt. The chiral Pt-Ir alloy could be simply synthesized by co-electrodeposition from dissolved metal precursors in the simultaneous presence of a lyotropic liquid crystal together with the chiral templates. The plating gel was efficiently used to elaborate chiral-imprinted mesoporous Pt-Ir films on 2D gold-coated glass slides and also on 3D Ni foam as supports. The resulting materials reveal a smooth outermost surface, as well as a dense and homogeneous Pt-Ir layer with mesopores having a hexagonal order with an Ir content of 10 at%. The chiral information inside the mesopores could be perfectly retained even after removing the chiral templates. This feature could be directly characterized by the secondary harmonic generation (SHG) spectroscopy, leading to an opposite signal for the two different chiral configurations of the Pt-Ir alloy films imprinted with opposite enantiomers. However, several parameters of the SHG characterization must be further optimized. One problem is, for example, that the light beam which hits the surface is generating local heat, which can lead to a reorganization of the surface atoms, and thus a loss of the chiral information. It would also be quite important to study the SHG signal as a function of the thickness of the Pt-Ir films and the amount of chiral imprinted sites.

The improved features of the chiral-encoded mesoporous Pt-Ir alloys allow the material to be further applied as both electrocatalyst and heterogeneous catalyst for enantioselective electrosynthesis and conventional asymmetric synthesis, respectively. Due to this better structural and electrochemical stability, the enantioselectivity of up to 90 % could be reached, even after several electrocatalytic cycles. Apart from enantioselective electrosynthesis, the chiral mesoporous metals could also be used for the selective production of chiral molecules *via* simple hydrogenation. In this case, chiral Pt-Ir films were deposited on 3D Ni foam as support in order to further enhance the overall active surface area. The highly porous Pt-Ir films were employed as a heterogeneous catalyst for a selective chiral synthesis *via* hydrogenation in an aqueous solution. It was possible to achieve an enantiomeric excess of up to 85 % even after many consecutive catalytic cycles. In the future, more information is still required to understand the impact of the alloying on the stability of chiral features, especially at the atomic level. For example, how the surface composition affects the strength of ion adsorption at specific sites could be studied more closely in order to come up with a mechanistic explanation of electroreduction reactions. In the case of asymmetric hydrogenation, the design of a novel flow-through reactor would be very beneficial in enhancing the production rate of chiral synthesis.

Apart from asymmetric synthesis, discrimination of enantiomers on the chiral mesoporous metals has also been examined. In this case, the chiral-imprinted mesoporous Pt-Ir was employed as a working electrode in combination with electroanalytical techniques, both classic ones, such as cyclic voltammetry and differential pulse voltammetry, as well as electrochemiluminescence. The chiral-encoded Pt-Ir electrode revealed an excellent ability to discriminate between DOPA enantiomers using the DPV technique. It also showed exceptional electrochemical stability, even after several detection cycles. The chiral information of the Pt-Ir film could withstand even very high oxidation potentials of up to 1.8 V vs Ag/AgCl, which has not been possible with the previously reported monometallic analogs. Therefore, it was possible to employ the chiral metal alloy in order to explore an alternative

readout approach based on electrochemiluminescence, which generally requires a high anodic potential. The studied amino acid, phenylalanine (PA), is acting in this case as a model analyte and also as a co-reactant when combined with the luminophore  $[\text{Ru}(\text{bpy})_3]^{2+}$ . The selected PA enantiomer was electrochemically oxidized on the metal surface and reacted with the oxidized  $[\text{Ru}(\text{bpy})_3]^{3+}$ , eventually yielding a very pronounced ECL signal. Under optimized conditions, the luminescence has up to 20 times higher amplitude for the imprinted enantiomer, compared to its stereochemical counterpart. Such well-pronounced discrimination has not been achieved with traditional electrochemical techniques. These findings open up perspectives for developing real chiral ECL sensors with high selectivity and sensitivity. Further studies should be directed towards an improvement of the stability of the light emission and try to expand the detection to other chiral compounds, especially those belonging to the family of amino acids, as they all have by definition an amino group, which is essential for the reaction mechanism.

All in all, this thesis has allowed us to make an important step forward with respect to the design and development of novel materials based on chiral-imprinted mesoporous metals by following several strategies, i.e., molecular grafting and alloying of metal, with many potential applications ranging from asymmetric synthesis to chiral recognition. The use of these sophisticated structures could be further expanded in the near future. For example, combining the chiral metal alloys with a semiconductor, forming a hetero-junction, could eventually allow enantiomeric discrimination based on photo-electrochemistry and even lead to the development of enantioselective photoelectrochemical synthesis. Recently, chiral features related to the chiral-induced spin selectivity effect (CISS) have been shown to have a significant impact on some extremely important reactions, such as the oxygen evolution reaction (OER) and water splitting.[254-256] Hence, an interesting route for future studies could be to test whether the developed chiral metals could equally promote this type of reaction, which are important for many current hot topics of research, such as the development of new generations of metal-air flow batteries or fuel cells, and in a more general sense the field of hydrogen technology.

# Synthèse hautement énantiosélective de molécules chirales sur des électrodes métalliques mésoporeuses modifiées

## Résumé

Sopon BUTCHA

La chiralité est une caractéristique très importante, car elle joue un rôle clé dans divers domaines de notre vie quotidienne, allant de la biologie à la chimie et à la physique, avec des applications spécifiques allant de la science des matériaux et des surfaces à la chimie analytique et à la pharmacie. Dans le contexte de ces deux derniers sujets, la reconnaissance spécifique de la chiralité est cruciale, soit pour développer des capteurs et des concepts de séparation énantiosélectifs, soit pour concevoir des systèmes catalytiques permettant la synthèse hautement stéréosélective de molécules chirales.

Bien que la synthèse asymétrique de composés chiraux ait été considérée comme l'une des stratégies les plus prometteuses pour produire des composés énantiomériquement purs (EPC), elle souffre encore de quelques inconvénients, tels qu'un contrôle imparfait de la stéréochimie ou une récupération difficile du catalyseur après la réaction. Ainsi, il existe toujours un fort besoin de développer des systèmes catalytiques alternatifs présentant de bonnes performances globales. Dans cette thèse, des métaux mésoporeux encodés avec des informations chirales sont proposés comme matériaux présentant d'excellentes performances en tant qu'(électro)catalyseurs hétérogènes en termes d'excès énantiomérique, de rendement et de stabilité structurelle et électrochimique. Bien que des métaux monométalliques mésoporeux imprimés avec une information chirale aient déjà été élaborés et testés comme catalyseurs pour la synthèse asymétrique de composés chiraux,

ils souffrent de temps de réaction plutôt longs et de l'interférence de réactions non spécifiques sur certaines parties de leur surface, conduisant finalement à un faible excès énantiomérique.

Afin de contourner ces inconvénients, le premier chapitre de cette thèse présente une stratégie alternative pour fonctionnaliser la surface externe d'électrodes de platine (Pt) mésoporeuses chirales avec des ligands organosoufrés. Cette modification vise à diminuer le degré de réactions indésirables à l'interface externe de l'électrode. Les résultats ont révélé que l'enrobage d'une électrode de Pt avec un ligand thiol pouvait considérablement augmenter l'excès énantiomérique de la molécule désirée au-delà de 90%. Plus important encore, nous avons pu surmonter de cette manière la limitation des travaux précédents qui utilisaient une approche d'électrosynthèse pulsée nécessitant des temps de réaction de plusieurs jours. Le nouveau concept de protection permet d'atteindre un excès énantiomérique élevé, même avec une électrosynthèse en régime statique, en quelques heures. Néanmoins, la stabilité structurelle et électrochimique quelque peu limitée du Pt monométallique chiral entraîne une diminution de son activité lorsqu'il est utilisé pour plusieurs cycles électrocatalytiques.

Pour surmonter cette limitation, une nouvelle stratégie d'impression de propriétés chirales dans des alliages métalliques mésoporeux a également été étudiée. Dans les chapitres 2 et 3, un métal promoteur, l'iridium (Ir), a été associé au Pt pour générer un alliage platine-iridium (Pt-Ir). L'alliage métallique mésoporeux à empreinte chirale a été synthétisé par co-électrodéposition à partir de précurseurs métalliques en présence simultanée de cristaux liquides lyotropes formant une phase hexagonale incluant les molécules chirales. En ajustant les conditions expérimentales telles que les potentiels déposés et densités de courant, l'alliage a présenté une surface externe relativement lisse, une couche homogène et dense, et une porosité élevée avec un arrangement hexagonal bien ordonné de mésopores. La formation de la structure de l'alliage a été confirmée par spectroscopie photoélectronique à rayons X (XPS), révélant une composition élémentaire 90:10 at% de Pt et Ir. De plus, deux types de matériaux, des lames de verre recouvertes d'or en deux dimensions (2-D) et

des mousses de Ni poreuses en trois dimensions (3-D), ont été utilisés comme substrat pour le dépôt des alliages mésoporeux chiraux de Pt-Ir. Notamment, en raison de la stabilité structurelle accrue de l'alliage Pt-Ir chiral préparé, la génération de signaux optiques d'harmoniques secondaires (SHG) a montré des preuves indépendantes de la présence d'informations chirales par une réponse SHG significativement différente entre une lumière circulairement polarisée à gauche et à droite.

Le matériau conçu a ensuite été appliqué à la fois comme catalyseur hétérogène et comme électrocatalyseur pour la catalyse asymétrique via l'hydrogénation et l'électroréduction respectivement. Dans le cas de l'électrosynthèse, une énantiosélectivité de presque 100% a pu être atteinte. De plus, les électrodes ont montré une stabilité électrochimique exceptionnelle en préservant un excès énantiomérique allant jusqu'à 90%, même après plusieurs cycles catalytiques, ce qui n'a pas pu être obtenu avec le Pt monométallique mésoporeux chiral rapporté précédemment. L'alliage Pt-Ir chiral nanostructuré a ensuite été utilisé comme catalyseur hétérogène pour l'hydrogénation asymétrique de cétones aromatiques simples. Dans ce cas, les films Pt-Ir chiraux ont été déposés sur une mousse de nickel à haute surface, afin d'améliorer l'accessibilité des sites imprimés par les précurseurs moléculaires. Un effet synergique entre la porosité élevée de la mousse de nickel, le métal mésoporeux et les caractéristiques chirales a permis de concevoir des matériaux hybrides avec des caractéristiques prometteuses pour la catalyse asymétrique. Dans des conditions expérimentales optimisées, en particulier lorsqu'elles sont combinées avec une approche d'hydrogénation pulsée, un degré très élevé d'énantiosélectivité allant jusqu'à 85% a été obtenu, même après plusieurs cycles catalytiques successifs. Même si les taux de production (en termes de rendement et de conversion) obtenus à partir de l'électrosynthèse et de la synthèse asymétrique hétérogène sont très modestes et doivent encore être optimisés, une amélioration remarquable par rapport à d'autres travaux récents a été obtenue en termes d'excès énantiomérique (%ee) qui est généralement supérieur à 80 %.

Outre la synthèse asymétrique de composés chiraux, la discrimination énantiomérique est également un sujet essentiel en ce qui concerne d'autres applications potentielles, notamment dans les sciences analytiques. Par conséquent, les alliages mésoporeux de Pt-Ir chiral ont également été utilisés comme substrats pour la discrimination chirale. Il est intéressant de noter que les films d'alliage ont présenté une performance significativement améliorée en termes de reconnaissance énantiosélective de molécules chirales, par rapport au Pt monométallique chiral. Avec une technique électrochimique classique, la voltampérométrie différentielle à impulsions (DPV), une capacité remarquable de discrimination énantiosélective des deux énantiomères de la 3,4-dihydroxyphénylalanine (DOPA) avec des valeurs de sélectivité autour de 14,0 a pu être obtenue, par rapport à une valeur de 1,5 pour les surfaces de Pt monométalliques. En outre, la stabilité électrochimique des alliages Pt-Ir chiraux s'améliore considérablement, ce qui a été confirmé par l'oxydation des électrodes en alliage Pt-Ir à des potentiels positifs relativement élevés pendant de nombreux cycles, puis par la réutilisation des électrodes comme substrat pour la discrimination chirale. Une stabilité électrochimique exceptionnelle de l'alliage chiral Pt-Ir a été observée même en exposant les électrodes à des potentiels positifs élevés pendant 40 cycles. En comparaison, les caractéristiques chirales des surfaces de Pt pur ont été entièrement effacées même après moins de 10 cycles d'oxydation.

Toutes ces observations nous ont motivés à utiliser ces alliages mésoporeux Pt-Ir chiraux pour d'autres stratégies possibles d'analyse chirale. Dans ce travail, la surface de l'alliage a été testée comme matériau d'électrode pour la discrimination énantiomérique par électrochimieluminescence (ECL). La phénylalanine (PA), qui se présente sous forme de L-PA et de D-PA, a été étudiée comme un acide aminé modèle qui peut servir simultanément d'analyte cible et de coréactif, avec le luminophore  $[Ru(bpy)_3]^{2+}$ , pour générer des signaux ECL d'amplitude différente, en fonction de la stéréochimie des énantiomères. Les résultats ont démontré que des signaux de luminescence 20 fois plus élevés étaient obtenus pour le bon énantiomère par rapport à son antipode.

En résumé, cette thèse souligne que la conception de ces surfaces d'électrodes chirales ouvre des perspectives fascinantes dans le cadre global des technologies chirales, allant de la catalyse asymétrique utilisant des voies électrochimiques et chimiques à une discrimination énantiomérique efficace utilisant à la fois des méthodes électrochimiques traditionnelles et des stratégies d'analyse opto-électrochimiques.

Mots clés : Empreinte chirale, Métaux mésoporeux, Synthèse asymétrique, Discrimination énantiomérique

# Highly enantioselective synthesis of chiral molecules at modified mesoporous metal electrodes

## Summary

Sopon BUTCHA

Chirality is an essential feature because it plays a key role in various areas of our daily life, ranging from biology to chemistry and physics, with specific applications going from materials and surface science to analytical chemistry and pharmaceuticals. In the context of the latter two topics, specific chiral recognition is crucial, either to develop enantioselective sensors and separation concepts or to design catalytic systems that allow the highly stereoselective synthesis of chiral molecules.

Although the asymmetric synthesis of chiral compounds has been considered as one of the most promising strategies for producing enantiomerically pure compounds (EPC), it still suffers from a couple of drawbacks, such as an imperfect control of the stereochemistry or a complicated recovery of the catalyst after the reaction. Thus, there is still a strong need to develop alternative catalytic systems with good overall performance. In this thesis, mesoporous metals encoded with chiral information are proposed as materials showing excellent performances as heterogeneous (electro)catalysts in terms of enantiomeric excess, yield, and structural as well as electrochemical stability. Although chiral-imprinted mesoporous monometallic metals have been previously elaborated and tested as catalysts for the asymmetric synthesis of chiral compounds, they suffer from rather long reaction times and the interference of unspecific reactions at parts of their surface, eventually leading to low enantioselective excess.

In order to circumvent these drawbacks, the first chapter of this thesis presents an alternative strategy to functionalize the non-selective part of the

surface of chiral-imprinted mesoporous platinum (Pt) electrodes with organosulfur ligands. This modification aims to diminish the degree of undesired reactions at the non-selective interface of the electrode. The results revealed that coating a Pt electrode with a thiol ligand could dramatically enhance the enantiomeric excess of the desired enantiomer above 90%. Most importantly, we could overcome in this way the limitation of the previous work that was using a pulsed electrosynthesis approach requiring reaction times of several days. The new protection concept allows achieving high enantiomeric excess, even with steady-state electrosynthesis, in a few hours. Nevertheless, the somewhat limited structural and electrochemical stability of chiral-encoded monometallic Pt results in a decrease in its activity when using it for several electrocatalytic cycles.

To overcome this limitation, a novel strategy to encode chiral features on mesoporous metal alloys was also studied. In chapters 2 and 3, a promoter metal, iridium (Ir), has been combined with Pt to generate a platinum-iridium (Pt-Ir) alloy. The chiral-imprinted mesoporous metal alloy has been synthesized by co-electrodeposition from metal precursors in the simultaneous presence of lyotropic liquid crystals forming a hexagonal phase together with the chiral templates. By fine-tuning the experimental conditions such as deposited potentials and current densities, the alloy exhibited a relatively smooth external surface, a homogeneous and dense layer, and a high porosity with a well-ordered hexagonal arrangement of mesopores. The formation of the alloy structure has been confirmed by x-ray photoelectron spectroscopy (XPS), revealing an elemental composition of 90:10 at% of Pt and Ir. Moreover, two types of materials, two-dimensional (2-D) gold-coated glass slides and three-dimensional (3-D) porous Ni foams, have been employed as substrates for the deposition of the chiral mesoporous Pt-Ir alloys. Notably, owing to the enhanced structural stability of the prepared chiral Pt-Ir alloy, Secondary Harmonic Generation (SHG) showed independent evidence for the presence of chiral information by a significantly different SHG response with left- and right-hand circular polarized light.

The designed material was further applied as both an electrocatalyst and a heterogeneous for asymmetric catalysis *via* electroreduction and hydrogenation, respectively. In the case of electrosynthesis, the enantioselectivity of almost 100% could be reached. Furthermore, the electrodes showed exceptionally electrochemical stability by preserving an enantiomeric excess of up to 90%, even after several catalytic cycles, which was not possible to achieve with the chiral mesoporous monometallic Pt reported previously. The nanostructured chiral encoded Pt-Ir alloy was further used as a heterogeneous catalyst for the asymmetric hydrogenation of simple aromatic ketones. In this case, the chiral Pt-Ir films were deposited on a high surface area of nickel foam, to improve the accessibility of the imprinted sites by guest molecules. A synergistic effect between the high porosity of the Ni-foam, the mesoporous metal, and the chiral features allowed the designing of hybrid materials with promising features for asymmetrical catalysis. Under fine-tuned experimental conditions, particularly when combined with a pulsed hydrogenation approach, a very high degree of enantioselectivity of up to 85% has been obtained, even after several successive catalytic cycles. Even though the production rate (in terms of %yield) obtained from both electrosynthesis and heterogeneous asymmetric synthesis were very modest and still need to be further optimized, a remarkable improvement with respect to other recent work was achieved in terms of enantiomeric excess (%ee) which is generally higher than 80%.

Apart from the asymmetric synthesis of chiral compounds, enantiomeric discrimination is also a vital topic with respect to other potential applications, especially in analytical sciences. Therefore, the developed chiral-encoded mesoporous Pt-Ir alloys were also employed as substrates for chiral discrimination. Interestingly, the alloy films exhibited a significantly improved performance in terms of enantioselective recognition of chiral molecules compared to the chiral encoded monometallic Pt. Initially, with a classic electrochemical technique, i.e., the differential pulse voltammetry (DPV), a remarkable ability to enantioselective discrimination of the two 3,4-dihydroxyphenylalanine (DOPA) enantiomers with selectivity values around

14.0 could be obtained, compared to a value of 1.5 for monometallic Pt surfaces. Furthermore, the electrochemical stability of the chiral Pt-Ir alloys dramatically improves, confirmed by oxidizing the Pt-Ir alloy electrodes at relatively high positive potentials for many cycles and then using the electrodes again as a substrate for chiral discrimination. The outstanding electrochemical stability of the chiral Pt-Ir alloy was observed even when exposing them to high positive potentials for 40 cycles. In comparison, the chiral features of pure Pt surfaces were entirely erased even after less than 10 oxidation cycles.

All these observations have motivated us to use such chiral mesoporous Pt-Ir alloys for other possible chiral readout strategies. Herein, the alloy surface was tested as an electrode material for enantiomeric discrimination using electrochemiluminescence (ECL). Phenylalanine (PA), presenting in L-PA and D-PA forms, has been studied as a model amino acid that can simultaneously serve as a target analyte and as a co-reactant, together with the luminophore,  $[\text{Ru}(\text{bpy})_3]^{2+}$ , for generating ECL signals of different amplitude, depending on the stereochemistry of the enantiomers. The results demonstrated that 20-fold higher luminescence signals were obtained for the proper enantiomer compared to its antipode.

In summary, this thesis emphasizes that the advanced design of these chiral electrode surfaces opens up fascinating perspectives in the global frame of chiral technologies, ranging from asymmetric catalysis using electrochemical and chemical routes to efficient enantio-discrimination using both traditional electrochemical methods and opto-electrochemical readout strategies.

Keywords: Chiral imprinting, mesoporous metals, asymmetric synthesis, enantiomeric discrimination

## References

1. Malgras V, Ataee-Esfahani H, Wang H, Jiang B, Li C, Wu KCW, et al. Nanoarchitectures for mesoporous metals. **Advanced Materials**. 2016;28(6):993-1010.
2. McCusker L, Liebau F, Engelhardt G. Nomenclature of structural and compositional characteristics of ordered microporous and mesoporous materials with inorganic hosts (IUPAC Recommendations 2001). **Pure and Applied Chemistry**. 2001;73(2):381-94.
3. Zdravkov B, Čermák J, Šefara M, Janků J. Pore classification in the characterization of porous materials: A perspective. **Open Chemistry**. 2007;5(2):385-95.
4. Simon P, Gogotsi Y. **Materials for electrochemical capacitors**. Nanoscience and technology: a collection of reviews from Nature journals: World Scientific; 2010. p. 320-9.
5. Chang F, Zhou J, Chen P, Chen Y, Jia H, Saad SM, et al. Microporous and mesoporous materials for gas storage and separation: a review. **Asia-Pacific Journal of Chemical Engineering**. 2013;8(4):618-26.
6. Wright PA. Microporous framework solids. 2007.
7. Kresge aC, Leonowicz M, Roth WJ, Vartuli J, Beck J. Ordered mesoporous molecular sieves synthesized by a liquid-crystal template mechanism. **Nature**. 1992;359(6397):710-2.
8. Beck JS, Vartuli JC, Roth WJ, Leonowicz ME, Kresge C, Schmitt K, et al. A new family of mesoporous molecular sieves prepared with liquid crystal templates. **Journal of the American Chemical Society**. 1992;114(27):10834-43.
9. Wu S-H, Mou C-Y, Lin H-P. Synthesis of mesoporous silica nanoparticles. **Chemical Society Reviews**. 2013;42(9):3862-75.
10. Liang J, Liang Z, Zou R, Zhao Y. Heterogeneous catalysis in zeolites, mesoporous silica, and metal-organic frameworks. **Advanced Materials**. 2017;29(30):1701139.

11. Da'na E. Adsorption of heavy metals on functionalized-mesoporous silica: A review. **Microporous and Mesoporous Materials**. 2017;247:145-57.
12. Chew T-L, Ahmad AL, Bhatia S. Ordered mesoporous silica (OMS) as an adsorbent and membrane for separation of carbon dioxide (CO<sub>2</sub>). **Advances in colloid and interface science**. 2010;153(1-2):43-57.
13. Knežević NŽ, Durand J-O. Large pore mesoporous silica nanomaterials for application in delivery of biomolecules. **Nanoscale**. 2015;7(6):2199-209.
14. Gou K, Wang Y, Xie L, Guo X, Guo Y, Ke J, et al. Synthesis, structural properties, biosafety and applications of chiral mesoporous silica nanostructures. **Chemical Engineering Journal**. 2021;421:127862.
15. Lashgari N, Badiei A, Mohammadi Ziarani G. Modification of mesoporous silica SBA-15 with different organic molecules to gain chemical sensors: a review. **Nanochemistry Research**. 2016;1(1):127-41.
16. Rao H, Wang X, Du X, Xue Z. Mini review: Electroanalytical sensors of mesoporous silica materials. **Analytical Letters**. 2013;46(18):2789-812.
17. Laskowski Ł, Laskowska M, Vila N, Schabikowski M, Walcarius A. Mesoporous silica-based materials for electronics-oriented applications. **Molecules**. 2019;24(13):2395.
18. Gao M, Zeng J, Liang K, Zhao D, Kong B. Interfacial assembly of mesoporous silica-based optical heterostructures for sensing applications. **Advanced Functional Materials**. 2020;30(9):1906950.
19. Yeung KL, Han W. Zeolites and mesoporous materials in fuel cell applications. **Catalysis Today**. 2014;236:182-205.
20. Ying Y, Kamarudin S, Masdar M. Silica-related membranes in fuel cell applications: An overview. **International Journal of Hydrogen Energy**. 2018;43(33):16068-84.
21. Liang C, Li Z, Dai S. Mesoporous carbon materials: synthesis and modification. **Angewandte Chemie International Edition**. 2008;47(20):3696-717.

22. Yamauchi Y, Kuroda K. Rational design of mesoporous metals and related nanomaterials by a soft-template approach. **Chemistry–An Asian Journal**. 2008;3(4):664-76.
23. Ren Y, Ma Z, Bruce PG. Ordered mesoporous metal oxides: synthesis and applications. **Chemical Society Reviews**. 2012;41(14):4909-27.
24. Wei L, Hu N, Zhang Y. Synthesis of polymer–mesoporous silica nanocomposites. **Materials**. 2010;3(7):4066-79.
25. Shi J-l, Zhang L-x. Nanocomposites from ordered mesoporous materials. **Journal of Materials Chemistry**. 2004;14(5):795-806.
26. Yan Y, Chen G, She P, Zhong G, Yan W, Guan BY, et al. Mesoporous nanoarchitectures for electrochemical energy conversion and storage. **Advanced Materials**. 2020;32(44):2004654.
27. Walcarius A. Mesoporous materials and electrochemistry. **Chemical Society Reviews**. 2013;42(9):4098-140.
28. Zhu G, Zhao Y, Su L, Qiu P, Luo W. Recent advances on the synthesis of mesoporous metals for electrocatalytic methanol oxidation. **Emergent Materials**. 2020;3(3):291-306.
29. Ismail AA, Bahnemann DW. Mesoporous titania photocatalysts: preparation, characterization and reaction mechanisms. **Journal of Materials Chemistry**. 2011;21(32):11686-707.
30. Liu Y, Ma H, Han XX, Zhao B. Metal–semiconductor heterostructures for surface-enhanced Raman scattering: synergistic contribution of plasmons and charge transfer. **Materials Horizons**. 2021;8(2):370-82.
31. Yang X, Qiu P, Yang J, Fan Y, Wang L, Jiang W, et al. Mesoporous materials–based electrochemical biosensors from enzymatic to nonenzymatic. **Small**. 2021;17(9):1904022.
32. Malgras V, Ji Q, Kamachi Y, Mori T, Shieh F-K, Wu KC-W, et al. Templated synthesis for nanoarchitected porous materials. **Bulletin of the Chemical Society of Japan**. 2015;88(9):1171-200.
33. Attard GS, Bartlett PN, Coleman NR, Elliott JM, Owen JR. Lyotropic liquid crystalline properties of nonionic surfactant/H<sub>2</sub>O/hexachloroplatinic acid

- ternary mixtures used for the production of nanostructured platinum. **Langmuir**. 1998;14(26):7340-2.
34. Haji Modh Yasin H. **Controlled electrodeposition of metal nanocentres for catalysis**: University of Southampton; 2010.
  35. Bartlett PN. Electrodeposition of nanostructured films using self-organizing templates. **The Electrochemical Society Interface**. 2004;13(4):28.
  36. Liang Y-C, Juan Y-W, Lu K-T, Jeng U-S, Chen S-A, Chuang W-T, et al. Formation process of mesostructured PtRu nanoparticles electrodeposited on a microemulsion lyotropic liquid crystalline template as revealed by *in-situ* XRD, SAXS, and XANES. **The Journal of Physical Chemistry C**. 2012;116(50):26649-55.
  37. Yamauchi Y, Momma T, Fuziwara M, Nair SS, Ohsuna T, Terasaki O, et al. Unique microstructure of mesoporous Pt (H<sub>1</sub>-Pt) prepared via direct physical casting in lyotropic liquid crystalline media. **Chemistry of materials**. 2005;17(25):6342-8.
  38. Attard GS, Bartlett PN, Coleman NR, Elliott JM, Owen JR, Wang JH. Mesoporous platinum films from lyotropic liquid crystalline phases. **Science**. 1997;278(5339):838-40.
  39. Bartlett P, Gollas B, Guerin S, Marwan J. The preparation and characterisation of H<sub>1</sub>-e palladium films with a regular hexagonal nanostructure formed by electrochemical deposition from lyotropic liquid crystalline phases. **Physical Chemistry Chemical Physics**. 2002;4(15):3835-42.
  40. Makino S, Yamauchi Y, Sugimoto W. Synthesis of electro-deposited ordered mesoporous RuO<sub>x</sub> using lyotropic liquid crystal and application toward micro-supercapacitors. **Journal of power sources**. 2013;227:153-60.
  41. Jiang B, Li C, Dag Ö, Abe H, Takei T, Imai T, et al. Mesoporous metallic rhodium nanoparticles. **Nature communications**. 2017;8(1):15581.
  42. Bartlett PN, Marwan J. Preparation and characterization of H<sub>1</sub>-e rhodium films. **Microporous and Mesoporous Materials**. 2003;62(1-2):73-9.

43. Elliott JM, Attard GS, Bartlett PN, Coleman NR, Merckel DA, Owen JR. Nanostructured platinum (H<sub>1</sub>-ePt) films: effects of electrodeposition conditions on film properties. **Chemistry of materials**. 1999;11(12):3602-9.
44. Yamauchi Y, Momma T, Kitoh H, Osaka T, Kuroda K. Fabrication of mesoporous Pt inside micrometer channels via "solvent-evaporation-mediated direct physical casting". **Electrochemistry communications**. 2005;7(12):1364-70.
45. Nelson PA, Elliott JM, Attard GS, Owen JR. Mesoporous nickel/nickel oxide a nanoarchitected electrode. **Chemistry of materials**. 2002;14(2):524-9.
46. Bartlett PN, Birkin PN, Ghanem MA, de Groot P, Sawicki M. The electrochemical deposition of nanostructured cobalt films from lyotropic liquid crystalline media. **Journal of the Electrochemical Society**. 2001;148(2):C119.
47. Zhao D-D, Xu MW, Zhou W-J, Zhang J, Li HL. Preparation of ordered mesoporous nickel oxide film electrodes via lyotropic liquid crystal templated electrodeposition route. **Electrochimica Acta**. 2008;53(6):2699-705.
48. Zhou W-J, Zhao D-D, Xu M-W, Xu C-L, Li H-L. Effects of the electrodeposition potential and temperature on the electrochemical capacitance behavior of ordered mesoporous cobalt hydroxide films. **Electrochimica Acta**. 2008;53(24):7210-9.
49. Bender F, Mankelov RK, Hibbert DB, Gooding JJ. Lyotropic liquid crystal templating of groups 11 and 12 metal films. **Electroanalysis: An International Journal Devoted to Fundamental and Practical Aspects of Electroanalysis**. 2006;18(16):1558-63.
50. Luo K, Walker CT, Edler KJ. Mesoporous Silver Films from Dilute Mixed-Surfactant Solutions by Using Dip-Coating. **Advanced Materials**. 2007;19(11):1506-9.
51. Lim H, Kani K, Henzie J, Nagaura T, Nugraha AS, Iqbal M, et al. A universal approach for the synthesis of mesoporous gold, palladium and

- platinum films for applications in electrocatalysis. **Nature Protocols**. 2020;15(9):2980-3008.
52. Chen S-A, Lu K-T, Lin T-L, Chen J-M. Tailored Alloying Extent and Structural Evolution of Mesostructured PtRu Nanoparticles on Microemulsion Lyotropic Liquid-Crystalline Phases with Varied Heptane Concentrations. **The Journal of Physical Chemistry C**. 2016;120(43):24770-9.
  53. Yamauchi Y, Tonegawa A, Komatsu M, Wang H, Wang L, Nemoto Y, et al. Electrochemical synthesis of mesoporous Pt–Au binary alloys with tunable compositions for enhancement of electrochemical performance. **Journal of the American Chemical society**. 2012;134(11):5100-9.
  54. Attard GS, Leclerc SA, Maniguet S, Russell AE, Nandhakumar I, Bartlett PN. Mesoporous Pt/Ru alloy from the hexagonal lyotropic liquid crystalline phase of a nonionic surfactant. **Chemistry of materials**. 2001;13(5):1444-6.
  55. Yamauchi Y, Nair SS, Momma T, Ohsuna T, Osaka T, Kuroda K. Synthesis and characterization of mesoporous Pt–Ni (H<sub>1</sub>–Pt/Ni) alloy particles prepared from lyotropic liquid crystalline media. **Journal of Materials Chemistry**. 2006;16(23):2229-34.
  56. Callister WD, Rethwisch DG. **Materials science and engineering: William D. Callister, David G. Rethwisch**: Wiley; 2011.
  57. HIGHLIGHTS P. Platinum alloys: A selective review of the available literature. **Platinum Metals Rev**. 2013;57(3):202-13.
  58. Livingstone SE. **The Chemistry of Ruthenium, Rhodium, Palladium, Osmium, Iridium and Platinum: Pergamon Texts in Inorganic Chemistry, Volume 25**: Elsevier; 2016.
  59. Rao CR, Trivedi D. Chemical and electrochemical depositions of platinum group metals and their applications. **Coordination Chemistry Reviews**. 2005;249(5-6):613-31.
  60. Baumgärtner M, Raub J. The electrodeposition of platinum and platinum alloys. **Platinum Metals Review**. 1988;32(4):188-97.

61. Hyun S, Kraft O, Vinci RP. Mechanical behavior of Pt and Pt-Ru solid solution alloy thin films. **Acta materialia**. 2004;52(14):4199-211.
62. Baraka A, Hamed H, Shaarawy H. Electrodeposition of platinum metal and platinum-rhodium alloy on titanium substrates. **Journal of materials engineering and performance**. 2003;12(1):5-13.
63. Hu Y, Zhang H, Wu P, Zhang H, Zhou B, Cai C. Bimetallic Pt-Au nanocatalysts electrochemically deposited on graphene and their electrocatalytic characteristics towards oxygen reduction and methanol oxidation. **Physical Chemistry Chemical Physics**. 2011;13(9):4083-94.
64. Zaera F. Chirality in adsorption on solid surfaces. **Chemical Society Reviews**. 2017;46(23):7374-98.
65. Maher TJ, Johnson DA. Review of chirality and its importance in pharmacology. **Drug development research**. 1991;24(2):149-56.
66. Kasprzyk-Hordern B. Pharmacologically active compounds in the environment and their chirality. **Chemical Society Reviews**. 2010;39(11):4466-503.
67. Tian C, Xiu P, Meng Y, Zhao W, Wang Z, Zhou R. Enantiomerization mechanism of thalidomide and the role of water and hydroxide ions. **Chemistry – A European Journal**. 2012;18(45):14305-13.
68. Vargesson N. Thalidomide-induced teratogenesis: History and mechanisms. **Birth Defects Research Part C: Embryo Today: Reviews**. 2015;105(2):140-56.
69. Ogawa M, Murae M, Gemba R, Irie T, Shimojima M, Saijo M, et al. L-DOPA, a treatment for Parkinson's disease, and its enantiomer D-DOPA inhibit severe fever with thrombocytopenia syndrome virus infection in vitro. **Journal of Infection and Chemotherapy**. 2022;28(3):373-6.
70. Pàmies O, Bäckvall J-E. Combination of enzymes and metal catalysts. A powerful approach in asymmetric catalysis. **Chemical Reviews**. 2003;103(8):3247-62.
71. Roos G, Roos C. **Chapter 3 - Isomers and Stereochemistry**. In: Roos G, Roos C, editors. *Organic Chemistry Concepts*. Boston: Academic Press; 2015. p. 43-54.

72. Valev VK, Baumberg JJ, Sibilia C, Verbiest T. Chirality and chiroptical effects in plasmonic nanostructures: fundamentals, recent progress, and outlook. **Advanced Materials**. 2013;25(18):2517-34.
73. Xia Y, Zhou Y, Tang Z. Chiral inorganic nanoparticles: origin, optical properties and bioapplications. **Nanoscale**. 2011;3(4):1374-82.
74. Gellman AJ. Chiral surfaces: accomplishments and challenges. **ACS nano**. 2010;4(1):5-10.
75. Baiker A. Reflections on chiral metal surfaces and their potential for catalysis. **Catalysis Today**. 2005;100(1):159-70.
76. McFadden CF, Cremer PS, Gellman AJ. Adsorption of chiral alcohols on "Chiral" metal surfaces. **Langmuir**. 1996;12(10):2483-7.
77. Zor E, Bingol H, Ersoz M. Chiral sensors. **TrAC Trends in Analytical Chemistry**. 2019;121:115662.
78. Horvath JD, Koritnik A, Kamakoti P, Sholl DS, Gellman AJ. Enantioselective separation on a naturally chiral surface. **Journal of the American Chemical Society**. 2004;126(45):14988-94.
79. Sholl DS, Gellman AJ. Developing chiral surfaces for enantioselective chemical processing. **AIChE Journal**. 2009;55(10):2484-90.
80. Lorenzo MO, Haq S, Bertrams T, Murray P, Raval R, Baddeley C. Creating chiral surfaces for enantioselective heterogeneous catalysis: R, R-tartaric acid on Cu (110). **The Journal of Physical Chemistry B**. 1999;103(48):10661-9.
81. Humblot V, Raval R. Chiral metal surfaces from the adsorption of chiral and achiral molecules. **Applied surface science**. 2005;241(1-2):150-6.
82. Hazen RM, Sholl DS. Chiral selection on inorganic crystalline surfaces. **Nature Materials**. 2003;2(6):367-74.
83. Attard GA. Electrochemical studies of enantioselectivity at chiral metal surfaces. **The Journal of Physical Chemistry B**. 2001;105(16):3158-67.
84. Yang L, Liu J, Sun P, Ni Z, Ma Y, Huang Z. Chiral nanoparticles: Chiral ligand-free, optically active nanoparticles inherently composed of chiral lattices at the atomic scale. **Small**. 2020;16(24):2070134.

85. Switzer JA, Kothari HM, Poizot P, Nakanishi S, Bohannon EW. Enantiospecific electrodeposition of a chiral catalyst. **Nature**. 2003;425(6957):490-3.
86. Pachón LD, Yosef I, Markus T, Naaman R, Avnir D, Rothenberg G. Chiral imprinting of palladium with cinchona alkaloids. **Nature Chemistry**. 2009;1(2):160-4.
87. Wattanakit C, Saint Côme YB, Lapeyre V, Bopp PA, Heim M, Yadnum S, et al. Enantioselective recognition at mesoporous chiral metal surfaces. **Nature communications**. 2014;5(1):3325.
88. Yutthalekha T, Warakulwit C, Limtrakul J, Kuhn A. Enantioselective recognition of DOPA by mesoporous platinum imprinted with mandelic acid. **Electroanalysis**. 2015;27(9):2209-13.
89. Yutthalekha T, Wattanakit C, Lapeyre V, Nokbin S, Warakulwit C, Limtrakul J, et al. Asymmetric synthesis using chiral-encoded metal. **Nature communications**. 2016;7(1):12678.
90. Wattanakit C, Yutthalekha T, Assavapanumat S, Lapeyre V, Kuhn A. Pulsed electroconversion for highly selective enantiomer synthesis. **Nature communications**. 2017;8(1):2087.
91. Assavapanumat S, Ketkaew M, Kuhn A, Wattanakit C. Synthesis, characterization, and electrochemical applications of chiral imprinted mesoporous Ni surfaces. **Journal of the American Chemical Society**. 2019;141(47):18870-6.
92. Wattanakit C, Kuhn A. Encoding chiral molecular information in metal structures. **Chemistry – A European Journal**. 2020;26(14):2993-3003.
93. Schöck M, Otero R, Stojkovic S, Hümmelink F, Gourdon A, Stensgaard I, et al. Chiral close-packing of achiral star-shaped molecules on solid surfaces. **The Journal of Physical Chemistry B**. 2006;110(26):12835-8.
94. Izumi Y. **Modified Raney nickel (MRNi) catalyst: Heterogeneous enantio-differentiating (asymmetric) catalyst**. *Advances in catalysis*. 32: Elsevier; 1983. p. 215-71.

95. Shukla N, Gellman AJ. Chiral metal surfaces for enantioselective processes. **Nature Materials**. 2020;19(9):939-45.
96. Francis AJ, Salvador PA. Chirally oriented heteroepitaxial thin films grown by pulsed laser deposition: Pt(621) on SrTiO<sub>3</sub>(621). **Journal of Applied Physics**. 2004;96(5):2482-93.
97. Francis AJ, Koritnik AJ, Gellman A, Salvador PA. Chiral surfaces and metal/ceramic heteroepitaxy in the Pt/SrTiO<sub>3</sub>(621) system. **Surface Science**. 2007;601(9):1930-6.
98. Kelso MV, Tubbesing JZ, Chen Q, Switzer JA. Epitaxial electrodeposition of chiral metal surfaces on silicon(643). **Journal of the American Chemical Society**. 2018;140(46):15812-9.
99. BelBruno JJ. Molecularly imprinted polymers. **Chemical Reviews**. 2019;119(1):94-119.
100. Behar-Levy H, Neumann O, Naaman R, Avnir D. Chirality induction in bulk gold and silver. **Advanced Materials**. 2007;19(9):1207-11.
101. Assavapanumat S, Yuthalekha T, Garrigue P, Goudeau B, Lapeyre V, Perro A, et al. Potential-induced fine-tuning of the enantioaffinity of chiral metal phases. **Angewandte Chemie International Edition**. 2019;58(11):3471-5.
102. Assavapanumat S, Gupta B, Salinas G, Goudeau B, Wattanakit C, Kuhn A. Chiral platinum–polypyrrole hybrid films as efficient enantioselective actuators. **Chemical Communications**. 2019;55(73):10956-9.
103. Nasirpouri F. **Electrodeposition of Nanostructured Materials**: Springer International Publishing; 2016.
104. Zangari G. Electrodeposition of alloys and compounds in the era of microelectronics and energy conversion technology. **Coatings**. 2015;5(2):195-218.
105. Spieker WA, Liu J, Miller JT, Kropf AJ, Regalbuto JR. An EXAFS study of the co-ordination chemistry of hydrogen hexachloroplatinate(IV): 1. Speciation in aqueous solution. **Applied Catalysis A: General**. 2002;232(1):219-35.

106. Yasin HM, Denuault G, Pletcher D. Studies of the electrodeposition of platinum metal from a hexachloroplatinic acid bath. **Journal of Electroanalytical Chemistry**. 2009;633(2):327-32.
107. Knowles WS. Asymmetric hydrogenations (Nobel Lecture). **Angewandte Chemie International Edition**. 2002;41(12):1998-2007.
108. Noyori R. Asymmetric catalysis: science and opportunities (Nobel Lecture). **Angewandte Chemie International Edition**. 2002;41(12):2008-22.
109. Sharpless KB. Searching for new reactivity (Nobel Lecture). **Angewandte Chemie International Edition**. 2002;41(12):2024-32.
110. Hargittai I. The 2021 chemistry Nobel laureates and asymmetric organocatalysis. **Structural Chemistry**. 2022;33(1):303-5.
111. List B, Lerner RA, Barbas CF. Proline-catalyzed direct asymmetric aldol reactions. **Journal of the American Chemical Society**. 2000;122(10):2395-6.
112. Ahrendt KA, Borths CJ, MacMillan DWC. New strategies for organic catalysis: The first highly enantioselective organocatalytic Diels–Alder reaction. **Journal of the American Chemical Society**. 2000;122(17):4243-4.
113. Laidler KJ. A glossary of terms used in chemical kinetics, including reaction dynamics (IUPAC Recommendations 1996). **Pure and Applied Chemistry**. 1996;68(1):149-92.
114. NobelPrize.org. **Popular information, The Nobel Prize in Chemistry 2001**: Nobel Prize Outreach AB; 2022 [Available from: <<https://www.nobelprize.org/prizes/chemistry/2001/popular-information/>>].
115. Zaera F. Regio-, stereo-, and enantioselectivity in hydrocarbon conversion on metal surfaces. **Accounts of Chemical Research**. 2009;42(8):1152-60.
116. Gladiali S. Guidelines and methodologies in asymmetric synthesis and catalysis. **Comptes Rendus Chimie**. 2007;10(3):220-31.

117. Wiebe A, Gieshoff T, Möhle S, Rodrigo E, Zirbes M, Waldvogel SR. Electrifying organic synthesis. **Angewandte Chemie International Edition**. 2018;57(20):5594-619.
118. Liu Z, Deng Z, Davis SJ, Giron C, Ciais P. Monitoring global carbon emissions in 2021. **Nature Reviews Earth & Environment**. 2022;3(4):217-9.
119. Ghosh M, Shinde VS, Rueping M. A review of asymmetric synthetic organic electrochemistry and electrocatalysis: concepts, applications, recent developments and future directions. **Beilstein Journal of Organic Chemistry**. 2019;15:2710-46.
120. Schotten C, Nicholls TP, Bourne RA, Kapur N, Nguyen BN, Willans CE. Making electrochemistry easily accessible to the synthetic chemist. **Green Chemistry**. 2020;22(11):3358-75.
121. Pollok D, Waldvogel SR. Electro-organic synthesis – a 21<sup>st</sup> century technique. **Chemical Science**. 2020;11(46):12386-400.
122. Panke S, Held M, Wubbolts M. Trends and innovations in industrial biocatalysis for the production of fine chemicals. **Current opinion in Biotechnology**. 2004;15(4):272-9.
123. Yamamoto K, Kuriyama M, Onomura O. Asymmetric electrosynthesis: Recent advances in catalytic transformations. **Current Opinion in Electrochemistry**. 2021;28:100714.
124. Yang H-P, Wang H, Lu J-X. Alkaloid-induced asymmetric hydrogenation on a Cu nanoparticle cathode by electrochemical conditions. **Electrochemistry Communications**. 2015;55:18-21.
125. Yang H-P, Fen Q, Wang H, Lu J-X. Copper encapsulated alkaloids composite: An effective heterogeneous catalyst for electrocatalytic asymmetric hydrogenation. **Electrochemistry Communications**. 2016;71:38-42.
126. Yue Y-N, Wu D, Zeng S, Yang M-P, Wang H, Lu J-X. Alkaloid-induced asymmetric hydrogenation on bimetallic Pt@Cu cathodes under electrochemical conditions. **New Journal of Chemistry**. 2017;41(16):7853-6.

127. Blaser H, Spindler F, Studer M. Enantioselective catalysis in fine chemicals production. **Applied Catalysis A: General**. 2001;221(1-2):119-43.
128. Heitbaum M, Glorius F, Escher I. Asymmetric heterogeneous catalysis. **Angewandte Chemie International Edition**. 2006;45(29):4732-62.
129. Xie R, Chu L-Y, Deng J-G. Membranes and membrane processes for chiral resolution. **Chemical Society Reviews**. 2008;37(6):1243-63.
130. Wang Y, Chen AM. Enantioenrichment by Crystallization. **Organic Process Research & Development**. 2008;12(2):282-90.
131. Frontana-Urbe BA, Little RD, Ibanez JG, Palma A, Vasquez-Medrano R. Organic electrosynthesis: a promising green methodology in organic chemistry. **Green Chemistry**. 2010;12(12):2099-119.
132. Chang X, Zhang Q, Guo C. Asymmetric electrochemical transformations. **Angewandte Chemie International Edition**. 2020;59:12612.
133. Zhang F, Li H. Water-medium organic synthesis over active and reusable organometal catalysts with tunable nanostructures. **Chemical Science**. 2014;5(10):3695-707.
134. Ghosh M, Shinde VS, Rueping M. A review of asymmetric synthetic organic electrochemistry and electrocatalysis: concepts, applications, recent developments and future directions. **Beilstein Journal of Organic Chemistry**. 2019;15(1):2710-46.
135. Moutet J-C, Saintl-Aman E, Tran-Van F, Angibeaud P, Utile J-P. Poly(glucose-pyrrole) modified electrodes: A novel chiral electrode for enantioselective recognition. **Advanced Materials**. 1992;4(7-8):511-3.
136. Dong L, Zhang Y, Duan X, Zhu X, Sun H, Xu J. Chiral PEDOT-based enantioselective electrode modification material for chiral electrochemical sensing: mechanism and model of chiral recognition. **Analytical Chemistry**. 2017;89(18):9695-702.
137. Mallat T, Orglmeister E, Baiker A. Asymmetric catalysis at chiral metal surfaces. **Chemical Reviews**. 2007;107(11):4863-90.

138. Bohannon EW, Kothari HM, Nacic IM, Switzer JA. Enantiospecific electrodeposition of chiral CuO films on single-crystal Cu(111). **Journal of the American Chemical Society**. 2004;126(2):488-9.
139. Gottarelli G, Lena S, Masiero S, Pieraccini S, Spada GP. The use of circular dichroism spectroscopy for studying the chiral molecular self-assembly: An overview. **Chirality**. 2008;20(3-4):471-85.
140. Wattanakit C. Chiral metals as electrodes. **Current Opinion in Electrochemistry**. 2018;7:54-60.
141. Wattanakit C, Kuhn A. Encoding chiral molecular information in metal structures. **Chemistry—A European Journal**. 2020;26:2993.
142. Nelson PA, Elliott JM, Attard GS, Owen JR. Mesoporous nickel/nickel oxide nanoarchitected electrode. **Chemistry of Materials**. 2002;14(2):524-9.
143. Evans SAG, Elliott JM, Andrews LM, Bartlett PN, Doyle PJ, Denuault G. Detection of hydrogen peroxide at mesoporous platinum microelectrodes. **Analytical Chemistry**. 2002;74(6):1322-6.
144. Imokawa T, Williams K-J, Denuault G. Fabrication and characterization of nanostructured Pd hydride pH microelectrodes. **Analytical Chemistry**. 2006;78(1):265-71.
145. Neouze M-A, Schubert U. Surface modification and functionalization of metal and metal oxide nanoparticles by organic ligands. **Monatshefte für Chemie - Chemical Monthly**. 2008;139(3):183-95.
146. Mandal S, Phadtare S, Sastry M. Interfacing biology with nanoparticles. **Current Applied Physics**. 2005;5(2):118-27.
147. Dong BH, Hinstroza JP. Metal nanoparticles on natural cellulose fibers: Electrostatic assembly and *in-situ* synthesis. **ACS Applied Materials & Interfaces**. 2009;1(4):797-803.
148. Jadhav S. Self-assembled monolayers (SAMs) of carboxylic acids: an overview. **Open Chemistry**. 2011;9(3):369-78.
149. Guay-Bégin A-A, Chevallier P, Faucher L, Turgeon S, Fortin M-A. Surface modification of gadolinium oxide thin films and nanoparticles using poly(ethylene glycol)-phosphate. **Langmuir**. 2012;28(1):774-82.

150. Kang X, Chen S. Electronic conductivity of alkyne-capped ruthenium nanoparticles. **Nanoscale**. 2012;4(14):4183-9.
151. Ramanath G, Cui G, Ganesan PG, Guo X, Ellis AV, Stukowski M, et al. Self-assembled subnanolayers as interfacial adhesion enhancers and diffusion barriers for integrated circuits. **Applied Physics Letters**. 2003;83(2):383-5.
152. Ghilane J, Delamar M, Guilloux-Viry M, Lagrost C, Mangeney C, Hapiot P. Indirect reduction of aryldiazonium salts onto cathodically activated platinum surfaces: Formation of metal-organic structures. **Langmuir**. 2005;21(14):6422-9.
153. Noël J-M, Zigah D, Simonet J, Hapiot P. Synthesis and immobilization of Ag<sup>0</sup> nanoparticles on diazonium modified electrodes: SECM and cyclic voltammetry studies of the modified interfaces. **Langmuir**. 2010;26(10):7638-43.
154. Marshall ST, O'Brien M, Oetter B, Corpuz A, Richards RM, Schwartz DK, et al. Controlled selectivity for palladium catalysts using self-assembled monolayers. **Nature Materials**. 2010;9(10):853-8.
155. Jin L, Liu B, Duay SS, He J. Engineering surface ligands of noble metal nanocatalysts in tuning the product selectivity. **Catalysts**. 2017;7(2):44.
156. Eklund SE, Cliffl DE. Synthesis and catalytic properties of soluble platinum nanoparticles protected by a thiol monolayer. **Langmuir**. 2004;20(14):6012-8.
157. Vericat C, Vela M, Benitez G, Carro P, Salvarezza R. Self-assembled monolayers of thiols and dithiols on gold: new challenges for a well-known system. **Chemical Society Reviews**. 2010;39(5):1805-34.
158. Hopkinson MN, Richter C, Schedler M, Glorius F. An overview of N-heterocyclic carbenes. **Nature**. 2014;510(7506):485-96.
159. Engel S, Fritz E-C, Ravoo BJ. New trends in the functionalization of metallic gold: from organosulfur ligands to N-heterocyclic carbenes. **Chemical Society Reviews**. 2017;46(8):2057-75.
160. Cao Z, Kim D, Hong D, Yu Y, Xu J, Lin S, et al. A Molecular surface functionalization approach to tuning nanoparticle electrocatalysts for

- carbon dioxide reduction. **Journal of the American Chemical Society**. 2016;138(26):8120-5.
161. Zhang L, Wei Z, Thanneeru S, Meng M, Kruzyk M, Ung G, et al. A polymer solution to prevent nanoclustering and improve the selectivity of metal nanoparticles for electrocatalytic CO<sub>2</sub> reduction. **Angewandte Chemie International Edition**. 2019;58(44):15834-40.
162. Floridia Addato MA, Rubert A, Benítez G, Zelaya E, Cabello G, Cuesta A, et al. Electrochemical desorption of thiolates and sulfur from nanoparticle and planar platinum surfaces. **The Journal of Physical Chemistry C**. 2013;117(15):7589-97.
163. Floridia Addato MaA, Rubert AA, Benítez GA, Fonticelli MH, Carrasco J, Carro P, et al. Alkanethiol adsorption on platinum: chain length effects on the quality of self-assembled monolayers. **The Journal of Physical Chemistry C**. 2011;115(36):17788-98.
164. Łukaszewski M, Soszko M, Czerwiński A. Electrochemical methods of real surface area determination of noble metal electrodes—an overview. **International Journal of Electrochemical Science**. 2016;11(6):4442-69.
165. Himmelhaus M, Gauss I, Buck M, Eisert F, Wöll C, Grunze M. Adsorption of docosanethiol from solution on polycrystalline silver surfaces: an XPS and NEXAFS study. Presented at the Todai Symposium 1997 and the 6th ISSP International Symposium on Frontiers in Synchrotron Radiation Spectroscopy, Tokyo, Japan, 27–30 October 1997.1. **Journal of Electron Spectroscopy and Related Phenomena**. 1998;92(1):139-49.
166. Kakiuchi T, Sato K, Iida M, Hobara D, Imabayashi S-i, Niki K. Phase separation of alkanethiol self-assembled monolayers during the replacement of adsorbed thiolates on Au(111) with thiols in solution. **Langmuir**. 2000;16(18):7238-44.
167. Finklea H, Yoon K, Chamberlain E, Allen J, Haddox R. Effect of the metal on electron transfer across self-assembled monolayers. **The Journal of Physical Chemistry B**. 2001;105(15):3088-92.

168. Rouhana LL, Moussallem MD, Schlenoff JB. Adsorption of short-chain thiols and disulfides onto gold under defined mass transport conditions: Coverage, kinetics, and mechanism. **Journal of the American Chemical Society**. 2011;133(40):16080-91.
169. Losic D, Shapter J, Gooding J. Concentration dependence in microcontact printing of self-assembled monolayers (SAMs) of alkanethiols. **Electrochemistry communications**. 2001;3(12):722-6.
170. Wilbur JL, Kumar A, Kim E, Whitesides GM. Microfabrication by microcontact printing of self-assembled monolayers. **Advanced Materials**. 1994;6(7-8):600-4.
171. Perl A, Reinhoudt DN, Huskens J. Microcontact printing: limitations and achievements. **Advanced Materials**. 2009;21(22):2257-68.
172. Kuhn A, Martel D. Localized electrodeposition by patterned redox-active monolayers. **ChemPhysChem**. 2001;2(11):688-91.
173. Butcha S, Assavapanumat S, Ittisanronnachai S, Lapeyre V, Wattanakit C, Kuhn A. Nanoengineered chiral Pt-Ir alloys for high-performance enantioselective electrosynthesis. **Nature Communications**. 2021;12(1):1314.
174. Assavapanumat S, Butcha S, Ittisanronnachai S, Kuhn A, Wattanakit C. Heterogeneous enantioselective catalysis with chiral encoded mesoporous Pt-Ir films supported on Ni foam. **Chemistry – An Asian Journal**. 2021;16(21):3345-53.
175. Kodama Y, Imoto M, Ohta N, Kitani A, Ito S. Selective reduction of acetophenone to 1-phenylethanol in aqueous media. **Journal of Electroanalytical Chemistry**. 2001;507(1):103-9.
176. Cantu DC, Padmaperuma AB, Nguyen M-T, Akhade SA, Yoon Y, Wang Y-G, et al. Erratum to “A Combined Experimental and Theoretical Study on the Activity and Selectivity of the Electrocatalytic Hydrogenation of Aldehydes”. **ACS Catalysis**. 2019;9(3):1738-.
177. Bondue CJ, Koper MTM. Electrochemical reduction of the carbonyl functional group: The importance of adsorption geometry, molecular

- structure, and electrode surface structure. **Journal of the American Chemical Society**. 2019;141(30):12071-8.
178. Matanović I. Selectivity control for electroreduction of ketones. **Nature Catalysis**. 2019;2(3):186-7.
179. Maier NM, Franco P, Lindner W. Separation of enantiomers: needs, challenges, perspectives. **Journal of Chromatography A**. 2001;906(1-2):3-33.
180. Bloom B, Lu Y, Metzger T, Yochelis S, Paltiel Y, Fontanesi C, et al. Asymmetric reactions induced by electron spin polarization. **Physical Chemistry Chemical Physics**. 2020;22:21570-82.
181. Yoon TP, Jacobsen EN. Privileged chiral catalysts. **Science**. 2003;299(5613):1691-3.
182. Avnir D. Molecularly doped metals. **Accounts of Chemical Research**. 2014;47(2):579-92.
183. Chen L, Wang X, Lu W, Wu X, Li J. Molecular imprinting: perspectives and applications. **Chemical Society Reviews**. 2016;45(8):2137-211.
184. Katz A, Davis ME. Molecular imprinting of bulk, microporous silica. **Nature**. 2000;403(6767):286-9.
185. Elgavi H, Krekeler C, Berger R, Avnir D. Chirality in copper nanoalloy clusters. **The Journal of Physical Chemistry C**. 2012;116(1):330-5.
186. El Sawy EN, Birss VI. A comparative study of the electrodeposition of nanoporous Ir and Pt thin films. **Journal of The Electrochemical Society**. 2013;160(9):386-93.
187. Sawy ENE, Molero HM, Birss VI. Methanol oxidation at porous co-electrodeposited Pt-Ir thin films. **Electrochimica Acta**. 2014;117:202-10.
188. Kwon S, Ham DJ, Kim T, Kwon Y, Lee SG, Cho M. Active methanol oxidation reaction by enhanced CO tolerance on bimetallic Pt/Ir electrocatalysts using electronic and bifunctional effects. **ACS Applied Materials & Interfaces**. 2018;10(46):39581-9.
189. Kwon S, Ham DJ, Lee SG. Enhanced H<sub>2</sub> dissociative phenomena of Pt-Ir electrocatalysts for PEMFCs: an integrated experimental and theoretical study. **RSC Advances**. 2015;5(68):54941-6.

190. Wu F, Murakami H, Yamabe-Mitarai Y, Harada H, Katayama H, Yamamoto Y. Electrodeposition of Pt–Ir alloys on nickel-base single crystal superalloy TMS-75. **Surface and Coatings Technology**. 2004;184(1):24-30.
191. Bu L, Ding J, Guo S, Zhang X, Su D, Zhu X, et al. A General method for multimetallic platinum alloy nanowires as highly active and stable oxygen reduction catalysts. **Advanced Materials**. 2015;27(44):7204-12.
192. Ramírez-Crescencio F, Redón R, Herrera-Gomez A, Gomez-Sosa G, Bravo-Sanchez M, Fernandez-Osorio A-L. Facile obtaining of Iridium (0), Platinum (0) and Platinum (0)-Iridium (0) alloy nanoparticles and the catalytic reduction of 4-nitrophenol. **Materials Chemistry and Physics**. 2017;201:289-96.
193. Zhu J, Sakaushi K, Clavel G, Shalom M, Antonietti M, Fellingner T-P. A general salt-templating method to fabricate vertically aligned graphitic carbon nanosheets and their metal carbide hybrids for superior lithium ion batteries and water splitting. **Journal of the American Chemical Society**. 2015;137(16):5480-5.
194. Yang X, Lin Z, Zheng J, Huang Y, Chen B, Mai Y, et al. Facile template-free synthesis of vertically aligned polypyrrole nanosheets on nickel foams for flexible all-solid-state asymmetric supercapacitors. **Nanoscale**. 2016;8(16):8650-7.
195. Huynh TT, Dang NN, Pham HQ. Bimetallic PtIr nanoalloy on TiO<sub>2</sub>-based solid solution oxide with enhanced oxygen reduction and ethanol electro-oxidation performance in direct ethanol fuel cells. **Catalysis Science & Technology**. 2021;11(4):1571-9.
196. Assavapanumat S, Ketkaew M, Garrigue P, Lapeyre V, Reculosa S, Wattanakit C, et al. Hierarchical multiporous nickel for oxygen evolution reaction in alkaline media. **ChemCatChem**. 2019;11(24):5834-.
197. Dorovskikh SI, Vikulova ES, Kal'nyi DB, Shubin YV, Asanov I, Maximovskiy EA, et al. Bimetallic Pt, Ir-containing coatings formed by MOCVD for medical applications. **Journal of Materials Science: Materials in Medicine**. 2019;30(6):1-12.

198. Sioncke S, Verbiest T, Persoons A. Second-order nonlinear optical properties of chiral materials. **Materials Science and Engineering: R: Reports**. 2003;42(5-6):115-55.
199. Kauranen M, Verbiest T, Persoons A. Chiral materials in second-order nonlinear optics. **Journal of Nonlinear Optical Physics & Materials**. 1999;08(02):171-89.
200. Kauranen M, Verbiest T, Maki JJ, Persoons A. Second-harmonic generation from chiral surfaces. **The Journal of chemical physics**. 1994;101(9):8193-9.
201. Maki JJ, Kauranen M, Persoons A. Surface second-harmonic generation from chiral materials. **Physical review B**. 1995;51(3):1425.
202. Verbiest T, Kauranen M, Persoons A. Second-order nonlinear optical properties of chiral thin films. **Journal of Materials Chemistry**. 1999;9(9):2005-12.
203. Wattanakit C. **Élaboration et application de matériaux poreux: études théoriques et expérimentales**: Bordeaux 1; 2013.
204. Priyadarshi S, Racu A, Pierz K, Siegner U, Bieler M, Duc H, et al. Reversal of coherently controlled ultrafast photocurrents by band mixing in undoped GaAs quantum wells. **Physical review letters**. 2010;104(21):217401.
205. Richardson F. Iridium as a high temperature material. **Platinum Metals Review**. 1958;2(3):83-5.
206. Butcha S, Lapeyre V, Wattanakit C, Kuhn A. Self-assembled monolayer protection of chiral-imprinted mesoporous platinum electrodes for highly enantioselective synthesis. **Chemical science**. 2022;13(8):2339-46.
207. Todoroki N, Watanabe H, Kondo T, Kaneko S, Wadayama T. Highly enhanced oxygen reduction reaction activity and electrochemical stability of Pt/Ir (111) bimetallic surfaces. **Electrochimica Acta**. 2016;222:1616-21.
208. Fadoni M, Lucarelli L. Temperature programmed desorption, reduction, oxidation and flow chemisorption for the characterisation of heterogeneous catalysts. Theoretical aspects, instrumentation and

- applications. **Studies in surface science and catalysis**. 1999;120:177-225.
209. Walczak MM, Dryer DA, Jacobson DD, Foss MG, Flynn NT. pH dependent redox couple: An illustration of the Nernst equation. **Journal of Chemical Education**. 1997;74(10):1195.
210. Prinz J, Gröning O, Brune H, Widmer R. Highly enantioselective adsorption of small prochiral molecules on a chiral intermetallic compound. **Angewandte Chemie**. 2015;127(13):3974-8.
211. Gao P, Lin CH, Shannon C, Salaita GN, White JH, Chaffins SA, et al. Studies of adsorbed saturated alcohols at platinum(111) electrodes by vibrational spectroscopy (EELS), Auger spectroscopy, and electrochemistry. **Langmuir**. 1991;7(7):1515-24.
212. Hilmi A, Belgsir EM, Le'ger JM, Lamy C. Electrocatalytic oxidation of aliphatic diols on platinum and gold Part I: Effects of chain length and isomeric position. **Journal of Electroanalytical Chemistry**. 1995;380(1):177-84.
213. Hazzazi OA, Attard GA, Wells PB. Molecular recognition in adsorption and electro-oxidation at chiral platinum surfaces. **Journal of Molecular Catalysis A: Chemical**. 2004;216(2):247-55.
214. Jacobse L, Rost MJ, Koper MTM. Atomic-scale identification of the electrochemical roughening of platinum. **ACS Central Science**. 2019;5(12):1920-8.
215. Dean J, Taylor MG, Mpourmpakis G. Unfolding adsorption on metal nanoparticles: Connecting stability with catalysis. **Science advances**. 2019;5(9):eaax5101.
216. Pinheiro Pires AP, Arauzo J, Fonts I, Domine ME, Fernández Arroyo A, Garcia-Perez ME, et al. Challenges and opportunities for bio-oil refining: A review. **Energy & Fuels**. 2019;33(6):4683-720.
217. Mohan D, Pittman CU, Steele PH. Pyrolysis of wood/biomass for bio-oil: A critical review. **Energy & Fuels**. 2006;20(3):848-89.

218. Lin SD, Sanders DK, Albert Vannice M. Influence of metal-support effects on acetophenone hydrogenation over platinum. **Applied Catalysis A: General**. 1994;113(1):59-73.
219. Lopez-Ruiz JA, Andrews E, Akhade SA, Lee M-S, Koh K, Sanyal U, et al. Understanding the role of metal and molecular structure on the electrocatalytic hydrogenation of oxygenated organic compounds. **ACS Catalysis**. 2019;9(11):9964-72.
220. Argyle MD, Bartholomew CH. Heterogeneous catalyst deactivation and regeneration: a review. **Catalysts**. 2015;5(1):145-269.
221. Chen Z, Wang Q, Wu X, Li Z, Jiang Y-B. Optical chirality sensing using macrocycles, synthetic and supramolecular oligomers/polymers, and nanoparticle based sensors. **Chemical Society Reviews**. 2015;44(13):4249-63.
222. Trojanowicz M. Enantioselective electrochemical sensors and biosensors: A mini-review. **Electrochemistry Communications**. 2014;38:47-52.
223. Zhang X, Yin J, Yoon J. Recent advances in development of chiral fluorescent and colorimetric sensors. **Chemical reviews**. 2014;114(9):4918-59.
224. Tokunaga T, Okamoto M, Tanaka K, Tode C, Sugiura M. Chiral liquid chromatography– circular dichroism– NMR for estimating separation conditions of chiral HPLC without authentic samples. **Analytical chemistry**. 2010;82(10):4293-7.
225. McCarroll ME, Billiot FH, Warner IM. Fluorescence anisotropy as a measure of chiral recognition. **Journal of the American Chemical Society**. 2001;123(13):3173-4.
226. Lämmerhofer M. Chiral recognition by enantioselective liquid chromatography: mechanisms and modern chiral stationary phases. **Journal of Chromatography A**. 2010;1217(6):814-56.
227. Bigdeli A, Ghasemi F, Fahimi-Kashani N, Abbasi-Moayed S, Orouji A, Ivrih ZJ-N, et al. Optical nanoprobe for chiral discrimination. **Analyst**. 2020;145(20):6416-34.

228. Scriba GK. Chiral recognition in separation science—an update. **Journal of Chromatography a**. 2016;1467:56-78.
229. Dong J, Lu Y, Xu Y, Chen F, Yang J, Chen Y, et al. Direct imaging of single-molecule electrochemical reactions in solution. **Nature**. 2021;596(7871):244-9.
230. Liu Y, Zhang H, Li B, Liu J, Jiang D, Liu B, et al. Single biomolecule imaging by electrochemiluminescence. **Journal of the American Chemical Society**. 2021;143(43):17910-4.
231. Dong J, Xu Y, Zhang Z, Feng J. Operando imaging of chemical activity on gold plates with single-molecule electrochemiluminescence microscopy. **Angewandte Chemie**. 2022;134(14):e202200187.
232. Sojic N. **Analytical electrogenerated chemiluminescence: from fundamentals to bioassays**: Royal Society of Chemistry; 2019.
233. Han D, Goudeau B, Manojlovic D, Jiang D, Fang D, Sojic N. Electrochemiluminescence loss in photobleaching. **Angewandte Chemie**. 2021;133(14):7764-8.
234. Guo W, Ding H, Gu C, Liu Y, Jiang X, Su B, et al. Potential-resolved multicolor electrochemiluminescence for multiplex immunoassay in a single sample. **Journal of the American Chemical Society**. 2018;140(46):15904-15.
235. Zanut A, Fiorani A, Canola S, Saito T, Ziebart N, Rapino S, et al. Insights into the mechanism of coreactant electrochemiluminescence facilitating enhanced bioanalytical performance. **Nature communications**. 2020;11(1):2668.
236. Du F, Chen Y, Meng C, Lou B, Zhang W, Xu G. Recent advances in electrochemiluminescence immunoassay based on multiple-signal strategy. **Current Opinion in Electrochemistry**. 2021;28:100725.
237. Hesari M, Ding Z. Electrogenenerated chemiluminescence: light years ahead. **Journal of The Electrochemical Society**. 2015;163(4):H3116.
238. Ahmadi A, Attard G, Feliu J, Rodes A. Surface reactivity at “chiral” platinum surfaces. **Langmuir**. 1999;15(7):2420-4.

239. Toda T, Igarashi H, Uchida H, Watanabe M. Enhancement of the electroreduction of oxygen on Pt alloys with Fe, Ni, and Co. **Journal of The Electrochemical Society**. 2019;146(10):3750-6.
240. Stamenkovic VR, Fowler B, Mun BS, Wang G, Ross PN, Lucas CA, et al. Improved oxygen reduction activity on Pt<sub>3</sub>/Ni(111) *via* Increased Surface Site Availability. **Science**. 2007;315(5811):493.
241. Voci S, Zinna F, Arrico L, Grass S, Bouffier L, Lacour J, et al. Chiroptical detection of a model ruthenium dye in water by circularly polarized-electrochemiluminescence. **Chemical Communications**. 2020;56(44):5989-92.
242. Zinna F, Voci S, Arrico L, Brun E, Homberg A, Bouffier L, et al. Circularly-polarized electrochemiluminescence from a chiral bispyrene organic macrocycle. **Angewandte Chemie International Edition**. 2019;58(21):6952-6.
243. Liu C, Yao J, Xiao C, Zhao T, Selvapalam N, Zhou C, et al. Electrochemiluminescent chiral discrimination with a pillar [5] arene molecular universal joint-coordinated ruthenium complex. **Organic Letters**. 2021;23(10):3885-90.
244. Lin X, Zhu S, Wang Q, Xia Q, Ran P, Fu Y. Chiral recognition of penicillamine enantiomers using hemoglobin and gold nanoparticles functionalized graphite-like carbon nitride nanosheets via electrochemiluminescence. **Colloids and Surfaces B: Biointerfaces**. 2016;148:371-6.
245. Song Y, Lu S, Hai J, Liang K, Sun S, Meng G, et al. Nitrogen-doped chiral CuO/CoO Nanofibers: An enhanced electrochemiluminescence sensing strategy for detection of 3, 4-Dihydroxy-phenylalanine enantiomers. **Analytical Chemistry**. 2021;93(33):11470-8.
246. Zhao C, Xu S, Su Y, Zhao G. Chiral discrimination for enantiomers of amino acids using an electrochemiluminescence method. **Analyst**. 2002;127(7):889-91.
247. Miao W, Choi J-P, Bard AJ. Electrogenated chemiluminescence 69: The Tris (2,2'-bipyridine) ruthenium (II),(Ru(bpy)<sub>3</sub><sup>2+</sup>)/tri-*n*-propylamine

- (TPrA) system revisited A new route involving TPrA<sup>•+</sup> cation radicals. **Journal of the American Chemical Society**. 2002;124(48):14478-85.
248. Klymenko OV, Svir I, Amatore C. A new approach for the simulation of electrochemiluminescence (ECL). **ChemPhysChem**. 2013;14(10):2237-50.
249. Sentic M, Milutinovic M, Kanoufi F, Manojlovic D, Arbault S, Sojic N. Mapping electrogenerated chemiluminescence reactivity in space: mechanistic insight into model systems used in immunoassays. **Chemical Science**. 2014;5(6):2568-72.
250. Hersbach TJ, Ye C, Garcia AC, Koper MT. Tailoring the electrocatalytic activity and selectivity of Pt (111) through cathodic corrosion. **ACS Catalysis**. 2020;10(24):15104-13.
251. Olsson L, Fridell E. The influence of Pt oxide formation and Pt dispersion on the reactions  $\text{NO}_2 \rightleftharpoons \text{NO} + 1/2 \text{O}_2$  over Pt/Al<sub>2</sub>O<sub>3</sub> and Pt/BaO/Al<sub>2</sub>O<sub>3</sub>. **Journal of Catalysis**. 2002;210(2):340-53.
252. Gattrell M, Kirk D. A study of the oxidation of phenol at platinum and preoxidized platinum surfaces. **Journal of the Electrochemical Society**. 1993;140(6):1534.
253. Zu Y, Bard AJ. Electrogenerated chemiluminescence. 66. The role of direct coreactant oxidation in the ruthenium Tris (2,2') bipyridyl/triethylamine system and the effect of halide ions on the emission intensity. **Analytical chemistry**. 2000;72(14):3223-32.
254. Naaman R, Waldeck DH. Chiral-induced spin selectivity effect. **The journal of physical chemistry letters**. 2012;3(16):2178-87.
255. Ghosh K, Zhang W, Tassinari F, Mastai Y, Lidor-Shalev O, Naaman R, et al. Controlling chemical selectivity in electrocatalysis with chiral CuO-coated electrodes. **The Journal of Physical Chemistry C**. 2019;123(5):3024-31.
256. Zhang W, Banerjee-Ghosh K, Tassinari F, Naaman R. Enhanced electrochemical water splitting with chiral molecule-coated Fe<sub>3</sub>O<sub>4</sub> nanoparticles. **ACS Energy Letters**. 2018;3(10):2308-13.

## Author's Biography

- Name:** SOPON BUTCHA
- Date of Birth:** 24 February, 1995
- Place of Birth:** Maha Sarakham, Thailand
- Current Address:** 182 Moo 9 Khaow, Mueang, Maha Sarakham 44000
- Education:** Bachelor of Science in Chemistry (Honours program), First-class honours, Suranaree University of Technology, Nakhon Ratchasima, Thailand (2013-2016)
- Doctor of Philosophy in Materials Science and Engineering (International program), Vidyasirimedhi Institute of Science and Technology, Rayong, Thailand (2017-2021)
- Doctor of Philosophy in Physical Chemistry, University of Bordeaux, France (2018-2021)
- Scholarship:** Recipient of the full scholarship from Vidyasirimedhi Institute of Science and Technology (VISTEC)
- Recipient of the Franco-Thai Scholarship Program from French Embassy
- Recipient of the graduate research fund from the National Research Council of Thailand (NRCT) (N41B650204)
- Academic Publication:** **Butcha S**, Yu J, Pasom Z, Bertrand G, Wattanakit C, Sojic N, Kuhn A. Electrochemiluminescent enantioselective detection with chiral-imprinted

mesoporous metal surfaces. **Chemical Communication**. 2022; (*Accepted Manuscript*)

**Butcha S**, Lapeyre V, Wattanakit C, Kuhn A. Self-assembled monolayer protection of chiral-imprinted mesoporous platinum electrodes for highly enantioselective synthesis. **Chemical Science**. 2022;13(8):2339-46.

Assavapanumat S, **Butcha S**, Ittisanronnachai S, Kuhn A, Wattanakit C. Heterogeneous enantioselective catalysis with chiral encoded mesoporous Pt-Ir films supported on Ni foam. **Chemistry - An Asian Journal**. 2021;16(21):3345-53.

**Butcha S**, Assavapanumat S, Ittisanronnachai S, Lapeyre V, Wattanakit C, Kuhn A. Nanoengineered chiral Pt-Ir alloys for high-performance enantioselective electrosynthesis. **Nature Communications**. 2021;12(1):1314.

Suttipat D, **Butcha S**, Assavapanumat S, Maihom T, Gupta B, Perro A, Sojic N, Kuhn A, Wattanakit C. Chiral macroporous MOF surfaces for electroassisted enantioselective adsorption and separation. **ACS Applied Materials & Interfaces**. 2020;12(32): 36548-57.